The influence of dipolar doping on charge injection and transport in small molecular organic semiconductors

Dissertation

zur Erlangung des akademischen Grades

Dr. rer. nat.

eingereicht an der

Mathematisch-Naturwissenschaftlich-Technischen Fakultät

der Universität Augsburg

von

Alexander Johann Ludwig Hofmann

Augsburg, Februar 2020

1. Gutachter: Prof. Dr. Wolfgang Brütting
2. Gutachter: Prof. Dr. Hubert Krenner
Datum der mündlichen Prüfung: 8. Juli 2020

Abstract

The present work investigates the effect of dipolar doping on charge injection and charge carrier dynamics in organic semiconducting thin films. In this context, the term dipolar doping refers to the dilution or doping of a non-polar matrix molecule with a polar guest. For this purpose, the hole-conductors *N*,*N*'-Di(1-naphthyl)-*N*,*N*'-diphenyl-(1,1'-biphenyl)-4,4'-diamine (NPB) and 4,4-*N*,*N*'-Dicarbazole-1,1'-biphenyl (CBP) will serve as the host molecules. Dopants include Tris-(8-hydroxyquinoline) aluminum (Alq_3) and OXD-7 (1,3-bis[2-(4-tert-butylphenyl)-1,3,4-oxadiazo-5-yl]benzene. The main focus, however, is on the system NPB:Alq_3, which has also been studied extensively in the past [1–3].

In general, doping of (organic) semiconductors is a well known concept to tune conductivity [4] or optimize emitting properties of OLEDs [5]. The specific effect of doping with polar species, however, was not thoroughly investigated so far, although many guest molecules are indeed polar [6]. Because organic molecules are extended objects, their orientation with respect to the substrate surface [7], other molecules in the film [8] or e.g. the direction of light output from OLEDs [9] plays a crucial role in device performance. The key figure of polar molecules in this regard is their permanent dipole moment, arising from the non-uniform charge distribution on the molecule. If this dipole moment does not orient perfectly isotropic, it will lead to the build-up of a giant surface potential (GSP) and thus to a macroscopic dielectric polarization of the organic film. Despite this being a known fact [1, 7, 10], the implications of such high potentials on charge transport and injection within and into an organic layer stack have only been studied recently [3, 7, 11].

Dipolar doping now allows to introduce and tune the GSP in a former unpolar organic material [2]. The concentration dependence of the magnitude of the GSP in dipolar doped systems is the first major part of this work. Additionally, dipolar doping can be utilized to create hole conducting films that exhibit a GSP, which allow to study the impact of film polarization also in the hole conducting layer (HTL) of an OLED. In neat film, a GSP was previously seen mostly for electron conductors [6, 12]. Therefor, the prototypical, hole conducting mixture NPB:Alq_3 is investigated at different doping concentrations and with varied substrate material with respect to hole injection and charge transport.

The mixtures are studied in single-layer, monopolar devices with only the HTL present, as well as bilayer OLEDs with Alq_3-doped NPB as HTL and neat Alq_3 as electron transport layer, respectively. The latter are treated as metal insulator semiconductor (MIS) structures following and applying our recently developed method of charge extraction by linearly increasing voltage (CELIV) on polar OLEDs [13, 14]. Furthermore, ultraviolet photoelectron spectroscopy allows to compare the electrical observations with the energy alignment between contact and doped NPB.

For all device types, an optimum in device performance and carrier injection for moderate doping concentrations of about 5 % is found. By comparing all different methods with a focus on charge injection barriers, a complex relationship of carrier transport, substrate workfunction, modified injection and the effect of polarization is found. This effectively manipulates charge carrier injection across the metal-organic interface and charge transport in the device.

Kurzzusammenfassung

Die vorliegende Arbeit befasst sich mit den Auswirkungen von polarer Dotierung auf Ladungsträgertransport und -injektion in organischen Halbleitern. „Polare Dotierung“ bezieht sich hierbei auf das Verdünnen oder Dotieren einer unpolaren Matrix aus organischen Molekülen mittels polaren Gast-Molekülen. Für diesen Zweck dienen die organischen Lochleiter *N*,*N*'-Di(1-Naphthyl)-*N*,*N*'-Diphenyl-(1,1'-Biphenyl)-4,4'-Diamin (NPB) und 4,4-*N*,*N*'-Dicarbazole-1,1'-Biphenyl (CBP) als Matrix. Dotiert werden sie mit Tris-(8-Hydroxyquinolin) Aluminium (Alq_3) und 1,3-bis[2-(4-tert-butylphenyl)-1,3,4-oxadiazo-5-yl]Benzen (OXD-7). Der Fokus dieser Arbeit liegt allerdings auf dem System NPB:Alq_3, welches auch vorher bereits gründlich untersucht wurde [1–3].

Im Allgemeinen ist die Dotierung von (organischen) Halbleitern eine etablierte, zentrale Methode zur Optimierung der Leitfähigkeit [4] oder der Emittereigenschaften von organischen Leuchtdioden [5]. Die Folgen einer Dotierung mit polaren Molekülen im Speziellen wurde allerdings bisher noch nicht systematisch untersucht, obwohl viele häufig verwendete Dotanden durchaus polare Moleküle sind [6].

Organische Moleküle sind ausgedehnte Objekte mit komplexen Formen, deren Orientierung zur Substratoberfläche [7], zu anderen Molekülen in der Schicht [8] oder auch zum Emissionsvektor einer OLED [9] einen großen Einfluss auf die Effizienz des Bauteils hat. Die wichtigste Eigenschaft von polaren Molekülen ist in diesem Zusammenhang ihr permanentes Dipolmoment, das sich auf eine ungleichmäßige Verteilung der Elektronendichte im Molekül zurückführen lässt. Falls sich das Dipolmoment nicht vollständig isotrop orientiert, hat es ein makroskopisches Oberflächenpotential (engl. *giant surface potential*, GSP) bzw. eine dielektrische Polarisation der gesamten Dünnschicht zur Folge. Die Existenz des GSP ist bereits seit einiger Zeit bekannt [1, 7, 10]. Seine Auswirkungen auf den Ladungstransport bzw. -injektion in Bezug auf organische Halbleiter werden erst seit kurzem häufiger untersucht [3, 7, 11].

Das Konzept der polaren Dotierung erlaubt nun, ein GSP in ursprünglich unpolare organische Matrizen einzubauen [2]. Mittels Dotierung lassen sich auch polare Lochleiter herstellen, die im weiteren Verlauf der Arbeit eine Untersuchung der Auswirkungen des GSP auf die Lochleiterschicht in einer OLED erlauben. In undotierten Schichten wurde ein GSP bisher hauptsächlich in Elektronenleitern beobachtet [6, 12]. Exemplarisch wird dazu das Mischsystem NPB:Alq_3 in verschiedenen Konzentrationen und auf verschiedenen Substraten in Bezug auf Lochinjektion und Lochtransport näher untersucht. Es werden sowohl monopolare Bauteile, die ausschließlich Lochtransport aufweisen, als auch vollständige OLEDs verwendet. Bei OLEDs kommt dabei eine im Laufe dieser Arbeit mit entwickelte neue Methode zum Einsatz, die diese OLEDs wie sog. Metall-Isolator-Halbleiter-Dioden (engl. *metal-insulator-semiconductor*, MIS) behandelt und Rückschlüsse auf die Energiebarriere für Ladungsinjektion erlaubt [13, 14]. Des Weiteren stehen Ergebnisse aus der ultravioletten Photoelektronenspektroskopie zur Verfügung, die einen Vergleich mit der Ausrichtung der Energieniveaus von NPB am Kontakt ermöglichen. Mittels des Vergleichs verschiedener Messmethoden im Bezug auf die Injektionseigenschaften kann der Effekt des GSP auf verschiedene Parameter im Bauteil nachgewiesen werden, deren Zusammenspiel in sämtlichen Bauteiltypen zu einem Optimum bei moderaten Dotierkonzentrationen von ca. 5 % führt.

Contents

I

Introduction

Introduction

Global industrialization and digitalization have kept accelerating in both, development of new technologies and demand of resources over the past decades as such that most extrapolations of our future demand in energy, resources and the overall effect on the climate draw a gloomy picture of a possible future. Thereby, energy consumption and production is by far not the only problem to be addressed. The large amount of electronic devices manufactured within the last years, including those required for clean energy sources, has lead to a rapid increase in the demand on scarce resources like rare earth metals [15, 16]. Furthermore, it is widely agreed in the academic world that a transfer to renewable energies is without alternative to meet even the bare minimum in climate goals [17, 18]. Although recent development has transferred the public and political discussion about human impact on earth's climate from fact to believe, another inevitable problem will as well force the transfer from fossil to renewable energy. Whether because of rising costs, diminishing sources or both, "peak oil", the point of maximum crude oil extraction, is threatening the traditional oil based industry [19].

Reducing our energy needs and carbon footprint as well as sourcing necessary materials to allow manufacturing electronics for energy harvesting, lighting and daily needs might be viewed as this century's most demanding challenges. Research and improvement of alternative technologies like organic electronics is thus an important contribution to this further development.

Resources for modern electronics

The material requirement and greenhouse gas emissions connected to the manufacturing of electronic devices has come to more attention, alongside the social impact of mining precious resources. Classic semiconductors, integrated circuits and display technologies require a manifold set of different materials. For example, light emitting diodes are expected to rise the need for rare earth elements like Europium, Terbium or Yttrium [20] besides the semiconductors of Indium, Gallium or Arsenic. Other consumer electronics like a cell phone also require considerate amounts of Lithium or Gold besides e.g. Silicon [21]. Currently, only about 20 % of global electronic waste is recycled [22], thus extracting and refining required materials from the soil can take a great effort. In a 2017 report, Cook *et al.* gave an estimate of 38 kg solid rock mined per 100 g of extracted minerals for the production of an average smart phone [23]. For Gold, the yield can be even less with 1 kg pure metal per 1.5 T of rock, not counting released toxic waste [24]. Additionally, resource extraction often is accompanied by local armed conflicts, human rights abuse [25] or environmental pollution [24, 26]. The exact source for various materials needed to produce specific electronic devices and thus the impact of all aforementioned factors is seldom known. An exception is made by the company Fairphone in publishing the supply chain for their smartphone, including mines, smelters, factories and resellers, which is reproduced in parts in Figure I.1. Despite the efforts, the map is an on-going process, as

Figure I.1.: Supply chain of a contemporary electronic device at the example of a cell phone ("Fairphone 2"). Shown are known mines and pits for various raw materials, sub-contractors for individual parts like adhesives, integrated logic or glass. The assembly is in China, re-sellers in Europe. Drawn after reference [28].

not all sub-contractors, smelters and refiners list their sources [27]. The map still illustrates that the production of such a device is a global business and it is not surprising that about 80 % of all greenhouse gas emissions in the lifespan of a phone can be credited to its production [23]. It is thus of large interest to find alternative material classes with less need for rare or expensive materials and that lead to less energy consumption during the production of electronic devices.

Harvesting and saving energy

Besides the problem of sourcing materials for the production, also new sources for the energy required for their operation are needed. Fortunately, a large set of technologies to harvest "green energy" already exists and has long since reached market maturity. For example, traditional silicon based photovoltaic cells exhibit a peak lab efficiency of 28 % of power conversion efficiency [29], module efficiencies are usually lower at around 20 % maximum [30]. As of 2019, in Germany, 8.2 % of electricity is generated using photovoltaics with a total marked share of renewables of 43 %, combined with a huge possibility for further extensions [31]. In terms of energy use, a big figure in global energy consumption is lighting, which in 2016 consumed 17 % of global electricity [32] or about 6.5 % of the world's total primary energy in 2010 [33]. The carbon footprint of that amount of energy is reduced by a large amount by the replacement of incandescent lamps with so-called solid-state lighting techniques like LEDs [32].

Organic electronics

Organic electronics, besides other emerging techniques like perovskites, can provide solutions for both, efficient energy harvesting and a low demand on rare materials. White organic light emitting diodes meanwhile exhibit a luminous efficacy comparable to the usual benchmark of $100\,\mathrm{lm\,W^{-1}}$ [34,35] of a standard fluorescent lamp [32]. While many efficient OLED emitters initially also contained heavy metals like Irid-

ium [6,36], pure organic dyes meanwhile exist that potentially eliminate the need for precious materials [37,38]. Besides, among the biggest advantages of OLEDs in lighting is the potential for large area light sources of almost natural color, leading to a uniform diffuse illumination in contrast to the traditional spot lights of incandescent lamps or LEDs [39]. Another aspect is flexibility, both in size or shape and mechanically, which allows to create efficient, global illumination designs with optimal light distribution [39].

On the side of energy generation, top laboratory efficiencies of organic photovoltaics (OPV) are roughly at 17 % [29, 40], with module figures between 5 % to 12 % [41]. Many top-performing materials in organic photovoltaics are also purely organic, either small molecules or polymers [40, 42]. Furthermore, OPV already exhibits a "cradle to grave" energy payback time of three months [43] and projections for large scale production are as low as one day [44]. Similar to OLEDs, flexible and lightweight design enables solar energy to be utilized in areas where traditional "sun farms" with large, rigid modules are not possible, for example in big cities [45]. For these areas, an estimate of 1.4 TW in potential solar power for facade and roof-top installations has been calculated for Germany alone [31]. To put this into perspective, the total amount of electricity consumed in Germany in 2017 is reported to be 520 TWh, which, at a daily illumination of eight hours, would require roughly 46 days to be collected from the sun in the best case.

Challenges and research

Despite these promising results, many aspects of organic electronics are still unknown and require further research. Organic molecules can be considered extended objects that can have different properties in thin films, depending on their orientation to incident light, the contact area or also other species of organic semiconductors [7–9]. In case of OLEDs, the orientation of the emitter molecules will influence the device performance, as light is emitted perpendicular to the transition dipole moment and can be trapped in the OLED, if emitted parallel to the surface [46]. The effect of the transition dipole has thus been studied extensively in the past [47, 48]. However, many of the molecules used in organic electronics also have a permanent dipole moment [6]. If this permanent dipole moment is not distributed perfectly isotropic, it will lead to a macroscopic dielectric polarization of the organic film [1]. Besides the physics behind the orientation mechanism upon film growth [7] and the correlation of both, permanent and transition dipole moment [48], also the influence of this macroscopic polarization on device performance is still under investigation [3, 7, 49].

In this work, the concept of dipolar doping [2] will be utilized to tune the magnitude of the macroscopic polarization in organic films. Therefor the non-polar host *N*,*N*'-Di(1-naphthyl)-*N*,*N*'-diphenyl-(1,1'-biphenyl)-4,4'-diamine (NPB) is doped with the polar guest tris-(8-hydroxyquinolate)aluminum (Alq_3) and the influence of these dopants on hole injection and transport is investigated. In the course of this work, the effect of doping on the magnitude of the polarization, interface injection barriers and bulk hole transport through dipolar doped layers is elucidated.

II

Basic concepts, preparation and characterization

1. Basic concepts of organic semiconducting devices

Parts of the following chapter have been taken from my previous work [50] and were extended or updated where necessary.

1.1. Organic semiconductors

The following section will give a short overview of organic semiconductors, their characteristic properties and physics with special focus on their use in organic semiconducting devices.

1.1.1. Introduction to organic semiconductors

The term *organic semiconductors* refers to a material class governed by organic chemistry that exhibits semiconducting properties: most notably emission and absorption of light in the visible range and sufficient conductivity to be used in electronics [51]. Organic chemistry on the other hand is the chemistry of the element Carbon and its compounds [52], thus *organic semiconductors* (OSCs) are mostly hydro-carbons [51], sometimes containing also other elements like Oxygen, Nitrogen or Sulfur.

Available materials are generally classified into two major types based on their chemistry and, accordingly, the process of film formation. *Polymers*, that interlink into entangled chains and form layers similar to those of commonly used plastics, and so-called *small molecules* or *low molecular weight* materials, typically forming amorphous [53] or polycrystalline films. Additionally, organic compounds can form rigid molecular crystals as a potential third group, showing comparably good semiconducting properties [51]. However, despite being among the first OSCs studied, their practical use in devices is limited [51, 53].

To understand the semiconducting properties of organic compounds, the electronic structure of the element Carbon and hydrocarbons has to be discussed. The ground-state electronic configuration of Carbon is $1s^2\,2s^2\,2p^2$ [52], hybrid orbitals exist in a covalent Carbon-Carbon double bond, where it will form the so-called sp^2 hybridization. Here, one p orbital, e.g. p_z remains unvaried, while the $2s$ orbital together with both p_x and p_y form the hybrid sp^2 orbital [52]. In an organic compound the sp^2 orbitals form the σ-bonds, whereas the overlapping neighboring p_z orbitals correspond to the π-bond perpendicular to the σ-bonds [52], overall leading to the C=C double bond. While the σ-bond is comparably strong and responsible for the structural backbone of the molecule, the π-bonds are weak enough to allow $\pi - \pi^*$ excitations in the range of a few electron volts and hence in the visible range of the electromagnetic spectrum [53]. The smallest species of hydrocarbons exhibiting the C=C bond, ethene, is drawn in Figure 1.1, together with a sketch of the energy diagram.

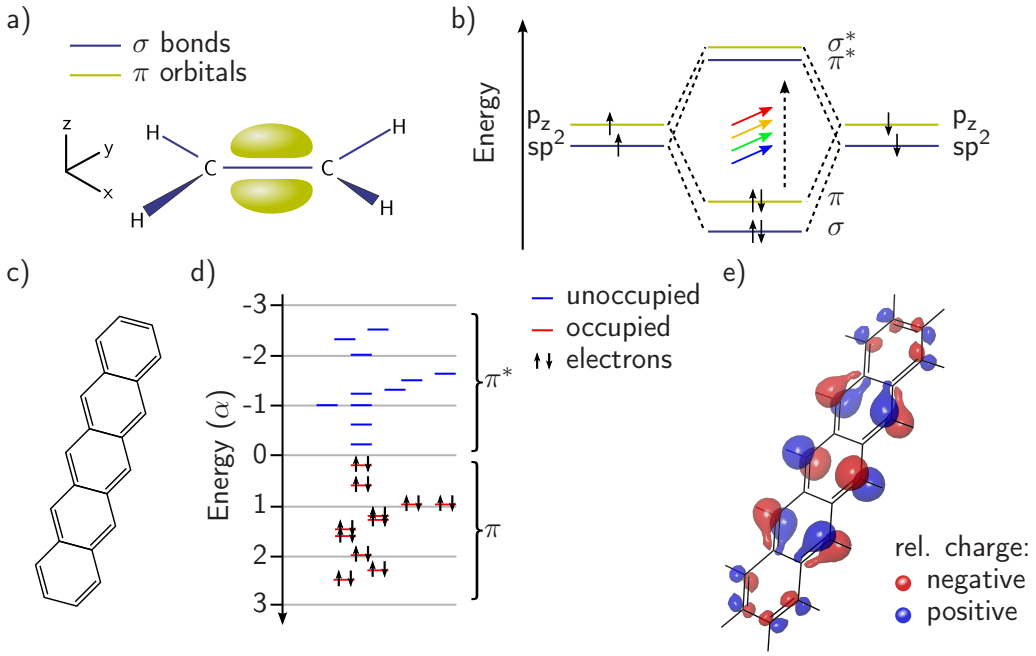

Figure 1.1.: **a)** Basic example of an sp^2 hybridized C=C double bond at the ethylene molecule. The π-bond is perpendicular to the hydrogen-carbon plane and hence visible above and below. **b)** Sketch of the energy level diagram of ethylene in ground and excited state. **c)** Chemical structure of the pentacene molecule and **d)** energetic distribution of occupied and unoccupied molecular orbitals of pentacene calculated with the Hückel theory. **e)** Spatial electronic density distribution of the first HOMO of pentacene.

Although it can already be considered an organic semiconductor, larger structures are typically of more interest.

In a C=C chain, each of the Carbon atoms has one free electron in the p_z orbital to form the π bond and any additional atom in the chain will again add one p_z electron. In such a structure, single and double bonds will alternate across the molecule, forming a so-called *conjugated* hydrocarbon [53]. The most prominent prototypical species of organic semiconductors are therefore aromatic hydrocarbons also known as acenes like benzene or pentacene [52]. Although typically drawn as such, the alternation, specifically the position of the double bond, is not fixed. Instead, the π-electrons are delocalized across all adjacent conjugated bonds given an overlap of the p_z-wavefunctions [52], leading to a combined *molecular orbital* (MO). Ultimately, excitations of the molecule likewise distribute over the whole π-system, leading to the terms of the *highest occupied molecular orbital* (HOMO) and the *lowest unoccupied molecular orbital* (LUMO) resembling π_{molecule} and π^*_{molecule}, respectively [54]. Hence, the exact semiconducting properties are dependent on the size or length of the conjugated π-electron system, and its spatial distribution over the molecule [53]. As organic chemistry allows for manifold variations and combinations of compounds, fine-tuned electronic structures and specifically tailored properties are therefore possible.

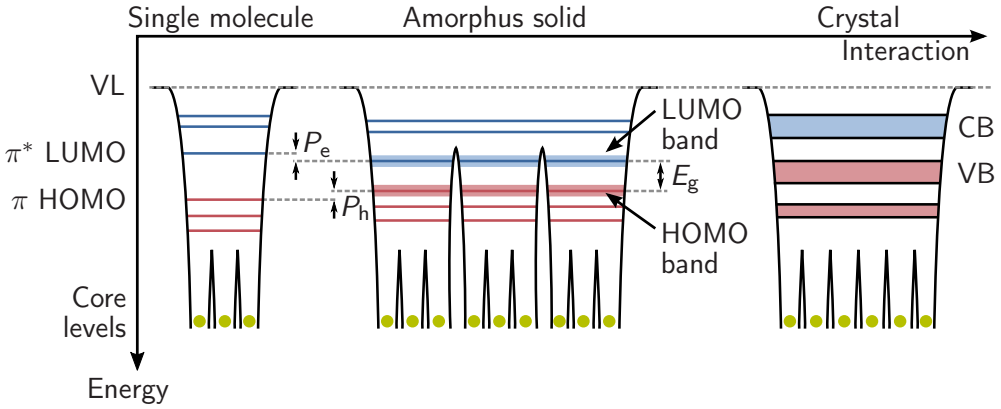

Figure 1.2.: Electronic structure of OSC from a single molecule to amorphous solids and crystals. With rising intermolecular interaction, energetic disorder of individual MOs increases, leading to an increasing bandwidth, eventually leading to conduction (CB) and valence bands (VB) in organic crystals. Polarization energies P_e and P_h reduce the energy gap E_g compared to the single molecule. Redrawn from ref. [53].

In organic molecular solids, the intermolecular interaction is usually dominated by Van-der-Waals forces, only very few organic salts might exhibit ionic bonding [54]. On one hand, this leads to the fact that in organic solids, the properties of the individual molecules remain mostly unaltered compared to the single molecule [54]. In literature, organic molecular solids are therefore sometimes referred to as oriented gasses [54], in contrast to the covalent bonding in Silicon or Germanium semiconductors. On the other hand, however, this also means that the energetic overlap between wavefunctions of individual MOs is also small. This implicates a number of differences between organic semiconducting solids and classic, inorganic semiconductors spanning from macroscopic quantities like melting point or hardness, to microscopic properties concerning charge generation and transport, as well as optical excitations [53].

The energy of the molecular orbitals is typically given in *electron volt* (eV) with respect to the vacuum level positioned at 0 eV. In this work, the sign of the energy of individual molecular orbitals is by convention set to be positive with the energy scale pointing downward. Higher energy levels thus represent a higher distance to the vacuum level.

1.1.2. Electronic structure and excitation in organic solids

In classic semiconductors, the strong covalent bonding leads to a delocalization of electrons of individual atoms over a comparable large crystal lattice. Together with energetic dispersion, this results in the well-known band structure of semiconductors, the most basic of which would exhibit one valence (VB) and one conduction (CB) band. In Figure 1.2, the evolution of the electronic structure from a single molecule to organic solids is sketched. The potential well of the molecule on the left depicts three occupied and unoccupied molecular orbitals, the adjacent ones with the lowest energetic difference are the HOMO and LUMO levels, respectively. With the only

interaction between molecules being weak Van-der-Waals forces, both occupied and unoccupied states in the solid mainly represent those in the single molecule [53]. Still, energetic dispersion affects individual molecular orbitals, overall leading to very narrow intermolecular bands with a bandwidth $< 0.2\,\mathrm{eV}$ [53], see Figure 1.2. Additional to the dispersion and subsequent formation of narrow HOMO and LUMO-bands, electronic polarization of neighboring molecules in a solid might stabilize a charged species by screening effects [53]. The resulting polarization energies P_e and P_h lead to an effectively lower energy gap E_g in solids compared to the gas phase of the molecule.

In inorganic crystalline semiconductors, electronic transitions and hence absorption and emission of light, is governed by the energy gap between valence and conduction band. For organic molecular solids, the term applies to the transition between HOMO and LUMO, respectively. Upon optical or electrical excitation of a classic semiconducting material, an excited electron is generated on the conduction band. The binding energy of the *exciton*, the bound state of both excited electron and generated hole, is governed by the Coulomb interaction:

$$E_\mathrm{bind} = \frac{\mathrm{e}^2}{4\pi\varepsilon\varepsilon_0} \cdot \frac{1}{r_\mathrm{c}} \,, \tag{1.1}$$

where r_c is the distance between the two carriers and ε the dielectric constant of the material. The binding energy for electrons and holes in two different materials ($\varepsilon = 3$ and $\varepsilon = 12$) is drawn in Figure 1.3. An electron-hole pair can be considered free, when its binding energy is smaller than the thermal energy of the system, $E_\mathrm{bind} < \mathrm{k_B}T$. Thus, the maximum Coulomb radius of a just bound pair is

$$r_\mathrm{c} = \frac{\mathrm{e}^2}{4\pi\varepsilon\varepsilon_0 \mathrm{k_B}T} \,. \tag{1.2}$$

The actual distance of electron and hole can be approximated with the exciton Bohr radius, which in case of simple, hydrogen like wavefunctions of electrons [55] is given by

$$r_\mathrm{b} = r_0 \varepsilon \frac{\mathrm{m_e}}{m_\mathrm{eff}} \,, \tag{1.3}$$

where m_eff is the effective mass of the electron in the semiconductor, $\mathrm{m_e}$ the mass of a free electron in vacuum and $r_0 = 0.53\,\text{Å}$ the Bohr radius of hydrogen. Usually, $m_\mathrm{eff} < \mathrm{m_e}$ in inorganic semiconductors and $m_\mathrm{eff} > \mathrm{m_e}$ in organics [55]. In inorganic semiconductors, the strong bonding and corresponding high delocalization of electrons leads to a high ability of polarization, resulting in a high dielectric constant ($\varepsilon_\mathrm{Si} \approx 12$, $\varepsilon_\mathrm{Ge} \approx 15$) and also a low effective mass m_eff [54, 55]. Hence, electron and hole distances in the range of a 10 nm can be higher than the respective crystal lattice constants by an order or magnitude [54]. A drastic example is $r_\mathrm{b} = 24\,\mathrm{nm}$ for excitations in Germanium [56], the radius is marked in Figure 1.3 with a vertical line. For organic semiconductors, the calculation of a Bohr radius with the given equation is to be handled with care as the theory is more complex [55, 57]. In case of C_{60}, an estimation with $m_\mathrm{eff} \approx 0.12\mathrm{m_e}$ and $\varepsilon_{C_{60}} = 4.5$ yields $r_\mathrm{b} = 2.0\,\mathrm{nm}$ [57]. As a side note, C_{60} is a relatively large conjugated π-system, and the dielectric constant is also quite high. A value of $r_\mathrm{b} = 2\,\mathrm{nm}$ for the Bohr radius might therefore be considered

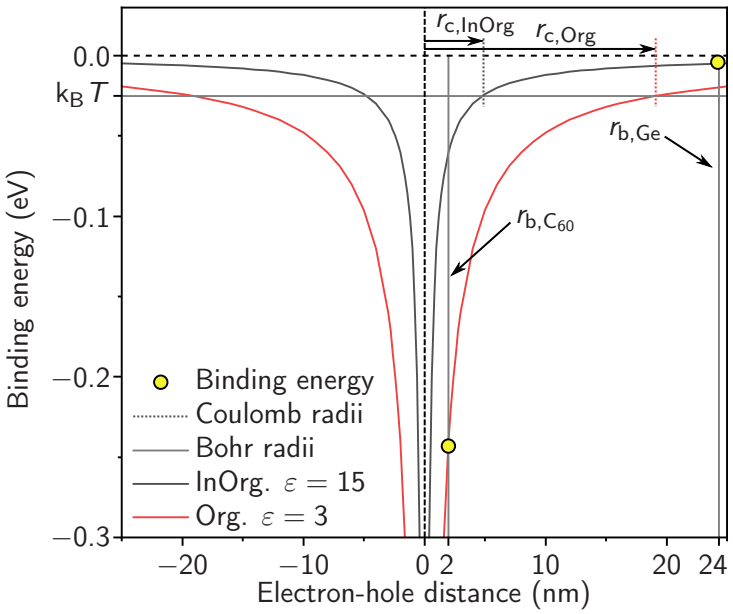

Figure 1.3.: Calculated binding energies versus electron-hole distance for organic ($\varepsilon = 3$) and inorganic ($\varepsilon = 15$) semiconductors. Exciton binding energies (intersection between calculated energy plots and Bohr radii) for OSC are below $k_B T$, whereas inorganic semiconductors land above. Adapted from ref. [55].

approaching the upper limit. To retain a bound excitonic state, the condition for stable excitons can be formulated as

$$\gamma = \frac{r_c}{r_b} \overset{!}{>} 1 \ , \tag{1.4}$$

while $\gamma < 1$ would lead to unbound carriers upon (photo-)excitation.

Combining these findings, at least two different types of excitons can be distinguished, one of each prevailing in either organic or inorganic semiconductors. For inorganic species, binding energies of the so called *Wannier excitons* [54] are typically lower than 25 meV, hence lower than the thermal energy at room temperature. A high Bohr radius leads to $\gamma < 1$ and as a result, inorganic solar cells are generally considered to directly generate unbound electrons and holes upon light absorption [58].

In contrast, for OSC, the excitation is primarily bound to one molecule, and must diffuse in that bound state from one molecule to another [54]. The Bohr radius of the exited electron-hole pair is therefore much smaller, as the typical size of organic molecules is in the range of 10 Å. Together with the lower dielectric constant ($\varepsilon \approx 3$) of organic semiconductors, the exciton binding energy will be in the order of 1 eV [53]. This *Frenkel exciton* is therefore not possible to be dissociated by thermal excitation, organic solar cells will likewise not generate free carriers directly by light absorption. Methods for charge generation in so called *excitonic solar cells* [58, 59] are described in Section 1.2.2.

1.1.3. Charge transport in organic solids

The macroscopic quantity for the movement of charge carriers in a semiconductor is the electric current density j. It is typically composed of two individual contributions,

the *drift current* induced by the external electric field and the *diffusion current* caused by a concentration gradient of carriers in the device [51]. Hence,

$$j = \underbrace{\mathrm{e}n\mu F}_{\text{drift}} - \underbrace{\mathrm{e}D\frac{\delta n}{\delta x}}_{\text{diffusion}} \ , \tag{1.5}$$

with the elementary charge e, the mobility μ, the charge carrier density n and the diffusion constant D. Strictly speaking, at least the electric field, the mobility and the diffusion constant might exhibit anisotropy [60] depending on the direction of charge travel and thus should more accurately be described by tensors, e.g. $\vec{j} = \mathrm{e}n\boldsymbol{\mu}\vec{F} - \mathrm{e}\mathbf{D}\nabla n$. However, in the scope of this work, the scalar interpretation is sufficient.

In OSC, usually both drift and diffusion have to be considered. Diffusive transport especially gains importance in the space charge regime [51], for carrier injection and for neutral species, like excitons (see sections 1.1.4 and 1.1.5 for reference). The main determining factor for carrier drift is their mobility μ, usually given in units of $\mathrm{cm^2\,V^{-1}\,s^{-1}}$. It is linked to the conductivity σ_c of the material by

$$\sigma_\mathrm{c} = \mathrm{e}n\mu \tag{1.6}$$

and also to the diffusion constant D of the specific species with the Einstein relation [61] where

$$\mathrm{e}D = \mu \mathrm{k_B}T \ . \tag{1.7}$$

Typical values for the mobility in organic semiconductors are in the range of 10^{-6} to $10^{-3}\,\mathrm{cm^2\,V^{-1}\,s^{-1}}$, where values for electrons and holes can strongly differ for the same material. Also, exceptionally high mobilities for electrons have been reported for highly crystalline perylene [62] with $\approx 10\,\mathrm{cm^2\,V^{-1}\,s^{-1}}$, as well as very low values like $10^{-8}\,\mathrm{cm^2\,V^{-1}\,s^{-1}}$ for holes in amorphous Alq_3 [63]. To put that into perspective, the hole and electron mobilities in Germanium are both in the range of $10^3\,\mathrm{cm^2\,V^{-1}\,s^{-1}}$ [54].

The comparably low mobilities in OSC are a direct consequence of their specific electronic structure, which is described in Section 1.1.2. The absence of a pronounced band structure does not allow free movement of charge carriers across multiple molecules. Instead, for each step, the potential well from one molecule to another has to be overcome again. Charge transport in organic semiconductors is thus generally described as an *activated hopping process*. Different models exist to describe this process, the most used is probably the model introduced by Bässler in 1993 [64]. The sketch in Figure 1.4 depicts the basic idea of the model. Charge carriers, electrons or holes, move between individual sites exhibiting localized states. These states are subject to energetic disorder, originating from stochastic changes in the polarization energies [54], which are dependent on a large set of individual coordinates [64]. The distribution of these states' energies is given by the *density of states* (DOS) $G(E)$ that in the Bässler model is considered to be of Gaussian [64] shape with the standard deviation or "width" of σ:

$$G\left(E\right) = \sqrt{2\pi\sigma^2}\exp\left(-\frac{E^2}{2\sigma^2}\right) \ . \tag{1.8}$$

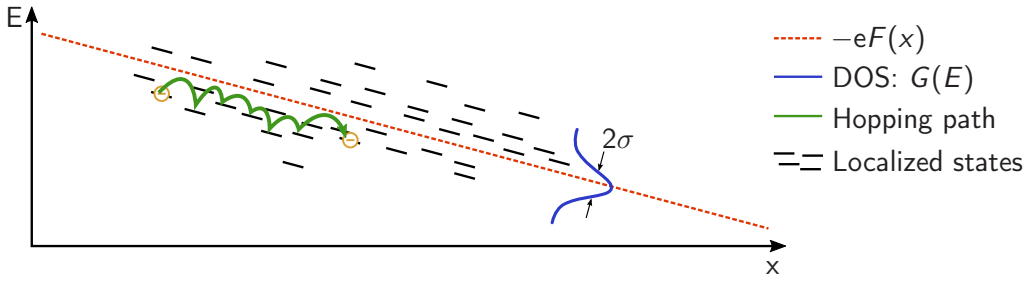

Figure 1.4.: Sketch of the hopping process of charge carriers in organic molecular solids. The electric field gradient defines the net direction of travel for charge carriers hopping from one localized state to another. Redrawn from ref. [54].

The energy E is hereby given relative to the center of the distribution. The Gaussian distribution in energy is the reason why this model is also commonly referred to as the *gaussian disorder model* (GDM). Additional to the distribution of the density of states, the model contains a hopping probability or rate ν_{ij} [54] from one site i to another j referred to as the Miller-Abrahams equation [65] with

$$\nu_{ij} = \nu_0 \exp\left(-2\gamma\Delta R_{ij}\right) \cdot \begin{cases} \exp\left(\dfrac{E_j - E_i - eF\left(x_j, x_i\right)}{k_B T}\right) & \text{for } E_i < E_j \\ 1 & \text{for } E_i > E_j \end{cases}, \tag{1.9}$$

where ν_0 is a prefactor, $E_{i,j}$ are the energies of the respective sites i and j in the distribution of $G(E)$, $F\left(x_j, x_i\right)$ is the electric field between the positions of the sites x_i and x_j and ΔR_{ij} the hopping distance between both sites. γ is the decay constant of the wavefunction, which can also be described as the molecular coupling factor. With the mean site distance denoted as a, the product of $2\gamma a = \Gamma(\Sigma)$ is considered to be the overlap parameter. Because of the orientation dependence of molecular coupling and the stochastic distribution of the mean site distance [64], $\Gamma(\Sigma)$ is also given by a Gaussian distribution with a standard deviation of Σ [54]. The defining parameters of the Bässler or Gaussian disorder model are hence the two disorder parameters, σ in Equation 1.8 and Σ [54]. Following Equation 1.9, a downward hopping from an energetically higher to a lower state, i.e. $E_i > E_j$ requires no additional activation. The other direction has to be activated with an energy given by $E_{act} = E_j - E_i - eF\left(x_j, x_i\right)$, which is the energetic difference between the transport sites [54, 64].

Unfortunately, no straightforward analytic solution incorporating the Bässler model exists to describe the movement of charge carriers in OSC with simple quantities. Bässler himself therefore utilized the Monte Carlo approach to calculate a finite set of hopping sites in periodic boundary conditions to simulate a time-of-flight experiment [64]. One result of this experiment is the temperature dependence of the mobility in disordered systems [54, 64], which calculates to

$$\mu(\sigma, T) = \mu_0 \exp\left[-\left(\frac{2\sigma}{3k_B T}\right)^2\right]. \tag{1.10}$$

The prefactor μ_0 can be considered as the ideal mobility without disorder and at very high temperatures. From Equation 1.10 follows that measured data must show a $\ln\mu \propto 1/T^2$ dependence of μ on the temperature for the GDM to be applicable.

In Equation 1.10 the mobility is not dependent of the field, despite the fact that this behavior is often observed. Experimentally, in organic semiconductors, a field dependence of the mobility is found to be very similar to that in inorganic insulators, described by the Poole-Frenkel law [54]:

$$\mu_{\mathrm{PF}} = \mu_0 \exp\left(-\frac{\Delta_0 - \beta_{\mathrm{PF}}\sqrt{F}}{\mathrm{k_B}T_{\mathrm{eff.}}}\right) \ , \ T_{\mathrm{eff.}}^{-1} = T^{-1} - (T')^{-1} \ . \tag{1.11}$$

Here, all factors μ_0, Δ_0, β_{PF} and T' are constant. β_{PF} is mostly referred to as the field-enhancement factor [54] that obeys the characteristic relation of $\ln \mu_{\mathrm{PF}} \propto \beta_{\mathrm{PF}}\sqrt{F}$. As already suggested from the drawing in Figure 1.4, the existence of an electric field will "tilt" the density of states [65]. This will lead to a reduction of hopping activation energy and hence to higher mobilities for higher electric fields.

The GDM includes the field dependence for the mobility with

$$\mu(\sigma, T, F, \Sigma) = \mu_0 \exp\left[-\left(\frac{2\sigma}{3\mathrm{k_B}T}\right)^2\right] \cdot \begin{cases} \exp\left[C(\sigma^2 - \Sigma^2)\sqrt{F}\right] & \text{for } \Sigma < 1.5 \\ \exp\left[C(\sigma^2 - 2.25)\sqrt{F}\right] & \text{otherwise} \end{cases} , \tag{1.12}$$

where C is a numerical constant [64, 65]. Although the equation now generally resembles the Poole-Frenkel law with $\ln \mu \propto \beta_{\mathrm{PF}}\sqrt{F}$, this relation does not hold any more for low fields [65]. The discrepancy of the GDM to the observed Pool-Frenkel type field dependence in many OSC for lower fields can stem from the fact that the GDM neglects the influence of individual hopping sites on each other. As an addition to Bässler's model, the so called *correlated disorder model* (CDM) includes the interactions of energies of adjacent transport sites [51, 65, 66], where

$$\mu_{\mathrm{CDM}} = \mu_0 \exp\left[-\left(\frac{3\sigma_{\mathrm{d}}}{5\mathrm{k_B}T}\right)^2\right] \exp\left\{C_0\left[\left(\frac{\sigma_{\mathrm{d}}}{\mathrm{k_B}T}\right)^{3/2} - \Sigma_{\mathrm{CDM}}\right]\sqrt{\frac{\mathrm{e}FR}{\sigma_{\mathrm{d}}}}\right\} \ . \tag{1.13}$$

In this equation, σ_{d} denotes the dipolar disorder between individual sites, whereas R is the hopping distance and C_0 an empirical constant. Σ_{CDM} corresponds to Σ^2 in the GDM in Equation 1.12. The CDM is reported to resemble both the Pool-Frenkel field dependence of μ as well as the $\ln \mu \propto 1/T^2$ behavior over a broader range of fields and temperatures compared to the GDM alone [51].

All previous considerations presumed only one species of molecules taking part in the charge transport in the semiconductor. In mixtures, or simply if defects exist in the bulk material, carriers might be subjected to trapping or de-trapping effects, which will ultimately affect the mobility. If μ_{tl} is the trap-free mobility for the respective material, a concentration c of traps with the energetic depth of E_{t} can reduce the mobility following the Hoesterey and Letson formula [51]

$$\mu = \mu_{\mathrm{tl}}\left[1 + c\exp\left(\frac{E_{\mathrm{t}}}{\mathrm{k_B}T}\right)\right]^{-1} \ . \tag{1.14}$$

1.1.4. The metal/organic interface and carrier injection

The injection of charge carriers into organic semiconductors and at the same time the selection of properly injecting contacts is crucial for the overall device performance. At a contact between a metallic and a semiconducting layer, the probability

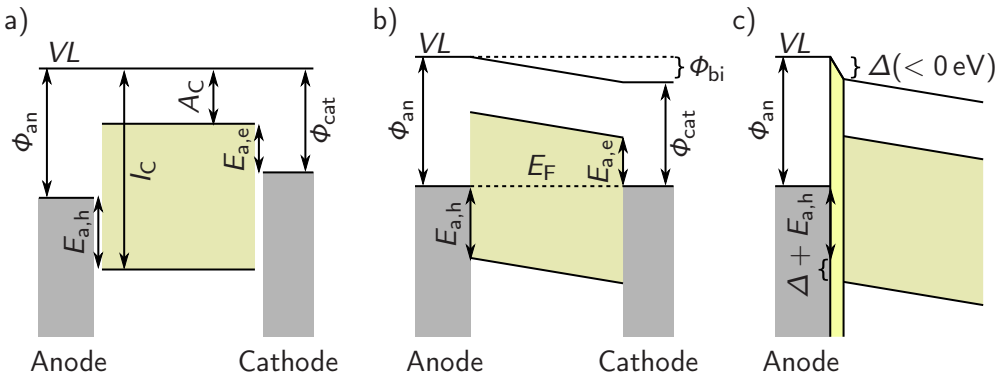

Figure 1.5.: Sketch of the band diagram of a metal-semiconductor interface at both anode and cathode **a)** with individual materials without contact and **b)** in contact. **c)** Shows the formation of an additional interface dipole (given in yellow). Redrawn from refs. [54, 67].

for a transition of an electron from one layer onto another is governed by the energy difference between initial and final states, usually termed *injection barrier* or *activation energy*. Knowing the energy difference between contact and semiconductor is therefore the first step to analyze carrier injection.

Injection Barrier

In case of metallic contacts and originally for inorganic semiconductors, the energetics can be deduced as follows. The energy required to remove an electron from the surface of a metal is defined as the *workfunction* Φ [54]. In the simple picture of an undoped semiconductor, the material parameters can be stripped down to two important quantities for electron or hole injection, which are the *ionization potential* I_C and the *electron affinity* A_C. The former is defined as the difference between the HOMO and the vacuum level (VL), whereas the latter is the distance between VL and LUMO. In Figure 1.5, a semiconducting layer sandwiched between two metals of different workfunction (where $\Phi_{an} > \Phi_{cat}$) is sketched, without (a) and with (b) direct contact to each other. Without contact, the vacuum levels of metals and the semiconductor are aligned. The energetic barrier or activation energy $E_{a,c}$ for injection of electrons from the cathode to the LUMO, neglecting the vacuum in between, is easily visible and amounts to

$$E_{a,e} = \Phi_{cat} - A_C \ . \tag{1.15}$$

Likewise, the extraction of electrons from the HOMO to the anode or the injection of holes into the semiconductor is defined by the ionization potential and the workfunction of the anode Φ_{an} [54] with

$$E_{a,h} = I_C - \Phi_{an} \ . \tag{1.16}$$

Upon contacting, any external current flow equalizes the Fermi levels of both metals, leading to a shift in vacuum level equal to the difference between the metal workfunctions. With the semiconductor of a thickness d_s in between, the contact potential difference leads to an intrinsic built-in field F_{bi} of

$$F_{bi} = \frac{\Phi_{an} - \Phi_{cat}}{d_s} \ . \tag{1.17}$$

An externally applied voltage will therefore have to be higher than the internal field for an effective current flow [54]. Still, the fundamental problem of an activation energy or barrier that has to be overcome for carrier injection remains and might be even more complicated than the simple energy difference presented above. In the following, a few basic concepts governing the actual barrier and limits for carrier injection are discussed.

Interface dipoles

At the contact between metal and OSC, a so-called *interface dipole* will lead to a change in workfunction and vacuum levels as seen in Figure 1.5c, modifying the energy barrier at the interface. The magnitude of the dipole Δ governs the size of the step of the vacuum level, which in turn shifts the energy level of the organic layer ideally by the same value, where

$$E_{\mathrm{a,e}} \rightarrow \Phi_{\mathrm{cat}} - A_{\mathrm{C}} + \Delta_{\mathrm{C}} \quad \text{and}$$
$$E_{\mathrm{a,h}} \rightarrow I_{\mathrm{C}} - \Phi_{\mathrm{an}} - \Delta_{\mathrm{A}} \ .$$

Note that Δ is defined to be negative in case of a downward shift of energy levels as seen in Figure 1.5 and can be different for anode and cathode. In case of organic small molecules deposited on metal, indeed $\Delta < 0\,\mathrm{eV}$ usually holds, leading to an increase in effective barrier for holes and a decrease for electrons [67]. The reasons for dipole formation are manifold, some of which are chemical interactions or charge transfer and redistribution [67]. Also, metal induced interface states have been discussed for OSC, where electrons from the metal redistribute into the bandgap of the organic layer [68]. The height of the barrier can also be modified by deliberately introducing dipole layers such as self-assembled monolayers of polar molecules [69] or the introduction of interlayers between metal and the active semiconducting materials [70, 71].

For many organic molecules with an interface to metals or metal oxides, Greiner *et al.* have published a universal dependence of the interface dipole and resulting injection barrier on the difference of contact workfunction and the ionization potential of the organic [72]. A theoretical description was later given by Ley *et al.* [73], which will be discussed in more detail in Section 6.4.3. The main conclusion from their work, however, is that even perfectly aligned energy levels between contact and OSC will never yield an injection barrier smaller than a few 100 meV, which would be the case in the simple picture of equations 1.15 and 1.16.

Barrier lowering by image charge

It has been shown that the *Richardson-Schottky effect*, comprising an image charge induced in the metal contact due to the charges present in the semiconductor [51,54], can effectively lower the injection barrier at the metal-semiconductor interface. In this theory, electrons injected into the semiconductor experience a potential consisting of not only the intrinsic potential barrier $E_{\mathrm{a,e}}$, but additionally the image potential of

$$E_{\mathrm{image}} = -\frac{\mathrm{e}^2}{16\pi\varepsilon\varepsilon_0 \cdot x} \ , \tag{1.18}$$

which is arising from the Coulomb force between an electron and its image charge in the metal. Together with the externally applied field F_{ext} the overall potential as

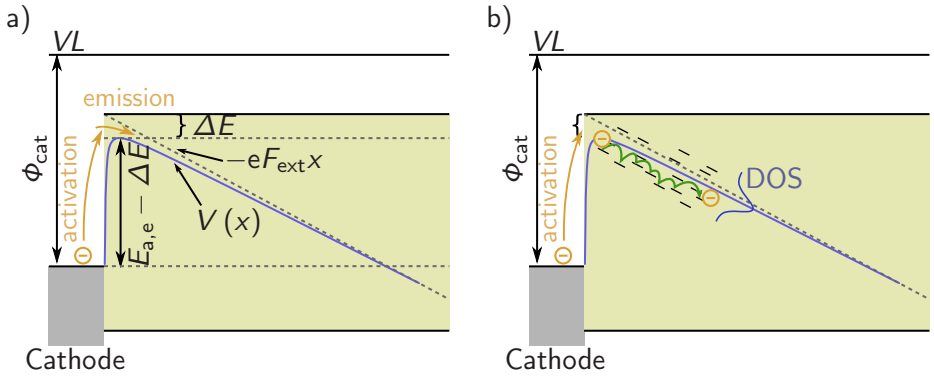

Figure 1.6.: Sketch of processes involved in thermionic emission and barrier lowering through image charge using the example of electron injection. **a)** For classic semiconductors, thermal activation and emission into the bulk is sufficient. **b)** For OSC, the density of states and hopping transport has to be taken into account. Redrawn from ref. [51].

shown in Figure 1.6a can be summed up to

$$V(x) = E_{\mathrm{a,e}} - \frac{\mathrm{e}^2}{16\pi\varepsilon\varepsilon_0 \cdot x} - \mathrm{e}F_{\mathrm{ext}}x \ . \tag{1.19}$$

The maximum of this potential then calculates to

$$x_{\mathrm{m}} = \sqrt{\frac{\mathrm{e}}{16\pi\varepsilon\varepsilon_0 F_{\mathrm{ext}}}} \ , \tag{1.20}$$

which is therefore dependent on the external field and, most importantly, not located at the interface. Instead, with usual values for the dielectric constant being $\varepsilon \approx 3$, a film thickness around 100 nm and voltages in the range of 1 V to 5 V, the potential maximum is located at a distance between 1 nm and 4 nm away from the heterojunction. The barrier reduction at the position of this maximum, x_{m}, calculates to

$$V(x_{\mathrm{m}}) = \Delta E = \mathrm{e}\sqrt{\frac{\mathrm{e}F_{\mathrm{ext}}}{4\pi\varepsilon\varepsilon_0}} \tag{1.21}$$

and amounts to a few 100 meV for typical material parameters.

Injection processes

Different models exist to describe the process to overcome a potential energy barrier for successful carrier injection into an organic semiconductor. Besides thermal activation, one possibility is a tunneling of charge carriers, described e.g. by *Fowler-Nordheim tunneling* [51], originally developed to model an electron current through vacuum. The tunneling barrier for electrons in this case is described as a triangular shape, consisting of the applied electric field and the abrupt change at the metal/vacuum (semiconductor) interface. The current in this case is approximated to be

$$j_{\mathrm{FN}}(F_{\mathrm{ext}}) \approx {F_{\mathrm{ext}}}^2 \exp\left(-\frac{4\sqrt{2m^*\Phi_{\mathrm{el}}}}{3\hbar\mathrm{e}F_{\mathrm{ext}}}\right) \ , \tag{1.22}$$

with the effective carrier mass m^* and the electrode workfunction Φ_{el}. In this theory, however, the aforementioned image charge barrier lowering is ignored, which is only

feasible for very high barriers [51]. Additionally, the tunneling distance required is determined by the linear decay of the electric field and can be calculated to be in the range of 10 nm. In disordered, organic semiconductors, this is unlikely to occur without scattering.

A different process is the so called *thermionic emission* that, following the Richardson-Schottky effect for image charge barrier lowering, leads to a thermally activated process. The activation energy for carrier injection can be calculated to $E_\mathrm{a} - \Delta E$, where ΔE is the barrier lowering due to image charges. A thermally activated charge carrier in the adjacent electrode consequently has a higher probability to be injected into the semiconductor, if it can be emitted into the bulk at the position of minimum barrier x_m. The resulting current for the activated process then calculates to

$$j_\mathrm{te} = A^* \cdot T^2 \exp\left(-\frac{E_\mathrm{a} - \beta\sqrt{F_\mathrm{ext}}}{\mathrm{k_B}T}\right) , \tag{1.23}$$

where $\beta = \sqrt{\mathrm{e}^3/4\pi\varepsilon\varepsilon_0}$. $A^* = 4\pi\mathrm{e}m^*{\mathrm{k_B}}^2h^{-3}$ is the Richardson constant [54], proportional to the effective mass m^* of the charge carrier in question. From Equation 1.23, the characteristic field dependence of

$$\ln\left(j\left(F\right)\right) \propto \sqrt{F} \tag{1.24}$$

arises as a principal relation to test for the existence of carrier injection via thermionic emission. This effect, however, can only be a limiting case for OSC, as distances in the range of 1 nm or more between contact and potential maximum can already span over more than one molecular layer. For OSC it is hence unlikely that a single thermally activated jump allows for effective carrier injection [74]. Carriers would have to overcome multiple molecules to the potential maximum without recombining at the electrode, which is only possible in very ideal conditions [51, 54]. Additionally, the diffusion current commonly found in disordered organic semiconductors is not accounted for. Following the principal route of the thermionic emission theory, Scott and Malliaras have proposed an addition to the model that includes surface recombination and carrier diffusion [75]. In their description of injection, most of the injected carriers will recombine at the electrode, as the emission distance from the electrode to the potential maximum is larger than the molecular distance. The injection current for such a device is then given by [75]

$$j_\mathrm{sc} = 4\Psi(f)^2 N_0 \mathrm{e}\mu F_\mathrm{ext} \exp\left(-\frac{E_\mathrm{a}}{\mathrm{k_B}T}\right) \exp\left(\sqrt{f}\right) , \tag{1.25}$$

where $f = F\mathrm{e}^3/\left(4\pi\varepsilon\varepsilon_0(\mathrm{k_B}T)^2\right)$ is the reduced electric field, N_0 is the carrier density at the interface, μ the carrier mobility and $\Psi = f^{-1} + f^{-1/2} - f^{-1}\sqrt{1+2\sqrt{f}}$.

Still, all presented models can describe the injection current only in very special cases. Even the Scott and Malliaras formula yet neglects the energetic disorder of the DOS. An analytical model for carrier injection into disordered systems was presented by Arkhipov *et al.*, taking image charge, hopping transport and disorder into account [74] (see Figure 1.6b). In their model, a thermally activated jump similar to the Richardson-Schottky type thermionic emission raises a carrier not directly to the tip of the potential well, but into a tail state of the DOS in the disordered material [51]. If the DOS then provides enough states at the same or lower energy,

the charge carrier can continue by hopping transport in the coulomb potential of the image charge and the external applied field. The model was successfully applied to different types of organic small molecules and polymers [51], but again is limited to specific relations of hopping activation energy and injection barrier. For even more accurate description of carrier injection, microscopic simulations of charge carrier interaction and movement are needed [74].

1.1.5. Space charge and other current limiting effects

Besides carrier injection, bulk processes further limit charge transport in (organic) semiconductors. Because either one of both can be the decisive limiting factor, a distinction is made between *injection limited* and *non-injection limited* contacts to semiconductors. Injection limited contacts have been described in the previous section. For very small voltages, often a drift or *ohmic* current dominates the characteristic for non-injection limited contacts. In this case, the current is given by

$$j_\Omega = en\mu \cdot \frac{V}{d} \ , \tag{1.26}$$

where e is the elementary charge, n the charge carrier density, V the applied voltage, d the thickness of the device and μ the mobility of the respective charge carrier. If the amount of charge carriers injected is larger than the bulk conductivity can carry away, carriers might grow a *space charge region*, shielding further carrier injection. Conventionally, electrodes that are able to inject more carriers than bulk transport can cope with are called *ohmic contacts*, although the current-voltage characteristic of such an electrode does not have to follow Ohm's law [51]. In a simple approximation, neglecting possible charge redistribution and resulting inhomogeneities in the electric field, the total charge stored in the capacitance of the device is less or equal $q = {\varepsilon\varepsilon_0 V}/{d}$. The charge will travel the distance d with its mobility μ, hence the transit time is $\tau = {d^2}/{\mu V}$ [51]. Accordingly, the current calculates to $j = q/\tau = {\varepsilon\varepsilon_0\mu V^2}/{d^3}$. Unfortunately, the electric field is not homogeneous and because of this, the above equation has to be corrected [51]. The detailed derivation of the so called *Child's law of space charge limited current* would leave the scope of this work, hence only the result is given, where

$$j_{\mathrm{SCL}} = \frac{9}{8}\varepsilon\varepsilon_0\mu\frac{V^2}{d^3} \tag{1.27}$$

is the general *Mott-Gurney equation* [54] for single-carrier *space charge limited current* (SCLC). The deviation from the crude approximation above is, surprisingly, only a factor of ${9}/{8}$, close to one [51]. Equation 1.27 still neglects diffusion of charge carriers through the device as well as the dependence of the mobility on external factors and adds some specific requirements on carrier density at the contact [1]. Nevertheless, it represents the maximum current a device that is not injection limited can carry [1]. From this equation, two crucial requirements are evident for a device to show SCL current: In a current-voltage characteristic, the current must be proportional to V^2 and inverse proportional to the cubic of the device thickness, d^3. Analyzing space charge limited currents to calculate the mobility of organic materials is a well-established method, although it is argued that pure space charge limitation is seldom observed [76].

The first addition that can be made to Equation 1.27 towards a more realistic description of OSC is to add the field dependence of the mobility described in the Poole-Frenkel law given in Equation 1.11 of Section 1.1.3. An approximation of the SCLC including the characteristic field dependence of the Poole-Frenkel law can be calculated [1] to

$$j_{\mathrm{SCL}} \approx \frac{9}{8}\varepsilon\varepsilon_0\mu\frac{V^2}{d^3}\exp\left(0.89\beta\sqrt{\frac{V}{d}}\right) \ . \tag{1.28}$$

Another specialization of the space charge principle is the incorporation of trapped charges into the equation. When those traps are distributed e.g. exponentially in energy, trap filling will occur depending on the applied voltage and the current might be rising with a higher slope compared to the trap-free case until all traps have been filled. It is common practice to define the factor

$$l = \frac{E_{\mathrm{t}}}{\mathrm{k_B}T} \tag{1.29}$$

where E_{t} is the trap depth in energy with a distribution $N_{\mathrm{t}} \propto \exp(-l)$ [51]. The *trapped charge limited current* (TCLC) [1] is then given by

$$j_{\mathrm{TCL}} = N_0\mu\mathrm{e}\left(\frac{\varepsilon\varepsilon_0 l}{N_{\mathrm{t}}\mathrm{e}(l+1)}\right)^l\left(\frac{2l+1}{l+1}\right)^{l+1}\frac{V^{l+1}}{d^{2l+1}} \ , \tag{1.30}$$

where N_0 is the density of states. Most importantly, the current follows the relation

$$j_{\mathrm{TCL}} \propto \frac{V^{l+1}}{d^{2l+1}} \tag{1.31}$$

with $l = 1$ for a space charge (SCLC) equivalent, and $l > 1$ for additional trapped charges. As a special case of this universal relation, setting $l = 0$ will lead to the ohmic case where $j_{\mathrm{omic}} \propto {}^{V}/_{d}$.

When measuring organic devices, the limiting factors will change depending on at least the current density and voltage. Very often, ohmic transport with $j \propto {}^{V}/_{d}$ is observed for low voltages, followed by trapped charge limited current with $l > 1$ and eventually transfers to SCLC for high fields [77].

1.1.6. Optical properties

The term- or *Jablonski diagram* in Figure 1.7 shows the very basic electronic transitions of OSC using the example of optical excitation. The electronic ground state is the singlet state S_0, where *singlets* are states whose electrons are coupled antiparallel to form a spin-quantum number of $S = 0$. *Triplets*, in contrast, have a spin-quantum number of $S = 1$ with parallel alignment of electron spins. Excitations and transitions of organic semiconductors exist in the π-orbital between ground (π) and excited state (π^*) as described in Section 1.1.1, where unpaired electrons from the π^* and the remaining π electron form a two particle system [51]. The overall spin angular momentum of the system is described with Eigenvalues S and M_{s}. In a simple picture, they are composed from the sum of the individual single electron parts s and m_{s}. With electron spin up ($\uparrow$) and Eigenvalues $s = 1/2$ and $m_{\mathrm{s}} = 1/2$,

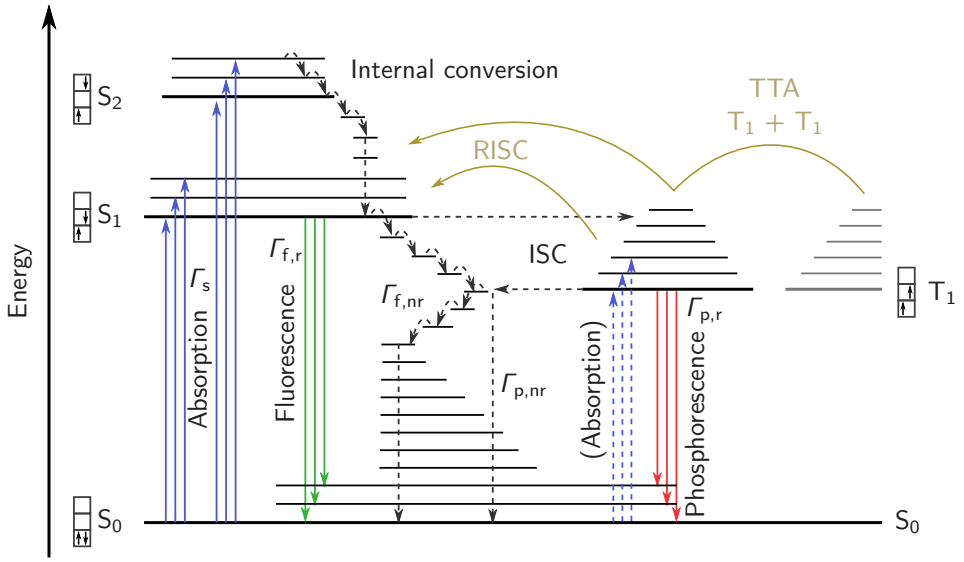

Figure 1.7.: Jablonski diagram showing the very basic processes of absorption and emission in OSC (after ref. [54]) as well as additional effects mainly concerning the radiative efficiency of OLEDs (after ref. [53,78]). Drawn with solid horizontal lines is the electronic ground state S_0 with two singlet (S_1, S_2) and one triplet excitation (T_1), as well as their respective vibronic states. Internal conversion will lead to a relaxation of higher energetic excited states to the lowest excited state, $S_2 \rightarrow S_1$. Transitions are colored blue for absorption (rate Γ_s for singlets), the direct absorption into the triplet is unlikely and thus illustrated with dashed arrows. Fluorescent emission (rate $\Gamma_{f,r}$) from the singlet is green and phosphorescent emission (triplet, rate $\Gamma_{p,r}$) is drawn in red. Non-radiative transitions from exited states to lower energetic states or to the ground state are depicted by dashed vertical lines and steps, the rates are $\Gamma_{f,nr}$ and $\Gamma_{p,nr}$ for singlets and triplets, respectively. The horizontal dashed line shows the inter-system crossing (ISC) converting a singlet to a triplet. Sketched in yellow are the processes of triplet-triplet-annihilation (TTA) and reverse inter-system crossing (RSIC), see text for further explanation.

as well as spin down ($\downarrow$) with $s = 1/2$ and $m_s = -1/2$, the four combinations of the single-electron spin-wavefunctions are as follows:

$$
\begin{aligned}
|\uparrow_1\uparrow_2\rangle &\rightarrow S = 1, M_s = 1 \\
\frac{1}{\sqrt{2}}\Big(|\uparrow_1\downarrow_2\rangle + |\downarrow_1\uparrow_2\rangle\Big) &\rightarrow S = 1, M_s = 0 \\
|\downarrow_1\downarrow_2\rangle &\rightarrow S = 1, M_s = -1 \\
\frac{1}{\sqrt{2}}\Big(|\uparrow_1\downarrow_2\rangle - |\downarrow_1\uparrow_2\rangle\Big) &\rightarrow S = 0, M_s = 0
\end{aligned}
$$

The first three of them with $S = 1$ form the triplet, the last with $S = 0$ is the singlet. Transitions from and to the ground state as well as between states are shortly summarized in the following paragraphs.

Excitation, injection and exciton recombination

Electrical injection and electron-hole pair formation is independent of spin selection rules an will therefore distribute equally over all four different spin wavefunctions. As a result, injected excitons will form 75 % of triplets, whereas only 25 % result in singlet excitation. Upon absorption, photons usually excite the singlet term [54] due to spin selection rules, the absorption rate is classified by the constant Γ_s. Direct triplet absorption requires a transition from the singlet ground state to the triplet excited state, which is normally forbidden [54] and the absorption rate Γ_t is therefore small (see the paragraph about ISC for explanation). Additional to the purely electronic terms, levels shifted to higher energies by vibronic interaction exist that as well can be excited. However, electrons in those vibronic states will quickly relax non-radiatively to the lower pure electronic excitation. Excitation of higher level singlets and triplets (S_2, S_3, T_2, T_3 etc.) are generally of very short lifetime in the order of a few pico seconds [54], they relax non-radiatively over vibronic substates to the respective first excited state via *internal conversion*. Thus, emission usually occurs from the lowest excited state, which is often also referred to as *Kasha's rule* [51].

Emission

Lifetimes of the first level excited states range from 10^{-9} s up to 10^{-6} s for S_1, the radiative decay of the S_1 state is termed *fluorescence* with the rate constant $\Gamma_{f,r}$. For triplets, the lifetime can exceed a few seconds, decaying radiatively over *phosphorescence* [54] with the rate constant $\Gamma_{p,r}$. Not every excitation S_1 or T_1 will decay radiatively, non-radiative decay rates are denoted $\Gamma_{f,nr}$ and $\Gamma_{p,nr}$. The energetic difference between absorption and emission due to the non-radiative relaxation of vibronic excitations leads to a redshift of the emission to lower energies with respect to absorption, which is termed *Stokes-shift*.

Inter system crossing / ISC

Normally, in a system classified only by its spin-quantum numbers, transitions from triplet to singlet states via so called *inter system crossing* (ISC), are forbidden. This rule can partially be broken by spin-orbit coupling, which is only weakly present in pure hydrocarbons, though very strong in metal complexes e.g. containing Iridium [79]. Hence, the direct absorption from S_0 to T_1 is also only possible due to spin orbit coupling and often very weak. With stronger ISC, however, fluorescence is partially weakened in the favor of a higher phosphorescent rate, while at the same time the phosphorescent lifetime is lowered [54].

Secondary processes

Two triplet states in an OSC may annihilate to a ground state leaving behind an excited singlet state or a triplet state. This so called *triplet-triplet annihilation* (TTA) leads to long-lived delayed fluorescence in the range of a few µs [80] for materials showing only very low phosphorescence. TTA can enhance the efficiency of fluorescent OLEDs, but will likewise have the converse effect on mainly phosphorescent devices [81]. The process has been extensively studied as a route to more efficient fluorescent OLEDs, however, the conversion rate from triplets to singlets is around 38 % at maximum, leaving room for improvement through other processes [78]. A different process that stands in contrast to the inter system crossing, is the *reverse inter system crossing* (RISC). When the energy difference of one excited triplet and singlet state is small and in the range of 100 meV or less, triplet states can convert

to singlets by thermal energy. Despite this so called *thermally activated delayed fluorescence* (TADF) being endothermic, highly efficient OLEDs employing the effect have been presented [78].

1.1.7. Molecular dipole moments, orientation and polarization

Organic semiconducting molecules all are extended objects with a complex structure and charge distribution. An asymmetric structure leads to the formation of *permanent dipole moments* (PDM) in OSC, just as it is the case for other polar molecules like H_2O or N_2O [7]. Additionally, wavefunctions of individual molecular orbitals $HOMO^n$ and $LUMO^n$ are differently distributed over the molecule. Electronic transitions for absorption and emission are hence also only occurring in specific directions of the molecule, the *transition dipole moments* (TDMs) are therefore oriented with respect to the molecular axes. Accordingly, the distribution of orientational angles of emitting molecules in the film plays a crucial role in light absorption, emission, outcoupling and device performance [7, 82, 83]. The determination of the emitter orientation has been a key field in research in the past years [9, 48]. Besides the implications on optical properties of the device, molecular orientation also affects the orientation of the permanent dipole moment, where the correlation of both TDM and PDM orientation is also subject to current research [48]. If the orientation of the PDMs in an organic layer is not completely isotropic, the *giant surface potential* (GSP) as a macroscopic polarization of the film will arise, which affects multiple properties of the device [3, 10–12]. The characterization of the GSP and specifically its impact on hole injection into the device is a central part of this work and will be discussed further in the experimental section.

Permanent dipole moments

Magnitude and direction of the PDM depend on the charge distribution of the molecule, which in turn is dependent on the chemical structure. In Figure 1.8 the polar molecule OXD-7 is depicted in its three conformers. The electron density is also plotted below the skeletal formulas together with the direction of the PDM and selected transition dipole moments. All of them were calculated in the gas phase using the Schrödinger Materials Science suite [84] with the quantum chemical application Jaguar [85, 86]. Calculations were done using the basis set 6-31G** with the B3LYP-D3 functional for hydrocarbons or LACV3P**++ with M06-2X-D3 in case of metal complexes. Although it is chemically the same molecule, the calculated magnitude and direction of the permanent dipole varies between all three conformers from 3 D to 6 D, which is consistent with literature data [87]. Usually, the composition of a given material is unknown regarding different conformers, whether in powder form or in the thin film after deposition. If significant differences in the calculated dipole moments exist, assumptions have to be made on the prevailing conformer or any form of mixing and hence the effective dipole moment. Also, the molecules polarizability is not a priori known, neither can possible changes of its geometry in thin film be predicted with simple gas-phase simulations. In the case of this work, a weighted average using a Boltzmann statistic based on the conformational energy is used in the case of the OXD-7 molecule, which yields a value of (5.40 ± 1.35) D.

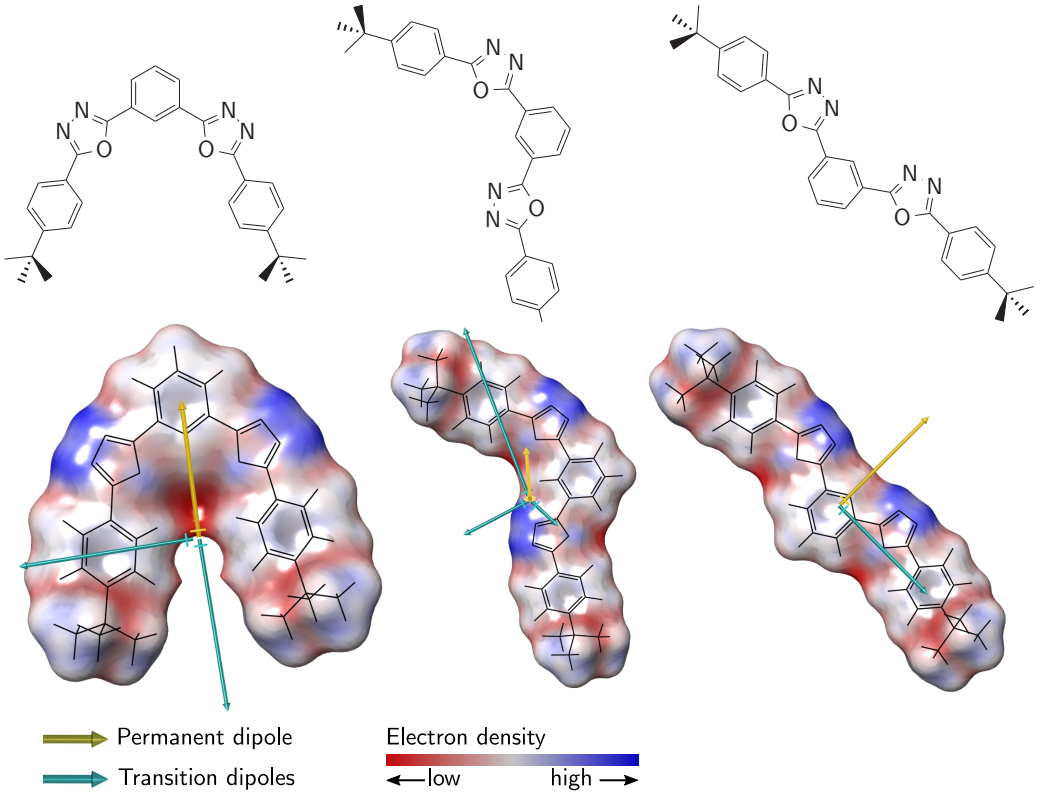

Figure 1.8.: The three known conformers of the molecule OXD-7, skeletal Lewis formulas at the top, 3D renderings with electron density on the bottom. In the renderings, also the permanent and most likely transition dipole moments are given. The length of the arrows is related to the magnitude of the dipole moments.

Polarization and interface charge

Upon vacuum processing of the organic film, a non-isotropic orientation in the film will lead to a so-called *spontaneous orientation polarization* (SOP) for many organic materials [6]. Accordingly, both PDM and the TDMs of a molecule will have a preferential orientation with respect to the surface normal, which in some cases can even be detected independently [48]. It has been found that the deposition technique plays a crucial role concerning the molecular orientation in the films [88] and some proposals to explain the orientation exist [7, 89]. Experimentally, an increased orientation can be assumed for many materials when diluted in non-polar host systems [2, 48]. The exact mechanisms behind SOP, however, are to date not fully understood and subject to ongoing research [7], though it has been reproduced in simulation for selected molecules [47]. One effect of the SOP itself on organic LEDs is, however, known for almost 20 years. At first, Berleb *et al.* reported a negative interfacial charge density σ at the NPB/Alq_3 interface in two-layer OLEDs incorporating those materials [90]. Later on Ito *et al.* directly observed a significant potential drop in Alq_3 thin films via a Kelvin probe [10] and related this to the existence of oriented dipoles in the film. Both measurement techniques are described in detail in Section 3.2 and Sec-

tion 3.1, respectively. The mutual link of both phenomena was, however, not initially known and suggested some years later by Noguchi *et al.* [12]. In the following part, an overview on orientation polarization will be given.

The polarization of an organic thin film can be defined as $\vec{P}_0$ [7] with

$$\vec{P}_0 = \sum_i \frac{\vec{p}_i}{L^3}, \tag{1.32}$$

where $\vec{p}_i$ is the PDM of the molecule indexed i with magnitude $|\vec{p}_i| = p$ in the film of volume L^3. Interesting for the measurement is the component of the film polarization perpendicular to the surface normal. With only one component in the film, thus ignoring doping or different conformers, the "z" component calculates to $\vec{p}_i \cdot \vec{z}$. It is linked to the orientational angle of the individual molecules θ_i with

$$\vec{p}_i \cdot \vec{z} = p \cos\theta_i \tag{1.33}$$

leading to an overall film polarization of [7]

$$P_0 = \vec{P}_0 \cdot \vec{z} = \frac{p \sum_i \cos\theta_i}{L^3} \ . \tag{1.34}$$

The average angle of all molecules in the film can be calculated with the number density of molecules per volume n to

$$\langle \cos\theta \rangle = \frac{\sum_i \Phi(\theta_i) \cos\theta_i}{nL^3}, \tag{1.35}$$

where $\Phi(\theta)$ is the distribution function for molecules existing in the specific angle θ [7,48]. Note that the orientational angle in Equation 1.35 contributes non-linearly to the result and hence the preferential orientation $\theta_{\max}$ of the PDM at the maximum of $\Phi(\theta_{\max})$ does not necessarily correspond to the average orientation [7]. Equation 1.34 can then be rewritten to

$$P_0 = p \langle \cos\theta \rangle n \ . \tag{1.36}$$

Assuming the unlikely case that all dipoles in the layers would orient exactly parallel to the surface normal and $\langle \cos\theta \rangle = 1$, the absolute maximum polarization in a film [2,10,48] is given by

$$P_{\max} = \frac{p}{V_{\mathrm{mol}}} = \frac{p \cdot \rho \mathrm{N_A}}{M} \ , \tag{1.37}$$

where ρ is the density of the material in the film, M the molar mass and $\mathrm{N_A}$ Avogadro's constant. The magnitude of the polarization is given in dipole moment per unit volume and therefore corresponds to the equivalent interface charge density at the film surface, hence $P_0 = \sigma_{\mathrm{s}}$. With $\sigma_{\max} = P_{\max}$, an alignment factor Λ can be defined [2,48] describing the degree of orientation perpendicular to the film surface, with

$$\Lambda = \frac{\sigma_{\mathrm{s}}}{\sigma_{\max}} \ . \tag{1.38}$$

In the above framework, $\Lambda = \langle \cos\theta \rangle$. If σ_{s} is known or measured for example with impedance spectroscopy (see Section 3.2) or Kelvin probe (see Section 3.1), the average orientational angle can be estimated [91].

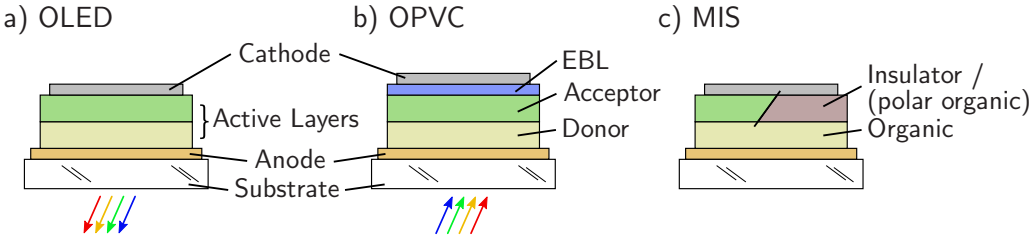

Figure 1.9.: Sketches of the stacks of different organic semiconducting devices. **a)** Basic Two-layer OLED **b)** Organic solar cell with donor/acceptor interface and electron blocking layer. **c)** Metal-insulator-semiconductor device with either polar or insulating layer.

Giant surface potential

In case of a uniform polarization throughout the film, the potential drop induced by the polarization [7] can be calculated to

$$\Delta V = \int_0^d \frac{\vec{P}_0}{\varepsilon\varepsilon_0}\,\mathrm{d}x = \frac{p\,\langle\cos\theta\rangle\,n}{\varepsilon\varepsilon_0}d = \frac{\sigma_\mathrm{s}}{\varepsilon\varepsilon_0}d\ , \tag{1.39}$$

where d is the thickness of the film and ε its dielectric constant. The induced potential drop ΔV over that distance will also lead to a gradient in vacuum level and surface workfunction with respect to the substrate levels. It thus corresponds to the giant surface potential measured e.g. with Kelvin probe, see Section 3.1 for details.

1.2. Organic semiconducting devices

Within this work, energetic and transport properties of organic materials are investigated in various device types. With the differences between organic and inorganic semiconductors outlined in the previous sections, some distinctive features and properties of organic semiconducting devices have to be taken into account. While the organic light emitting diode (OLED) is the primary use case for most of the materials investigated, organic photovoltaic cells (OPVC) can also give a vital insight on built-in device properties. Metal insulator semiconductor (MIS) devices additionally allow to probe specific transport phenomena in single layer material systems. The layer stacks of all three device types are sketched in Figure 1.9, a more detailed description of the individual functions of each layer is given in the sections below.

1.2.1. Organic light emitting diodes (OLEDs)

In an *organic light emitting diode* (OLED), the radiative recombination of charge carriers injected through the electrodes causes the emission of, ideally, visible light. The spectra of so-called electroluminescent materials are governed by the energetics of exciton recombination over the molecular energy gap or more complex excited states between two different materials [78]. The first reports on visible emission from organic molecular crystals or films date back to the middle of the last century, but required a few 1000 V to operate [92, 93]. In 1987, Tang and van Slyke proposed a two-layer diode, which allowed low voltage operation and decent light emission [94].

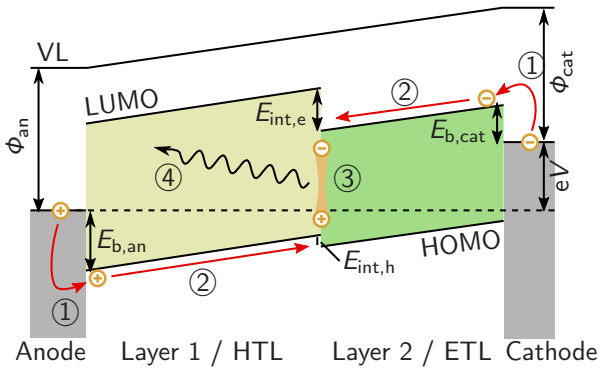

Figure 1.10.: Band diagram of an OLED at its driving voltage above V_{bi}. The numbered processes for light generation are ① charge injection, ② carrier transport, ③ exciton formation and ④ exciton recombination and photoemission. Adapted and modified from ref. [1].

Their OLED, based on Alq_3 and diamine, reached an external quantum efficiency (EQE) of 1 % at voltages below 10 V.

Although state of the art OLED stacks are more complex [95], the simple two-layer approach as sketched in Figure 1.9a is still used today to study device physics, just as in this work.

Working principle

The working principle is similar to that of an inorganic LED [54], a simple energy diagram describing the elementary processes is given in Figure 1.10. Above the built-in voltage V_{bi}, mainly defined by the workfunction difference of anode and cathode, charges are injected into the respective molecular orbitals of the semiconductor, marked in Figure 1.10 as process ①. To enhance hole injection from the substrate to the active layers, organic semiconducting devices often utilize an additional *hole injection layer* (HIL) to lower $E_{b,an}$. Similar layers can exist on the cathode side, too. Assisted by the electrical field, resulting from internal fields and the applied voltage, carriers drift to the interface of both layers (process ②), where energetic barriers between levels of these layers ($E_{int,e}$ and $E_{int,h}$) can hinder further charge transport, promoting exciton formation at the interface (process ③). Due to their specific function in charge transport, both layers are commonly referred to as *electron transport layer* (ETL) and *hole transport layer* (HTL). Additionally, on the cathode side, *hole blocking layers* (HBL) and likewise *electron blocking layers* (EBL) at the anode can be incorporated to increase carrier selectivity of the contacts. In the case sketched in Figure 1.10, the intrinsic barrier for electrons $E_{int,e}$ from ETL to HTL is higher than the hole barrier $E_{int,h}$ from HTL to ETL, allowing holes to penetrate Layer 2, leading to exciton formation in this layer. This is usually the case for NPB/Alq_3 OLEDs, where the HTL is composed of NPB and Alq_3 is the electron transport layer [1]. In modern OLEDs, the introduction of a specific *emission layer* (EML) tailored for light emission significantly enhances the efficiency. Energetically, this layer can be constrained to the HOMO of the HTL and the LUMO of the ETL, leading to a charge carrier confinement in the emission layer between the combined charge transfer and blocking layers [96]. Further optimization of the emission layer

can be achieved by doping a radiant dye molecule with a few weight percent into a transporting matrix material [5, 36, 83]. Doping allows to design the transport material in the emission layer independently of the emitting species, further optimizing exciton generation and charge transport.

The energy of the formed charge transfer exciton and hence the emission is limited by the smallest HOMO/LUMO difference, further lowered by the exciton binding energy. Excitons can then transfer to electronically-excited singlet or triplet states, both of which can decay radiatively in process ④ and contribute to the electroluminescence of the device [54] (see Section 1.1.6 for reference).

Efficiency

A general equation for the efficiency of an organic light emitting diode is given by the external quantum efficiency η_{EQE} that can be written as [97]

$$\eta_{\mathrm{EQE}} = \eta_{\mathrm{IQE}} \cdot \eta_{\mathrm{out}} = \gamma \cdot \eta_{\mathrm{r}} \cdot q_{\mathrm{eff}} \cdot \eta_{\mathrm{out}} \ . \tag{1.40}$$

Here, η_{EQE} is linked to the internal quantum efficiency η_{IQE} with the outcoupling factor η_{out}. Internally, the efficiency is determined by the charge carrier balance of injected electrons and holes and generated excitons γ, the radiative exciton fraction η_{r} and the effective radiative quantum efficiency q_{eff}. The individual factors of Equation 1.40 are defined as follows.

γ The charge carrier balance γ is defined by the ratio of formed electron-hole pairs and injected carriers in the device. To achieve carrier balances near unity, appropriate blocking and transport layers should be used [36]. Also, injection contacts ought to be energetically aligned properly to counteract imbalanced carrier densities. Additionally, recombination statistics have to be considered when designing the device [98].

η_{r} The fraction of generated excitons that could recombine radiatively is governed by spin selection rules and amounts to $\eta_{\mathrm{r}} = 0.25$ for pure fluorescent materials, whereas phosphorescent emitters can reach $\eta_{\mathrm{r}} = 1$ [98], see Section 1.1.6 for an explanation. With hybrid processes like thermally activated delayed fluorescence (TADF) [99] or tripplet-tripplet annihilation (TTA) [80], the radiative exciton fraction can also be enhanced for fluorescent materials.

q_{eff} While η_{r} defines the maximum of radiative decay, q_{eff} is defined by the fraction of radiative and non radiative decay of excitons that could emit light [98], which is heavily dependent on the layer stack and micro cavities in the OLED. Therefore, the factor q_{eff} is strictly speaking a dependent quantity of $q_{\mathrm{eff}}\,(q_{\mathrm{int}})$, where q_{int} is the intrinsic radiative quantum efficiency. The latter is defined by the rate equation

$$q_{\mathrm{int}} = \frac{\Gamma_{\mathrm{r}}}{\Gamma_{\mathrm{nr}} + \Gamma_{\mathrm{r}}} \ , \tag{1.41}$$

where Γ_{r} and Γ_{nr} are the radiative and non-radiative decay rates, respectively [98]. The effective radiative quantum efficiency $q_{\mathrm{eff}}\,(q_{\mathrm{int}})$ is then linked to q_{int} via the so called Purcell-factor F, where

$$q_{\mathrm{eff}} = \frac{F \cdot \Gamma_{\mathrm{r}}}{\Gamma_{\mathrm{nr}} + F \cdot \Gamma_{\mathrm{r}}} \ . \tag{1.42}$$

The Purcell factor describes the effect of the same name and accounts for the change of radiative decay rates in media incorporated into layer stacks of different refractive indices and in the vicinity of metal layers [98].

η_{out} Although the theoretical limit of the aforementioned factors can reach 100 % for phosphorescent or TADF emitters, if all effects are taken into account [36, 78], the outcoupling of light from the OLED to the surrounding air is still a crucial factor. In its simplest description from ray optics,

$$\eta_{\text{out}} = \frac{1}{2{n_{\text{org}}}^2} \,, \tag{1.43}$$

where n_{org} is the simplified refractive index of the layer stack. With values for organic layers in between $n_{\text{org}} = 1.6$ and 1.8 the maximum outcoupling efficiency will calculate to $\eta_{\text{out,max}} \approx 20\,\%$ [98].

Characteristics

The current of an organic light emitting diode ideally follows the ordinary diode characteristic given by the Shockley equation [100]

$$j_{\text{led}}(V) = j_0 \left[\exp\left(\frac{\mathrm{e}V}{n\mathrm{k_B}T}\right) - 1\right] \,, \tag{1.44}$$

that relates the current density j to the voltage V using the reverse-bias saturation current density j_0 and the diode ideality factor n, as well as the elementary charge e and the temperature T. The ideality factor is $n = 1$ for an ideal p-n-junction with only bimolecular recombination and in absence of trapping. For organic semiconductors, the value of n can give insight on the recombination and transport processes in the device. For example, in case of trap assisted recombination a value of $n = 2$ is often observed [101], much higher values have no direct equivalence.

The above equation, however, lacks all influences besides the pure junction, such as series and parallel resistances. The Shockley equation is hence modified [102] to include R_{s} and R_{p} to

$$j(V) = j_0 \left[\exp\left(\frac{\mathrm{e}\,(V - j(V)R_{\text{s}})}{n\mathrm{k_B}T}\right) - 1\right] + \frac{V - j \cdot R_{\text{s}}}{R_{\text{p}}} \,. \tag{1.45}$$

In the original Shockley equation, the reverse bias saturation current j_0 is described by the amount of charge carriers generated over the bandgap [100], which can be expressed as follows [102]

$$j_0 = j_{00} \exp\left(\frac{-E_{\text{gap}}}{\mathrm{k_B}T}\right) \,, \tag{1.46}$$

where E_{gap} is the p-n-junction bandgap and j_{00} a constant dependent on the electronic coupling strength of the material [103, 104]. The temperature dependence of both $j(V)$ and j_0 theoretically allows the extraction of the bandgap from constant-current temperature dependent measurements [105]. Shockley's description of the $j(V)$ characteristic was based on classic semiconductor theory, also including respective charge injection models and transport characteristics consistent with inorganic devices. For OLEDs it has been shown that the model of thermionic emission (see

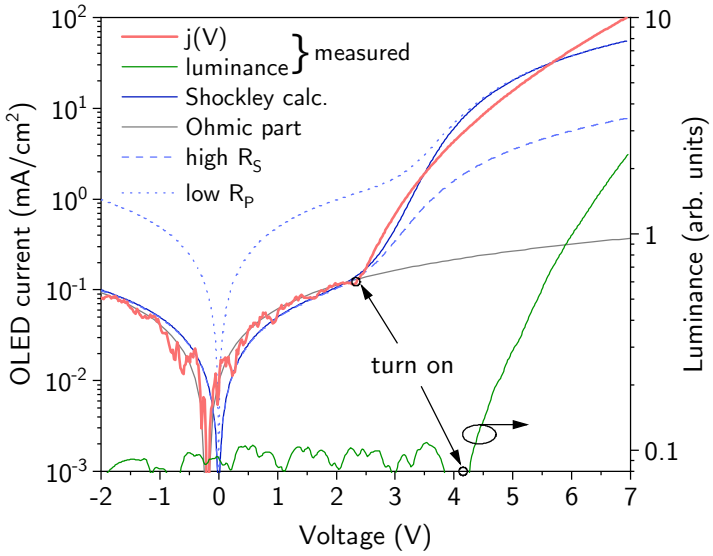

Figure 1.11.: Exemplary characteristic of an OLED measured on an NPB/Alq_3 device plotted in logarithmic scale for the current density. Drawn is the measured characteristic (red) and the extrapolation of its linear part (gray). The calculation of an equivalent device with the Shockley theory from Equation 1.45 is blue, changes for low parallel and low series resistances are shown with dotted and dashed lines, respectively. Additionally, the measured luminance of the device is given plotted on the right. Unfortunately, the dynamic range of the luminance in that particular example is very low, leading to a larger noise at low intensities.

Section 1.1.4 for reference) is not likely to describe the device. Pure space charge limited current without trapping is a tough constraint as well [106].

In Figure 1.11, a typical OLED characteristic is plotted alongside with the observed light output and a calculated Shockley curve. The impact of different changes in resistances have been calculated with otherwise identical parameters. In the example given in Figure 1.11, the low parallel resistance stems from the use of a polymeric hole injection layer and its lateral conductance. A higher series resistance limits the device current especially for higher voltages. Although the general form of the characteristic is described, the parameters to calculate the curve are way out of range of what would be reasonable for the device in question. Especially the ideality factor of $n \approx 10$ is a striking argument that the simple Shockley equation cannot be used to describe the whole OLED characteristic [106], or should at least not be applied to the whole measurement, but rather to individual working points of the device, only.

Some characteristic data as well as limiting factors can still be obtained by the analysis of the graph, especially the electrical and optical turn on voltages. The first is derived e.g. by a linear fit of the exponential part emerging from the ohmic background mainly defined by the parallel shunt resistance, whereas the latter is extrapolated from the measured luminance. By fitting the Shockley equation to the exponential part only, insights on the recombination mechanics in the device can be gained through the ideality factor [107].

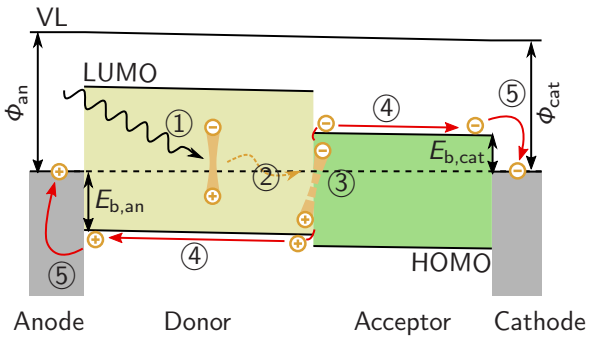

Figure 1.12.: Band structure of a donor-acceptor type organic solar cell in short circuit condition during illumination. The numbered processes for light absorption and carrier generation are ① absorption and exciton formation, ② exciton diffusion, ③ exciton dissociation and generation of individual carriers, ④ carrier diffusion and ⑤ charge extraction.

1.2.2. Organic photovoltaics (OPV)

The first notable organic photovoltaic cell was fabricated by Tang *et al.* using Copper phthalocyanine (CuPc) and a perylene derivative [108] which yielded $\eta \approx 0.95\,\%$ efficiency, compared to around $\eta \approx 0.1\,\%$ for single layer devices of that time [109]. In his design approach, two materials with different electron and hole affinities are brought together creating the so called *donor-acceptor interface*, instead of relying on the work functions of the electrodes to create a built-in potential for exciton dissociation. Consequently, charge separation mainly occurs at this interface, hence optimizing its structure and morphology is crucial for device performance [110]. Over time, multiple different device architectures have evolved, ranging from a planar contact of two adjacent layers (*planar heterojunction*, PHJ) to a mixture of both (*bulk heterojunction*, BHJ). Other variations of cell architectures involving a combination of neat and mixed layers can exhibit higher efficiencies by reducing parasitic recombination in the bulk and enhancing contact selectivity [111]. An exemplary stack design for a two-layer organic solar cell is presented in Figure 1.9b. The active layers are sandwiched between two electrodes, where, similar to the OLED, hole-injection and *exciton blocking layers* (EBL) can enhance the cell efficiency. Light absorption can take place in any of the layers, the large exciton binding energy will lead to bound electron-hole pairs that have to diffuse to the donor-acceptor interface for charge separation.

Efficiency and working principle

In this work, organic solar cells mainly function as a prototypical device to probe device properties without the aim to produce highly efficient cells. The device structure in form of a planar heterojunction is hence similar to the light emitting counterparts, refer to Figure 1.9 for a comparison. The efficiency of a solar cell can be described by its external (η_{EQE}) and internal (η_{IQE}) quantum efficiencies, where external and internal efficiencies are linked through the amount of optical losses upon coupling

light into the cell, given by R [112]. Thus

$$\eta_{\mathrm{EQE}} = \eta_{\mathrm{IQE}} \cdot (1 - R) \ . \tag{1.47}$$

For organic solar cells, the internal quantum efficiency can then be described by the absorption efficiency η_{A}, the amount of exitons reaching a dissociation site through diffusion η_{ED} and the efficiency of charge dissociation and carrier generation at these sites η_{CT}. Finally, the charge transport and collection efficiency is represented by η_{CC} [112], resulting to

$$\eta_{\mathrm{IQE}} = \eta_{\mathrm{A}} \cdot \eta_{\mathrm{ED}} \cdot \eta_{\mathrm{CT}} \cdot \eta_{\mathrm{CC}} \ . \tag{1.48}$$

The individual parts of the internal quantum efficiency are strongly linked to the working principle of an organic solar cell, which is best explained with the energy diagram of a cell in short circuit condition at hand, see Figure 1.12.

η_{A} At first, light absorption and the formation of excitons has to take place, denoted as process ① in Figure 1.12. OSCs can show very high absorption, reaching high optical density with thin layers of ≈100 nm [113] leading to high η_{A}, although in a limited spectral range.

η_{ED} However, the generated excitons, being neutral species, have to diffuse randomly to the dissociation sites as their motion cannot be affected by electric fields (process ②). As a result, a trade-off exists between high absorption and exciton diffusion length, typically lowering η_{ED} for high film thicknesses [114].

η_{CT} The charge transfer efficiency η_{CT} combines the efficiency for the formation of a charge transfer state as well as its dissociation into free carriers (process ③). The exact mechanism behind the formation of such a state and the accompanied energy losses governing η_{CT}, however, are still under investigation [114–116].

η_{CC} In η_{CC}, charge transport of separated carriers is then governed by the charge carrier mobility, which can be affected by traps and recombination (④). Finally, the collection of charges at the electrodes (⑤) again limits the cell efficiency, as interface energetics and morphology are generally quite complex [114].

Characteristics

The characteristics of a solar cell distinguish between a dark and an illuminated current, as shown in Figure 1.13. The dark current ideally follows that of an ordinary diode and can thus again be described by the Shockley equation given in Equation 1.44. In case of an illuminated solar cell, the equation is ideally only shifted downward by the photogenerated current j_{Phot}, hence

$$j_{\mathrm{light}}(V) = j_0 \left[\exp\left(\frac{\mathrm{e}V}{n \mathrm{k_B} T} \right) - 1 \right] - j_{\mathrm{Phot}} \ . \tag{1.49}$$

This equation will lead to a short circuit current equal to the photogenerated current $j_{\mathrm{sc}} = j_{\mathrm{light}}(0\,\mathrm{V}) = j_{\mathrm{Phot}}$. Parasitic recombination of charge carriers as well as non-ideal shunt and series resistances, however, will reduce the short circuit current.

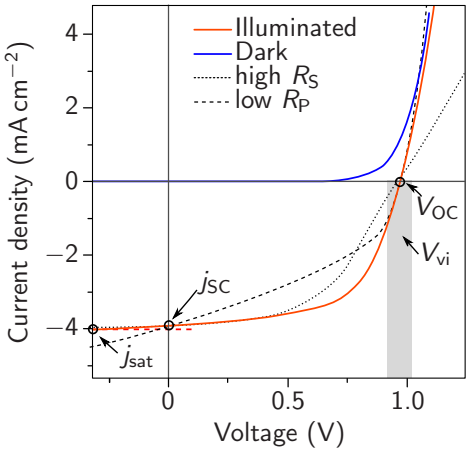

Figure 1.13.: Exemplary characteristic of an organic solar cell. Shown is the dark and illuminated measurement as well as some key parameters for solar cell performance. Dotted and dashed lines represent cells with different defects, namely low parallel or high series resistance.

The negative bias saturation current under illumination is $j_{\mathrm{sat}} \rightarrow j_{\mathrm{light}}(-\infty\,\mathrm{V}) = |j_0 + j_{\mathrm{Phot}}|$. The photocurrent j_{Phot} is thus usually in between j_{sc} and j_{sat} and hence not directly available from the illuminated characteristics.

Including parallel R_{p} and series resistances R_{s} again leads to a modified Shockley equation [102] similar to the OLED case in Equation 1.45:

$$j(V) = j_0 \left[\exp\left(\frac{\mathrm{e}\,(V - j(V)R_{\mathrm{s}})}{n\mathrm{k_B}T}\right) - 1\right] + \frac{V - j(V)R_{\mathrm{s}}}{R_{\mathrm{p}}} - j_{\mathrm{Phot}}\,. \tag{1.50}$$

The form of the characteristic can give qualitative information on R_{S} and R_{P}, shown with dashed and dotted lines in Figure 1.13. A finite parallel resistance R_{p} induces a constant ohmic increase in current larger than j_{sc} for increasing negative bias, whereas a large R_{s} flattens the curve for higher voltages [102, 117]. Consequently, saturation for illuminated solar cells might never be reached in reverse bias for real devices. Not directly accessible from the measured characteristics is the built-in voltage V_{bi}, depending on the device stack chosen, it may be above or below the open circuit voltage [118]. Similar to the OLED case a direct fit of the Shockley equation, especially in the illuminated case, will not lead to reasonable results. Fitting of the exponential tail of the dark characteristics, however, can be used to draw conclusions on the ideality factor n.

Solving Equation 1.49 with $j(V)$ set to zero leads to the open circuit voltage V_{OC} with

$$V_{\mathrm{OC}} = \frac{n\mathrm{k_B}T}{\mathrm{e}} \ln\left(\frac{j_{\mathrm{sc}}}{j_0}\right)\,. \tag{1.51}$$

Here, the photogenerated current is compensated by the dark recombination current. This equation limits V_{OC} by light intensity through the short circuit current and intrinsically to the bandgap of the semiconductor due to an equilibrium condition for generation and recombination across this gap [102]. The latter condition is again

similar to the OLED case in Equation 1.46,

$$j_0 = j_{00} \exp\left(\frac{-E_{\mathrm{PVG}}}{n\mathrm{k_B}T}\right) , \tag{1.52}$$

where E_{PVG} in this case denotes the photovoltaic gap. Combining Equation 1.51 and Equation 1.52, the open circuit voltage can be approximated to

$$V_{\mathrm{OC}} = \frac{E_{\mathrm{PVG}}}{\mathrm{e}} - \frac{n\mathrm{k_B}T}{\mathrm{e}} \ln\left(\frac{j_{00}}{j_{\mathrm{sc}}}\right) . \tag{1.53}$$

In OPVC, charge separation occurs at the interface between donor and acceptor with the help of an intermediate *charge transfer state* (CT) between the HOMO of the donor and the LUMO of the acceptor. Empirically, the open circuit voltage of organic solar cells was found to be

$$\mathrm{e}V_{\mathrm{OC}} = |\mathrm{HOMO_D}| - |\mathrm{LUMO_A}| - \mathrm{e}V_{\mathrm{dev}} = E_{\mathrm{CT}} - \mathrm{e}V_{\mathrm{dev}} , \tag{1.54}$$

where $\mathrm{HOMO_D}$ and $\mathrm{LUMO_A}$ are the energy levels of the HOMO and LUMO of donor and acceptor, respectively, defining also the maximum energy of the charge transfer state E_{CT}. V_{dev} is the deviation from the transport gap typically found to be around 0.6 eV [119–121]. The relation of the photovoltaic gap to E_{CT} and the reduction by the remaining energy losses to V_{OC} are subject of current research [115] and would exceed the scope of this work. From the temperature dependence of V_{OC} gained from Equation 1.53, however, the extraction of E_{PVG} from an extrapolation of temperature dependent measurements is often suggested and discussed [122].

1.2.3. Metal-insulator-semiconductor devices (MIS)

Metal-insulator-semiconductor (MIS) devices are often utilized to probe specific semiconductor parameters, in fact, they are sometimes referred to as the "most useful device" to study semiconductor parameters [103]. This stack, however, is also found e.g. in photodetectors [123], where it is the base structure for charge coupled devices (CCDs) in digital cameras [103]. The device stack comprises a semiconducting layer sandwiched between a metal contact and an insulating layer, as seen in Figure 1.9c. Despite the stack design, three requirements are usually given for a device to be entitled a MIS-device [103]. At first the bandgap or at least the resistance of the insulator has to be large to inhibit any static current flow. Instead, only transient signals due to space charge should exist and being measured on the device. The second constraint is that no (mobile) charges exist in the device except those injected into the semiconductor and their respective image charge in the metal contact. At last, the original definition of MIS devices requires flat-band conditions in the semiconductor at zero external bias, possible by the strict requirement of a perfect ohmic contact at the semiconductor side. Within this work, the concept of MIS devices is transferred to polar OLEDs, where the insulating layer is replaced by a polar organic layer with giant surface potential; refer to Chapter 5 for further reference.

A specific feature of MIS diodes is their capacitive response to the applied voltage that in the beginning simply corresponds to the signal of two capacitors in series $C_{\mathrm{ges}} = (1/C_{\mathrm{ins}} + 1/C_{\mathrm{d}})^{-1}$. Here C_{ins} is the insulator capacitance and C_{d} the depletion layer capacitance of the semiconductor. The specific notion of the depletion layer

is made, because upon charge injection, the semiconductor might get conductive at areas of high injected charge density, reducing the effective depletion layer thickness and hence increasing its capacitance with dependence on voltage. This is specifically true for OLEDs with a polar layer, where the accumulation regime occurs at a transition voltage relative to the magnitude of the giant surface potential [1]. For further elaboration of this effect, refer to e.g. Section 3.2.1.

1.3. Electrical modeling and simulation

This section will provide a brief overview on the electrical models behind the simulations made in the experimental chapters. A comprehensive explanation of definition and implementation of a drift-diffusion simulation would go beyond the scope of this work. Still, a short introduction on drift-diffusion models is given. All models are implemented in and used with the commercially available software package Setfos, available in versions 4.6 and 5.0 [124]. The combined analysis and measurement platform Paios [125] is also linked to the Setfos software that is used for most fitting and measurement-to-simulation modeling.

1.3.1. Principal methods for electrical modeling

So far, all equations given are based on standard semiconductor theory and comprise bulk transport or injection currents, only. A complete description of the device current as a whole is thus not possible. To describe more complicated systems that might include multi-layer stacks or different electrode configurations, the *drift-diffusion model* (DD or DDM) has evolved and is generally used in many simulation tools. The DDM, however, only covers electrical properties of the system. For any optical absorption or emission calculations additional models have to be consulted and coupled to the respective electrical properties.

Usually, a system of differential equations is created based on the continuity equations for charge carrier densities and the Poisson equation, describing the link to the electric potential [53]. Hence, the initial set of equations (for electrons) can be written as

$$\frac{\partial E(x,t)}{\partial x} = \frac{\mathrm{e}}{\varepsilon\varepsilon_0}\left(p(x,t) - n(x,t)\right) \tag{1.55}$$

$$\frac{\partial n(x,t)}{\partial t} = \frac{1}{\mathrm{e}}\frac{\partial J_\mathrm{e}(x,t)}{\partial x} - R(x,t) + G(x,t) \tag{1.56}$$

$$J_\mathrm{e} = \underbrace{\mathrm{e}\mu_\mathrm{e}\left(x,t,E\right) n(x,t) E(x,t)}_{\text{drift}} + \underbrace{\mathrm{e}D(\mu_\mathrm{e})\frac{\partial n(x,t)}{\partial x}}_{\text{diffusion}} \tag{1.57}$$

where Equation 1.55 is the Poisson equation, Equation 1.56 the continuity equation for electrons and Equation 1.57 the net electron current density [61]. In the latter, both contributions to the overall current density are already included, the first expression relates to the drift current of carriers driven by the electric field. The second term describes the diffusion current with diffusion constant D, usually linked to the charge carrier mobility by the Einstein relation $\mathrm{e}D = \mu \mathrm{k_B} T$ [61]. In all equations, $n(x,t)$ is the time and position dependent electron density and μ_e the electron

mobility. Additional and analogous to Equations 1.56 and 1.57, current density and continuity equations have to be created for the hole current $J_\mathrm{h}(x,t)$ and hole density $p(x,t)$ with hole mobility μ_h, too. Further individual contributions to the above equations can be summarized as follows:

- **Mobility μ:**
  In the simplest way, the mobility is described by a constant factor. Usually, though, at least the Poole-Frenkel field dependent mobility presented earlier in Equation 1.11 is included [61, 126], hence

$$\mu(E) \propto \exp\left(\sqrt{\frac{E}{E_0}}\right) \ . \tag{1.58}$$

  For more complicated systems, Gaussian or correlated disorder might also be of interest. The general equations are described in Section 1.1.3.

- **Carrier generation G(x,t):**
  In the continuity equation (1.56), carrier generation processes are included only with the general abbreviation $G(x,t)$. In Setfos the carrier generation can be linked to the absorption profiles that are gained by transfer matrix calculations of the layer stack, in turn defined by the individual materials' complex refractive indices [126]. In total, the optical carrier generation is then defined by the spatial generation profile $g(x)$ from optical simulations and the generation efficiency G_opt with $G(x,t) = g(x)G_\mathrm{opt}$.

- **Carrier recombination R(x,t):**
  Bimolecular, radiative recombination in organic semiconductors is described with the Langevin type recombination, where the recombination rate is given by

$$R(x,t) = \frac{\eta \mathrm{e}}{\varepsilon\varepsilon_0} n(x,t)p(x,t)\left(\mu_\mathrm{e}(x,t) + \mu_\mathrm{h}(x,t)\right) \tag{1.59}$$

  with the Langevin recombination efficiency η. In more sophisticated simulations, especially in the case of bipolar transport [53], trapping of charge carriers can play a role in non-radiative recombination. In Setfos, the Shockley-Read-Hall recombination is included to simulate trap mediated recombination channels [126].

- **Radiative recombination, exciton physics**
  To achieve simulated emission or absorption in OLEDs or OPV, specific coupling between the aforementioned recombination or generation rates is needed. This can either be done directly, by linking the generated charges to the optical absorption density as given above, or by including additional excitonic models to the system. A similar approach is used in simulated emission, where the generated spatial exciton density is coupled to the emission profile [126].

For a successful numerical solution of that set of differential equations, suitable boundary conditions have to be defined. In the simplest case, the so-called *ohmic injection* where the injection current is not limiting the device current, boundaries are

set for the charge carrier density at the contacts to be constant in time. Additionally, carrier densities for electrons and holes are linked to each other with

$$n_{\mathrm{h}} \cdot n_{\mathrm{e}} = {N_0}^2 \exp\left(-\frac{E_{\mathrm{g}}}{\mathrm{k_B}T}\right) \ , \tag{1.60}$$

where E_{g} is the HOMO-LUMO gap and N_0 the density of states [126]. The carrier densities for holes at the anode (e.g. $x = 0$) and electrons at the cathode (e.g. $x = d$) can be linked to the respective electrode's injection barrier with a Boltzmann statistic, thus

$$n(x = 0, d) = N_0 \exp\left(\frac{E_{\mathrm{inj}}}{\mathrm{k_B}T}\right) \ . \tag{1.61}$$

If different injection models are to be used, the boundary conditions have to be changed, for a definition of possible injection barriers, see Section 1.1.4. A thermionic emission model, for example, will not define constant carrier densities, but instead bind electron and hole currents at the interface to the framework described in Equation 1.23 defined in Section 1.1.4 [126].

Additionally, each individual layer in the stack will require transfer equations to allow for carrier transfer between layers. Without any further assumption, the HOMO-HOMO or LUMO-LUMO splitting between both adjacent layers' energy levels can be utilized to link both sides' carrier densities using Boltzmann statistics [126]. For more sophisticated models, the transfer of carriers at an interface can in first principle be derived from the Miller-Abrahams theory [61] describing the hopping process from one molecule to another as given in Equation 1.9.

Simulation of AC impedance and transient signals

So far, only steady state currents can be calculated by solving Equations 1.55 to 1.57. For calculating the capacitive response of polar devices or transient signals like CELIV, additions to the model are needed. For impedance, the implementation in Setfos first calculates the steady state response of the device and afterwards applies a small perturbation signal. All quantities (potential, carrier and trap densities) are then expressed by their extended form of $A(x,t) = A_0(x,t) + A_{\mathrm{AC}}(x,t) \cdot \exp(i\omega t)$, where A_0 is the steady state solution. Inserting the AC equations in the already solved steady state problem results in a set of linear equations with the unknown parameters being A_{AC} [126]. Further calculation of the impedance can then follow the route also taken in experiment [3] as AC current and voltage relate to the impedance with $Z = {}^{j_{\mathrm{AC}}}/_{V_{\mathrm{AC}}}$, see Section 2.6.1. For transient simulations, a discretization of the device in finite elements has to be performed in order to consistently solve the drift-diffusion equations, allowing the analysis of time dependent changes of, e.g., the external potential in a CELIV experiment [127].

1.3.2. Drift diffusion on polar organic materials

The existence of non-isotropic orientation in organic layers alongside a non-zero permanent dipole moment leads to the buildup of the GSP and also an equivalent sheet-charge density at the interfaces of a polar layer. In case of most known polar materials the GSP is positive, leading to negative interfacial charges at the bottom of the organic layer, the one facing the substrate or underlying layers during film

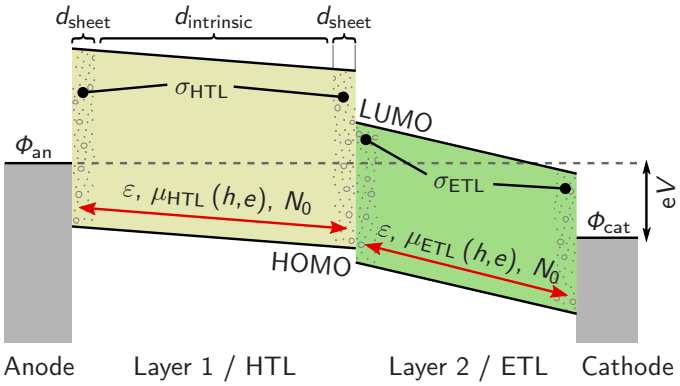

Figure 1.14.: Band structure of a polar OLED with a GSP in both HTL and ETL. The doped layers representing the interface charges are shaded, the intrinsic (undoped) part is sandwiched in between. The total layer count in simulation for this device is eight, where HTL and ETL are built up of three layers each. The main parameters put into simulation are marked in the picture, a summary with default values can be found in Table 1.1.

evaporation, whereas positive charges reside on the other side. The key part of simulating polar organic layers as introduced by Altazin *et al.* in 2016 [3] is to reproduce the existence of this sheet-charges in the simulated device. To extend the formalism to doped HTL OLEDs, a second polar layer has to be introduced, the simulated stack design is given in Figure 1.14. Again, the GSP is introduced by mimicking the sheet charge density at the interfaces of the polar layers by static doping and the doping density is calculated in accordance to the GSP or interface charge density. For a given sheet charge density σ or GSP ΔE, the doping density for acceptor or donor doping is given by

$$n_{\text{sheet}} = \frac{\sigma}{d_{\text{int}} \cdot \text{e}} = \frac{\Delta E \varepsilon \varepsilon_0}{d_{\text{int}} \cdot \text{e}} \,, \tag{1.62}$$

where d_{int} is the thickness of the sheet charge layer. For the common case of a non-inverted GSP, like with Alq_3, the acceptor doping forming negative charges is applied at the bottom layer, facing anode or HTL, whereas donor doping is needed at the opposite end. In simulation, these doping densities are time invariant and are therefore also not included in any calculated carrier profiles or densities. Instead, the Poisson equation in 1.55 is modified with acceptor and donor densities according to

$$\frac{\partial E(x,t)}{\partial x} = \frac{\text{e}}{\varepsilon \varepsilon_0} \left(p(x,t) - n(x,t) - A_{\text{doping}} + D_{\text{doping}} \right)$$

which also modifies the local electric field [126]. The resulting gradient successfully reproduces the features seen in experiment on polar OLEDs, including the accumulation of holes at the HTL/ETL interface that leads to the observed transition in measured capacitance. A detailed survey of the method is given by Altazin *et al.* in reference [3], the default parameters used within this work are given in Table 1.1.

In simulation, additional boundaries exist or are of large impact on the convergence of the calculation that in experiment might not be visible. For example, the sheet charge density, the density of states and the change in electric field have to stay in a

Quantity	Default Value & Unit		Meaning
μ_{h,Alq_3}	1×10^{-8}	$cm^2\,V^{-1}\,s^{-1}$	hole mobility of Alq_3
μ_{e,Alq_3}	5×10^{-3}	$cm^2\,V^{-1}\,s^{-1}$	electron mobility of Alq_3
$\mu_{h,NPB}$	2.4×10^{-4}	$cm^2\,V^{-1}\,s^{-1}$	hole mobility of NPB
$\mu_{e,NPB}$	1×10^{-7}	$cm^2\,V^{-1}\,s^{-1}$	electron mobility of NPB
N_{0,Alq_3}	1.5×10^{24}	cm^{-3}	density of states Alq_3
$N_{0,NPB}$	2×10^{24}	cm^{-3}	density of states NPB
σ_{Alq_3}	1.5	$mC\,m^{-2}$	sheet charge Alq_3
σ_{NPB}	0	$mC\,m^{-2}$	sheet charge NPB
ε_{Alq_3}	3.5	–	dielectric const. Alq_3
ε_{NPB}	3.5	–	dielectric const. NPB
$E_{HOMO,NPB}$	5.5	eV	HOMO NPB
$E_{LUMO,NPB}$	2.3	eV	LUMO of NPB
E_{HOMO,Alq_3}	5.8	eV	HOMO Alq_3
E_{LUMO,Alq_3}	2.6	eV	LUMO of Alq_3
$\Phi_{cathode}$	2.5 to 3.5	eV	cathode workfunction
Φ_{anode}	4.5 to 5.4	eV	anode / HIL WF

Table 1.1.: Default or example data for simulating polar OLEDs used in the scope of this work. Not all parameters are exact, as they might have to be changed to account for e.g. different injection barriers; also, the exact parameter set for field dependent mobilities or disorder models are omitted here.

certain relation to each other, otherwise high numeric errors can result in erroneous calculation of energy bands or effective carrier densities. Hence, multiplicative values like the dielectric constant and the sheet charge density can be modified accordingly in favor of convergence by accepting a larger difference to measured values, if the overall calculated quantities are acceptable.

2. Materials, sample preparation and characterization

2.1. Materials

The following sections will give a short overview on the materials incorporated into the devices studied in the scope of this work. Each section will explain a certain set of molecules grouped by their function in the devices. For a description of possible layers and functionalities in each device type, refer to the individual topics in Section 1.2. A table containing an overview of material parameters for all materials is given at the end of this section. The list of suppliers for the respective materials can be found in Section A.1 of the appendix.

2.1.1. Hole transporting and matrix materials

The hole transport layer of an organic light emitting diode should at least feature a HOMO level favoring hole injection for typical anode workfunctions and exhibit a considerably high hole mobility. With a relatively low ionization energy, hole transporting materials reversibly form radical cations, leading to preferential hole transport [54]. Two organic molecules have been mainly used in the scope of this work to function as hole transport layer, as well as matrix in case of doped systems.

NPB

One of the most widely studied, prototypical hole transporters is the molecule NPB (*N*,*N*'-Di(1-naphthyl)-*N*,*N*'-diphenyl-(1,1'-biphenyl)-4,4'-diamine), as seen in Figure 2.1a, with the molecular formula $C_{44}H_{32}N_2$. The structure of NPB is very similar to that of its sister molecule α-NPD. Both terms haven been used as synonyms in literature in the past years and also the molecules themselves may not have been distinguished thoroughly. Differences, although subtle, do exist however and affect device performance [128]. Within the scope of this work, the term NPB refers to the molecule without additional methylene groups. In OLEDs it is reportedly used as hole transport or injection layer, as well as electron blocker or host for doped systems [129]. Its HOMO and LUMO levels are 5.4 eV and 2.4 eV, respectively [1, 130], leading to a gap of 3 eV. NPB is thus absorbing in near UV, while emitting blue at around 430 nm wavelength [131]. Although considered a non-polar material, NPB does have a dipole moment between 0.6 D [6] and 1.6 D [47] and shows a small GSP in thin films [6,12]. The hole mobility is typically given within an order of magnitude of $1 \times 10^{-4}\,\mathrm{cm^2\,V^{-1}\,s^{-1}}$ [13] and charge transport in NPB shows signs of correlated disorder [129].

CBP

The second hole transporter is the molecule CBP (4,4-*N*,*N*'-Dicarbazole-1,1'-biphenyl), $C_{36}H_{24}N_2$. Compared to NPB, CBP shows a considerably higher HOMO level

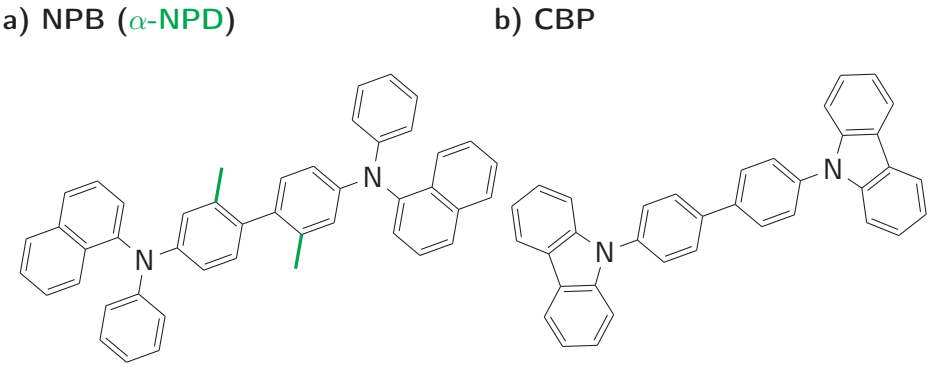

Figure 2.1.: The two main hole transporting materials studied in the scope of this work. **a)** NPB (*N,N'*-Di(1-naphthyl)-*N,N'*-diphenyl-(1,1'-biphenyl)-4,4'-diamine), which must not be mistaken with α-NPD that adds two methylene groups to the center of the molecule (green bonds). **b)** CBP (4,4'-Bis(carbazol-9-yl)biphenyl).

of between 5.6 eV [132] and 6 eV [133] and the LUMO is reported to be around 2.1 eV [132, 133]. The hole mobility is an order of magnitude higher than in NPB with approximately $1 \times 10^{-3}\,\mathrm{cm^2\,V^{-1}\,s^{-1}}$ [70] . CBP is non-polar with no permanent dipole moment possible to calculate for a single molecule [12]. Thin films processed from CBP, however, show a small and negative GSP [12], which can be reproduced in simulations, where the average dipole moment of a CBP molecule in the film is calculated to 0.9 D [47].

2.1.2. Electron transporting and emitting materials

In contrast to the previously described hole transporting materials, all of the materials described in the following section exhibit a strong permanent dipole moment. Additionally, all of the shown materials can be used as emitting species in either a diluted guest-host system, which is usually done with $Ir(ppy)_2(acac)$, or as neat film ETL and emitter in the case of Alq_3. Furthermore, Alq_3 and OXD-7 exhibit high electron mobilities and are therefore often employed for electron transport in devices.

Alq_3

The probably most prominent example for an electron transporting and emitting material is Alq_3 (Tris-(8-hydroxyquinoline)aluminum, $C_{27}H_{18}AlN_3O_3$), drawn in Figure 2.2a. It has been used in the first successful OLEDs in 1987 by Tang and van Slyke [94] in the dual-use configuration as ETL and emitter. With an aluminum ion in the center, surrounded by three quinolin-8-olate ligands, Alq_3 exists in a facial and a meridional isomer, where the latter one is more stable and by far dominant in thin films [134]. The permanent dipole moment of Alq_3 is calculated to values between 4.4 D and 6.0 D [12, 47] and shows a preferred orientation leading to a macroscopic giant surface potential [1] of roughly $40\,\mathrm{mV\,nm^{-1}}$ [12] with approximately 10 % of oriented dipoles in a neat film [2], which will be analyzed further also in the scope of this work. In contrast to the permanent dipole moment, the transition dipole moments are reported to be of isotropic orientation [9]. Electron trans-

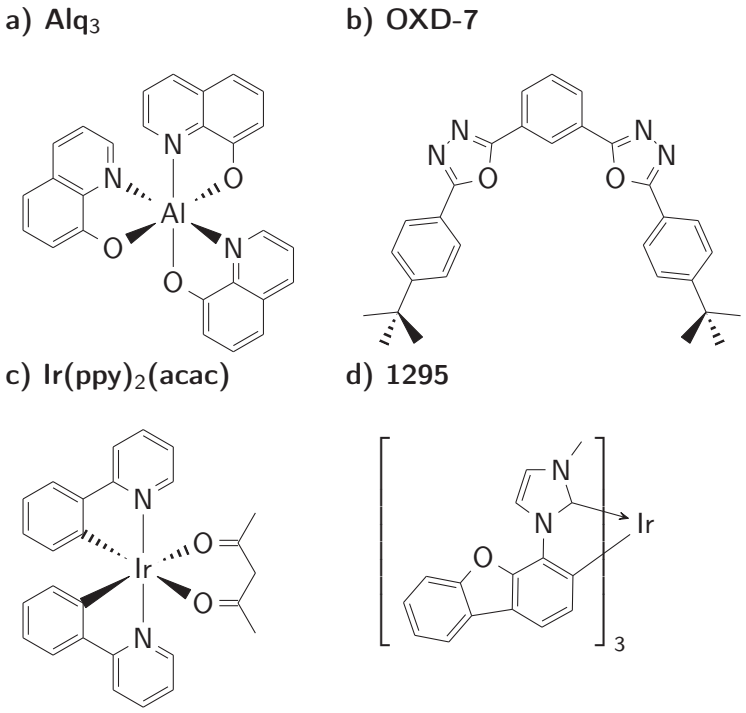

Figure 2.2.: Electron transporting materials and emitters. **a)** Meridonal Tris-(8-hydroxyquinolate)aluminum (Alq_3), **b)** OXD-7, **c)** Ir(ppy)2(acac) and **d)** 1295, known in literature as Ir(dbfmi).

port in Alq_3 has been studied extensively with various methods [1, 135, 136] and the mobility typically ranges between $1 \times 10^{-6}\,\mathrm{cm^2\,V^{-1}\,s^{-1}}$ and $1 \times 10^{-5}\,\mathrm{cm^2\,V^{-1}\,s^{-1}}$. While Alq_3 can show hole current, its mobility is orders of magnitude lower at about $10^{-8}\,\mathrm{cm^2\,V^{-1}\,s^{-1}}$ [63]. The gap of roughly 2.7 eV resides between a HOMO at 5.7 eV and a LUMO of 2.7 eV to 3.0 eV [1, 137] and leads to a green emission with a maximum around 520 nm [1, 94].

OXD-7

The oxadiazole derivative OXD-7 (1,3-bis[2-(4-tert-butylphenyl)-1,3,4-oxadiazo-5-yl] benzene, $C_{30}H_{30}N_4O_2$) was initially proposed as blue emitter and electron transporting material together with similar molecules by Hamada *et al.* in 1992 [138]. It became a widely used electron transporting material [139, 140] but can also be used as host [141] or UV emitter [142]. The molecule, depicted in Figure 2.2b, has a rotational degree of freedom at the bonds to the center benzene ring and hence exists in multiple different conformers [143], where one of the three statistically most likely ones is drawn [87]. OXD-7 has a single-molecule dipole moment of 3.5 D to 6.5 D depending on the conformer, where the value for the one shown in Figure 2.2b according to Emelyanova *et al.* is 6.2 D [87]. Energetically, with slight variations depending on the conformer, HOMO and LUMO are at roughly 6.5 eV and 2.3 eV, respectively [87]. In thin films, OXD-7 exhibits strong orientation polarization with a neat-film giant surface potential of around $80\,\mathrm{mV\,nm^{-1}}$ [12]. Concerning charge transport, the electron mobility is rather high with values from $2 \times 10^{-5}\,\mathrm{cm^2\,V^{-1}\,s^{-1}}$

measured with SCLC [144] up to $1 \times 10^{-4}\,\mathrm{cm^2\,V^{-1}\,s^{-1}}$ gained from time-of-flight measurements [143]. No reliable literature data on hole mobility could be found.

Ir(ppy)$_2$(acac) and **1295**

Ir(ppy)$_2$(acac) (bis(2-phenylpyridine)iridium(III)acetylacetonate, $C_{27}H_{23}IrN_2O_2$) visible in Figure 2.2c, is one of the most widely studied organic emitter molecules, as it allows extraordinary high quantum efficiencies [36, 145]. The molecule shows highly oriented growth, which can be studied both optically and electrically [48]. With a permanent dipole moment of 2 D and a possible relative orientation of more than 30 % [48] in neat films, Ir(ppy)$_2$(acac) shows a giant surface potential of roughly $100\,\mathrm{mV\,nm^{-1}}$, which has also been investigated in the scope of this work. Ir(ppy)$_2$(acac) emits in the green with a HOMO of 5.5 eV and a LUMO of 3.0 eV [146].

The second Ir compound is the organometallic carbene complex initially named Ir(dbfmi) [147,148] (tris(*N*-dibenzofuranyl-*N*'-methylimidazole)iridium(III), the sum-formula is $C_{48}H_{33}IrN_6O_3$). Its working title "1295", given by chemists at BASF, comprises a set of molecules with three equal ligands, each of which contains an imidazole and a dibenzofuran group extended with an additional functional group [91]. The variant 1295-A used in the scope of this work equals the original Ir(dbfmi) as depicted in Figure 2.2d and contains only one phenylic sidegroup. With a gap of 2.9 eV it is a blue emitter, HOMO and LUMO reside at 5.1 eV and 2.2 eV, respectively [91]. Both isomers of the molecule, facial and meridional, have strongly differing dipole moments of 8.6 D and 5.4 D [91]. It has been shown within this work that the complex 1295-A is one of the few polar organic materials that exhibit an inverse GSP slope of $(-51.7 \pm 11.0)\,\mathrm{mV\,nm^{-1}}$, see Section 3.1.2. The substance is not commercially available and has been synthesized at the Technical University of Braunschweig by Kristoffer Harms and Hans-Hermann Johannes. We were supplied with different batches of varying purity. The material available for this work is a mixture of the facial and meridional isomers, where the vast majority (>95 %) of molecules is meridional, elsewhere usually denoted as mer-1295A [91].

2.1.3. Injecting and charge generation layers

The following materials serve either as hole injection layer or carrier generation layer by light absorption e.g. in time-of-flight experiments (see Section 6.2). The exact function is depending on the specific device, a short description of the material is as follows.

PEDOT:PSS

The probably most widely used hole injection layer in organic semiconductors is the polymer mixture PEDOT:PSS shown in Figure 2.3a, which is typically processed from solution via spin-coating. Poly(3,4-ethylene dioxythiophene) (PEDOT, sometimes denoted as PEDT) is a conductive polymer with outstanding conductivity of up to $550\,\mathrm{S\,cm^{-1}}$ that is blended with poly(styrene sulfonate) (PSS), which, amongst other things, enables aqueous processing [149]. The conductivity of the blend PEDOT:PSS is typically lower than for pure PEDOT, but can be tuned by adding different solvents [150], also reaching almost metallic conductivity [151]. PEDOT:PSS films are almost completely transparent in the visible and near infrared range [152, 153], and typically feature a low surface roughness [154].

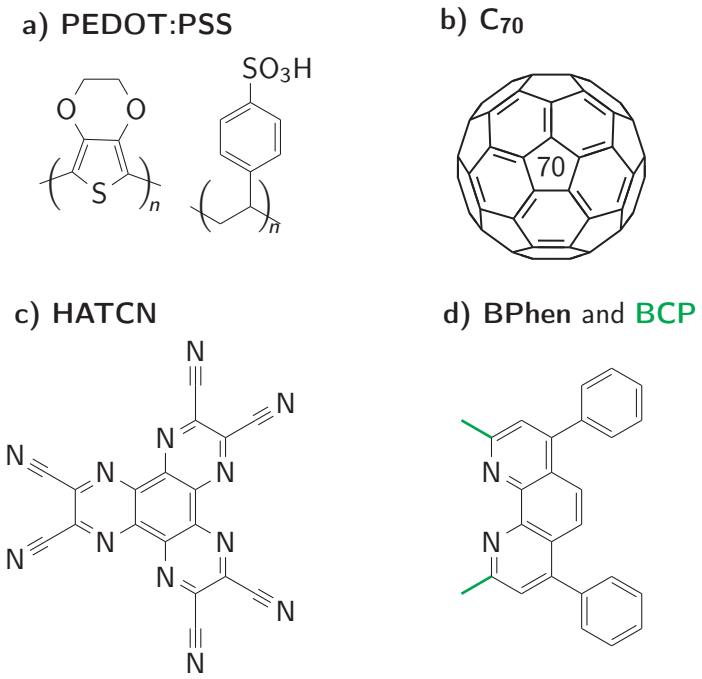

Figure 2.3.: (Organic) injecting, blocking and absorbing layers. **a)** The polymer blend PEDOT:PSS, **b)** the fullerene C_{70} used as charge generation layer, **c)** the small molecule hole-injector HATCN and **d)** shows Bathophenanthroline (BPhen) and Bathocuproine (BCP, with sidegroups in green).

Important for the hole injecting feature of a contact is its workfunction. Additional to adding water solubility to the polymer, the PSS anion also plays a crucial role in stabilizing the workfunction of the blend to values acceptable for hole injection into common organic substances [155]. In general, the absolute value of the workfunction depends on the solvents and additives to the blend, as well as post-treatment of the spin-coated film [117]. During this work, four different PEDOT:PSS derivatives are used to modify the workfunction Φ of the substrate. The first is "CLEVIOS™ P VP AI 4083" (further designated as AI4083), which has a nominal workfunction of 5.2 eV [156]. Without post-treatment by heating in vacuum, however, it is reported to be around $\Phi = 4.7\,\text{eV}$ to 4.8 eV [117, 157]. Following the order of rising workfunction, next in line is "CLEVIOS™ P VP CH 8000" (CH8000) with $\Phi = 5.15\,\text{eV}$ for an un-treated film [157]. CH8000 additionally shows a low conductivity, minimizing leakage currents in large area spin-coated layers. With 5.7 eV [117], the workfunction of "CLEVIOS™ HIL 1.3" (HIL1.3) is considerably larger. The highest workfunction could be reached using the pH-neutral formulation "CLEVIOS™ HIL1.3N" with 5.7 eV to 6.0 eV [8, 158].

HATCN

HATCN (1,4,5,8,9,11-hexaazatriphenylenehexacarbonitrile, $C_{18}N_{12}$), as shown in Figure 2.3c, is also often used on the hole-injection side. Because it is a small molecular material processed via thermal evaporation, it can also serve as a top-contact to the organic layer stack for inverted structures [159] or hole-only devices. The molecule's energy levels are considerably higher than the active materials' levels

with the HOMO of HATCN being reported at roughly 9.5 eV to 9.9 eV and a LUMO of 5.7 eV to 6 eV [160–162]. Ultraviolet photoelectron spectroscopy shows that the LUMO of HATCN processed on ITO is very close to the Fermi level, enabling charge transfer between the HATCN-LUMO and the next organics' HOMO level [161]. On metals, the LUMO of HATCN is even reported to be partially filled, resulting in an almost metallic behavior of HATCN with subsequent good injection into adjacent organic layers [163]. The workfunction of the combined ITO/HATCN contact has been measured to be up to 6.1 eV [161].

Fullerene C_{70}

Fullerenes, also known as "bucky balls", are a family of spherically shaped, hollow molecules, consisting of alternating penta- and hexagonal structures as depicted in Figure 2.3b. They got their name by their inventors, Kroto *et al.*, who used architect Buckminster-Fuller's studies on spheroidal structures to verify their findings [164] and eventually got awarded with the Nobel price of Chemistry in 1996. Fullerenes, in the form of C_{60}, have a long tradition in the role of electron acceptors for organic solar cells, probably starting with Sariciftci *et al.* in 1992 [165]. Albeit fullerenes as a whole were dominating the class of electron acceptors for years [166], they are slowly being replaced by non-fullerene acceptors due to superior solar cell performance [167].

Both, C_{60} and C_{70}, share many parameters, for example, HOMO and LUMO of C_{70} are reported to be similar to C_{60} [168]. Still, the values of HOMO and LUMO of C_{60} and C_{70} vary considerably with source and layer structure chosen for measurement, the HOMO is given with 6.1 eV to 6.4 eV [169, 170], whereas values in the range of 4.1 eV to 4.5 eV can be found for the LUMO [169–171]. Concerning carrier mobility, fullerenes exhibit an extraordinary high ability to accept electrons [172] with the electron mobility being in the range of $1\,\mathrm{cm^2\,V^{-1}\,s^{-1}}$ for C_{60} to $1 \times 10^{-3}\,\mathrm{cm^2\,V^{-1}\,s^{-1}}$ for C_{70} [173]. In the scope of this work, C_{70} is used as charge generation layer in time-of-flight experiments to determine the hole mobility of other organic compounds. For this purpose, C_{70} was preferred over C_{60} because of its superior absorption in the visible and near infrared wavelength range [174].

BCP and BPhen

Bathocuproine (BCP, $C_{26}H_{20}N_2$) shown in Figure 2.3d is used as en exciton blocking layer [175] in many organic solar cells and light emitting devices [176, 177]. It is an electron transport material [178] with a bandgap of roughly 3.5 eV to 4 eV and a LUMO at 3.0 eV [170, 175, 176]. The high gap is blocking exciton transfer to this layer in most cell configurations [176], while allowing electron transfer from common acceptor materials. BCP is usually applied only in very thin layers, thick layers have a negative influence on solar cell performance [176], the optimum seems to be around a few nm [179]. While BCP additionally protects the active layers from being penetrated by the cathode material, the same effect of metal doping enables effective transport of charge carriers [176]. Although seldom addressed in literature, the molecule exhibits a permanent dipole moment of 2.9 D and a thin-film GSP of $12\,\mathrm{mV\,nm^{-1}}$ to $33\,\mathrm{mV\,nm^{-1}}$ [12].

Bathophenanthroline (4,7-diphenyl-1,10-phenanthroline, $C_{24}H_{16}N_2$) with the trivial name BPhen lacks the two methyl groups of BCP and is widely used as an electron transporting material [180]. Like BCP, it can also act as hole [162] and exciton blocking layer in OLEDs and organic photovoltaics [181, 182]. The electron

mobility is relatively high with $4 \times 10^{-4}\,\mathrm{cm^2\,V^{-1}\,s^{-1}}$ [183], no data is available for the hole mobility. Energetically, the HOMO of BPhen resides at about 6.4 eV, where the LUMO is at 2.9 eV [180]. With the resulting high gap of more than 3 eV, as BPhen is practically transparent in the visible range [184].

2.1.4. Materials for electrodes and substrates

Processing of all samples is started on glass substrates coated with a transparent conductive oxide (TCO), acting typically as anode of the device. The top cathode layer is processed from a thermally evaporated metal of either Gold or a combination of Calcium topped with Aluminum, the workfunctions of which are given in Figure 2.4. Frequent TCOs are indium oxide, zinc oxide and tin oxide [185], where currently indium oxide layers are the most common for organic photovoltaics and LEDs. To enhance conductivity and control bandgap and workfunction, the oxides are doped [186]; in the case of indium oxide it is usually tin resulting in the common ITO (Indium-Tin-Oxide, In_2O_3:SnO_2).

The substrate base material for this work is BK7-glass with a nominal thickness of 0.7 mm. They are coated with a sputtered ITO layer of (90 ± 5) nm or (145 ± 10) nm thickness with a conductivity of $30\,\Omega/\square$ and $20\,\Omega/\square$, respectively [187]. ITO thin films are largely transparent with a transmission higher than 90 % in the visible range due to its bandgap, while the free-carrier plasma resonance leads to reflection in the infrared [185, 188]. The surface properties of ITO and its impact on device performance was studied extensively and as a result, ITO is usually pre-treated with UV-ozone or O_2-plasma cleaning [189–191]. The plasma etching or ozone cleaning not only removes residual contaminants and reduces surface roughness, it also heavily influences the ITO workfunction. Whereas literature values for the workfunction of pristine ITO range from 4.2 eV to 4.8 eV, a plasma treated surface can reach up to 5.2 eV [189]. Values measured for ITO in the scope of this work range between 4.5 eV to 4.8 eV, depending on substrate, pre-treatment and measurement technique (see Section 6.3.1 and Section 3.1.1). The effect on workfunction due to plasma or O_3 treatment can, however, diminish with time [191].

ITO is the de-facto standard of substrates in organic LEDs and photovoltaics, its replacement, however, is also subject to current research [192]. Indium is a deficient element in nature and has been identified a major cost factor in organic solar cells [193]. High brittleness and processing temperatures complicate the use of ITO thin films in flexible electronics [192,194], therefore especially post-processed PEDOT films, silver nanowires or graphene are promising candidates for its replacement [192, 194, 195].

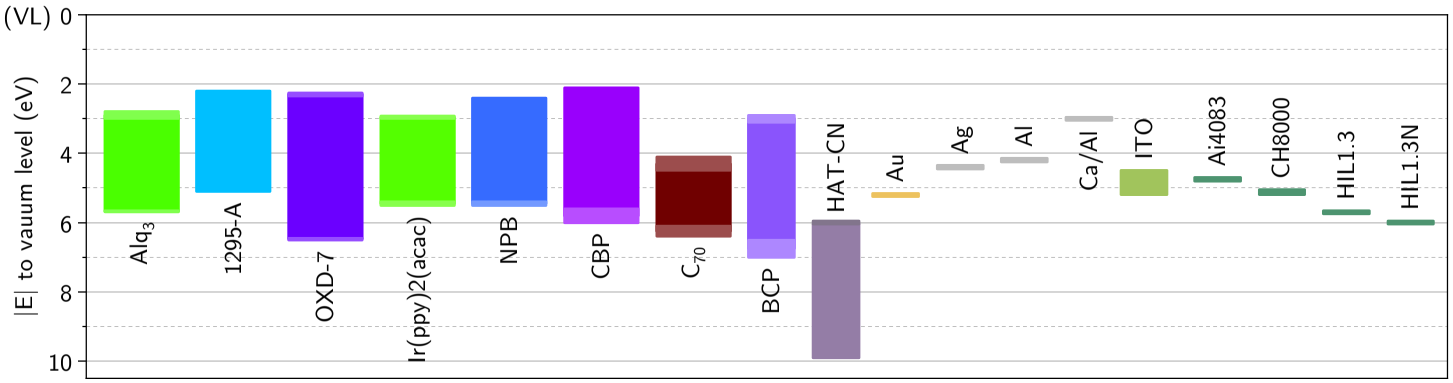

Figure 2.4.: Sketched energy diagram of all materials addressed in this section. The energy of HOMO and LUMO is given with respect to the vacuum level, metals are represented with their workfunction. Errors in lighter color show the spread of values observed in literature, see the table below for references.

Material	HOMO	LUMO [eV]	ref.	μ_h	μ_e [$cm^2 V^{-1} s^{-1}$]	ref.	p [D]	ref.
Alq_3	5.7	2.7 - 3.0	[1, 137]†	10^{-8}	10^{-5} to 10^{-6}	[63, 135, 136]	4.3 ± 0.2	[11, 47]
mer-1295A	5.1	2.2	[91]	– –	– –		5.4	[91]†
OXD-7	6.5	2.3	[87]‡	– –	10^{-5} to 10^{-4}	[143, 144]	5.5 ± 1.5	[87]
$Ir(ppy)_2(acac)$	5.5	3.0	[146]†	– –	– –		2.5	[6]
NPB	5.4	2.4	[1, 130]‡	10^{-4}	– –	[13]	0.5	[12, 47]
CBP	5.6 - 6.0	2.1	[132, 133]‡	10^{-3}	– –	[70]	0.9	[47]
C_{70}	6.1 - 6.4	4.1 - 4.5	[171]†, [169]‡, [170]	– –	10^{-3}	[173]	– –	
BCP	6.5 - 7.0	3.0	[170, 175, 176]‡	– –	– –		2.9	[12]
HATCN	9.5 - 9.9	5.7 - 6.0	[160]†, [161]‡, [162]	– –	– –		0.0	calc.

Table 2.1.: Literature values for selected quantities of all described materials, sources are given in the column behind the respective values. The dipole moment of HATCN has been calculated, see Section 1.1.7 for details. If the information was available from the publication, measurement techniques to obtain the HOMO levels can be either †) cyclic voltametry or ‡) photoelectron spectroscopy. In most cases, the LUMO is gained by subtracting the optical gap, though it could be available directly from cyclic voltametry.

2.2. Sample preparation and handling

2.2.1. Thermal evaporation

Small molecular systems, such as Alq_3 or NPB, can be efficiently processed using a thermal deposition method. For organics, this technique is generally referred to as *organic molecular beam deposition* (OMBD). The process not only allows precise control over the film thickness and processing parameters such as substrate temperature, but also offers the possibility to create mixtures of arbitrary molecules. In addition to organic molecules, during this work, also metals acting as electrode materials are processed using thermal evaporation. One OMBD chamber used to create thin film devices studied in the scope of this work is drawn in Figure 2.5, together with a sketch of the working principle.

The growth process

The growth process for (organic) molecules in thermal evaporation is generally considered to be a non-equilibrium process [53]. The source material is heated above its sublimation temperature, leading to a gas stream of material away from the sources to the substrate. In case of metals often melting can also occur, but is only rarely observed for organics. During evaporation, complex dynamics of molecule adsorption at the surface and desorption from the surface govern the amount of material available for film growth, while diffusion at the surface allows for a certain amount of reorganization. Similar to atomic thermal evaporation, three basic growth modes are identified. These are layer-by-layer growth, island growth and a combination of both, comprising islands starting to grow on the first closed monolayer. The main difference to atomic growth, however, is that organic molecules should be considered "extended objects" [53]. Although some of them can have an almost spherical shape, their orientation provides another set of degrees of freedom and has a great impact on overall device performance. As the interaction potential between surface and molecule and two adjacent molecules is likely to be different [53], preferential orientation depends on the surface material and temperature and can also change during film growth. One example for surface dependent orientation is the rod-shaped, flat perylene derivative diindenoperylene, which forms well defined, almost upright standing monolayers on a SiO_X substrate [196], while lying down flat on polycrystaline gold [197]. The substrate temperature reproducibly controls the orientation of another rod-shaped molecule α-sexithiophene between mostly lying down and upright standing for low or high temperature substrates, respectively [198]. In case of mixtures the re-organization and hence orientation of molecules depends on the properties of both materials. Thus, in a guest-host system, the glass transition temperature of the host material affects the amount of orientation of the guest [199].

Thickness monitoring

Typically, the growth process is monitored in-situ by quartz crystal microbalances held into the stream of molecules. The resonant frequency of the quartz crystal changes with its mass and hence the amount of adsorbed material. To precisely calculate the adsorbed material's thickness on the crystal, not only the mass, but also its acoustic impedance needs to be known [200], which is unfortunately not available for most organic materials. The thickness measurement is hence calibrated ex-situ by cross-checking the actual thickness with e.g. a profilometer or ellipsometry.

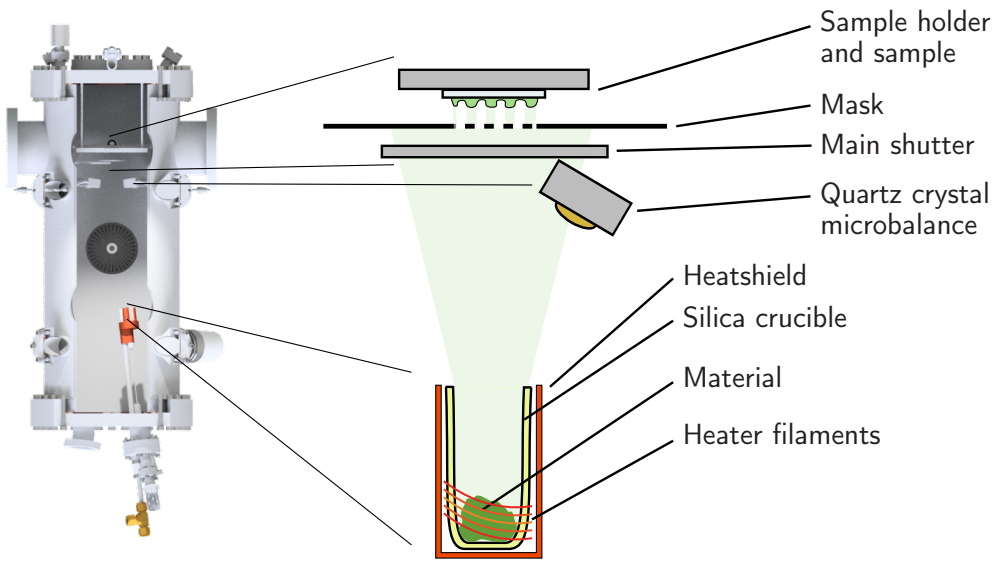

Figure 2.5.: Technical rendering in profile of one of the chambers used to create the organic thin films for this work. Visible is one of the four sources to evaporate materials, as well as sample holding, masking and shutter equipment. To enhance the mean free path of evaporated molecules and reduce the risk for contamination through oxygen or water, the main chambers for OMBD are typically evacuated to pressures in the range of 10^{-7} mbar. Usually, film growth is monitored in-situ with a quartz-crystal micro balance.

This procedure also allows for correction of the geometric difference between crystal and sample-plane. Although this usually leads to reproducible results within an error range of 5 % over the film area for single materials, in case of doping, the total film thickness of the mixture does not necessarily have to be the exact sum of the individual species virtual thicknesses as monitored by the crystals.

On the doping ratio in thermal evaporation

Usually, the doping percentage is given in volume ratio, which is directly accessible from the evaporation procedure and gained from the individual partial thicknesses or growth rates of each material, host and dopant. However, due to different molar masses and densities of host and dopant, the weight and particle percentage can be different from the volume percentage. When ρ_D and ρ_H are the densities of dopant and host, respectively, the weight percentage of the deposited material is given by

$$X_\rho = \frac{d_\mathrm{D}\rho_\mathrm{D}}{d_\mathrm{D}\rho_\mathrm{D} + d_\mathrm{H}\rho_\mathrm{H}} = \frac{\rho_\mathrm{D}}{\rho_\mathrm{D} + \left(\frac{1}{X_\mathrm{d}} - 1\right)\rho_\mathrm{H}} \,, \tag{2.1}$$

where X_d is the thickness or volume ratio. A similar equation can be found for the molar mass or particle ratio X_M, with the respective molar masses M_D and M_H. The volume per one mol, or the inverse molar volume is ${V_\mathrm{m}}^{-1} = \rho/M$, and therefore

$$X_\mathrm{M} = \frac{{V_\mathrm{m,D}}^{-1}}{{V_\mathrm{m,D}}^{-1} + \left(\frac{1}{X_\mathrm{d}} - 1\right){V_\mathrm{m,H}}^{-1}} \,. \tag{2.2}$$

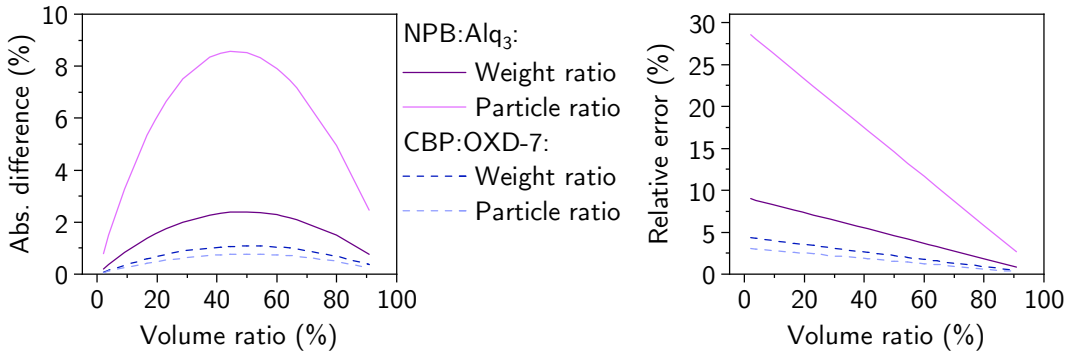

Figure 2.6.: Absolute and relative error of weight and particle ratio compared to the volume ratio at the example of the systems NPB:Alq_3 and CBP:OXD-7. Whereas the absolute difference shows a maximum at 1:1 mixtures, the relative error is highest for small doping ratios.

While the molar mass of a material can be calculated, its density in thin films is mostly unknown and the measurement difficult. Additionally, molar mass and density are usually of no simple dependence, i.e. a higher molar mass does not allow to infer a higher or lower density, and vice versa. Depending on miscibility of both materials, their probability to grow agglomerates or steric properties, the density of the mixed film can also be different from the simple weighted average. Furthermore, the density of the individual components can change in a grown thin film. This, in turn, would change the overall thickness of the film and hence the volume ratio. Both mass and molar ratio, however, keep unchanged.

In previous works, doping ratios were often given using the volume ratio [2, 48], whereas weight percent (wt%) is also typical in literature. The absolute difference and relative error of the volume ratio to mass or particle ratios depends on the proportion of molecular density and volume between dopant and host, two examples are plotted in Figure 2.6. Here, the parameters for Alq_3 are $M_{Alq_3} = 459.43\,\mathrm{g/mol}$ and $\rho_{Alq_3} = 1.19\,\mathrm{g/cm^3}$ [201]. For NPB they are $M_{NPB} = 588.74\,\mathrm{g/mol}$ and $\rho_{NPB} = 1.19\,\mathrm{g/cm^3}$ [201]. In case of CBP:OXD-7, the parameters are $M_{CBP} = 484.59\,\mathrm{g/mol}$ and $\rho_{CBP} = 1.18\,\mathrm{g/cm^3}$ [201] as well as $M_{OXD\text{-}7} = 478.58\,\mathrm{g/mol}$ and $\rho_{CBP} = 1.13\,\mathrm{g/cm^3}$ [87]. The difference between both is striking: whereas the absolute and relative difference between the measured volume doping percentage and the possible weight and particle ratios for CBP:OXD-7 is small and below 10 %, NPB:Alq_3 is off by 30 % for low doping ratios. The maximum absolute difference for both material sets is reached for a 1:1 mixture, meaning 50 % of volume percentage of Alq_3 in NPB leads to ≈52 wt% or 58 % of molecules in the film.

2.2.2. Spin-coating of polymeric layers

Polymeric layers like PEDOT:PSS are commonly fabricated using wet processing techniques, one of those is *spin-coating*. In this process, a solution of the material is dropped onto the sample, which is then spun around its surface normal at high speeds to form a uniform, thin layer of the material. The process can be split into different stages, which are illustrated in Figure 2.7. While the sample is fixed on the

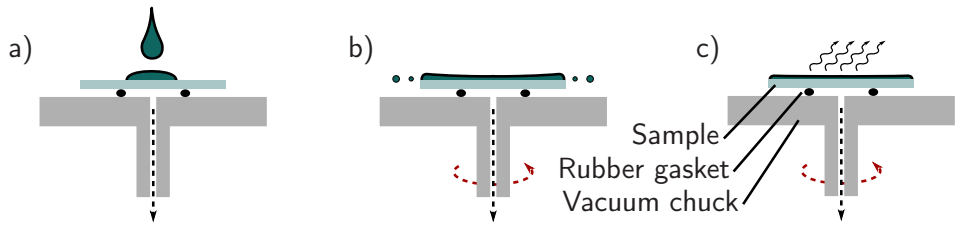

Figure 2.7.: Schematic illustration of the spin-coating process compressed into three steps. **a)** Dropping the solution on the substrate, **b)** acceleration to and rotation at the desired speed. Radial flow of the solution forms a mostly homogeneous film while excess solution is centrifuged away. **c)** Further thinning of the film due to evaporation of the solvent at the target speed.

rotation chuck via vacuum, the material is dropped on the substrate before rotation is started (step a)). During acceleration, excess solution is centrifuged away from the sample (step b)). This state of the process does not influence the overall film thickness, but the uniformity of the layer is reported to be better at high enough acceleration rates [202, 203]. Finally, a constant speed of rotation largely defines the resulting film thickness, besides intrinsic parameters of the solution (step c)). Evaporation of the solvent changes the viscosity and finally the thickness of the film at this state and allows the film to start drying. The equilibrium condition between liquid vapor pressure, liquid concentration in the film, viscosity and rotation speed at the end of the process stops the thinning of the film, but might not lead to dry films. After the spinning process, post-annealing or active drying of the film is needed to remove excess solvent, which could otherwise influence device performance [117].

For long spinning times and moderate concentrations, a general relation for the resulting film thickness can be given as

$$d_\infty \propto c_0\, \omega^{-1/2} \eta^{1/3} \ , \tag{2.3}$$

where d_∞ is the resulting film thickness, c_0 the initial concentration, ω the spinning speed and η the viscosity of the solution [204]. The latter is often unknown and dependent on the concentration, but can be related to the molecular mass M leading to the relation

$$d_\infty \propto c_0\, \omega^{-1/2} M^{a/3} \ , \tag{2.4}$$

with a material parameter a, which is reported to be near 0.75 for polymeric compounds [204]. The linear dependence of Equation 2.4 on the concentration c_0, however, allows to extrapolate the thickness, given the thickness is known for one or more concentrations.

2.2.3. Device architecture and sample handling

Within this work, organic semiconducting devices are all produced with ITO-coated glass as base substrate. The glass substrates with 0.7 mm nominal thickness are purchased pre-coated with 145 nm or 90 nm of ITO. All substrates with structured ITO layer for electrical measurements are ordered pre-structured and cut; Kelvin Probe measurements need unstructured ITO samples obtained by the same supplier, see

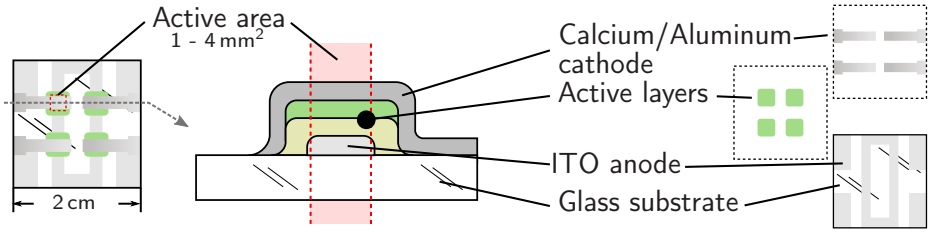

Figure 2.8.: Sketch of the device architecture and masking used for samples within this work. Samples were of quadratic shape with an overall area of 4 cm² and contained four individual pixels of 1 mm² to 4 mm², each. The active area is defined by the overlap of the ITO pattern and the top cathode.

Section A.1 for name and address. To remove residual contaminants prior to processing the devices, the substrates are cleaned in an ultrasonic bath with subsequently technical grade Acetone, UV grade Acetone and UV grade Isopropanol as solvent. Additionally, all samples are treated with either a UV/Ozone cleaner for 15 min, or in an oxygen plasma for 10 min unless otherwise noted. The surface treatment enhances the wetting capabilities and allows to spin-coat aqueous solutions like PEDOT:PSS. Additionally, it modifies the ITO workfunction, removes contaminants and the surface roughness is also said to be reduced [109], see Section 2.1.4 for details. This is especially important when processing thermally evaporated active layers directly on ITO without a spin-coated HIL. Judging from lab experience, especially the plasma treatment seems to remove edge defects of the ITO substrates, leading to a far better yield of devices without low shunt resistances, however, no systematic study has been performed on this matter. Polymer HILs were spin coated onto the substrates in a clean room environment with 5000 rpm in a model "Delta 6" spin coater from Süss MikroTec for 30 s, acceleration is chosen to reach final speed within 5 s. Each film is subsequently placed and dried on a hot plate for at least 30 min at 120 °C to 130 °C.

On one sample, four identical pixels are created by structuring the organic layer and subsequently the cathode with shadow masks during evaporation. The ITO layer is etched to an "O"-Shape to form a common anode for all four pixels, four individual contact pads at the sample corners assist to create the cathode contacts later on; the structure is shown in Figure 2.8 on the bottom right. Organic layers of individual pixels are separated from each other to reduce stray capacitance and crosstalk, however, the HIL covers the complete sample area as structures in spin-coated layers are not easily achievable. Shadow masks are placed as near as possible to the sample during evaporation to reduce the penumbra region around the pixel with uncontrolled thickness. The cathode contacts are created with four metal stripes between the outer contact pads and the pixel areas, Calcium and Aluminum have to be evaporated through the same masks without changing the sample positioning in between to allow for good overlap. By choosing from ITO and metal structures available in 1 mm or 2 mm nominal width, sample areas of 1 mm², 2 mm² or 4 mm² are possible. All pixels are typically of *common anode* design and resemble *bottom emitting* OLEDs or *bottom absorbing* solar cells, respectively.

Unless otherwise noted, to reduce oxygen or water contamination, samples are stored in a glovebox with pure N_2 atmosphere, where oxygen and water levels are typically kept below 0.1 ppm. Transfer between different measurement or manufac-

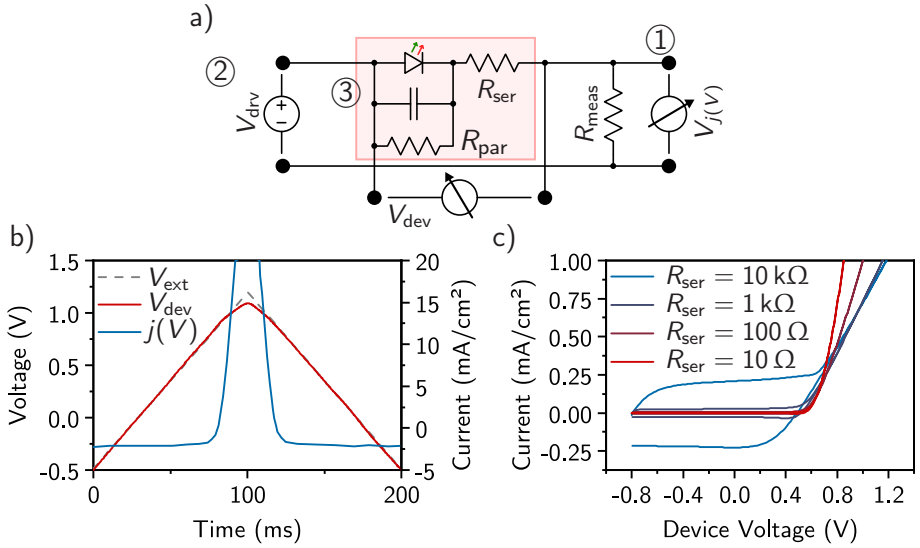

Figure 2.9.: **a)** Simple equivalent circuit combining the sample (red marked area) and external circuit for a basic current-voltage measurement. **b)** Characteristic measured on an organic diode with erroneous voltage correction on the sample. When the sample begins to draw current, the voltage drop over the sample is beginning to fall as its differential resistance drops. **c)** Simulated current-voltage characteristics with different RC-times. For higher RC-times, the characteristic is more and more dominated by the capacitive response.

turing chambers is done in evacuated or N_2-filled transfer rods, only profilometry and scanning probe microscopy has to be performed in ambient conditions.

2.3. Basic electrical characterization

When dealing with electrical devices, whether OLEDs or OPV, the electrical measurement of characteristics and alike is of high importance. While the measurement of a simple $j(V)$ dependence of a diode seems trivial, a few caveats exist that are worth a short discussion. In the following, some basic physics affecting electrical measurements are addressed and basic considerations about signal quality are elaborated.

2.3.1. Current-voltage characteristics

A current-voltage characteristic is, in its simplistic form, dependent on at least the following parameters, highlighted in the equivalent circuit given in Figure 2.9:

① The sample current j_{dev} flowing through the device, for example described by the Shockley equation given earlier. In a voltage-driven experiment, it is parameterized by the voltage drop over the sample, V_{dev}.

② The driving voltage V_{drv} of the measurement setup, e.g. applied by a *source measure unit* (SMU) or a wave-function generator. It is a priori not the same

as the voltage drop over the sample, but shared by at least the sample as well as contact and measurement resistances R_{con} and R_{meas}. Measurement equipment might be designed to countermeasure this effect by controlling the voltage according to an additional voltage probe near the sample in a 4-wire setup.

③ A possible capacitive response or displacement current j_{cap} due to changes in the driving voltage, if the measurement is made fast with respect to the RC-time. This, strictly speaking, is a combination of two effects, as the sample will have a different RC-time as the setup cabling itself. The latter, however, shall be neglected to simplify this basic discussion; besides, cabling effects are typically not visible for measurement frequencies below 1 MHz.

Mathematically, the above set of parameters can be summarized to describe the measured current $j(V)$ as

$$j(V) = j_{\mathrm{dev}}\left(V_{\mathrm{dev}}\right) + j_{\mathrm{cap}}\left(\frac{\mathrm{d}V_{\mathrm{dev}}}{\mathrm{d}t}\right) \ , \tag{2.5}$$

where the voltage drop at the sample is reduced by the voltage drop over external series resistances, e.g. measurement and contact resistances, thus

$$V_{\mathrm{dev}} = V_{\mathrm{drv}} - j_{\mathrm{dev}}\left(R_{\mathrm{meas}} + R_{\mathrm{con}}\right) \ . \tag{2.6}$$

By neglecting additional parallel or series capacitance, which might arise for example from unequal electrode coverage with different organic layers, the displacement current j_{cap} is dependent on the geometric capacitance C_{geo} and the voltage slope alone. Thus,

$$j_{\mathrm{cap}} = C_{\mathrm{geo}} \cdot \frac{\mathrm{d}V_{\mathrm{dev}}}{\mathrm{d}t} \tag{2.7}$$

is linearly dependent on capacitance and voltage slope. In Figure 2.9b a drift-diffusion simulation of a current-voltage characteristic of an organic diode is shown, where the series resistance has been varied. For high series resistances, both forward and backward scan of the measurement differ significantly. The same result would be achieved by changing measurement speed and/or geometric capacitance. The case when the displacement current is equal to the sample current, which in turn is limited by the series resistance of the device, is taken as an example. Then, at the point of maximum voltage V_{max} of the measured characteristics,

$$\frac{V_{\mathrm{max}}}{R_{\mathrm{ser}}} \approx C_{\mathrm{geo}}\frac{\mathrm{d}V}{\mathrm{d}t} = C_{\mathrm{geo}}\frac{V_{\mathrm{max}}}{t_{\mathrm{meas}}} \ , \tag{2.8}$$

where V_{max} is the maximal amplitude of the measurement, sweeping within the measurement time t_{meas} from 0 to $+V_{\mathrm{max}}$. Equation 2.8 can be rearranged to read

$$t_{\mathrm{meas}} = R_{\mathrm{ser}}C_{\mathrm{geo}} \equiv \tau \tag{2.9}$$

where τ is the RC-time or time-constant of the device concerning its geometric capacitance C_{geo}. This is of course a very rough approach to do, especially as the capacitive response will reach its maximum value shortly after the measurement began (the slope of $V(t)$ is constant), whereas Equation 2.8 is evaluated at the maximum

voltage. This will probably overestimate the maximum allowed measurement speed. It still means that the displacement current will increasingly dominate the measured characteristic, if the measurement timescale approaches the RC time of the device. As an example, a device with a series resistance of 100 Ω and a capacitance of 1 nF resulting to a time constant of 100 ns is considered. In this device, the drift current will only be visible in very fast measurements such as CELIV transients. However, as τ scales linearly with the resistance, it will reach 1 ms with $R_{\text{ser}} = 1\,\text{M}\Omega$, which is beginning to reach the timescales of fast $j(V)$ characteristics, if the measurement is recorded within a 100 ms time frame. A countermeasure to those problems is to do step-wise or ramped measurements, ensuring enough waiting-time at each recorded point in the characteristic to reach quasi-steady state prior to recording the measured current.

2.3.2. Signal noise and its elimination

Sources for signal noise in electrical measurements are manifold and range from intrinsic noise arising from individual electronic components in the measurement equipment to extrinsic sources such as interference. Examples for intrinsic noise are the thermal noise in resistors or "shot" and "flicker" noise found in transistors or diodes [205]. External interference can be caused by ground loops, improper shielding of either signal paths or nearby equipment such as pumps or monitors, or by RF-sources, an example being the well-known, sometimes audible disturbances caused by mobile phones in the vicinity of poorly shielded amplifiers.

The signal quality is typically quantified using the *signal to noise ratio* (SNR). It describes the relation of signal power to noise power, and is typically given in decibel,

$$SNR = 10 \cdot \log\left(\frac{P_{\text{signal}}}{P_{\text{noise}}}\right) \ . \tag{2.10}$$

In most cases, however, the signal is measured using its amplitude in contrast to the power. Using Ohm's law and with the assumption that signal and noise arise across the same impedance, i.e. are measured with the same measurement resistor R, the power calculates to $P = V^2 R^{-1}$, and thus

$$SNR \approx 20 \cdot \log\left(\frac{V_{rms,\text{signal}}}{V_{rms,\text{noise}}}\right) = 20 \cdot \log(snr) \quad \text{with} \tag{2.11}$$

$$snr = \frac{V_{rms,\text{signal}}}{V_{rms,\text{noise}}} \ , \tag{2.12}$$

where V_{rms} is the effective, root mean square (RMS) voltage of signal and noise. The higher the SNR, the better can the signal be distinguished from the noise. Providing that the signal noise is random, i.e. the mean value of the noise is zero and uncorrelated to the signal, the signal to noise ratio can be defined as

$$SNR = 20 \log\left(\frac{\overline{S}}{\sigma_S}\right) \ . \tag{2.13}$$

Here, the mean value $\overline{S}$ is the effective signal value and σ_S the standard deviation of the recorded signal [206]. A simple solution to rise the SNR is to average over

multiple measurements, as long as the noise is truly random. The sum $\overline{S_n}$ of n equal measurements for the signal $\overline{S}$ of the same experiment is $\overline{S_n} = n\overline{S}$, the variance ${\sigma_S}^2$ sums up for standard error propagation [207], thus

$$\sigma_n^2 = \sum_i^n \sigma_i^2 = n\sigma_S^2 \quad \Leftrightarrow \quad \sigma_n = \sqrt{n}\sigma_S \quad . \tag{2.14}$$

For the signal to noise ratio follows

$$snr_n = \frac{n\overline{S}}{\sqrt{n}\sigma_S} = \sqrt{n}\frac{\overline{S}}{\sigma_S} \tag{2.15}$$

and

$$SNR_n = 20\left[\frac{1}{2}\log(n) + \log\left(\frac{\overline{S}}{\sigma_S}\right)\right] = SNR + 10\log(n) \tag{2.16}$$

The amplitude ratio *snr* scales with the square root of n and the signal to noise ratio rises logarithmically, i.e. when increasing the number of averaged measurements by a factor of 10, the SNR increases by 10 dB [206]. Although the logarithm is not asymptotic and the SNR could therefore be raised almost infinitely, the absolute gain in signal quality per additional iteration will diminish. Whereas one additional averaging iteration increases the SNR by ≈0.5 dB, when 9 iterations were already made, it is ≈0.05 dB, when there were already 99. In practical use, more than 50 to 100 iteration are hence hardly beneficial, especially when taking possible damage and subsequent degradation of the sample due to electrical and thermal stress into account. Also, the above evaluation neglects the fact that most signals nowadays are recorded with digital equipment, which by design has a maximum absolute SNR that can be detected because of finite accuracy of the analog to digital conversion [208].

2.4. Kelvin probe

The Kelvin probe technique, initially named after its 19th century inventor Lord Kelvin [209, 210], allows to non-destructively measure the contact potential difference between two plane-parallel plates. A later variation, the *vibrating probe Kelvin probe* technique [211], which is the base of current setups, has initially been developed to measure contact potential differences of metals. It is now widely used to probe workfunctions of metals and semiconductors alike and can also give insights on band bending in organic devices [212]. Scanning Kelvin probe microscopy allows for spatial resolution in Kelvin probe images, revealing the local distribution of the semiconductors surface potential [213]. In the following, the basic mathematical framework is deduced for the vibrating probe Kelvin probe technique and a discussion of its application on organic semiconducting devices is given.

The basic setup is sketched in Figure 2.10a, alongside with the band schemes during measurement. The sample is mounted into a grounded sample holder and the tip brought into the vicinity of the sample surface. Its distance can be fine-tuned by a magnetic coil actuator that also allows for fast oscillation of the tip-sample spacing. This setup is called the *static plate earthed* setting, while setups with earthed tip are called *vibrating plate earthed*. Both techniques are mutually equal within the following framework, but have different properties concerning errors such as stray

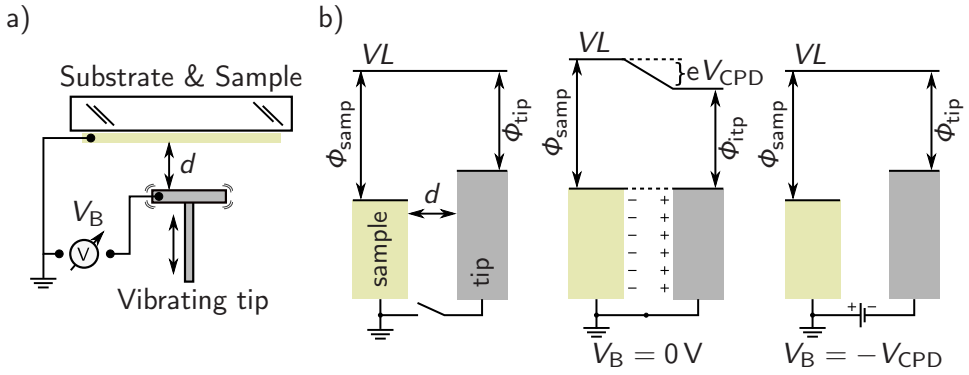

Figure 2.10.: a) Functional sketch of a Kelvin probe experiment with vibrating probe. Here, the sample is grounded, the backing potential V_B is applied on the tip while the distance d oscillates. **b)** Energy diagrams for three different stages of the Kelvin probe experiment. At first, sample and tip are without contact, the workfunctions differ with respect to the vacuum level *VL*. When shorting both, the Fermi levels align and surface charges counter the field gradient over V_{CPD}/d resulting in a measurable current. The current flow is countered with a backing potential V_B and equals zero, if $V_B = -V_{CPD}$. Drawn after ref. [210].

capacitance [214], which will be addressed later. For the Kelvin probe experiment, an electrical contact is established between sample and tip, allowing to control the voltage difference and to measure the current. If the voltage between sample and tip would be set to 0 V e.g. by short circuiting both, the potential difference V_{CPD} induced by the unequal substrate workfunctions is

$$e \cdot V_{CPD} = \Phi_{tip} - \Phi_{samp} \ . \tag{2.17}$$

It will induce a short-circuit current flow, until a redistribution of surface charges counters the field gradient. When the external applied voltage, also known as *backing potential* V_B, is exactly $V_B = -V_{CPD}$ the external current is zero. By changing the backing potential and detecting the current flow, e.g. with a lock-in technique, the zero-point can be measured, however, this setup is prone to errors in offsets and amplification [214–216]. Instead, the combination of sample and tip is treated as a plate capacitor, where field and charge inside are defined by the workfunction difference, the applied voltage and the dielectric in between. The current flow is then induced by the constantly vibrating probe, effectively changing the plate separation of the capacitor. In the simplest description [216], varying the distance of the capacitor's plates induces a change in charge due to a constant field in the capacitor defined by both, external voltage and contact potential difference. The voltage in the capacitor ΔV, its field F and capacitance C are given by

$$\Delta V = V_{CPD} + V_B \ , \tag{2.18}$$

$$F = \frac{\Delta V}{d} \ , \tag{2.19}$$

$$C = \frac{\varepsilon\varepsilon_0 A}{d} \ . \tag{2.20}$$

Here, A and d define area and distance of the sample-tip-capacitor with charge Q. This simple equation for the capacitance is of course neglecting all edge effects and stray capacitance, a short discussion is given further below. In a capacitor with time-dependent capacitance, the current is defined by

$$j = \frac{\mathrm{d}Q}{\mathrm{d}t} = \Delta V \frac{\mathrm{d}C}{\mathrm{d}t} \ . \tag{2.21}$$

The distance is now varied sinusoidally with amplitude d_A and an arbitrary phase ϕ around a mean spacing d_0, thus

$$d(t) = d_0 + d_\mathrm{A} \sin(\omega t + \phi) \ . \tag{2.22}$$

Inserting Equation 2.22 in Equations 2.20 and 2.21 yields

$$j(t) = -\varepsilon\varepsilon_0 A \Delta V \frac{d_\mathrm{A}\omega \cos(\omega t + \phi)}{\left[d_0 + d_\mathrm{A} \sin(\omega t + \phi)\right]^2} \ . \tag{2.23}$$

In this equation, the resulting current is proportional to the voltage difference ΔV and unless the mean spacing is much larger than the amplitude, the dependence on time is non trivial. Otherwise, if $d_0 \gg d_\mathrm{A}$, Equation 2.23 reduces to

$$j(t) \approx -\varepsilon\varepsilon_0 A \Delta V \frac{d_\mathrm{A}\omega \cos(\omega t + \phi)}{{d_0}^2} \ . \tag{2.24}$$

It is argued however, that this approximation requires several special requirements to be met and is therefore not applicable to real-world applications [216]. To measure V_CPD, the Kelvin probe system needs to determine the zero-point of the current in Equation 2.23, where $V_\mathrm{B} = -V_\mathrm{CPD}$. Requirements on signal-to-noise ratio and accuracy of amplifiers in terms of offsets typically complicate the measurement of exact zero points and requires the use of a lock-in technique [215, 216]. An easier approach, which is also utilized by the Kelvin probe system available for this work, is to vary the applied backing potential and record the current maxima from the measured signal, which are linear to ΔV according to Equation 2.23 and hence also V_CPD. A straight line fit of $j\,(t_\mathrm{max}, V_\mathrm{B})$ versus V_B will yield the zero-point backing potential at the intersect of the abscissa. The slope of this line fit is termed the gradient of the Kelvin probe measurement, which is proportional to $1/{d_0}^2$ and is therefore a measure of the sample-tip spacing [216], as the absolute distance is typically unknown.

Stray capacitance and errors

The basic theory above only applies to a perfect capacitor without size difference of the two plates and with uniform dielectric and spacing. Additionally, all influences of the cable resistance and capacitance are neglected. From Equation 2.23 follows that the current signal amplitude is proportional to the dielectric constant, the driving amplitude, sample area and the inverse square of the mean distance. The dielectric is fixed to $\varepsilon = 1$ due to vacuum, hence leaving driving amplitude and geometric factors to influence the SNR. Typically, the sample area is bigger than the area of the tip, and with V_B applied to the tip, its field gradient moves in the surrounding of sample and holder, the latter consisting of possible different metals, clamps and screws: altogether a non-trivial set of geometric constraints. Additionally, some parts of the

Kelvin probe assembly might vibrate in a different frequency, one example being the supply cables for the tip voltage [217]. The induced stray capacitance will cause an error in the measured potential difference $V_{\mathrm{VPC,meas}}$, which is dependent on the square of the distance and can be given as

$$\Delta V_{\mathrm{CPD}} = k{d_0}^2 \left(V_{\mathrm{CPD,real}} - V_{\mathrm{stray}}\right) \ , \tag{2.25}$$

where $V_{\mathrm{CPD,real}} - V_{\mathrm{stray}}$ is the voltage drop across the stray capacitance and k a constant [214] with

$$k \propto \frac{C_{\mathrm{stray}}}{A d_{\mathrm{A}}} \ . \tag{2.26}$$

Analogous, the correct contact potential difference is given [217] by

$$V_{\mathrm{CPC,real}} = \frac{V_{\mathrm{CPD,real}} - k{d_0}^2 V_{\mathrm{stray}}}{1 + k{d_0}^2} \ . \tag{2.27}$$

From Equations 2.25 and 2.26 it is evident that a reduction of stray capacitance is best achieved by reducing the sample-tip-spacing, hence a higher gradient is favorable during measurement. Other optimizations may include avoiding the resonant frequencies of the tip and minimizing the angle between tip and surface [217]. It is worth noting that the above equations are only equal for the static plate earthed configuration. A earthed tip and the potential applied to the sample leads to slightly different conditions and hence needs a separate discussion of possible errors [214].

Kelvin probe on organic semiconductors

In case of metallic samples, the Fermi level alignment between the metallic sample holder and the sample surface is guaranteed and a potential difference between both will induce surface charges to counter the field. The condition of $j\left(t, V_{\mathrm{B}}\right) = 0$, which will detect the point when no surface charge exists, thus corresponds to $V_{\mathrm{B}} = -V_{\mathrm{CPD}}$ and allows for a determination of the contact potential difference. When investigating organic and semiconducting samples with potentially poor electrical conductivity or band bending, charges might not accumulate solely on the surface, but additionally on the contact to the semiconducting film [212]. Still, the zero-point detection requires the field in the gap between sample and tip surface to be zero and the surface charge density of the tip is hence also $\sigma = 0$ in this case. The vacuum level again is aligned with that of the sample surface, although band bending may lead to charges in the semiconductor or in the contact region [212]. Arguably, the backing potential is applied to the tip in this case. A vibrating plate earthed setup would have to be treated separately, as the potential would be applied to the backside of the semiconductor and a specific assumption on the potential drop in the semiconductor cannot be made.

Any measured contact potential difference will nevertheless include all static surface charges of the organic semiconductor [212]. This fact, that amongst others allows to measure the giant surface potential of polar organic layers [10], will be utilized in the scope of this work in Section 3.1.

2.5. Charge extraction by linearly increasing voltage (CELIV)

As a method to extract charge carrier densities, mobilities and additionally some device-related properties like series resistance and (geometric) capacitance, charge extraction by linearly increasing voltage has gained a lot of attention in the past years. It has first been published by Juška *et al.* in 2000 as an alternative method to time-of-flight for probing the charge carrier mobility in microcrystalline silicon [218] and was shortly after applied to π-conjugated polymers by the same author [219]. In those publications, it was intended to extract information about the equilibrium charge carriers in the investigated semiconductors. Since then, the method has been numerously adapted and altered for probing photogenerated carriers in solar cells (Photo-CELIV) [220, 221] with variations trying to limit current flow prior to the extraction [222] to the methodically highly sophisticated "open circuit corrected charge carrier extraction" (OTRACE) [223], modified specifically for low recombination losses during measurement. From carrier density measurements on solar cells, conclusions on the recombination dynamics of photo-generated charges can be drawn [221, 224]. Additionally, electrically injected charge carriers can be investigated (i-CELIV) [225], which is a method that can also be applied to metal-insulator-semiconductor devices [226], hence called MIS-CELIV.

In the scope of this work, the MIS-CELIV technique is applied to polar OLEDs effectively forming "Polar-CELIV". The following sections will give a brief introduction to the basic CELIV experiment, its variations and associated parameter extraction. Simulations for CELIV transients are given in the experimental section in Chapter 5. Parts of the following section have been taken from my previous work in reference [50] and were extended or updated where necessary.

2.5.1. Introduction into CELIV

CELIV originally aims on extracting existing equilibrium charge carriers from the device by applying an increasing electrical field to the semiconductor. It is well known for the large number of quantities that can possibly be extracted from one measurement, most notably carrier mobility μ, sheet conductivity σ and charge carrier density n. To extract charge carriers present before the beginning of the experiment, the voltage ramp or slope rising with $S = \frac{\mathrm{d}V}{\mathrm{d}t}$ is applied in reverse direction and the current flowing through the device is recorded. The current measured at the device can be divided into two parts, the current caused by the actual extracted charge carriers Δj also referred to as *drift current* and the current caused by the capacitive response of the device named *displacement current*, j_0. The total current $j(t)$ can then be expressed as

$$j(t) = j_0 + \Delta j \ . \tag{2.28}$$

If Q is the total amount of charges present in the sample, then j_0 is constant for a linearly increasing voltage:

$$j_0 = \frac{1}{A} \cdot \frac{\mathrm{d}Q}{\mathrm{d}t} = \frac{C}{A} \cdot \frac{\mathrm{d}V}{\mathrm{d}t} = \frac{C}{A} \cdot S = \frac{\varepsilon\varepsilon_0}{d_{\mathrm{akt}}} \cdot S \ , \tag{2.29}$$

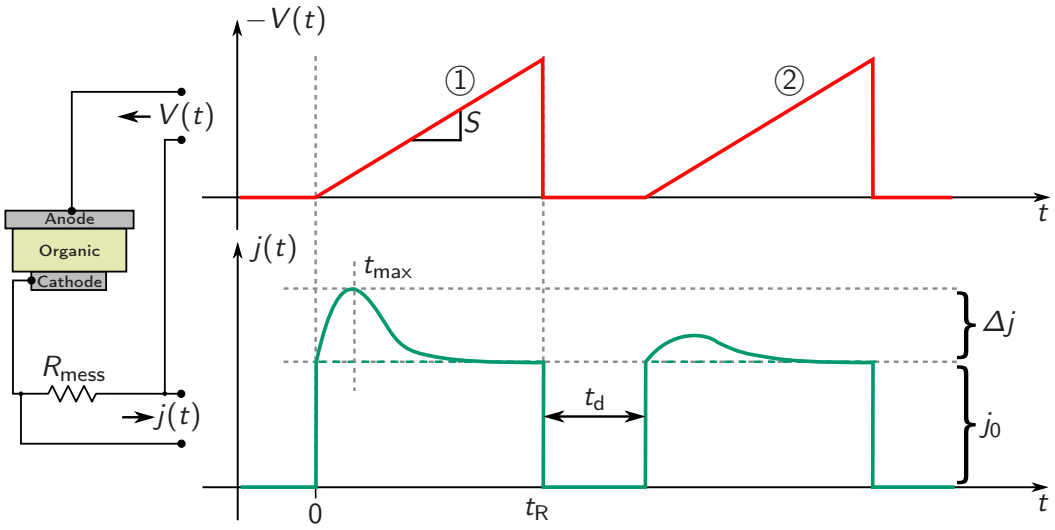

Figure 2.11.: Sketch of the original CELIV method. A linearly increasing voltage ramp $V(t) = S \cdot t$ is applied to the cell (on the left) in reverse and, e.g. by using a shunt resistance R_{mess}, the current flowing though the device $j(t) = j(0) + \Delta j$ is measured. The experiment involves two ramps ① and ②, which allows conclusions on charge carrier dynamics and relaxation mechanisms. Redrawn with modifications after ref. [219].

with the slope of the voltage ramp S, sample thickness d_{akt}, area A and the dielectric constant ε. The integral

$$n \propto \int_0^{t_{\text{R}}} j(t) - j_0 \, \mathrm{d}t \tag{2.30}$$

can then be used to calculate the charge carrier density extracted from the device during the ramp time t_{R}.

The two successive ramps seen in the original CELIV technique [218,219], see Figure 2.11, can be used to distinguish intrinsically present equilibrium charge carriers from those being caused by non-ideal conditions, e.g. non-blocking contacts [218]. Ideally, when using short delay times t_{d} between both pulses, the second current measurement should equal j_0. By varying t_{d} for real devices relaxations to the ground-state can be investigated.

To calculate carrier mobilities from CELIV transients, a deeper understanding of the underlying physics is needed. The measured transient alone can, however, be used to determine the conductivity of the active layers from the initial slope of the transient with

$$\sigma = \varepsilon\varepsilon_0 \frac{\mathrm{d}\left(j(t)/j(0)\right)}{\mathrm{d}t}\bigg|_{t=0} . \tag{2.31}$$

2.5.2. Theoretical models for CELIV

To derive further parameters in more detail, namely mobility μ and conductivity σ, a mathematical model for the experiment is required. Further on, the basic idea and theory as given by Juška *et al.* for the original CELIV method is given [218].

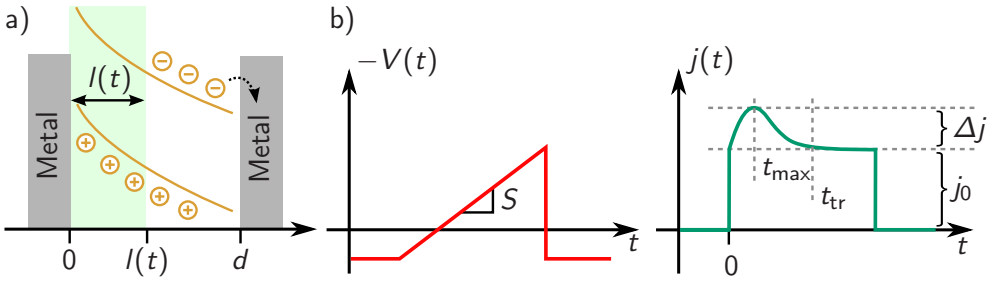

Figure 2.12.: **a)** Sketch of the field distribution in an organic semiconductor diode during CELIV. The model assumes a sharp-edged extraction zone. Redrawn from ref. [227] **b)** Voltage ramp and current response of a diode, t_{max} marks the maximum current of extracted charge carriers and t_{tr} denotes the time when all charges are extracted, $l(t_{tr}) = d$.

The basic dependence of the measured CELIV transient on the combination of displacement current $j(0)$ and drift current Δj has already been introduced in Section 2.5.1. To describe Δj in more detail, a simple model can be found when assuming that one of the electrodes is completely blocking injection of charge carriers and the charge in the device ρ is distributed evenly over the whole thickness d with carrier density n prior to extracting the charges. Furthermore, the extraction of charge carriers is considered to be complete and constant up to a specific depth $l(t)$ (for an illustration see Figure 2.12), so that at a time t in the region between $x = 0$ and $x = l(t)$ no charges are left in the device, whereas the density of charges for $l(t) < x < d$ still is unchanged and equals n [218]. Last but not least, charge transport is required to be unipolar, i.e. the mobility of electrons has to be much higher than the hole mobility, or vice versa, $\mu_e \gg\ll \mu_h$. Both constraints can be quite challenging to achieve in the scope of organic semiconductor diodes and will be discussed later on.

Under these assumptions, Juška calculated the current transient in two steps. Within the said limits, the charge distribution can be defined as

$$\rho(x,t) = \begin{cases} 0 & \text{for } 0 \leq x < l(t) \\ ne & \text{for } l(t) \leq x < d \end{cases} . \tag{2.32}$$

To calculate the charges extracted up to the extraction depth $l(t)$ at a time t, one has to integrate the Poisson-equation $\Delta\Phi(\mathbf{r}) = -\frac{\rho(\mathbf{r})}{\varepsilon}$ over the whole thickness of the organic layer

$$\frac{Q(t)}{\varepsilon\varepsilon_0} = \frac{nel(t)}{\varepsilon\varepsilon_0} = E(0,t) - E(d,t) , \tag{2.33}$$

with the permittivity ε and the elementary charge e. $E(0,t)$ is the field at the blocking contact, $E(d,t)$ at the opposite electrode.

The continuity equation of electrodynamics is $\frac{\partial\rho}{\partial t} = -\nabla j$. Integrating this equation over the distance between the electrodes yields

$$\int_0^d \frac{\partial\rho}{\partial t}\,\mathrm{d}x = ne\frac{\partial l(t)}{\partial t} = \Delta j = en\mu E(d,t) . \tag{2.34}$$

The electric field itself decreases linearly in the depletion zone, but it is constant where no extraction has jet occurred:

$$E(x,t) = \begin{cases} E(0,t) - \frac{enx}{\varepsilon\varepsilon_0} & \text{for } 0 \leq x < l(t) \\ E(d,t) & \text{for } l(t) \leq x < d \end{cases} . \tag{2.35}$$

For a linearly increasing voltage $V(t) = S \cdot t$,

$$\int_0^d E(x,t)\,\mathrm{d}x = St \tag{2.36}$$

applies to the external electrical field and therefore, after integration and combining with Equation 2.33, it is

$$St = d \cdot E(d,t) + l(t) \cdot \frac{E(0,t) - E(d,t)}{2} . \tag{2.37}$$

From combining Equation 2.34 with Equation 2.37 and Equation 2.33 as well as the definition of the conductivity $\sigma = en\mu$, follows a Riccati-style differential equation [218] for $l(t)$

$$\frac{\mathrm{d}l(t)}{\mathrm{d}t} + \frac{\sigma}{2\varepsilon\varepsilon_0 d} l(t)^2 = \frac{\mu St}{d} \tag{2.38}$$

Deducing the current transient:
The complete current density of the transient $(j(0) + \Delta j)$ at a position x and time t is

$$j(x,t) = \underbrace{\varepsilon\varepsilon_0 \frac{\mathrm{d}E(x,t)}{\mathrm{d}t}}_{j(0)} + \underbrace{\rho(x,t)\mu E(x,t)}_{\Delta j} . \tag{2.39}$$

To obtain $j(t)$, the average over $x \in [0,d]$ can be calculated. The carrier density within the extraction zone is zero and en otherwise. Thus,

$$\frac{1}{d}\int_0^d \Delta j\,\mathrm{d}x = \frac{1}{d}\int_0^d \rho(x,t)\mu E(x,t)\,\mathrm{d}x = \frac{en\mu}{d}\int_{l(t)}^d E(d,t)\,\mathrm{d}x \tag{2.40}$$

and accordingly

$$j(t) = \frac{1}{d}\int_0^d j(x,t)\,\mathrm{d}x = \frac{\varepsilon\varepsilon_0 S}{d} + \frac{en\mu E(d,t)\,[d - l(t)]}{d} . \tag{2.41}$$

By replacing $E(d,t)$ with Equation 2.34 and substituting $\frac{\mathrm{d}l(t)}{\mathrm{d}t}$ with Equation 2.38, the equation for the current transient [218] results to

$$j(t) = \frac{\varepsilon\varepsilon_0 S}{d} + \frac{\sigma}{\mu}\left(1 - \frac{l(t)}{d}\right)\left(\frac{\mu St}{d} - \frac{\sigma}{\varepsilon\varepsilon_0 d} l(t)^2\right) \tag{2.42}$$

It is apparent that a solution for this equation requires solving Equation 2.38 $(l(t))$ first.

The analytic solution given by Lorrmann *et al.* [227]

$$l(t) = \frac{\mu S}{d\zeta^2} t^2 \frac{\sqrt{3}\,\mathrm{Ai}'(\zeta) + \mathrm{Bi}'(\zeta)}{\sqrt{3}\,\mathrm{Ai}(\zeta) + \mathrm{Bi}(\zeta)} \,, \tag{2.43}$$

$$\text{with} \quad \zeta = \sqrt[3]{\frac{en\mu}{2\varepsilon\varepsilon_0 d}\frac{\mu S}{d} t^3} \tag{2.44}$$

unfortunately does not allow a direct identification of device parameters like μ, since the argument ζ of the Airy-function contains both, conductivity and mobility. Nevertheless, it is reportedly possible to fit the parameters in Equation 2.42 to measured transients [227]. For materials with very high or low conductivity, approximations can be found and calculated. For low conductivity, when the duration of the extraction pulse is much longer than the relaxation time of charges, $t_{\mathrm{tr}} \ll \frac{\varepsilon\varepsilon_0}{en\mu} = \tau_\sigma$, the change in the electrical field distribution has no noteworthy impact on the position of the extraction zone, which in turn is then only determined by the external electrical field. Then

$$\frac{\mathrm{d}l(t)}{\mathrm{d}t} + \underbrace{\frac{\sigma}{2\varepsilon\varepsilon_0 d} l(t)^2}_{\to 0} \approx \frac{\mu S t}{d} \tag{2.45}$$

with its solution

$$l_{\mathrm{low}}(t) = \frac{\mu S t^2}{2d} \,. \tag{2.46}$$

This applied to the equation for the current transient (Equation 2.42) leads to

$$j(t) = \frac{\varepsilon\varepsilon_0 S}{d} + \frac{\sigma}{\mu}\left(1 - \frac{1}{d}\underbrace{\frac{\mu S t^2}{2d}}_{l_{\mathrm{low}}(t)}\right) \underbrace{\left(\frac{\mu S t}{d} - \frac{\sigma}{2\varepsilon\varepsilon_0 d} l(t)^2\right)}_{\frac{\mathrm{d}l}{\mathrm{d}t}(t) \to \frac{\mathrm{d}l_{\mathrm{low}}}{\mathrm{d}t}(t)} \,. \tag{2.47}$$

Solving the above equation yields

$$j(t) = \frac{S}{d}\left[\varepsilon\varepsilon_0 + \sigma t\left(1 - \frac{\mu S t^2}{2d^2}\right)\right] \,. \tag{2.48}$$

From finding the extremum by taking the derivative follows the relation with the maximum of the transient t_{max} leading to μ_{low}

$$t_{\mathrm{max}} = d\sqrt{\frac{2}{3\mu S}} \quad \Leftrightarrow \quad \mu_{\mathrm{low}} = \frac{2}{3S}\left(\frac{d}{t_{\mathrm{max}}}\right)^2 \,. \tag{2.49}$$

In the same way, the approximation for high conductivity, where $t_{\mathrm{tr}} \gg \tau_\sigma$, leads to

$$t_{\mathrm{max}} = \sqrt[3]{\frac{\tau_\sigma d^2}{\mu S}} \quad \Leftrightarrow \quad \mu_{\mathrm{high}} = \frac{\tau_\sigma}{S t_{\mathrm{max}}}\left(\frac{d}{t_{\mathrm{max}}}\right)^2 \,. \tag{2.50}$$

Both cases are known to describe the conditions in real organic devices not very well [219, 227]. Over time, different numerical approximations were developed for specific material systems to account for, e.g., the redistribution of the electric field

during extraction. Some of them result to an extension of the low-conductivity case of Equation 2.49 to:

$$\mu = \frac{2d^2}{3St_{\max}^2\left(1+\chi\frac{\Delta j}{j_0}\right)}\ , \tag{2.51}$$

where Δj in this case refers to the maximum drift current $\Delta j(t_{\max})$ and χ is a numerical factor varying according to the system. Juška *et al.* published $\chi = 0.36$ to describe π-conjugated polymers [219], Bange *et al.* $\chi = 0.18$ for M3EH-PPV:CN-ether-PPV [228] and Deibel *et al.* $\chi = 0.21$ describing cells based on P3HT:$PC_{60}BM$ [229]. The validity of these equations, however, is limited to a specific range of relative extraction currents $\Delta j/j_0$ [227] and material systems. More advanced formulas to calculate the mobility from CELIV experiments have also been developed e.g. by Lorrmann *et al.*, who derived a parametric, numeric solution for Equations 2.43 and 2.44 [227]. Still, most of these simple formulas to extract mobility or other parameters from CELIV transients are tailored to specific device configurations or material systems. Instead, drift-diffusion simulations can be utilized by fitting CELIV transients to a suitable device model [13, 230].

2.5.3. CELIV on metal-insulator-semiconductor devices (MIS-CELIV)

One of the challenges of CELIV in general is the selectivity for one species of charge carriers. Electrons and holes excited through light irradiation or injected by electrical stimulation of the devices can only be separately probed with conventional CELIV transients if their mobilities differ by a considerate factor [232], but not orders of magnitude in order to show two distinct extraction peaks in the transients. Additionally, the extracted mobility is typically dependent on carrier profiles and recombination rates of extracted species [233].

To address those problems, an insulating layer can be introduced at one contact to selectively probe either electrons or holes, depending on the position of the insulator [226, 231]. Based on a metal-insulator-semiconductor device, the so called MIS-CELIV technique allows to measure injected charge carriers also on devices with non-ideal conditions for light absorption or film qualities, while providing excellent carrier selectivity. However, it needs an electrically dense insulating layer that effectively blocks carriers of the "wrong" species over a wide voltage range.

Figure 2.13 sketches such a two-layer device with insulating layer and the corresponding extraction transients. On the left side, a simple sketch of a MIS device is given, with the accumulation of holes visible at a non-zero offset voltage. The insulating layer is processed between the semiconducting layer and the anode contact. When a negative voltage is applied to the device, holes are injected from the cathode side; the negative potential at the anode will drive them to the insulator/semiconductor interface, where they will accumulate. The accumulation regime, where the majority of injected carriers reside at the interface and bulk carrier density is significantly lower, is a requirement for the MIS-CELIV technique to be valid and the main difference to previous CELIV measurements as well. Juška *et al.* have identified two conditions that will lead to that accumulation in normal MIS devices [231]. The first is easily met under ambient conditions and limits the effect of thermal diffusion of carriers with respect to the electric field by requiring the offset voltage V_{offs} at the beginning of the experiment to be larger than the thermal voltage, or $V_{\text{offs}} \gg {}^{k_B}/_{e}T$.

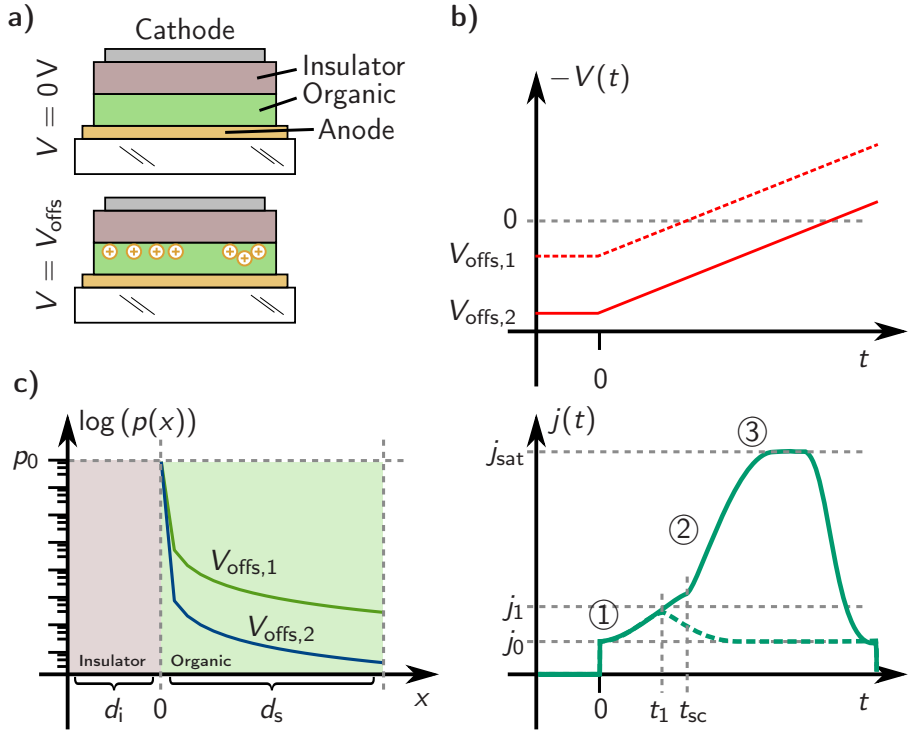

Figure 2.13.: **a)** Sketch of a diode with additional insulating layer (metal-insulator-semiconductor device) at two different voltages. With the positive contact at the top, holes as charge carriers cannot penetrate the insulating layer and will accumulate in the organic and at the interface between organic and insulator. **b)** Sketch of the MIS-CELIV measurement (lower graph) using two different offset voltages for carrier injection (upper graph), drawn after ref. [231]. The dashed line corresponds to $V_{\text{offs},1}$ with the so-called small charge extraction, whereas the straight line represents a full MIS-CELIV transient. **c)** Charge distribution and accumulation at the interface as modeled in the original MIS-CELIV framework.

Additionally, in original MIS-CELIV, the insulator capacitance has to be larger than the semiconductor capacitance ($C_{\text{ins}} \gg C_{\text{sem}}$), which can be achieved in MIS devices by having a very thin insulation layer with high dielectric constant. Fulfilling these constraints, the density of holes can be written as [231, 234]

$$\rho(x) = \rho_0 \left(1 + \frac{\mathrm{e}V_{\text{offs}}x}{2\mathrm{k_B}Td_{\text{i}}}\right)^{-1} , \tag{2.52}$$

where d_{i} is the thickness of the insulating layer. Some examples of this distribution are also given in Figure 2.13 part c). During extraction of the accumulated charges with rising voltage and dependent on the offset voltage at the start of the ramp, the extraction current ideally shows three different regimes ① to ③. The regimes are defined by the current limiting processes at the respective time, starting from diffusion limited current in region ①, to space charge limited current in ② to the displacement-current limit of the device' insulating layer in ③.

For regime ① in Figure 2.13b the current is not yet limited by space charge and

the time is $t < t_{\mathrm{sc}}$. Here, the general equation for the current transient $j(x,t)$ from standard CELIV (Equation 2.39) is still valid. Because the capacity of the insulator is required to be larger than that of the semiconductor, the current transient can be averaged over the whole semiconductor thickness d_{s} to achieve a time dependent description of the current. Unlike standard CELIV, no extraction zone exists as charge carriers start already accumulated at the interface, instead of being distributed over the film. Similar to the Equations 2.40 and 2.41, the transient over the whole device is then found [231] to be

$$j(t) = \frac{1}{d_{\mathrm{s}}} \int_0^{d_s} j(x,t)\,\mathrm{d}x = \frac{\varepsilon\varepsilon_0 S}{d_{\mathrm{s}}} + \frac{\varepsilon\varepsilon_0 \mu}{2d_{\mathrm{s}}} E\left(d_{\mathrm{s}},t\right)^2 \ , \tag{2.53}$$

where Gauss' law $\frac{\mathrm{d}E(x)}{\mathrm{d}x} = \frac{e\rho(x)}{\varepsilon\varepsilon_0}$ is applied to substitute the hole density in Equation 2.39. To solve the equation with respect to the electric field, the total one-dimensional current flow through the device is taken into account [233], where

$$j_{1\mathrm{D}}(x,t) = J_{\mathrm{C}}(x,t) + \varepsilon\varepsilon_0 \frac{\mathrm{d}E(x,t)}{\mathrm{d}t} \tag{2.54}$$

with the conductive current J_{C}. Considering a perfect insulator, the conduction current $J_{\mathrm{C}} = 0$, which leads to the time dependent differential equation for the electric field in MIS-CELIV by combining Equations 2.53 and 2.54

$$\frac{\varepsilon\varepsilon_0 S}{d_{\mathrm{s}}} + \frac{\varepsilon\varepsilon_0 \mu}{2d_{\mathrm{s}}} E\left(d_{\mathrm{s}},t\right)^2 = \varepsilon\varepsilon_0 \frac{\mathrm{d}E\left(d_{\mathrm{s}},t\right)}{\mathrm{d}t} \ . \tag{2.55}$$

It has an analytic solution

$$E\left(d_{\mathrm{s}},t\right) = \sqrt{\frac{2S}{\mu}} \tan\left(\frac{t}{t_{\mathrm{tr}}}\right) \tag{2.56}$$

with the transit time for carriers driven through the semiconductor by the external ramp

$$t_{\mathrm{tr}} = d_{\mathrm{s}}\sqrt{\frac{2}{S\mu}} \quad \text{or} \quad \mu = \frac{2}{S}\left(\frac{d_{\mathrm{s}}}{t_{\mathrm{tr}}}\right)^2 \ . \tag{2.57}$$

The transit time t_{tr} should not be confused with the space charge time t_{sc}, defined as the time needed for the first carrier in the device to travel the device thickness d_{s} in the field inside the device. The time t_{sc} can be estimated when calculating d_{s} by integrating the electric field in Equation 2.56 multiplied with the carrier mobility, thus

$$d_{\mathrm{s}} \stackrel{!}{=} \int_0^{t_{\mathrm{sc}}} \mu E\left(t\right)\,\mathrm{d}t = \left[-2d_{\mathrm{s}} \ln\left(\cos\frac{t}{t_{\mathrm{tr}}}\right)\right]_0^{t_{\mathrm{sc}}} \ . \tag{2.58}$$

Rearranging yields the approximate relation $t_{\mathrm{sc}}/t_{\mathrm{tr}} \approx 0.919$. Above t_{sc}, the measured current is limited by space-change [231], with

$$j(t) = \frac{9\varepsilon\varepsilon_0 S}{4d_{\mathrm{s}}} \frac{t^2}{t_{\mathrm{tr}}^2} \quad \Leftrightarrow \quad \frac{\Delta j}{j_0} = \frac{9}{4}\frac{t^2}{{t_{\mathrm{tr}}}^2} \ . \tag{2.59}$$

The transition between the extraction current governed by the aforementioned equations in region ① and the space charge limited current transient for times longer t_{sc} (given in Equation 2.59) in region ② leads to a kink in the extraction transient as seen in Figure 2.11 around t_{tr}. This can be used to calculate the carrier mobility from $t_{\mathrm{sc}} = 0.919 \cdot t_{\mathrm{tr}}$ and Equation 2.57. However, due to the nature of charge transport, especially in organic semiconductors, this transition is typically not observed [231, 234]. Thus, the transit time is normally not available directly from the measured transients, with one exception being the so called small-charge extraction [231] with very low V_{off}, when $\Delta j \ll j_0$ and the space charge limit is not reached.

In case of standard MIS-CELIV, one method is typically more suitable to estimate the transit time t_{tr}. With a dense insulator, the current through the device will never exceed the charging current of the insulator capacitance defined by ε_{i} and d_{i}. Thus, the saturation current j_{sat} in region ③ in Figure 2.11 is given by

$$j_{\mathrm{sat}} = \frac{\varepsilon \varepsilon_{\mathrm{i}} S}{d_{\mathrm{i}}} \ . \tag{2.60}$$

Instead of trying to observe the transition from drift to space charge region in the first place, the transient is tuned to suitable parameters in speed and voltage until a clear saturation is reached. Then, the transient is evaluated at the time t_1, where the extraction current equals the displacement current from the semiconductor's capacitance, i.e. $\Delta j = j_0$, or $j(t_1) = 2j_0$, respectively [231, 234]. In that case, from Equations 2.53 and 2.56 follows

$$t_1 = \frac{\pi}{4} t_{\mathrm{tr}} \quad \text{and hence} \quad \mu = \frac{\pi^2}{8S} \left(\frac{d_{\mathrm{s}}}{t_1} \right)^2 \ . \tag{2.61}$$

2.5.4. MIS-CELIV with non-ideal sample parameters

The aforementioned framework is only valid under the circumstances given in the very beginning of Section 2.5.3, most importantly a dense, i.e. electrically non-conducting insulator and a specific ratio of insulator and semiconductor capacitance of $C_{\mathrm{ins}} \gg C_{\mathrm{sem}}$. Also, charge transport is considered drift-dominated, whereas diffusion is not an issue [233].

One correction for non-ideal devices has already been given by Juška *et al.* to include the insulator capacitance [231] in the calculation, which has later been further evaluated by Sandberg *et al.* [233]. For non-ideal ratios of semiconductor and insulator capacitance and if the value of the latter is in the same range as the one of the semiconductor, the transient calculation can be adapted to the more general case of

$$j_0 = \varepsilon_0 S \left(\frac{d_{\mathrm{s}}}{\varepsilon_{\mathrm{s}}} + \frac{d_{\mathrm{i}}}{\varepsilon_{\mathrm{i}}} \right)^{-1} \tag{2.62}$$

for the displacement current [226, 231]. Also the drift current is changed to

$$j(t) = \frac{1}{d_{\mathrm{s}}} \int_0^{d_{\mathrm{s}}} j\,(x,t) \left[1 + \frac{\varepsilon_{\mathrm{s}} d_{\mathrm{i}}}{\varepsilon_{\mathrm{i}} d_{\mathrm{s}}} \right]^{-1} \mathrm{d}x \ . \tag{2.63}$$

The small signal transit time is then slightly modified to

$$t_{\mathrm{tr}} = d_{\mathrm{s}} \sqrt{\frac{2}{S\mu}\,(1+f)} \ , \tag{2.64}$$

where the correction applied to the transit time is dependent on the field distribution on the device, with

$$f = \frac{\varepsilon_\mathrm{s} d_\mathrm{i}}{\varepsilon_\mathrm{i} d_\mathrm{s}} = \frac{j_0}{j_\mathrm{sat} - j_0} \tag{2.65}$$

where ε_i, ε_s and d_i, d_s are dielectric constant and thickness of the insulator and semiconductor, respectively. The correction factor is by definition independent of the applied voltage ramp [231, 234], but can again only be evaluated if the device reaches saturation.

Analogous to Equation 2.61, the mobility can be calculated from t_1 for a finite insulator capacitance and if $j_\mathrm{sat} \gtrapprox 3.3 j_0$ [233] by taking the insulator displacement current into account with

$$\mu = \frac{\pi^2}{8 S^*} \left(\frac{d_\mathrm{s}}{t_1}\right)^2 (1+f) \ , \tag{2.66}$$

where $S^* = S/(1+f)$ is the corrected ramp over the semiconductor. The relation $j_\mathrm{sat} \gtrapprox 3.3 j_0$ also ensures that $t_1 < t_\mathrm{sc}$, meaning that the extracted carriers have not jet reached the opposite electrode. In the high capacitance limit, or when $j_\mathrm{sat} \gg j_0$, the correction factor will approach zero [233]. As a consequence, Equation 2.66 then equals Equation 2.61 and thus the initial approach by Juška *et al.* The same holds for the transit time in Equations 2.64 and 2.57.

Still, the theory is neglecting carrier diffusion. A more detailed picture on devices with finite insulator capacitance has been given by Sandberg *et al.* in 2017 [233]. By comparing the analytic framework for current transients with drift-diffusion simulation, they find an underestimation of the current transients and in turn an overestimation of the extracted mobilities, especially for low voltage ramps [233]. The difference stems from the neglection of background charge carriers in the semiconductor prior to the extraction. A high carrier density at the insulator-semiconductor interface promotes carrier diffusion into the bulk and although the density at the interface is still higher by orders of magnitude, bulk carrier density leads to a non-zero ohmic current through the device. In the framework given by Sandberg *et al.*, the characteristic diffusion time constant can be calculated to

$$t_\mathrm{D} = \frac{\mathrm{e} {d_\mathrm{s}}^2}{4\pi^2 \mu \mathrm{k_B} T} \ . \tag{2.67}$$

For Equation 2.66 to be valid, the condition $t_1 \ll t_\mathrm{D}$ has to be met, otherwise $\Delta j(t)$ is dominated by diffusion and the calculated mobility can be overestimated by orders of magnitude in the case of $t_1 > t_\mathrm{D}$. To counter that error, they introduce another correction factor into the mobility calculation, leading to

$$\mu = \frac{\pi^2 (1+f)}{8 S^*} \left(\frac{d_\mathrm{s}}{t_1}\right)^2 \left[1 + \frac{\pi^4 \mathrm{k_B} T}{2\mathrm{e} S^* t_1}\right]^{-1} \ . \tag{2.68}$$

Further evaluation of possible errors and pitfalls of the MIS-CELIV technique will be given in the experimental part on polar MIS-CELIV in Section 5.1.

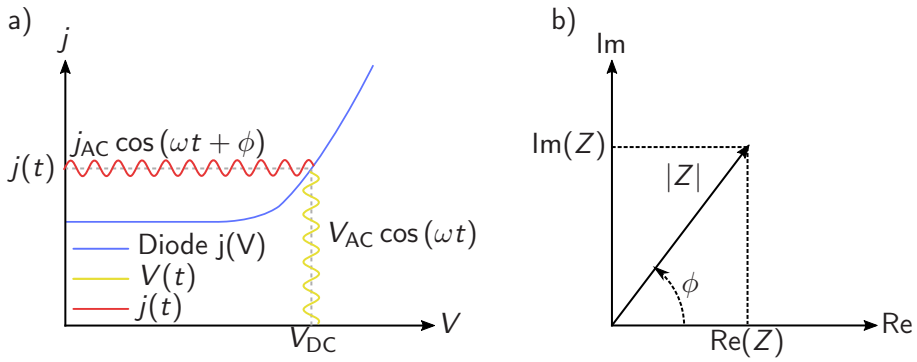

Figure 2.14.: a) Schematic illustration of impedance spectroscopy on an arbitrary diode. The applied AC voltage can be chosen at an arbitrary working point V_{DC}. For the calculation of the impedance the amplitude and phase of the AC response of the device is needed. **b)** Illustration of the dependence of the complex space (Re, Im) and its polar representation, draw after ref. [235].

2.6. Impedance spectroscopy

Impedance spectroscopy (IS) aims to measure the dynamics of a sample in the frequency domain by analyzing the characteristics of the complex impedance with respect to external constraints like voltage or frequency. Overall, three different methods exist to record the frequency response [235]. At first, a step function is applied to a sample and the resonant response of the device is measured. The detailed frequency dependence is then gained via a Fourier- or Laplace transformation. Secondly, instead of a step response, a signal consisting of white noise can be applied, the result has likewise to be post-processed to get single frequency data. The third technique, which is most commonly found and also utilized in the scope of this work, is to selectively measure the current response to a constant voltage, superimposed with a small sinusoidal modulation of constant frequency [235]. Impedance spectroscopy is a powerful tool to investigate various processes in OSC. In the past, it has been used to study frequency dependent transport characteristics [236, 237] as well as the density of carriers and traps in organic semiconductors [238–240]. It allows to study degradation mechanisms in OLEDs [180,241,242] or solar cells [243]. Impedance spectroscopy can also serve to investigate injection barriers with various techniques [14, 244] one of which has been co-developed within the scope of this work. Applied on organic diodes with polar layers, IS is one method to determine the magnitude of the giant surface potential [1, 2]. In the following section, the basic mathematical framework for capacitance-frequency and capacitance-voltage measurements using impedance spectroscopy is given. For a more detailed look on IS applied on polar diodes refer to Section 3.2 of the experimental part.

2.6.1. Measurement of complex impedance

To measure complex impedance of a device, a single-frequency, sinusoidal voltage is applied to the device [235, 245] (see Figure 2.14a for a sketch), consisting of a modulated AC signal with frequency ω and amplitude V_{AC},

$$V(t) = V_{AC}\cos(\omega t) = \mathrm{Re}\left(V_{AC}e^{i\omega t}\right) \ . \tag{2.69}$$

The measured current will follow the cosine with a phase shift of ϕ and amplitude j_{AC}

$$j(t) = j_{\mathrm{AC}} \cos(\omega t + \phi) = \mathrm{Re}\left(j_{\mathrm{AC}} \mathrm{e}^{i(\omega t+\phi)}\right) \ . \tag{2.70}$$

For now, any DC offset to the voltage, as needed for a voltage dependent measurement, is neglected. The phase ϕ is 0° only for an ohmic resistor, it is 90° or $\pi/2$ for an ideal capacitor and −90° or $-\pi/2$ for an ideal inductor. To calculate physical quantities like capacitance or resistance, the transfer functions between $V(t)$ and $j(t)$ for each device need to be known, which to solve in time domain is complex and difficult [235]. For example, the transfer functions for an ideal resistor, capacitor and inductor are

$$\begin{aligned} j_{\mathrm{res}}(t) &= \frac{1}{R} V(t) \quad , \\ j_{\mathrm{cap}}(t) &= C \cdot \frac{\mathrm{d}V(t)}{\mathrm{d}t} \quad \text{and} \\ j_{\mathrm{ind}}(t) &= \int \frac{V(t)}{L} \mathrm{d}t \ . \end{aligned} \tag{2.71}$$

It is evident that a combination of these formulas results in a complex set of differential equations. Instead, the problem is transferred into frequency domain via Fourier transformation and the complex expression is used. At first, the term of the complex impedance is introduced, where

$$Z(\omega) = \frac{V(t,\omega)}{j(t,\omega)} = Z_0 \mathrm{e}^{-i\phi(\omega)} \tag{2.72}$$

and $Z_0 = {}^{V_{\mathrm{AC}}}/_{j_{\mathrm{AC}}}$. Advantageous of this definition is that Z is, as a quantity in frequency domain, independent of the exact time. The response of the device is now characterized by the input frequency ω and its impedance $Z(\omega)$ including a frequency dependent phase $\phi(\omega)$. Usually, Z is a complex quantity given by

$$Z = Z' - iZ'' = R - iX \ , \tag{2.73}$$

where the real part corresponds to the ohmic resistance of the device. Thus, $Z' = R$ and Z'' is the resistance of the sample with respect to voltage changes, also referred to as *reactance* X [245]. Z can be seen as a vector quantity as sketched in Figure 2.14b, where besides its planar coordinates (R, X) also polar coordinates [235] with $(\phi, |Z|)$, where

$$|Z| = \sqrt{R^2 + X^2} \quad \text{and} \tag{2.74}$$

$$\phi = \tan^{-1}\left(\frac{X}{R}\right) \tag{2.75}$$

are common. The real and imaginary part of the impedance are then linked with the so called Kramers-Kronik relation [235]. The imaginary part of Z for example is given with

$$Z''(\omega) = -\left(\frac{2\omega}{\pi}\right) \int_0^\infty \frac{Z'(x) - Z'(\omega)}{x^2 - \omega^2} \, \mathrm{d}x \tag{2.76}$$

which requires a suitable model to describe Z' to be able to perform integration to infinity [245]. Still, the Kramers-Konik relation allows to test for the validity of a measured signal, a set of RC elements in series can mostly serve as an adequate model [246].

In practical measurement, voltage and current can be measured independently and by obtaining the phase shift e.g. by applying a sine-fit to both signals, ϕ and $|Z|$ can be calculated, which requires high-speed wavefunction generators and digitizers. Alternatively, AC current and voltage can be measured. The above framework up to now applies to a *capacitance-frequency* measurement, only. Measuring impedance, while applying a constant DC offset (*capacitance voltage*), however, is equally interesting. The AC voltage in Equation 2.69 is combined with a constant DC offset. The constant DC current will not interfere with the measured AC response, as long as the AC amplitude is a small signal compared to the DC working point. Typical values for V_{AC} are between 70 mV and 100 mV.

2.6.2. Impedance of selected circuits

Calculating complex circuits in time domain quickly complicates due to the need of differential transfer equations presented in Equation 2.71. Instead, they are expressed in their complex form [245]

$$\begin{aligned} Z_{\mathrm{res}} &= R \quad , \\ Z_{\mathrm{cap}} &= \frac{1}{i\omega C} \quad \text{and} \\ Z_{\mathrm{ind}} &= i\omega L \ . \end{aligned} \tag{2.77}$$

Like resistance, impedance follows the laws of Kirchhoff and Ohm, where serial circuit elements are summed up directly and parallel elements have to be summed over their reciprocal values. In case of two parallel circuit elements, for example capacitance and resistance of an RC element, the individual transfer functions given in Equation 2.77 calculate to

$$\frac{1}{Z_{\mathrm{RC}}} = \frac{1}{R} + \frac{1}{\frac{1}{i\omega C}} \Leftrightarrow Z_{\mathrm{RC}} = \frac{R}{1 + i\omega CR} \ . \tag{2.78}$$

An organic LED or solar cell, consisting of two stacked layers with individual capacitance, can be expressed in a very idealized form with two RC circuits in series ($C_{1,2}$ and $R_{1,2}$). In general, at least an additional series resistance R_{ser} will exist. Thus, the total impedance for such a structure is

$$Z_{\mathrm{OLED}} = R_{\mathrm{ser}} + \frac{R_1}{1 + i\omega C_1 R_1} + \frac{R_2}{1 + i\omega C_2 R_2} \ . \tag{2.79}$$

Both, real and imaginary part of Equation 2.79, are shown in Figure 2.15 alongside with its equivalent circuit. Besides the impedance, it is common to also plot the capacitance over frequency. It is calculated from the real part of the complex capacitance C^* of the circuit, as if the impedance was measured at a single capacitor. According to Equation 2.77, $Z_{\mathrm{cap}} = 1/i\omega C$, thus

$$C^* = \frac{1}{i\omega \left(Z' + iZ''\right)} \quad \text{and} \quad C = \mathrm{Re}(C^*) = \frac{-Z''}{\omega |Z|^2} \ . \tag{2.80}$$

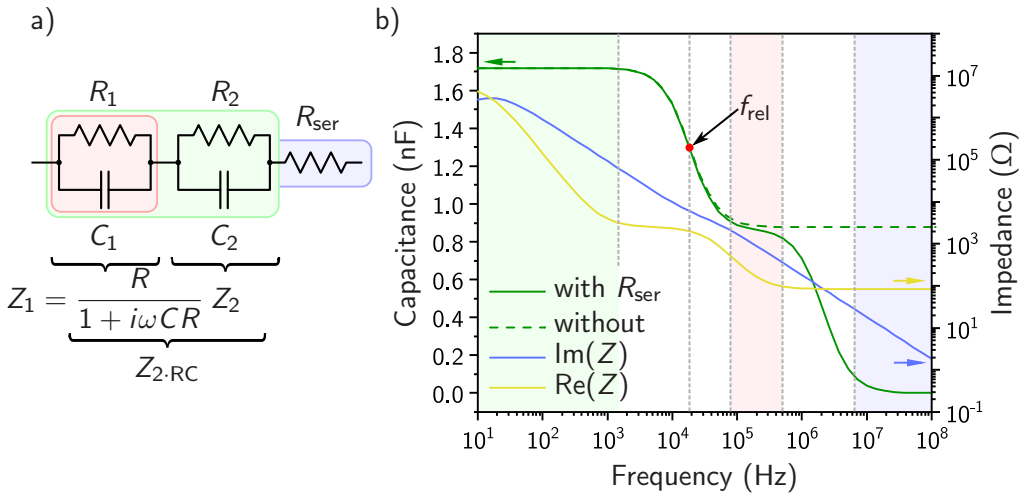

Figure 2.15.: a) Equivalent circuit and respective calculation for a two-RC element with series resistance. **b)** Calculated real and imaginary part of the impedance of a two-RC circuit with series resistance. The capacitance is calculated with and without series resistance. Shaded areas emphasize which part of the circuity is the defining element at the position of the graph.

For the OLED, described by Equation 2.79, in Figure 2.15 a transition between the capacitance dominated by the first RC element and the sum of both can be found at a characteristic frequency f_{rel}. An extreme value analysis [242] with $\omega = 2\pi f$ yields

$$f_{\mathrm{rel}} = \frac{1}{2\pi} \cdot \frac{R_1 + R_2}{R_1 R_2 \cdot (C_1 + C_2)} \,. \tag{2.81}$$

The evaluation of this frequency from measured impedance spectra and its temperature dependence allows to draw conclusions on transport and injection activation energies in the device. This is described in more detail in the experimental section in Section 5.2.

2.7. Ultraviolet photoelectron spectroscopy

Photoemission spectroscopy is the superordinate concept for detecting the density of states of a material by spectroscopically examining the kinetic energy of emitted electrons from an illuminated sample. It requires a monochromatic light source of known energy, which is typically either a X-ray source (*X-ray photoemission spectroscopy*, XPS) or an ultraviolet light source (*ultraviolet photoemission spectroscopy*, UPS) [51]. The technique is widely used to determine the energetic landscape of organic and inorganic materials [51,72,167,247] and interfaces [67,72,159]. A variation of UPS introduced by Sato *et al.* [248], *low energy*-UPS, aims on detecting sub-bandgap states and to accurately map the first HOMO level by reducing the excitation energy to a few electron volt. Photoelectron spectroscopy always probes the valence region of the device, the HOMO in case of organic semiconductors. Hence, UPS spectra, among others, allow to determine the energy barrier for hole injection between the Fermi-level and the HOMO of the semiconductor, as well as its workfunction. The

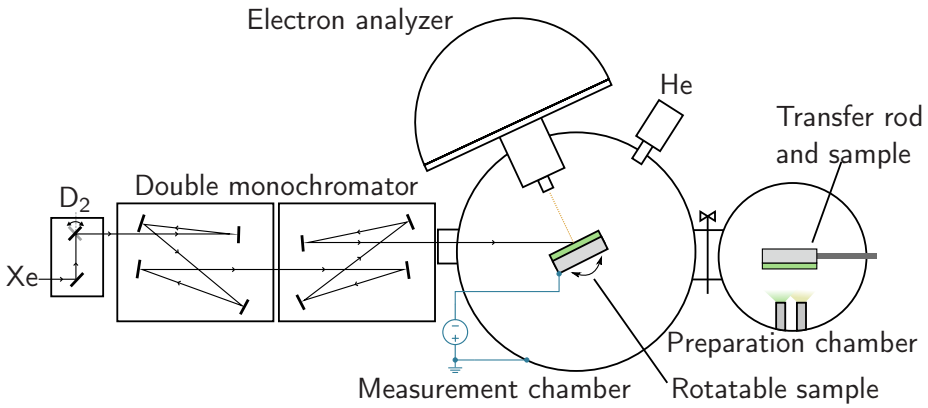

Figure 2.16.: Sketch of a UPS setup using the example of the setup available for the measurements in this work. In this case, it is equipped with two switchable light sources attached to a double monochromator to reduce stray light. An additional far-UV light source is connected directly to the measurement chamber without further filtering. The sample can be rotated in vacuum to reach optimal refraction angles. The setup comprises a second preparation chamber for evaporating organic materials, which allows a direct vacuum transfer of the sensitive organic surfaces. At the sample, usually a negative bias voltage is applied. Drawn after refs. [167, 247].

opposite technique, recording light emission from absorbed electrons, is called *inverse photoemission spectroscopy* (IPES) and allows to study the conduction region. This, however, was not attempted within this work.

A sketch of the working principle of a UPS experiment is shown in Figure 2.16, based on the setup made by Sato *et al.* [247, 248]. The sample is illuminated inside a high vacuum chamber and electrons emitted from the sample by the photoelectric effect are detected with a spectroscopic electron analyzer able to count electrons with respect to their kinetic energy. Monochromatic photons of energy $h\nu$ hit the surface and excite electrons in the occupied states of the sample. If $h\nu > \Phi_{\mathrm{samp}} + E_{\mathrm{b}}$, i.e. the excitation energy being higher than the workfunction and the binding energy of the sample, electrons are ejected into the vacuum [247]. The energetics of this process are sketched in Figure 2.17. For any energy higher than $\Phi_{\mathrm{samp}} + E_{\mathrm{b}}$, the surplus energy is transferred into kinetic energy of the ejected electron, hence

$$E_{\mathrm{kin}} = h\nu - \Phi_{\mathrm{samp}} - E_{\mathrm{b}} \ . \tag{2.82}$$

If sample and detector are electrically connected, the Fermi levels of both align. The difference in workfunction, however, will cause a potential difference between sample and detector ($\Phi_{\mathrm{samp}} - \Phi_{\mathrm{detector}}$) that will accelerate photoelectrons during their travel from the sample to the detector [247]. Additionally, the detector will only be able to detect the kinetic energy E'_{kin} with respect to its own workfunction. The overall energy conservation equation [247] with respect to the binding energy E_{b} of the electronic state to be observed is thus

$$E_{\mathrm{b}} = h\nu - E_{\mathrm{kin}} - \Phi_{\mathrm{samp}} = h\nu - E'_{\mathrm{kin}} - \Phi_{\mathrm{detector}} \ , \tag{2.83}$$

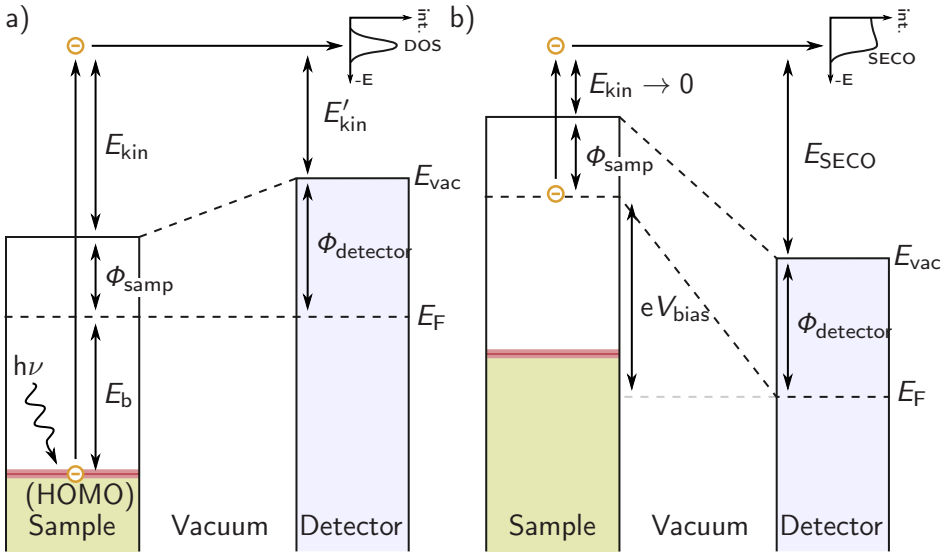

Figure 2.17.: a) Sketch of energy alignment between sample and detector during an UPS measurement without additional bias. The Fermi levels are aligned, apparent E'_{kin} and real E_{kin} kinetic energy differ by the workfunction difference of sample and detector. **b)** Situation when measuring with applied bias of V_{bias}. Depicted is the case for the secondary electron cutoff, those electrons leaving the sample after scattering without additional kinetic energy except the applied bias voltage. Both are drawn after refs. [167,247].

where E_b is given with respect to the Fermi level of the sample. Equation 2.83 allows to calculate the binding energy of an electronic state in the semiconductor with respect to the analyzer workfunction and the known photon energy. The onset of the emission with the smallest difference to the Fermi level is widely accepted as the hole injection barrier. However, a few limitations arise from that calculation that complicate the practical use. At first, $\Phi_{detector}$ has to be known precisely and the Fermi energy has to be leveled throughout the device [247]. Additionally, given that the detector will not detect the actual kinetic energy but only the apparent E'_{kin}, no information about the sample workfunction can be gained.

A usual countermeasure and method to determine Φ_{samp} is to apply an additional bias voltage V_{bias} between sample and detector. V_{bias} is typically negative and chosen large enough to lift the samples vacuum position considerably above that of the detector. This condition is sketched on the right in Figure 2.17. With the bias applied, photoelectrons are also accelerated from the sample towards the detector, hence even so-called *secondary electrons* are detected, which leave the sample without a considerable kinetic energy. In the measured energy diagram, the *secondary electron cutoff* (SECO) at E_{SECO} is therefore only dependent on the workfunction difference and the (negative) applied bias [247] and thus

$$\begin{aligned} E_{SECO} &= -eV_{bias} - \Phi_{detector} + \Phi_{samp} \quad \Leftrightarrow \\ \Phi_{samp} &= \Phi_{detector} + E_{SECO} - eV_{bias} \end{aligned} \tag{2.84}$$

This still requires the detector workfunction to be known, which is seldom the case and might also change over time. Instead, the energy scale is calibrated and $\Phi_{detector}$

calculated by obtaining the position of the Fermi-edge of a metallic sample or similar, one possibility is to measure the substrate just prior to processing the organics. As the binding energy for secondary electrons emitted directly from the Fermi-edge should be zero, it is possible to calculate the position of the Fermi-edge from the observed kinetic energy at a given photon energy. Including eV_{bias} in Equation 2.83 and calculating $E_{\mathrm{b}} = 0$ for $E'_{\mathrm{kin,Fermi}}$ yields

$$0 \stackrel{!}{=} E_{\mathrm{b}} = h\nu - E'_{\mathrm{kin,Fermi}} + eV_{\mathrm{bias}} - \Phi_{\mathrm{detector}} \quad \text{and}$$

$$eV_{\mathrm{bias}} - \Phi_{\mathrm{detector}} = E'_{\mathrm{kin,Fermi}} - h\nu \ . \tag{2.85}$$

The value of $E_\Delta = eV_{\mathrm{bias}} - \Phi_{\mathrm{detector}}$ is independent of the incident light energy and therefore valid for all further measurements on the same sample. Equations 2.83 and 2.84 can hence be rewritten to

$$E_{\mathrm{b}} = h\nu - E'_{\mathrm{kin}} + E_\Delta \quad \text{and} \tag{2.86}$$

$$\Phi_{\mathrm{samp}} = E_{\mathrm{SECO}} + E_\Delta \ . \tag{2.87}$$

This leaves the uniformity of the Fermi level, or energy levels in general, inside the semiconductor as a problem to discuss. In case of a metal, the condition of unbent levels is surely fulfilled, whereas a semiconductor might show band bending, especially under illumination [247] and with $h\nu > E_{\mathrm{gap}}$, which is necessary to detect photoelectrons from the HOMO levels and beyond. A phenomenological approximation for the potential drop in a semiconductor during measurement can be given as

$$\Delta V = j\rho d \ , \tag{2.88}$$

where j is the current density caused by photoemission, ρ the resistivity of the semiconductor and d its thickness. To minimize that potential and subsequent charging of the sample only j and d are points of action, ρ as a material parameter is constant in this case [247]. Reducing j would mean a reduced photon flux and likewise signal intensity, which is mostly undesired. For organic materials, the thickness is reduced instead to a few tens of nano-meters [247].

A more detailed, practical description on how to determine the parameters in question from UPS spectra is given in the experimental part in Section 6.3.

III

Dipolar doping of organic semiconductors

3. Giant surface potential of doped organic systems

As pointed out in Section 1.1.7, upon thermal evaporation of organic films, molecules can show spontaneous orientation polarization, leading to an overall film polarization. Recently, this effect has also been reported for doped systems, where the larger GSP for some diluted films compared to undoped layers was one key result [2]. Additionally, the direction of the GSP was found to influence electron injection into organic semiconductors by Noguchi *et al.* in 2013 [11]. A possible explanation by drift-diffusion simulation was given in 2016 by Altazin *et al.* [3]. Until now, no comprehensive study on the influence of the GSP on hole injection exists. One of the objectives of this work therefore is to study hole injection properties of polar HTLs in dependence on the magnitude of the GSP. From all polar materials that have been studied in the past and where literature data exists on the GSP in neat films, most are mainly electron conducting [6]. Hole conductors like NPB show only very weak film polarization and dipole moments, if any at all (see Section 2.1.1 for reference). To achieve hole conducting films with tunable GSP, the concept of *dipolar doping* is used instead, where a former unpolar host material is doped with a polar guest molecule, leading to an overall GSP inside a HTL. The following chapter will focus on the characterization of the GSP in doped organic films, especially on polar hole transport layers in OLEDs. Two different techniques, direct measurement via Kelvin probe and indirect determination by analyzing impedance spectra, are introduced. The material systems include NPB doped with Alq_3 and CBP doped with OXD-7 as well as neat polar materials. Additionally, the molecule code-named 1295 is briefly discussed, which shows a GSP with an inverse direction compared to the other investigated polar species.

3.1. Kelvin probe measurements

The measurement of the giant surface potential via Kelvin probe was, in case of organic semiconductors, pioneered by Ito *et al.* in 2003 [10] when the GSP for Alq_3 was reported. In this technique, consecutive Kelvin probe measurements are performed to record the change in surface potential of the organic film over a range of thicknesses. According to Equation 1.39, the polarization charge of the GSP leads to a potential drop in the film, which in turn causes a shift in the vacuum level and the Fermi level of the sample surface. A simple sketch of the band diagram as it is expected for polar and non-polar metal/organic interfaces and thin-films is drawn in Figure 3.1a and b, respectively, alongside with an example measurement. In the non-polar case, besides the interface dipole, additional band-bending can occur and would be measured with the Kelvin probe via a shift in vacuum levels [212]. With polar materials, the potential drop induced by the ordered dipoles in the film is much larger and the

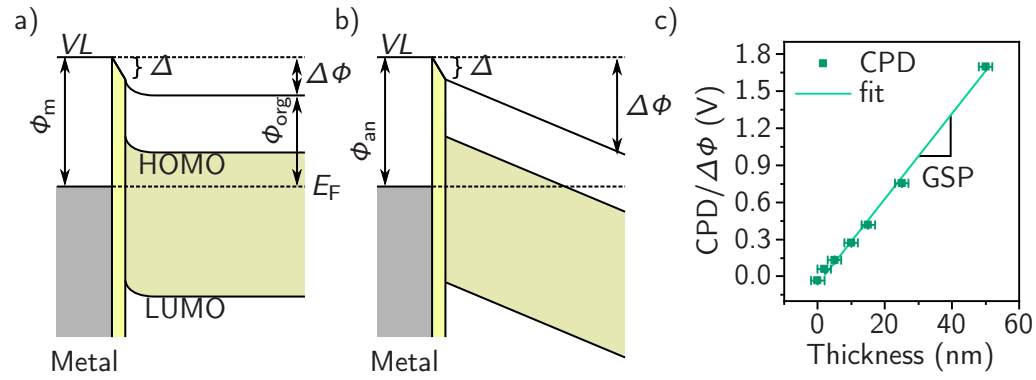

Figure 3.1.: **a)** Band diagram of a normal contact between metal and organic without GSP but, besides the interface dipole, possible band-bending at the metal/organic contact. **b)** Situation with additional GSP. The measured potential difference upon evaporation includes interface dipole and the potential drop induced by the GSP **c)** Example of consecutive Kelvin probe measurements of the contact potential difference and the GSP determined from the slope. a) and b) redrawn after ref. [10].

vacuum level shift directly resembles the effect of the GSP. In Equation 1.39, the potential drop is gained by integrating over the complete film polarization. It can be rewritten as

$$\frac{\Delta V_{\mathrm{CPD}}}{d} = \frac{\sigma}{\varepsilon\varepsilon_0} \ , \tag{3.1}$$

where $\frac{\Delta V_{\mathrm{CPD}}}{d}$ is the field induced by the polarization charge and in the following termed the GSP with the unit of $\mathrm{mV\,nm^{-1}}$. In the context of Kelvin probe measurements, it is sometimes also referred to as the *GSP slope*. From Equation 3.1, the interface charge density can be calculated with

$$\sigma = \frac{\Delta V_{\mathrm{CPD}}}{d}\varepsilon\varepsilon_0 \ , \tag{3.2}$$

the maximum error is given by

$$\Delta\sigma = \left|\frac{\varepsilon\varepsilon_0}{d}\right| \Delta V_{\mathrm{CPD}} + \left|\frac{\Delta V}{d^2}\varepsilon\varepsilon_0\right| \Delta d \tag{3.3}$$

To calculate the GSP from Kelvin probe measurements, the change in contact potential difference ΔV_{CPD} is measured over thickness. The description of the GSP in Equation 1.39 and its simplified form in Equation 3.1 does not include a possible change in GSP over thickness. If the measurement is conducted at multiple thicknesses the evaluation is therefore only valid, if a straight line fit is possible with minimal error. In Figure 3.1c, an example is given for $\mathrm{Alq_3}$. The first datapoint shows the CPD between Kelvin probe tip and the substrate and consecutive measurements resemble the growing film.

For the discussion of possible errors in the aforementioned measurement, a few assumptions have to be made. At first, the thickness of the evaporated film is in most cases only measured in situ using quartz crystal microbalances. Ex situ determination of the film thickness has been done on selected samples, however, poses its

own pitfalls. Profilometry requires to wipe or scratch parts of the film to create a measurable edge, ellipsometry often fails to detect the correct thickness due to the lack of suitable models and precise knowledge of the refractive index that can also depend on the preparation conditions of the film. During a multi-stage measurement of the GSP, it is therefore assumed that the experimentally obtained tooling factor needed to calculate the film thickness does not change. Fortunately, this requirement is met in the chamber in question, film thicknesses are reproducible within a range of 2 nm for a 50 nm film, leading to a relative error of 4 %. A random error in thickness and a systematic error induced by invalid thickness measurements have different impact on the overall result. While the first one will cause an increased uncertainty upon fitting the GSP to multiple measurements and will lose influence with a higher number of steps, the latter can be traced down to a direct factor in the calculated GSP. The second requirement is that the properties of the Kelvin probe setup, including the workfunction of the tip, do not change during consecutive measurements. This cannot be ruled out completely, however, repeated measurements of the same reference material allows to assume this error to be low. Besides, the absolute value of the tip workfunction is not needed to calculate the GSP slope. All parameters known to affect the measured CPD are kept constant for all samples of the same set and especially during consecutive evaporation, the CPD value for each datapoint in the calculation of the slope is averaged over multiple individual measurements. The resulting standard deviation, however, is typically very small in the range of a few mV. To avoid photoexcitation of the polar films, which is known to destroy the surface potential [10, 249], evaporation and measurement is done with all viewports covered with a dark-red acrylic glass, blocking all light below 600 nm.

In the following sections, the GSP of both, doped and undoped polar organic materials, as determined via Kelvin probe measurements, is analyzed and discussed. Additionally, different substrates and HILs are compared with literature data as a short benchmark for the Kelvin probe system. Measurements on the materials were, under my supervision, done by my students Vivien Wessels for Alq_3 and $Ir(ppy)_2(acac)$ during her bachelor thesis and Harry Karpenko for the system CBP/OXD-7 during his master thesis. My third student, Florian Graßl, was tasked to test and calibrate the Kelvin probe setup in the scope of his maters' lab project and he contributed Kelvin probe data on substrates. In all cases, the Kelvin probe system KP6500 acquired from McAllister Technical services, Berkeley, CA, USA was mounted at a vacuum chamber with a residual pressure of below 10^{-6} mbar. All data was analyzed and interpreted by myself.

3.1.1. Workfunction measurements on substrates and HILs

Besides the measurements of organic semiconductors, also different HILs based on PEDOT:PSS as well as ITO films have been investigated with respect to their workfunction in vacuum. The data is available partly as a side product from Kelvin probe series for GSP determination or from specific workfunction measurements. To calculate an absolute value for the workfunction of a film from the contact voltage potential difference, a calibration standard is needed. For this purpose, a freshly prepared layer of HIL1.3 on ITO with a workfunction of 5.7 eV proved to be practical as it reportedly reaches very similar results in different publications [8, 117, 167]. Also, it is known that HIL1.3 does not change its workfunction over a great variety

Name	Workfunction (eV) Meas.	Lit.	Sources
HIL1.3[1)]	5.70 ± 0.04	5.70	[8, 117, 167]
AI4083	4.97 ± 0.04	4.75 ± 0.05	[117, 157]
CH8000	5.07 ± 0.04	5.15	[157]
HIL1.3N	5.58 ± 0.04	5.85 ± 0.15	[8, 158]
ITO (UV/O_3)[2)]	4.54 ± 0.10	5.2	[250]
ITO (Plasma)	4.89 ± 0.04	5.55 ± 0.35	[189, 210]

Table 3.1.: Measured and literature data for the workfunction of different HILs as well as differently treated ITO surfaces. 1) HIL1.3 was used as the standard for all further calculations, the error is the standard deviation of multiple CPD values from the Kelvin probe measurement. 2) Literature value is given for the film directly after treatment, whereas the measurement was conducted after a considerate amount of time. See text for further explanation.

of UPS measurements (personal communication with Andreas Opitz at the Humboldt University of Berlin, September 30, 2019). Therefore, different measurements of HIL1.3 with otherwise same parameters in the Kelvin probe setup have been averaged to provide the calibration standard and the respective error from the standard deviation.

The results of all measurements on the PEDOT:PSS formulations AI4083, CH8000, HIL1.3 and HIL1.3N are given in Table 3.1 together with ITO films of different surface treatment. Where multiple literature sources were available, literature data was averaged. Unfortunately, not all publications state the source or even measurement technique used to obtain the published values, sometimes pre-treatment of the substrate or post-treatment of the film is different or not thoroughly described.

Detached from the discussion of the GSP in the following, the absolute values of different HILs do follow the trend given in literature. The PEDOT:PSS derivatives AI4083 and CH8000 approach the literature values, only HIL1.3N is considerably lower. Arguably, however, the batch of HIL1.3N available for this work is old and might already have degraded. For ITO, two different surface treatments can be compared, either UV/Ozone cleaning or Oxygen plasma treatment. The measured values for both preparation conditions, however, are relatively small compared to the literature values. OV/Ozone cleaned samples were usually prepared and cleaned in advance and stored in an N_2 atmosphere for later measurement, whereas the plasma treated samples were measured directly after cleaning. It has been reported previously that ITO surfaces relax to lower workfunctions over time [210, 250]. The low workfunction of (4.54 ± 0.11) eV observed here should therefore be compared to a relaxed value. Yamashita *et al.* reports a loss of 0.5 eV to 4.7 eV for a relaxed, Ozone treated film 150 min after processing [250]. Depending on the specific stoichiometry of the ITO film prior to UV/O_3 treatment, a few 100 meV of difference can be assumed to be systematic. The measured value does therefore correspond to what is expected for a relaxed, Ozone treated ITO film. The Plasma cleaned surface reaches around 4.9 eV, which is 0.35 eV higher than the Ozone treated film. In literature, this difference ranges from (0.35 ± 0.35) eV to (0.85 ± 0.35) eV comparing as-prepared and relaxed UV/O_3 with Plasma treated ITO, respectively [189, 210, 250]. All over,

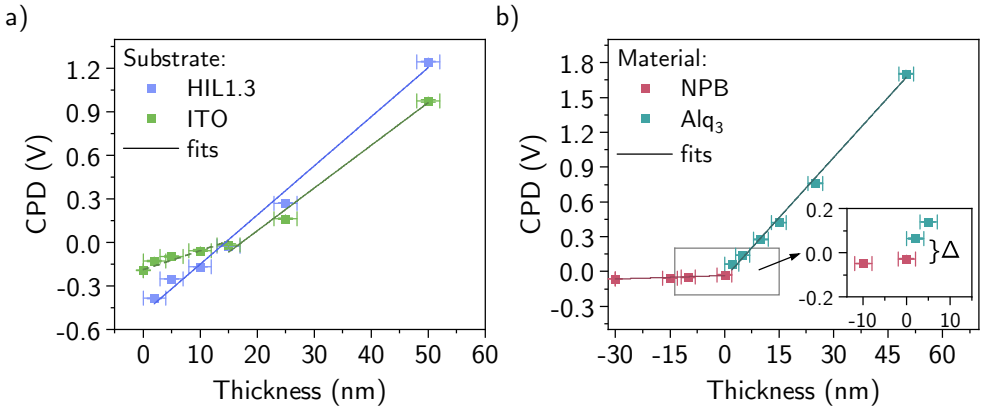

Figure 3.2.: **a)** Consecutive Kelvin probe measurements on Alq_3 films deposited on ITO and HIL1.3. The film on ITO shows a plateau of lower GSP in the first few nanometers fitted independently. **b)** NPB and Alq_3 measured during evaporation on the same sample. The inset magnifies the transition from NPB to Alq_3, visualizing the expected interface dipole. Datapoints for both plots are given with X and Y errors, although the latter is statistical and comparably small.

the measurements of the workfunctions of different PEDOT:PSS derivatives and ITO substrates agree well with literature data. This allows to expect further Kelvin probe measurements on organic molecules to be accurate, too.

3.1.2. Kelvin probe on undoped organic semiconductors

To study the buildup of the GSP and its dependence on external conditions like the chosen substrate, Alq_3 thin films were deposited on ITO, the PEDOT:PSS derivative HIL1.3 and NPB, of which the latter two were in turn processed on an ITO substrate. Experiments identical to these were already published in literature by different authors [10, 12], except the one with HIL1.3 on the substrate. A comparison should therefore allow to classify the measurements conducted in this work. Additionally, the materials $Ir(ppy)_2(acac)$, OXD-7, NPB and CBP have been investigated in neat film, with the latter two being usually considered un-polar.

Undoped NPB/Alq_3

In Figure 3.2, measurements of the GSP of Alq_3 on three different surfaces are shown, two on the usual substrates ITO and HIL1.3 and one, where Alq_3 was deposited on an NPB layer grown beforehand on the same ITO substrate. The error in thickness as given in the graphs is assumed to be 2 nm as stated above and ΔV_{CPD} is gained from the standard deviation of multiple measurements at the same point on the same device. For fitting, linear regression is done as described by York *et al.* [251, 252] to honor both Δd and ΔV_{CPD}. It is worth a note, however, that the results hardly differ, when omitting the error in thickness, as the spacing between individual points is large enough.

The resulting GSP slopes for Alq_3 are $(33.90 \pm 1.72)\,mV\,nm^{-1}$ on HIL1.3, on ITO $(29.50 \pm 3.28)\,mV\,nm^{-1}$ and $(34.60 \pm 1.75)\,mV\,nm^{-1}$, if grown on NPB. In case of

the measurement on ITO, the initial plateau was omitted, which itself has a slope of only $(16.20 \pm 2.98)\,\mathrm{mV\,nm^{-1}}$. Before comparing those to literature data, the specific behavior of Alq_3 on different substrates shall be discussed. On ITO, until the film thickness reaches ≈15 nm, the GSP of Alq_3 is roughly half (55 %) of its value at higher thicknesses. Most published Kelvin probe measurements with Alq_3 do not show such a pronounced thickness dependence but instead a linearly growing GSP on ITO [12, 212, 253, 254] as well as Silver [249]. Only in the data of Ito *et al.* published in 2002 [10], an inset shows the situation for low film thickness with a visibly lower slope at the beginning, though the author does not explicitly refer to that fact and the length scale is different by a factor of 10. In current theories that exist to explain the mechanism of the SOP, the interaction between molecule and surface plays a crucial role [7,47]. It is therefore possible that a certain minimum film thickness is necessary for a successful buildup of the GSP, thus especially the first few monolayers might show a different polarization. Alq_3 forms a triclinic crystal with lattice constants of roughly 10 Å, a monolayer of amorphous Alq_3 should hence also be around 1 nm thick. Though no definitive data exists on the exact growth conditions for Alq_3 on ITO, 15 nm seem to be thick enough to form a closed film of roughly 15 monolayers. Whereas the small plateau of 2 nm width in the data of Ito *et al.* might relate to this late buildup of the GSP due to surface effects, the 15 nm plateau observed here is more likely to stem from higher surface roughness, contamination or otherwise unfavorable growth conditions. On HIL1.3, no necessary minimum film thickness of this order of magnitude is observed. Instead, the GSP exists for all thicknesses and rises with slightly higher slope than on ITO. Both measurements are not detailed enough concerning individual steps in thickness to exactly reflect surface bound effects like interface dipole formation. Still, the SOP of Alq_3 yields slightly larger GSP on HIL1.3 compared to ITO, although both agree within error.

In OLEDs, however, Alq_3 is not directly deposited on the substrate. A better representation of the GSP in real devices should therefore be accomplished by a combined study of subsequently evaporated NPB and Alq_3, as published by Noguchi *et al.* in 2012 [12]. The respective measurement in our lab is shown in Figure 3.2b, the thickness is given relative to the NPB/Alq_3 interface. NPB as well as Alq_3 show the expected slopes indicating a GSP for both layers. NPB exhibits a slope of $(1.02 \pm 0.33)\,\mathrm{mV\,nm^{-1}}$ although considered non-polar in many publications, a detailed discussion is given further down. At 0 nm, directly at the interface between NPB and Alq_3, a small interface dipole can be identified as a small step between the last NPB measurement and the first Alq_3 layer of only 2 nm in thickness. Its height of about 0.1 V is on the lower side of literature data, as Noguchi *et al.* published approximately 0.2 V in a similar experiment [12]. For increasing film thickness Alq_3, however, builds up the giant surface potential quite linearly with the already mentioned $(34.60 \pm 1.75)\,\mathrm{mV\,nm^{-1}}$.

In conclusion, a slightly larger GSP of approximately $34\,\mathrm{mV\,nm^{-1}}$ is observed, if Alq_3 is evaporated on top of another organic layer, whereas directly on ITO the GSP is only $29.5\,\mathrm{mV\,nm^{-1}}$. This might be due to a reduced molecular orientation of Alq_3, if evaporated on inorganic ITO instead of an already existing organic layer.

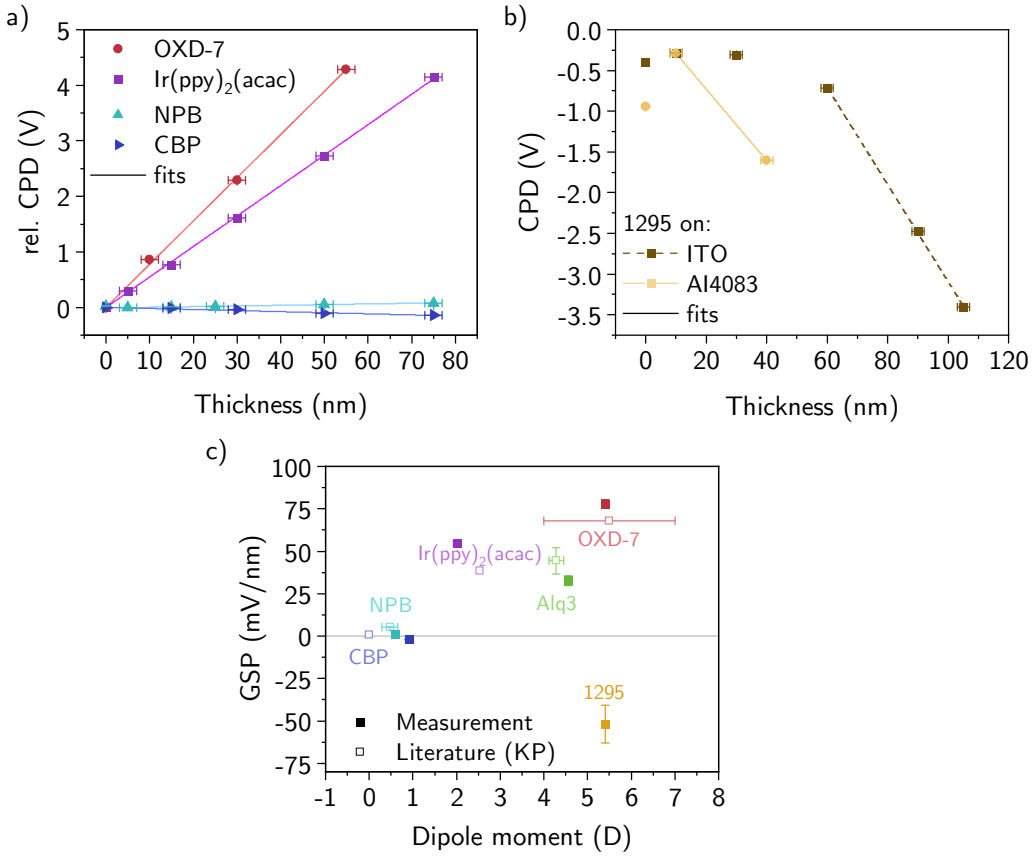

Figure 3.3.: **a)** Consecutive Kelvin probe measurements on $Ir(ppy)_2(acac)$, OXD-7, NPB and CBP. All films were deposited on ITO. The data is offset-corrected by the ITO contact voltage difference, hence starting all at a relative CPD of 0 V. **b)** Two Kelvin probe sequences with the Iridium complex 1295, directly on ITO and with Al4083 in between. **c)** Comparison of the measurements shown so far with literature data. The data of different references was combined and averaged, where possible, resulting in the errors for some of the materials [6, 10–12, 87, 253].

Further materials and comparison

Besides Alq_3, also other materials haven been investigated. The system CBP:OXD-7 has been studied in more detail in neat films as well as in doped configuration (see the next section). Additionally, the polar dye $Ir(ppy)_2(acac)$ as well as the Iridium complex 1295 were measured in neat films. In Figure 3.3a, the respective measurements are plotted offset corrected; the fits are given as straight lines. Series measured with 1295 are shown in Figure 3.3b on two different substrates. A visual comparison of different materials, following the form introduced by Osada *et al.* [6] is shown in Figure 3.3c with reference data gained from Kelvin probe measurements in literature. All values of the materials discussed so far are also summarized in Table 3.2, alongside with available single-molecule dipole moments. Because the obtained value of the GSP for a polar film depends on method (see discussion in Section 3.4), substrate and growth conditions, as seen with Alq_3, and possibly also purity, a direct compari-

Name	Dipole (D) lit.	calc.	GSP ($mV\,nm^{-1}$) lit.	meas.	dif. [%][4)]
Alq_3	4.3 ± 0.2	4.55	44.0 ± 7.8	32.7 ± 2.8	-27
OXD-7[1,2)]	5.5 ± 1.5	5.40	68	77.9 ± 2.5	16
$Ir(ppy)_2(acac)$[2)]	2.5	2.01	38	54.9 ± 1.1	43
NPB	0.47 ± 0.18	0.6	5.3 ± 0.1	1.12 ± 0.15	-79
CBP[2,3)]	0	0.0	0.7	-1.95 ± 0.16	178
1295[5)]	– –	5.4	N/A	-51.7 ± 11.0	N/A

Table 3.2.: Measured and literature data for the GSP and calculated as well as literature data for the single molecule dipole moment. For literature sources of the respective values see text or Table 2.1. 1) Dipole moment calculated from all conformers. 2) Only one reference measurement was found in literature for those materials, which were given without error. 3) Given is the single-molecule dipole moment. 4) The difference is calculated as the percentage of the normalized difference of measured data to literature. 5) No literature data publicly available

son with a single literature source is difficult. Hence, multiple sources were concerned and averaged, where feasible [6, 10–12, 87, 253]. Furthermore, only results measured with the Kelvin probe technique were included. For OXD-7, the value of the dipole moment is strongly dependent on the conformer [87], different sources therefore vary in value depending on how the dipole moment was calculated [6, 12, 87]. Emelyanova *et al.* published a comprehensive study on the molecule [87] containing data for all three conformers. The reference value was averaged over all three conformers as their relative energy is reported to be similar [87], although the error in dipole moment is therefore large. The value obtained in house for the same molecule instead could be calculated from a weighted average yielding a value of $(5.40 \pm 1.35)\,D$, see Section 1.1.7 for more information on the calculation. Other molecules showed only one conformer, the data for the calculated dipole moment of $Ir(ppy)_2(acac)$ was already published in [48].

For all five investigated materials, the calculated GSP resembles the general trend of the literature data. The offset between literature data (open rectangles in Figure 3.3c) and values obtained from Kelvin probe measurements within this work (filled rectangles), however, is not consistent over all materials. In the last column of Table 3.2, the relative difference between measured and reference data is given. Whereas $Ir(ppy)_2(acac)$ and OXD-7 exhibit a higher GSP in the measurements, Alq_3 is lower by $-27\,\%$, as is NPB with a difference of $-79\,\%$. Unlike other methods, the Kelvin probe technique adds only the thickness as an external parameter that is needed to calculate the GSP. Hence, although the differences can be caused by varying errors in tooling factor and thickness measurement, it is unlikely that this error differs from material to material but would be rather systematic to the chamber and setup. Also, the chosen substrate, though changing the GSP slightly, did not cause differences high enough to explain the discrepancy. From literature, two publications also add to the inconsistency, as Noguchi *et al.* published two distinctive Kelvin probe experiments with Alq_3 acquired from the same manufacturer, with $33\,mV\,nm^{-1}$ [11] and $48\,mV\,nm^{-1}$ [12], though in this case, on different substrates.

Two materials deserve special attention, namely CBP and 1295. Both show an inverse GSP in the measurements conducted for this work (negative slope in Figure 3.3a and b), with $(-1.95 \pm 0.16)\,\mathrm{mV\,nm^{-1}}$ and $(-51.7 \pm 11.0)\,\mathrm{mV\,nm^{-1}}$, respectively. CBP additionally does not possess a permanent dipole moment in single molecule DFT. Literature values on experimental results draw an inconsistent picture for CBP, as the calculated dipole moment on a single molecule is given as 0 D. Calculated values within this work also lead to 0 D. While Kelvin probe measurements by Noguchi *et al.* still lead to a small positive GSP of $0.7\,\mathrm{mV\,nm^{-1}}$, displacement current measurements recording the capacitive response of the device similar to impedance spectroscopy suggest it to be $-6.5\,\mathrm{mV\,nm^{-1}}$ [12]. Kelvin probe data obtained within this work also shows an inverse GSP for CBP, suggesting a PDM to be present on the molecule embedded in a thin film. This is supported by quantum chemical and kinetic monte carlo simulations published by Friederich *et al.* in 2018 [47]. They observe a polarization charge on simulated CBP films with dipole moment of (0.9 ± 0.4) D and a GSP of $(11.7 \pm 8.1)\,\mathrm{mV\,nm^{-1}}$, though no sign is given, it is assumed to be positive. As the molecule itself does not have an intrinsic PDM, it must arise during film formation and might therefore be influenced by the first monolayers' spontaneous orientation. For CBP it is thus possible to observe positive or negative GSP depending on processing conditions.

In case of 1295, due to a limited amount of material available for experiments, only very few Kelvin probe measurements could be performed, which does not allow for a fine grained investigation of the buildup of the GSP. Respective fits to calculate the GSP should therefore be taken with caution, especially for AI4083. The first series was measured on an ITO substrate and shows a pronounced plateau for thicknesses until approximately 60 nm, after which a strong negative GSP of $(-59.6 \pm 3.7)\,\mathrm{mV\,nm^{-1}}$ developed up to 105 nm as the maximum thickness measured. A second series on AI4083 was attempted, however the material was depleted before higher thicknesses could be reached. On PEDOT:PSS, the GSP amounts to only $(-43.8 \pm 4.2)\,\mathrm{mV\,nm^{-1}}$, leading to the comparably high error in Table 3.2. Like Alq_3, 1295 thus seems to require a considerate minimum film thickness for a stable GSP to build up on ITO in this experiment, whereas it seems to start earlier on PEDOT:PSS. Previously, only one material was also reported to show an inverse GSP. In 2013, Isoshima *et al.* published Kelvin probe measurements on tris(7-propyl-8-hydroxyquinolinolato) aluminum(III) ($Al(7\text{-}Prq)_3$), an Alq_3 derivative with propylene groups attached to each ligand, that amounted to $-118\,\mathrm{mV\,nm^{-1}}$ [255].

To conclude, the discrepancy observed for all measurements conducted during this work and literature values are well in range of expectation. From the current point of view, mostly material quality and processing conditions seem to influence the measured GSP at most, whereas known errors in thickness and determination of the CPD are small enough.

3.1.3. Kelvin probe on doped organic layers

Besides neat single and bilayer systems also doped layers have been investigated with Kelvin probe sequences to calculate the GSP. In the following, measurements of CBP doped with OXD-7 and NPB doped with Alq_3 are discussed. Figure 3.4 shows KP measurements on both series for the doped films in the top portion, whereas the resulting GSP is plotted against doping concentration in the bottom graphs. Values

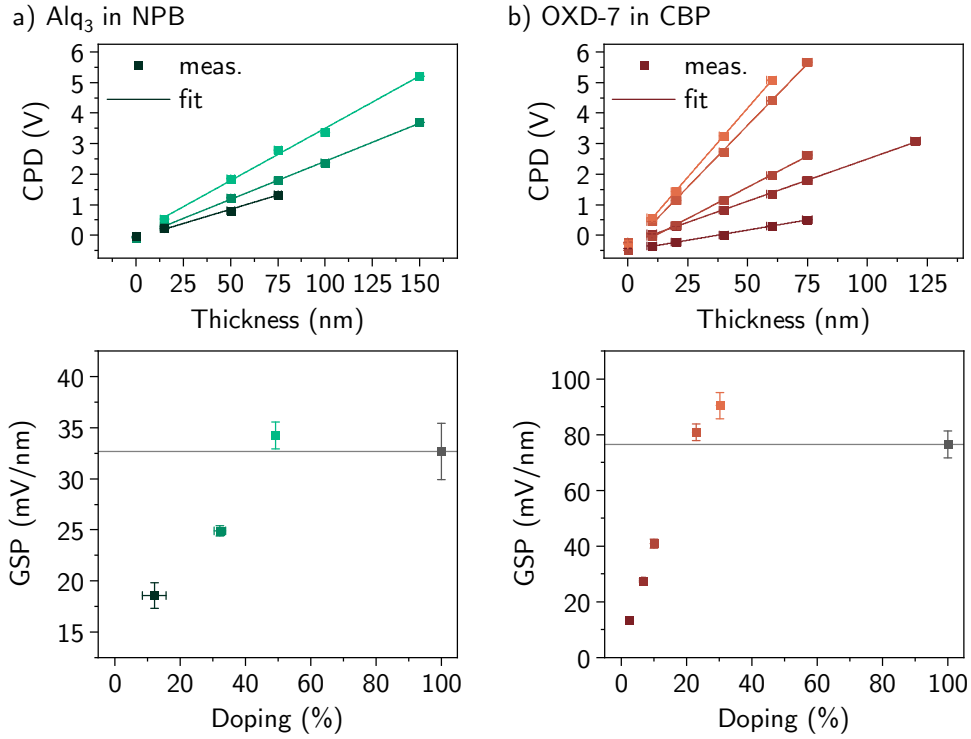

Figure 3.4.: Kelvin probe measurements on doped layers with **a**) NPB:Alq_3 and **b)** CBP:OXD-7. Please note the different scales for the GSP. Data for neat films at 100 % of "doping" are taken from the previous section, the value is also drawn with a horizontal line over the whole diagram as a guide to the eye.

for pure Alq_3 and OXD-7 have been taken from the measurements of the previous section and all data is summarized also in Table 3.3.

For series on doped layers, besides the sources for errors discussed in the scope of undoped films, a possible change in doping ratio during and between layers adds to the sources of errors. The concentration of both materials evaporated in the chamber must not change over a considerable amount of time, or has to be constantly monitored and adjusted to maintain a stable ratio over all films. Doping ratios given in Figure 3.4 are calculated using the average of all layers, whereas values for individual layers are obtained from the partial thickness of both host and dopant. This corresponds to the volume rate percentage that has also been used in the past [2, 48], a discussion of possible ways to define the doping ratio has been given in Section 2.2.1. Unfortunately, the change in doping rate over time was not recorded for the thickness dependence of Alq_3, for which the ratio of evaporation rates is used instead. Both ratios, however, are usually the same within their respective errors, as in the software, the rate is calculated from a derivative of the thickness. For all series, the doping rate during evaporation could be controlled very well, only the series for 12 % of Alq_3 shows higher error in doping rate.

A second difference to the neat-film series is that for doped materials, a broader spacing for individual thicknesses was chosen, mainly to reduce the material through-

Alq_3 in NPB:

Doping (%)	GSP ($mV\,nm^{-1}$)
12.2 ± 3.6	18.58 ± 1.25
32.3 ± 1.8	24.93 ± 0.50
49.3 ± 1.1	34.23 ± 1.32
100	32.65 ± 2.76

OXD-7 in CBP:

Doping (%)	GSP ($mV\,nm^{-1}$)
2.7 ± 0.4	13.32 ± 0.49
6.8 ± 0.5	27.63 ± 0.61
10.1 ± 0.5	40.88 ± 1.51
23.0 ± 0.6	80.78 ± 2.99
30.4 ± 0.6	90.38 ± 4.71
100	76.39 ± 4.80

Table 3.3.: Data from KP series on NPB:Alq_3 and CBP:OXD-7. 100 % of doping corresponds to the polar species only for which measurements are given in Section 3.1.2.

put and likewise the risk to contaminate the Kelvin probe chamber. Also, this leads to a more uniform doping concentration profile within the film without breaks, which might be important especially for low doping ratios. As a result, the existence of possible interface dipoles could not be checked, the substrate measurement and its CPD is hence excluded from the fits.

In both series, the GSP rises steadily and almost linearly with rising doping concentration. Furthermore, a common and probably most important feature from both series, as seen in the two lower graphs in Figure 3.4 is, that the highest GSP is not observed for a pure Alq_3 or OXD-7 film, but at a lower concentration between 30 % and 50 %. This has also been reported in the past for Alq_3 measured in OLEDs with doped ETL, also comprising NPB as host and Alq_3 as dopant [2]. In this publication, the maximum has been found at 50 % of doping, where the GSP decreases again for higher ratios until settling at the neat film value. Unfortunately, no doping concentrations higher than 50 % for Alq_3 and 30 % for OXD-7 had been investigated with Kelvin probe. The respective concentrations can therefore not be confirmed as the global maximum. Still, the general trend of observing a GSP higher than the neat film value as seen for both NPB and OXD-7 is surprising. In contrast, for $Ir(ppy)_2(acac)$ doped into CBP we observed only an increase in GSP with the maximum residing at the neat film [48]. Unfortunately, no further systematic study of the GSP in doped organic systems is known. The results will be compared and discussed further in Section 3.4, also with regard to the amount of orientation in the film, together with data obtained from impedance spectroscopy.

3.2. Determination of the GSP by impedance spectroscopy

Impedance spectroscopy was one of the first methods to observe the giant surface potential or, more precisely, the change in field distribution in the device induced by the GSP and its accompanying interface charges [1,90]. An OLED with polar organic materials in at least one layer shares properties of a classic diode and that of a MIS device described in Section 1.2.3. This combination will also play a crucial role for further investigation of the carrier dynamics and barriers in dipolar doped systems in Part IV and is also the reason why the magnitude of the GSP can be determined by

impedance spectroscopy. In this experiment, the capacitance is measured at constant frequency but varying voltage. Changes in capacitance or the phase of the measured response of the device usually relate to carrier injection or movement in the organic layers. A two layer device of polar organic semiconductors can show a transition between two regimes, the first governed by the capacitance of both layers and the second by the capacitance of only one layer. Without a direct change in capacitance of at least one layer, however, no transition or change in signal is expected at constant frequency, as the capacitance of a capacitor is usually voltage independent. The GSP, or rather the spontaneous orientation polarization and the resulting interface charges, induces a field gradient between two layers of different polarization. This results in a voltage dependent accumulation of charges that can be detected in the capacitive response of the device.

Measurements for this section were conducted either with the Paios measurement system from Fluxim AG, Winterthur, Switzerland or the Solartron Impedance Analyzer by Solartron Analytical, now Ametek Scientific Instruments in Hampshire, UK. The samples were mounted to a probe station in a glove box with N_2 atmosphere.

3.2.1. Correlating impedance transition voltage and GSP

In Figure 3.5, the basic principle behind the measurement of the GSP via impedance spectroscopy is sketched, where the drawing assumes a positive GSP for the ETL as it is observed for most polar materials. The HTL on the left is non-polar in this case. It will be shown, however, that the following description is valid as long as any GSP of the HTL is sufficiently lower than that of the ETL.

Beginning at the top left diagram in Figure 3.5, where the applied voltage is $V < V_{\mathrm{tr}}$, charge carriers at both, anode and cathode, might already penetrate the metal-organic interface of HTL or ETL, respectively, depending on the type of contact. However, because the field gradient through the device forbids their drift towards the interface, all carriers will eventually recombine at the contact, thus no effective injection is possible. A capacitance-voltage measurement of such a device, as long as leakage and other parasitic currents are kept low, will see the combined capacitance of ${C_{\mathrm{tot}}}^{-1} = {C_{\mathrm{ETL}}}^{-1} + {C_{\mathrm{HTL}}}^{-1}$, where both semiconductors act as dielectric between the contacts of two capacitors. The phase of the signal is near 90°, indicating an almost capacitive response. When the external voltage approaches the transition voltage V_{tr}, the additional field gradient caused by the GSP will allow the HTL to reach flat-band condition, despite the ETL being still reversely biased. At this point, holes can be injected successfully into the bulk of the HTL and their drift to the interface is favored by the field gradient, if $V > V_{\mathrm{tr}}$. By further increasing the external voltage to between $V_{\mathrm{tr}} < V < V_{\mathrm{inj}}$, injected holes will accumulate in the HTL and at the interface [13]. As a direct result, the charge carrier density in the hole transport layer is high enough to lower its impedance considerably, the measured overall capacitance of the device is now governed by the ETL only, $C_{\mathrm{tot}} \approx C_{\mathrm{ETL}}$. In the phase signal, a small peak towards lower phase indicates a finite ohmic resistance during carrier injection. Usually, the phase does not return to the initial value in the accumulated regime, indicating persisting carrier movement and resistance in the HTL also in accumulation. Up to now, only hole injection governed the measured response of the device. Electrons will be successfully injected into the OLED at and above the injection voltage V_{inj} and their drift to the interface for $V \geq V_{\mathrm{inj}}$ allows for radiative recombination.

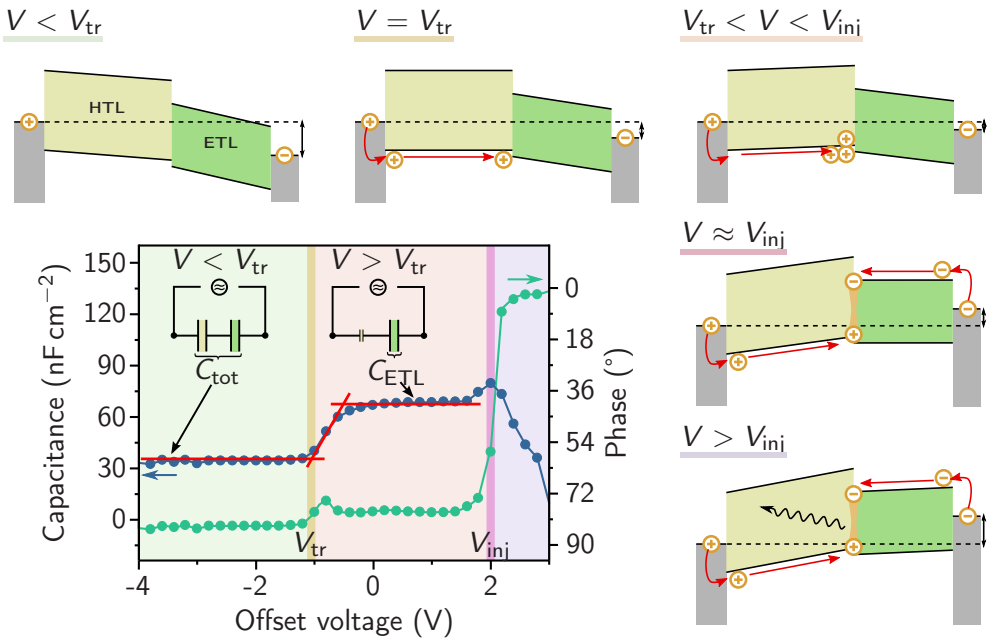

Figure 3.5.: Exemplary capacitance-voltage data of two prototypical materials (HTL and ETL), where in this case only the ETL is polar with positive GSP, alongside with schematic band diagrams illustrating the device's energetic status at specific voltage regions (regions in the plot and sketches match left to right and clockwise, respectively). Plotted is the capacitance (blue) and phase (green). Above the transition voltage V_{tr} the capacitance gradually increases from the total geometric capacitance C_{tot} eventually reaching its maximum value of C_{ETL} at a plateau between V_{tr} and V_{inj}. The device is injected with holes above V_{tr}, electrons follow above V_{inj}. The transition voltage is usually gained from the onset of the raise in impedance, as indicated by the red lines. The insets show two basic equivalent circuits for both the total capacitance (left) and in the case, where only C_{ETL} is visible (right).

In a polar device, the HTL is already positively biased and beyond flat-band, when the ETL field allows electron injection at $V \approx V_{inj}$. At this point, the impedance signal can again show a small increase in capacitance, as injected electrons at the cathode/organic interface lower the local resistance and effectively decrease the apparent thickness of the ETL. Directly above V_{inj}, however, increasing recombination and carrier density in the whole device will diminish the dielectric features of the semiconductors until, in impedance, ohmic behavior prevails. The measured capacitance will show a steep decrease and can even result to values $C_{tot} \leq 0$, while the phase quickly approaches zero.

For an ideal non-polar device, flat-band conditions are met simultaneously for all layers at the so-called built-in voltage V_{bi} that with $eV_{bi} \approx \Phi_{anode} - \Phi_{cathode}$ counters the built-in field defined by the contact potential difference of anode and cathode. Therefore, effective carrier injection, recombination at the interface and hence light emission will begin for voltages above V_{bi} for non-polar OLEDs. The difference in the hole-injection field indicated by V_{tr} and the normal built-in field set by V_{bi}, is

defined by the GSP field gradient applied over the thickness of the ETL, hence

$$GSP = \Delta E = \frac{V_{\mathrm{tr}} - V_{\mathrm{bi}}}{d_{\mathrm{ETL}}} \ . \tag{3.4}$$

Analogous, the interface charge density [1] can be calculated with

$$\sigma_{\mathrm{int}} = \Delta E \cdot \varepsilon_{\mathrm{ETL}}\varepsilon_0 = \frac{\varepsilon_{\mathrm{ETL}}\varepsilon_0}{d_{\mathrm{ETL}}} \left(V_{\mathrm{tr}} - V_{\mathrm{bi}}\right) = \frac{C_{\mathrm{ETL}}}{A_{\mathrm{ETL}}} \left(V_{\mathrm{tr}} - V_{\mathrm{bi}}\right) \ , \tag{3.5}$$

where A_{ETL}, $\varepsilon_{\mathrm{ETL}}$ and d_{ETL} are area, dielectric constant and thickness of the polar ETL. The GSP and σ are then linked to each other by the dielectric constant, only. In both equations, the key to calculate interface charge density or the magnitude of the GSP is the knowledge of the built-in voltage V_{bi}. Previously, it has been assigned to the peak position of electron injection in the impedance data, or $V_{\mathrm{bi}} = V_{\mathrm{inj}}$ [241]. However, it is not a priori known, if the peak observed in capacitance-voltage measurements and the internal field always coincide. A more detailed discussion is given in Section 3.3.1. An alternative method to gain the built-in field is to extrapolate the thickness dependence of the transition voltage, $V_{\mathrm{tr}}\left(d_{\mathrm{ETL}}\right)$ against $d_{\mathrm{ETL}} \to 0\,\mathrm{nm}$, which will allow to estimate V_{bi} according to

$$V_{\mathrm{tr}} = \Delta E \cdot d_{\mathrm{ETL}} + V_{\mathrm{bi}} = \frac{\sigma_{\mathrm{int}} d_{\mathrm{ETL}}}{\varepsilon_{\mathrm{ETL}}\varepsilon_0} + V_{\mathrm{bi}} \ , \tag{3.6}$$

where V_{bi} is the vertical intersect and the slope equals the GSP.

Determination of the transition voltage

The definition of the transition voltage V_{tr} above aims on the electric field distribution in the polar device. The change in capacitance is linked to the accumulated carrier density in the HTL. Different definitions and methods for determining the transition voltage can be discussed. Besides the point of the steepest slope during the transition, or the voltage needed to complete accumulation indicated by the point, where the measured capacitance equals C_{ETL}, one possibility is to extract the onset of the capacitance rise, when the transition occurs. This method has also been used previously by Jäger *et al.* [2], whereas Berleb *et al.* focused on the inflection point [90]. In a different approach besides impedance spectroscopy, when measuring the displacement current in dependence of the applied voltage, Noguchi *et al.* has defined the transition voltage by the accumulation voltage, which is the point where C_{ETL} is reached in impedance [12].

Within this work, the onset of the accumulation is defined to resemble V_{tr}, it is therefore related to the beginning of the process of charge carrier accumulation. In contrast to the inflection point or the finished accumulation, the onset is typically well pronounced in the measured data. However, the slope of the $C(V)$ curve during accumulation was found to be dependent on various factors, including the measurement frequency and hole injection barrier. Additionally, for low film thicknesses or low difference in GSP between HTL and ETL, the rise in capacitance can be overlain by beginning electron injection from the cathode. The onset of the transition can be obtained by fitting the sectionally defined function

$$C(V) = \begin{cases} C_{\mathrm{tot}} & \text{for } V < V_{\mathrm{tr}} \\ C_{\mathrm{tot}} + m\left(V - V_{\mathrm{tr}}\right) & \text{for } V \geq V_{\mathrm{tr}} \end{cases} \ . \tag{3.7}$$

Here, C_{tot} is the total, geometrical capacitance observed for both HTL and ETL and m the slope of the transition in a linear approximation, which is only valid shortly after the onset of the transition. An example of the determination of V_{tr} with both methods is given in Section 3.2.3.

Best practice to calculate the GSP

With Equation 3.4 and Equation 3.5, two different ways exist to calculate the nominally same parameter, the magnitude of the GSP or sheet charge density of a polar ETL. However, both require different additional measurement quantities besides V_{tr} and V_{bi} to calculate either the GSP in $\mathrm{mV\,nm^{-1}}$ or the sheet charge density in $\mathrm{mC\,m^{-2}}$. All parameters have different errors attached, which can be briefly summarized as follows. In general, the biggest error is expected to be in the chosen *dielectric constant* ε, which is usually assumed to be around $\varepsilon = 3$, where values between 2 to 5 have been found and the measurement is challenging [256]. For Alq_3, $\varepsilon = 3.5$ has been used in the past [2]. Still, it is preferred to avoid the need of a dielectric constant. Another error-prone quantity is the original position of the *built-in voltage* V_{bi}. This quantity cannot accurately be determined from impedance measurements on devices with only one thickness. Rather, a thickness variation is necessary, a discussion of this finding follows in Section 3.3. Usually, the *area of the sample* A can be determined ex-situ with considerable accuracy using optical microscopy, considering a sharp edge of the metal contact and assuming uniform resistance and injection over the whole contact area. The error in the fit of the *transition voltage* V_{tr} is dependent on multiple factors, including measurement accuracy and frequency dependence. For example, if the slope of the transition is low, a little change in the slope can cause a huge change in the extracted transition voltage.

If the impedance measurement could be conducted at full accumulation, that is, if a lowering of the measurement frequency does not increase the extracted ETL capacitance, the suggested method is to determine the interface charge density using Equation 3.5, as this does not require to know the dielectric constant. When the magnitude of the GSP is to be calculated, besides the built-in voltage, only the thickness is needed as an additional measured quantity, which, however, is not easily determined in some cases. Still, the GSP is best calculated using Equation 3.4.

3.2.2. Measurement and simulation of polar organic layers

The basic idea of simulating polar organic layers is presented in Section 1.3.2. In the following, devices with nominally un-polar HTL and various polar electron transport materials (Alq_3, OXD-7 and $Ir(ppy)_2(acac)$) are measured and the attempt is made to reproduce the devices in simulation. Also, different routes to extract GSP or interface charge density from impedance spectra will be discussed. In devices with OXD-7 and $Ir(ppy)_2(acac)$ CBP is used as HTL, whereas Alq_3 was deposited on NPB. Note that an in-depth study of simulating polar OLEDs is not part of this work, but was published by Altazin *et al.* in 2016 [3].

The simple devices provide a good benchmark and starting point to describe the methods for parameter extraction. Three devices with the same nominal ETL thickness of 50 nm (53 nm for Alq_3) are selected for the example, the $C(V)$ measurements are shown in Figure 3.6a. Whereas the transition for Alq_3 and OXD-7 occurs with only 0.5 V of difference at -1.03 V and -1.57, respectively, for $Ir(ppy)_2(acac)$, it is

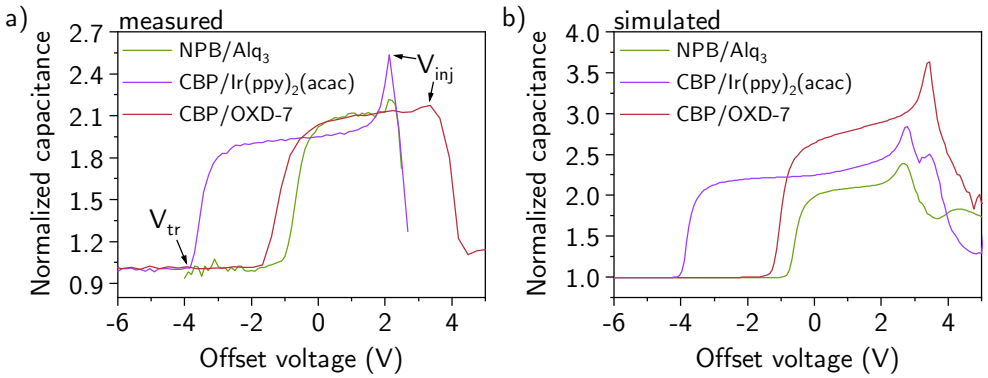

Figure 3.6.: **a)** Measurements of NPB/Alq_3, CBP/OXD-7 and $CBP/Ir(ppy)_2(acac)$, all with approximately 50 nm of ETL thickness. Measurements were taken at 13 Hz, each. **b)** Simulations to replicate the observed experimental data.

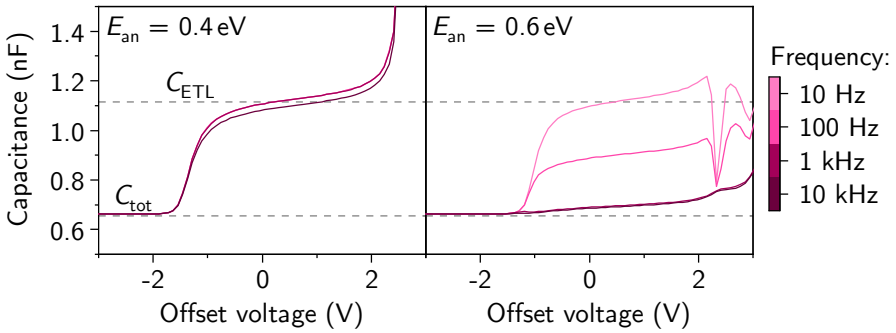

Figure 3.7.: Comparison of simulated $C(V)$ measurements on devices with different hole injection barriers as given in the graph. The high barrier device will need far lower measurement frequencies for successful extraction of the real ETL capacitance C_{ETL}. The values for C_{ETL} and C_{tot} are shown with dashed lines, their positions were calculated using the same parameters for thickness, area and dielectric constant.

−3.84 V. The peak in impedance, indicating the injection of electrons in the device at V_{inj} and ideally also the onset of light emission, though, occurs at the same position for $Ir(ppy)_2(acac)$ and Alq_3, whereas OXD-7 requires a 1.5 V higher applied voltage for turn-on. This inequality already indicates a difference in the built-in voltage V_{bi} in the OXD-7 device at least, which, besides V_{tr}, needs to be determined in order to calculate the GSP of the layers according to Equation 3.4. However, a few general considerations will be discussed beforehand.

To extract the transition voltage, voltage dependent capacitance measurements have to be conducted at a suitable frequency, as transition and accumulation are additionally frequency dependent. The frequency dependence is linked to the injection barrier at the anode [13] and will play a major role in determining carrier injection activation energies and barriers in Chapter 6. For extracting the GSP, one requirement is to reach high accumulation and therefore to adopt the frequency to a reasonably low value. An example emphasizing this effect is shown with two simulated polar OLEDs in Figure 3.7. Here, a polar device was simulated with non-polar

HTL and an interface charge density for the ETL of equivalent $1.8\,\mathrm{mC\,m^{-2}}$. To simulate two different injection barriers at the anode side, the offset between anode workfunction and HTL HOMO was varied between 0.4 eV to 0.6 eV. The high barrier device as shown on the right in Figure 3.7, needs low frequencies of about 10 Hz to reach the full accumulation regime, because its relaxation frequency is much lower than in the case for the low barrier device. There, in turn, the actual value of C_{ETL} is observed in average for all frequencies. Unfortunately, in the low frequency range, any parasitic conductance caused by conduction paths or lateral conductance of the layers will cause an additional signal in the low frequency range [241], which would overlay with the measured ETL capacitance. Last but not least, low frequency measurements need to drive the device at a certain DC offset voltage for a long time, which might increase electrical and thermal stress to the sample. Within this work, it was found to be most practical to extract the transition voltage from $C(V)$ measurements conducted at 5 Hz to 20 Hz, where odd values like 13 Hz are preferred to minimize the effect of harmonics of line-noise.

For the measurements shown in Figure 3.6a, the giant surface potential for $\mathrm{Alq_3}$ can be calculated to a quite high value of approximately $56\,\mathrm{mV\,nm^{-1}}$, although the global average over multiple other $\mathrm{Alq_3}$ samples prepared in this work is at $(47.2 \pm 1.3)\,\mathrm{mV\,nm^{-1}}$. Values for OXD-7 and $\mathrm{Ir(ppy)_2(acac)}$ are (98.3 ± 16.1) and $(124.3 \pm 34.3)\,\mathrm{mV\,nm^{-1}}$, respectively. The simulations shown in Figure 3.6b are calculated to fit the measured spectra as good as possible. As pointed out in Section 1.3.2, the polar nature of the ETL is replicated by introducing two doped layers alongside the ETL layer. A potential gradient arises from the doping and leads to the shift in hole injection voltage and the accumulation of holes above V_{tr}. This shift, however, is also dependent on the dielectric constant and the thickness of the layer, both directly correlate to V_{tr}. The simultaneous influence of thickness d, dielectric constant ε and the GSP or sheet charge density σ as well as the area of the device complicate a global high quality fit on the devices to a high extend. Numerical constraints add to the complexity, as high doping ratios in the sheet charge layers above $\approx 2\,\mathrm{mC\,m^{-2}}$ often hinder convergence or would require different thicknesses or material parameters.

While the model is not accurate enough to allow for an exact replica of the measured values in simulations, it still allows to emphasize the major differences between the three devices. At first, the GSP in the simulations is set to roughly the measured values of $56.5\,\mathrm{mV\,nm^{-1}}$ for $\mathrm{Alq_3}$, $98.3\,\mathrm{mV\,nm^{-1}}$ for OXD-7 and $121\,\mathrm{mV\,nm^{-1}}$ for $\mathrm{Ir(ppy)_2(acac)}$, while the dielectric constant is $\varepsilon = 2.7$ in all cases. The simulations tend to underestimate the influence of the sheet charge, which can be compensated e.g. by alternating the thickness or dielectric constant. In the example, a larger error in simulated device thickness was therefore accepted for two devices, where $d_{\mathrm{Alq_3}} = 60\,\mathrm{nm}$, $d_{\text{OXD-7}} = 47\,\mathrm{nm}$ and $d_{\mathrm{Ir(ppy)_2(acac)}} = 57\,\mathrm{nm}$. Of course, this also has a direct influence on C_{ETL}, which does not align as well as in measurement and the correction could as well have been done by accepting different GSP for simulation. Besides the problematic in reproducing the exact giant surface potential, the position of the V_{inj} peak in the spectra can be replicated qualitatively by large-gap semiconductors in simulation. This is in line with the situation of the CBP/OXD-7 device, in which both layers show high optical gaps. A more detailed study on that feature of the spectra is presented in Section 3.3. As a summary of the above investigation,

the simulations allow to reproduce most of the parameters gained by the experiment. The exact value of the giant surface potential or sheet charge density in simulation, however, seems to systematically differ from the measured or calculated values.

3.2.3. Calculation of the interface charge for multiple polar layers

Up to now, investigations specifically on the GSP have been done mostly on systems with only one polar layer, typically with a polar ETL and a non-polar HTL [1, 2]. Herein, both layers are polar, and both layers' polarity and orientation has to be considered independently. To extend the formalism introduced in the previous section to systems with two polar layers of different net dipole moment, two assumptions are made:

a) both layers' GSP are independent of each other to the extent that both polar layers' charge does not affect the magnitude of the giant surface potential of the other layer

b) the charge density or GSP of the top layer (ETL) is larger than the GSP of the bottom layer (HTL).

If those assumptions apply to the device, the change in electrical field at the interface between polar HTL and ETL can be treated as the sum of both individual contributions [12] and it is possible to relate the measured transition voltage of the device with two polar layers to the surface charge densities of both layers with

$$V_{\mathrm{tr}} = \frac{\sigma_{\mathrm{HTL}} d_{\mathrm{HTL}}}{\varepsilon_0 \varepsilon_{\mathrm{HTL}}} + \frac{\sigma_{\mathrm{ETL}} d_{\mathrm{ETL}}}{\varepsilon_0 \varepsilon_{\mathrm{ETL}}} + V_{\mathrm{bi}} \ . \tag{3.8}$$

Note that the surface potential of the HTL is defined positive at the interface of HTL and ETL. Also, the second requirement, $|\sigma_{\mathrm{HTL}}| < |\sigma_{\mathrm{ETL}}|$ is visible as an experimental constraint from this equation. If $|\sigma_{\mathrm{HTL}}| > |\sigma_{\mathrm{ETL}}|$, the transition voltage is expected to be higher than the built-in voltage V_{bi} and it would therefore be invisible and superimposed by increasing injection in the device. An example with four measurements on OLEDs with varied GSP in the HTL is shown in Figure 3.8. In this case, the HTL doping was changed from 0 % or pure NPB to 20 % of Alq_3 in NPB with pure Alq_3 on top. Here, the benefit of extracting the transition from the onset is also visible: For the highest doping ratio, the transition voltage is already positive but still more than 1 V away from V_{inj}. The inflection point would be affected by the electron injection, if it shifts by only 0.5 V.

If the surface potential of the top layer (ETL) is known as σ_{ETL}, the bottom layer's GSP is given by

$$\sigma_{\mathrm{HTL}} = \left(V_{\mathrm{tr}} - \frac{\sigma_{\mathrm{ETL}} d_{\mathrm{ETL}}}{\varepsilon_0 \varepsilon_{\mathrm{ETL}}} - V_{\mathrm{bi}} \right) \frac{\varepsilon_0 \varepsilon_{\mathrm{HTL}}}{d_{\mathrm{HTL}}} \ . \tag{3.9}$$

Again, the knowledge of the dielectric constants and exact thicknesses of the layers can be avoided, if area and capacitance are known. According to Equation 3.4, it is

$$\sigma_{\mathrm{HTL}} = \left(V_{\mathrm{tr}} - \frac{\sigma_{\mathrm{ETL}} A}{C_{\mathrm{ETL}}} - V_{\mathrm{bi}} \right) \frac{C_{\mathrm{HTL}}}{A} \ . \tag{3.10}$$

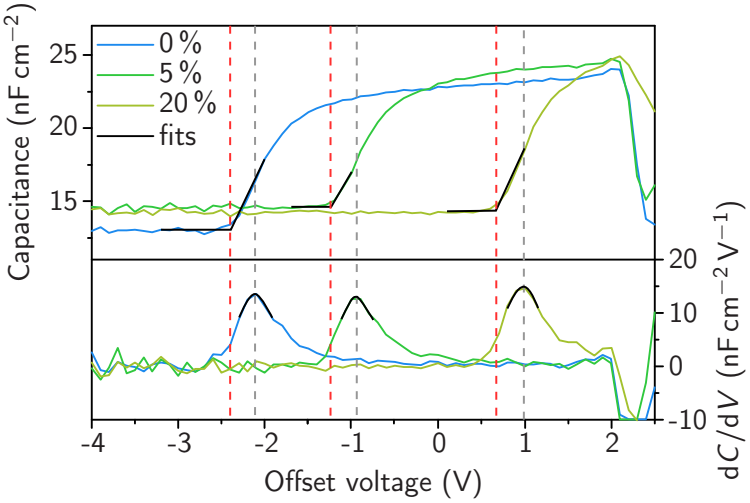

Figure 3.8.: A series of CV-measurements on doped NPB/Alq diodes. The transition voltages scales with the doping ratio and hence the GSP, where it is the lowest for no HTL doping. The top part shows the evaluation of the onset of $C(V)$ for V_{tr}, the bottom part is the 1$^{\mathrm{st}}$ derivative evaluated with a Gaussian peak-fit to get the inflection point. Vertical lines exist as a guide to the eye to show the position of the extracted points, where red is linked to the onset and gray relates to the inflection point.

Unfortunately, no direct relationship of doping density and GSP exists to date for any material combination. Hence, σ_{HTL} cannot be calculated without the knowledge of σ_{ETL}. However, if in a series of samples with doped HTL, a sample with non-polar HTL is produced with the same processing conditions, σ_{HTL} and hence the GSP of the doped layer can be gained by combining Equation 3.9 and Equation 3.5 to

$$\sigma_{\mathrm{HTL}} = \left(V_{\mathrm{tr,X}} - V_{\mathrm{tr,0\%}}\right) \frac{\varepsilon_{\mathrm{HTL}}\varepsilon_0}{d_{\mathrm{HTL}}} = \left(V_{\mathrm{tr,X}} - V_{\mathrm{tr,0\%}}\right) \frac{C_{\mathrm{HTL}}}{A} \ . \tag{3.11}$$

Here, $V_{\mathrm{tr,X}}$ is the transition voltage for the doped samples and $V_{\mathrm{tr,0\%}}$ the value in case of undoped HTL. Of course, assumption a) at the beginning of the section – the absence of any interference between the two potentials – is mandatory for this calculation. Most importantly, however, the built-in field does not have to be known.

3.2.4. Impedance of OLEDs with dipolar doped HTL

The extraction of the GSP of doped ETL OLEDs via impedance spectroscopy has already been published elsewhere [2]. Also, pure and doped single-layers can be investigated via Kelvin probe. However, no attempt was so far made to measure the GSP of both HTL and ETL in an OLED with two polar layers. With the framework given in Section 3.2.3, the magnitude of the giant surface potential and the amount of interface charges will be calculated from bilayer, double-polar OLEDs. Measured data and results on the system NPB:Alq_3 will be discussed in Section 3.2.5.

Similar to the case of unpolar HTL like already suggested in Section 3.2.3, different routes exist to calculate the GSP or interface charge density of the HTL from $C(V)$ measurements. Here, both layers equally affect the position of the transition voltage

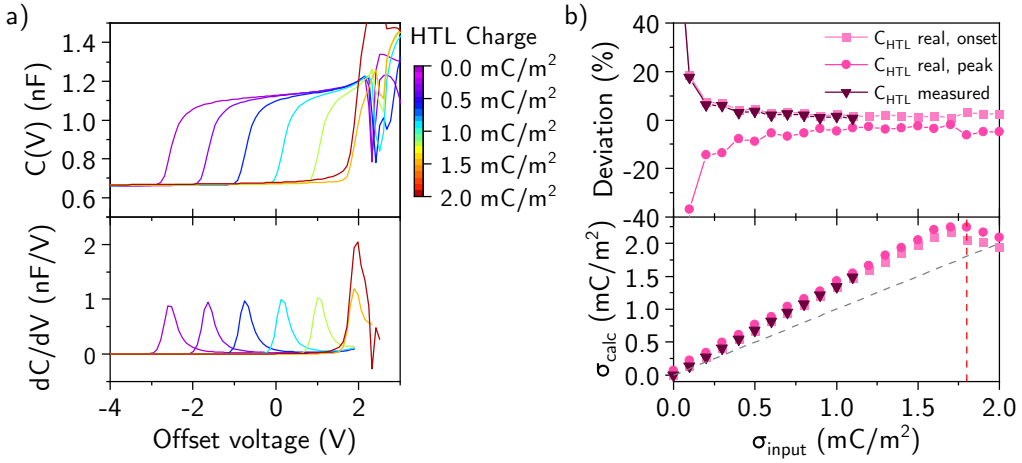

Figure 3.9.: **a)** Simulated impedance for an OLED with polar HTL, where the GSP of the HTL was varied up to a point larger than that of the ETL. Shown are the spectra itself, as well as their first derivative (bottom). **b) Top** Deviation from the average extracted interface charge depending on the method used to determine V_{tr}. **b) Bottom** Absolute, calculated interface charge with respect to the input charge density. Dark purple triangles indicate calculations made with C_{HTL} extracted from the spectra, in contrast to the (known) value put into simulation. The gray line indicates the one-to-one relation for exact extraction. The red vertical line shows the value of σ_{ETL}.

and to directly calculate the interface charge of one layer, the value of the other needs to be known. Again, either dielectric constants and thickness, or capacitance and area also have to be determined. The capacitance of both layers can be extracted from the total geometric capacitance and C_{ETL} when measured accurately. However, the error in determining both adds up to the calculation of C_{HTL}. In the end, the determination of the sheet charge density of the HTL requires known capacitance and dielectric constants following Equation 3.9 or Equation 3.10. For calculating the GSP of the doped HTL alone, however, a different route exists, if the same set of samples includes one without a polarity in the HTL with otherwise same properties of the ETL. Then, the HTL GSP is given by the difference of V_{tr} for doped and undoped cases, with the only additional parameter being the HTL thickness.

To assess the possible error of those routes for calculating the HTL sheet charge density, simulated data with varied HTL giant surface potential can be evaluated. For this purpose, the same device structure as used in Section 3.2.2 to show the frequency dependence has been calculated with $\sigma_{ETL} = 1.8\,\mathrm{mC\,m^{-2}}$ and σ_{HTL} varied from $0.0\,\mathrm{mC\,m^{-2}}$ to $2.0\,\mathrm{mC\,m^{-2}}$. A selection of the simulated spectra and the extracted data is shown in Figure 3.9a. In the graph, also the first derivative is given to compare different methods to determine the transition voltage, alongside with the evaluation of different errors. The calculated values of σ all show a constant overestimation by a factor of approximately 1.3, which can either be an error in the model or a systematic error in the method to extract the magnitude of the GSP or interface charge density. This question and the validity of the parameter extraction will also be tested on measured data in Section 3.2.5. For the sake of comparing possible sources for errors,

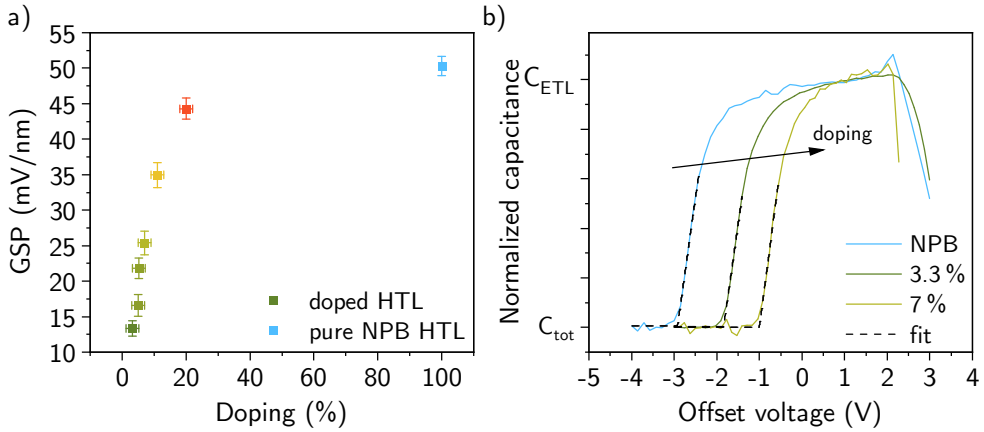

Figure 3.10.: a) GSP of the doped HTL in NPB:Alq_3/Alq_3 OLEDs calculated from $C(V)$ measurements. The coloring additionally illustrates the doping ratio. The data was calculated using the transition voltage difference approach, as described in the previous section. Note that, strictly speaking, a HTL with 100 % of Alq_3 doping is not possible, the value of an undoped Alq_3 ETL in a standard NPB/Alq_3 OLEDs is given as a guide to the eye in light blue. **b)** Three example $C(V)$ measurements normalized to both C_{tot} and C_{ETL} to emphasize the difference observed in V_{tr} upon doping. The extraction of the onset is done with the linear fits shown in dashed black.

the relative error from the average extracted interface charge density is considered, which differs only slightly. For both methods of determining V_{tr}, the largest difference from the average is observed for small input charge densities. The onset approach expectantly yields larger values, considering the inflection point always follows the onset in voltage. Both methods, however, seem to produce similar results for higher GSP. When all necessary parameters are precisely known and only V_{tr} has to be determined from the capacitance-voltage characteristics, the HTL GSP can thus be calculated up to the point where $\sigma_{HTL} \approx \sigma_{ETL}$, as indicated in Figure 3.9b with a red dashed line. In real world conditions, however, the calculation will fail much earlier. Also in simulated data, the determination of C_{ETL} for example is not possible with $\sigma_{HTL} > 1.1\,\mathrm{mC\,m^{-2}}$, because neither V_{tr} nor the plateau for C_{ETL} can be determined successfully in this case. The respective datapoints therefore end at this value in Figure 3.9b.

3.2.5. Impedance spectroscopy on polar HTL NPB:Alq_3 devices

To experimentally investigate a polar HTL device, samples were fabricated with a stack of ITO/NPB:$Alq_3(x)$/Alq_3/Ca/Al. The ITO substrates had to be either plasma-cleaned or treated with UV/O_3 for about one hour to yield samples without short circuits. The doping ratio was varied between 2 % and 20 % with the ratio being given in volume percent as calculated during evaporation. Most samples were cross-checked ex-situ with profilometry and while the exact thickness varies with an error of 2 nm to 5 nm, the doping ratio matches well with the individual thicknesses

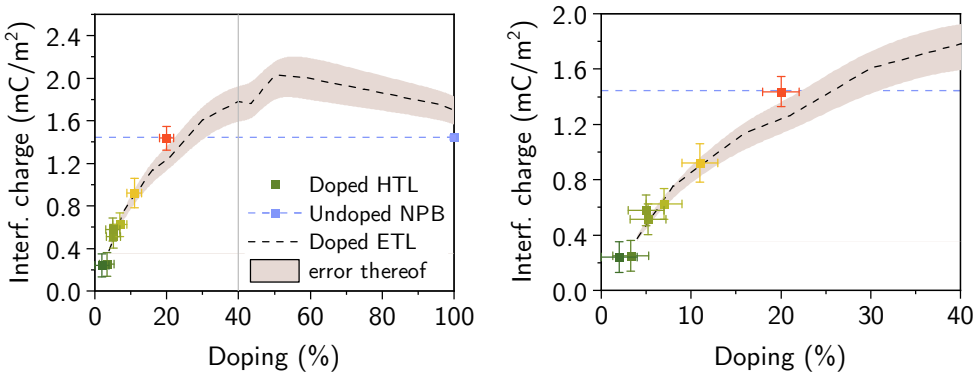

Figure 3.11.: Extracted interface charge density of the hole transport layer in dipolar doped OLEDs. The coloring additionally follows the doping ratio. For comparison, the densities for doped ETL obtained from ref. [2] is plotted in the same graph. The value of a pure Alq_3 ETL is given as a guide to the eye in light blue. On the right, the same plot is enlarged up to a maximum doping ratio of 40 %.

of NPB and Alq_3. However, not all samples allowed to independently distinguish the amount of evaporated NPB and Alq_3 as required to re-calculate the doping ratio, the ratio given is therefore always the nominal value.

In Figure 3.10, the extracted magnitudes of the GSP for doped HTL are shown, alongside with three exemplary impedance spectra. The data is calculated using the transition-voltage difference approach with the value of V_{tr} of an undoped HTL as reference. Thus, only the thickness of the hole transport layer is needed as additional parameter. For comparison, the equivalent GSP of the ETL extracted from a device with pure NPB HTL is shown in blue as the imaginary value of 100 % of doping. Of course, a device with both HTL and ETL made from neat-film Alq_3 cannot be measured, the term "100 %" doping can therefore be misleading. The extracted data follows the expected form, similar to what is seen in Kelvin probe measurements, where the GSP rises very fast for low to moderate doping ratios, almost approaching the neat-film value with only 20 % of doping. Unfortunately, as elaborated in the previous section, this also marks the approximate highest possible doping ratio suitable for investigation with impedance spectroscopy, since V_{tr} will be hidden by V_{bi} and no accumulation is experimentally observable. One possible way to remediate this issue would be to combine doped NPB:Alq_3 HTL with an ETL of even higher GSP, like observed for OXD-7. This, however, was not attempted within the scope of this work.

Besides the magnitude of the GSP, the amount of interface charges can be calculated using different measurement quantities. The result of this calculation is drawn in Figure 3.11, this time in direct comparison to the interface charge density for doped ETL. The reference taken from Jäger *et al.* [2] is plotted with a dashed line, the measurement error being underlain with a gray area. Except the measurement at 20 %, which differs slightly, the calculated densities for doped HTL match the values for doped ETL within error. In case of high doping, however, the transition voltage is already close to V_{inj} and therefore also close to the limit of maximum possible

interface charge to be determined. It is likely, that the relative error calculated from the quality of the fit to determine V_{tr} underestimates the actual error.

The good agreement of both datasets also allows to answer the open question of Section 3.2.4, on whether the observed multiplicative error in the extracted interface charge density is due to the simulation parameters or the method of calculating σ itself. Because no simple multiplicative error is visible here, the observed deviation in simulated impedance spectra seems to stem from erroneous parameters in the drift-diffusion model. The physical theory on the additive nature of the GSP is proven to be valid.

Further discussion of the data presented, in conjunction with the Kelvin probe results, follows in Section 3.4.2.

3.3. On the built-in voltage in polar OLEDs

In order to calculate the magnitude of the GSP from impedance measurements, the built-in field or voltage has to be known. As shortly noted already in Section 3.2.1, the onset of electron injection is visible from the measured capacitance-voltage graph. Previously, the position of this peak and hence V_{inj} was set equal to the built-in voltage V_{bi} [13, 90]. Besides the extraction from the injection peak, the thickness dependence of the transition voltage can be used to extract the built-in voltage by fitting Equation 3.6 to the measured data. In this section, the visibility of the built-in field in the signal will be evaluated by comparing all available experimental data, followed by simulations of impedance spectra.

3.3.1. Experimental methods to extract the built-in voltage from impedance

To compare both methods, namely extracting V_{bi} from the injection peak (V_{inj}) or fitting a ETL-thickness variation, three sets of samples with different hole injection layers can be taken into consideration. All samples were manufactured for various purposes over a time span of 4 years, measurements took place right after manufacturing but were re-evaluated again to extract the necessary information. All selected samples had the stack of ITO/<HIL>/NPB/$\mathrm{Alq_3}(x)$/Ca/Al, where the thickness of $\mathrm{Alq_3}$ is the thickness to be varied to extract V_{bi}. The NPB thickness is not important in this case as the GSP of NPB is considered small enough not to change the transition voltage outside the normal range of error, which has also been reported previously [90]. The HIL layer for the series is chosen to be either HIL1.3 or AI4083, whereas the third set of samples is processed directly on ITO. Single measurements are also available with the low-resistance PEDOT:PSS CH8000. ITO had to be plasma treated or left in UV/$\mathrm{O_3}$ cleaning for more than one hour in order to reduce defects at the ITO edge to a minimum. Otherwise, no successful electrical measurement is possible due to high leakage currents or short circuits. This is the case throughout all samples processed directly on ITO and is especially important for the expected workfunction of the anode. See Section 3.1.1 for a discussion on different anode workfunctions. The transition voltage V_{tr} is extracted from capacitance-voltage measurements conducted at different frequencies. As the transition from non-accumulated to the accumulated regime is also frequency depen-

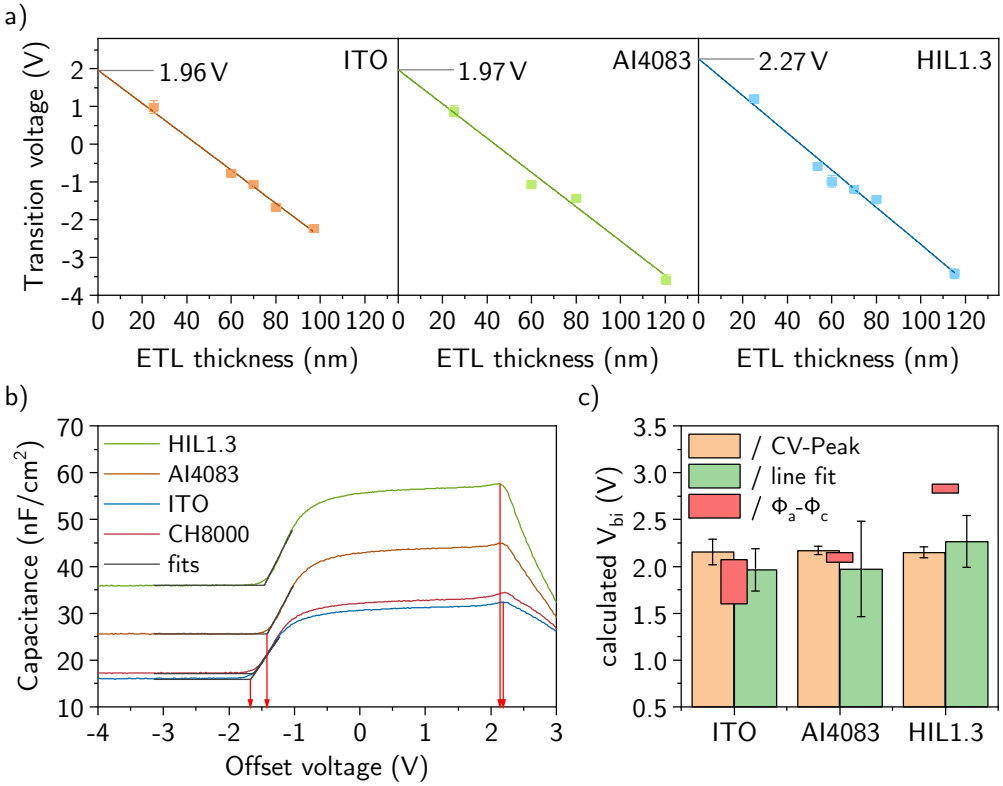

Figure 3.12.: Comparison of two methods for evaluation of the built-in field. **a)** Linear extrapolation of multiple individual measurements of V_{tr} from NPB/Alq_3 OLEDs with varying ETL thickness on three different anode materials. The error in thickness is obtained analogous to the Kelvin probe experiments, the voltage error is gained from averaging over all available diodes. **b)** Example $C(V)$ measurements to show the extraction of V_{inj} and V_{tr} for different anode materials. **c)** Extracted built-in voltages from onset (line-fit, a)) and peak-position (CV-peak, b)) in comparison with an estimate of possible built-in fields calculated from the electrode workfunctions ($\Phi_a - \Phi_c$). For the latter, the reference for ITO covers a large range, as its workfunction varies strongly with processing conditions. All values are also summarized in Table 3.4.

dent, this is expected to add to the overall systematic error. Also, the Alq_3 thickness was not always checked ex-situ by dedicated profilometry measurements, the error in thickness is hence also to be considered.

Values for V_{tr} are gained from the onset of the transition by the fit already described in Section 3.2.1. Subsequently, samples of same nominal thickness for the Alq_3 layer are averaged. The second method, extracting the peak position just before bipolar injection into the device, is not possible in an automated manner and is hence done graphically. For all three anode materials, available data and respective fits are shown in Figure 3.12a. Because of the huge timespan between the different samples, many systematic errors are expected to be seen that are otherwise hidden, if a set of samples is manufactured in short succession. Especially, any change in material quality or

Anode	Φ_a	Built-in voltage (V) V_{bi}	V_{inj}	$\Phi_a - \Phi_c$
HIL1.3	5.70 ± 0.04	2.27 ± 0.27	2.15 ± 0.06	2.88
AI4083	4.97 ± 0.04	1.97 ± 0.51	2.17 ± 0.04	2.15
ITO[1)]	4.98 ± 0.04	1.96 ± 0.23	2.15 ± 0.14	2.07

Table 3.4.: Results in calculating the built-in voltage from fitting $V_{tr}(d)$, the peak-fit in V_{inj} or the nominal, calculated built-in from the electrode workfunctions. 1) The ITO value refers to the plasma-cleaned surface. In case of a non-plasma cleaned surface, the workfunction is lower.

likewise degradation would increase the error when averaging over multiple samples of the same thickness, as would changing processing conditions or the accuracy of the thickness itself. Still, individual datapoints align very well at a straight line and the relative error gained from averaging multiple measurements is also small. The results of the evaluation are drawn in Figure 3.12c in the series labeled line-fit.

In Figure 3.12b, an example $C(V)$ measurement is shown, with the evaluation for V_{tr} and V_{inj} illustrated. The transition voltage differs by almost 500 mV between different anode materials. As the organic layers for all four samples have been processed simultaneously, the difference in V_{tr} can stem from either erroneous thicknesses or different built-in voltages. In fact, the characteristics are offset in vertical direction, which could indicate an error in thickness and thus d_{ETL}. However, because the usual uncertainty for simultaneously processed organic layers amounts to roughly 5 % in the evaporation chamber used to manufacture the devices, the vertical offsets observed here between different hole injection layers are unlikely to stem from the thickness error. Instead, both samples with an anode of high lateral resistance, i.e. the additionally shown CH8000 PEDOT:PSS derivative and ITO with no additional conducting polymer layer stretching between anode and cathode, show a much lower capacitance compared to HIL1.3 and AI4083. A high lateral conductance, however, can affect the impedance measurement and lead to higher measured capacitances by effectively increasing the measured sample area [241]. It can therefore be concluded that the high difference in transition voltage as seen in Figure 3.12b is also not rooted in a strong difference in thickness, but must be dependent on the built-in field.

In comparison, the peak-positions for V_{inj} are invariant of the anode material, which already indicates that V_{inj} is probably not directly linked to V_{bi} alone. The assumption is confirmed by comparing V_{bi} obtained from the line-fit according to Equation 3.6 and the peak position of V_{inj} as seen in Figure 3.12c. For further comparison, the measured workfunctions for each substrate given in Table 3.1 are combined with the workfunction of Calcium of 2.87 eV [257] to calculate the respective nominal built-in voltages. This calculation, alongside with the measured values, is given in Table 3.4. Although the built-in field cannot directly be inferred from the simple workfunction difference, some correlation would be expected. Considering that ITO was plasma treated, its workfunction is very similar to that of AI4083 PEDOT:PSS. HIL1.3, however, is higher by $\approx$0.7 eV, and is therefore expected to yield a higher built-in voltage than the other two. Indeed, V_{bi} extracted from Equation 3.6 for both ITO and AI4083 is similar, whereas the value for HIL1.3 is higher by 300 meV. In contrast, V_{inj} is almost constant for all anode materials with an

average value of 2.16 V. The chosen method to obtain V_{bi} from $C(V)$ measurements thus has a direct effect on the calculated GSP as it affects the GSP linearly (see e.g. Equation 3.4).

3.3.2. Simulated impedance spectra to extract the built-in field

To allow for a better understanding of the processes in the device, a set of impedance spectra is simulated in which the built-in field is swept by varying either the cathode or the anode workfunction. Additionally, the internal hole and electron barriers are varied by alternating HOMO and LUMO levels of Alq_3 and NPB, respectively. Preset parameters for the simulation are the sheet charge density of $1.9\,\mathrm{mC\,m^{-2}}$, the HOMO level of the HTL of 5.51 eV and the LUMO level of the ETL with 2.55 eV. The electrode workfunctions are calculated relative to these values, where the default anode barrier is 400 meV, resulting in an anode workfunction of 5.11 eV. For the cathode, it is 350 meV with $\Phi_c = 2.9\,\mathrm{eV}$. The results are summarized in Figure 3.13. In the third simulation the ETL gap is varied, while the other parameters are adjusted in a way that the injection barriers are not affected by the change of the ETL gap.

Directly visible from comparing varied anode and cathode barriers is that the change of the anode barrier does affect the position of the transition voltage shown in Figure 3.13a. The change in cathode barrier has no direct influence on V_{tr}, see Figure 3.13b. The peak position of maximum capacitance at V_{inj}, however, is mostly influenced by the position of the cathode workfunction or electron barrier, which is seen in Figure 3.13b. Note, that solving the drift-diffusion equations for voltages high above the injection is difficult, if not performed in steady state but in the impedance small perturbation regime. The large numerical error results in erroneous calculation of capacitances, leading to the high visible "noise" in the simulated spectra. Additionally, all barriers simulated here have to be kept within the outer-most energy levels of the organic layers, that is, the constellation of a nominal workfunction of 5.7 eV as observed for HIL1.3 and an HTL HOMO-level of 5.5 eV is impossible in simulation. It is known, that those "negative" barriers neither exist in real devices, but the barrier will approach a minimum of a few 100 meV instead [72]. Still, the built-in field influenced by the contact workfunctions can be altered even though no reduction in anode barrier is possible.

If the evaluation is restricted to the workfunctions of the contacts, the electron barrier on the ETL side is the only parameter affecting V_{inj}. It is worth noting, however, that the position of the peak of V_{inj} in simulation could also be shifted by altering the overall gap of the ETL, as seen in Figure 3.13c. The shift, however, was restricted to a certain range of parameters. An ETL gap resulting in a "negative" internal barrier between HTL and ETL HOMO, where the ETL HOMO is lower than the HTL counterpart, did not result in any visual accumulation and a very weak peak at V_{inj}, only. On the other hand, gaps leading to internal barriers greater than 0.5 eV did not cause any change in V_{inj} but instead kept it at a constant value. Besides, the peak at V_{inj}, from a simulation point of view, seems to resemble the point of flat-band conditions of the ETL rather than the built-in field alone. This can be depicted by plotting the simulated potential profile throughout the device for different external voltages, as seen in Figure 3.13d. The plot contains data for the minimum and maximum values for the gap as seen in impedance in Figure 3.13c, with 3.0 eV and 3.3 eV, respectively. In the first case, at the peak in $C(V)$ $V_{inj} \approx 2.45\,\mathrm{V}$, however,

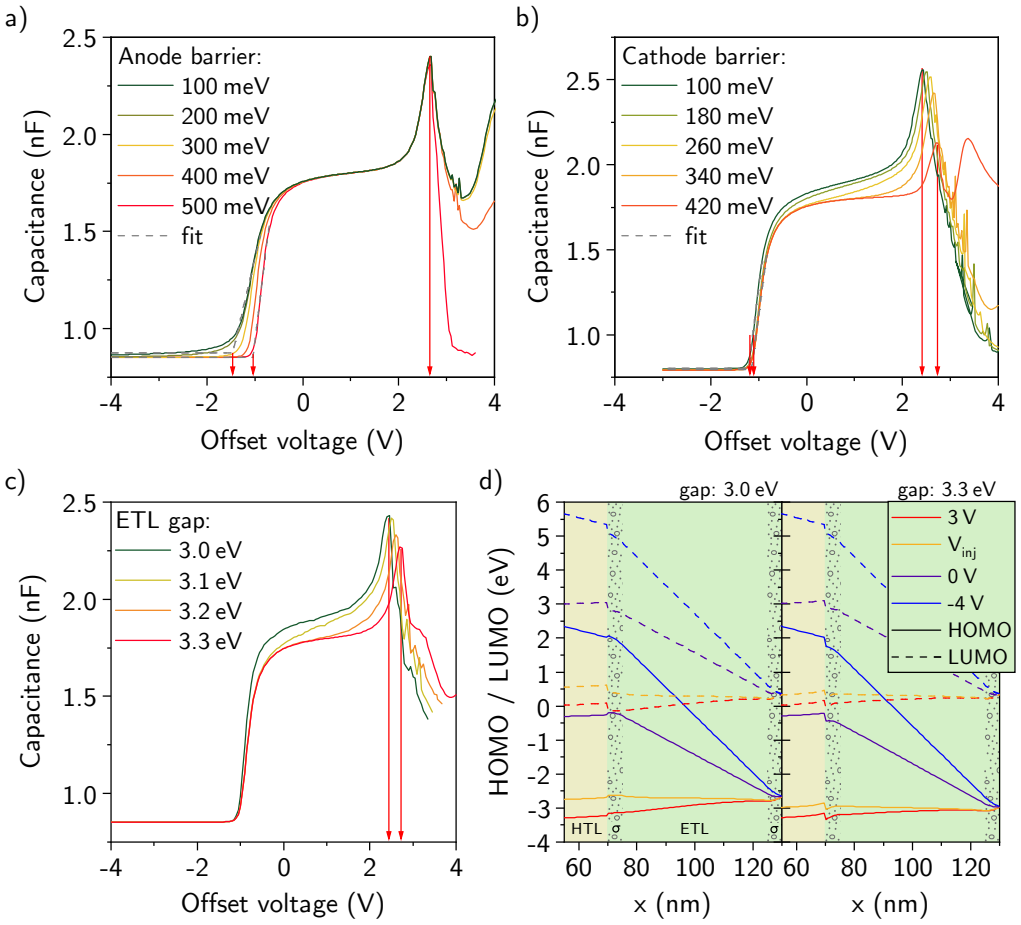

Figure 3.13.: Sets of simulated impedance spectra with different varied parameters for a device with a sheet charge density of nominally 1.9 mC m^{-2}. The HTL has a thickness of 70 nm, the ETL is 60 nm in total, including 5 nm sheet charge layers. Varied parameters are **a)** the anode barrier, by altering the anode workfunction, **b)** the cathode barrier, by varying the cathode workfunction, please note the different y-scale in this plot and **c)** the ETL gap, while keeping other parameters, especially the cathode workfunction, the same. **d)** Shows the position of HOMO and LUMO in the device for an ETL with different gap below and above its injection voltage V_{inj}. HTL and ETL are color-coded yellow and green, respectively; the shaded area depicts the presence of the interface charges in simulation. Here, $V_{\mathrm{inj}} \approx 2.45$ V for the device with an ETL gap of 3.0 eV (left), and approx. 2.7 V for the other (right).

for a gap of 3.3 eV, it is at around 2.7 V. The dark yellow lines in Figure 3.13d show the position of HOMO and LUMO throughout the device at this voltage and in both cases, this means flat-band for the ETL layer. Further profiles at applied voltages of −4 V, 0 V and 3 V are given for reference. These flat band conditions also should be dependent on the field induced by the interface charges and indeed, though not shown here, a dependence of V_{inj} on the GSP can be simulated for high gap devices.

In an ideal single layer device without GSP, interface dipoles or any pinning in effect, the flat band condition should occur at $V_{\mathrm{bi}} = \Phi_{\mathrm{a}} - \Phi_{\mathrm{c}}$. For a multilayer device with a giant surface potential, however, the situation is different to the extent that the accessible transition voltage at V_{tr} is affected by the contact potential difference, whereas the visible peak at ETL flatband does not resemble that change. Unless a definition of V_{tr} independent of the anode workfunction is possible, e.g. by fitting the point where the device reaches C_{ETL} in measurement, the relation $V_{\mathrm{bi}} := V_{\mathrm{inj}}$ should be treated with caution. Extracting V_{bi} from the slope of a thickness variation of the ETL is more realistic.

3.4. Conclusive evaluation of different methods

In the following sections, both, data obtained via Kelvin probe and Impedance Spectroscopy will be evaluated and compared. For further evaluation of the transport properties in doped hole transport layers, special focus is lain on the reproducibility and stability of extracted parameters and methods. Additionally, the degree of orientation polarization is calculated for all measured systems.

3.4.1. Undoped polar organic semiconductors

The giant surface potentials for the polar species Alq_3, OXD-7 and $Ir(ppy)_2(acac)$ could be measured with both Kelvin probe and impedance spectroscopy. Additionally, the nominally unpolar materials NPB and CBP as well as the polar 1295 have been investigated by Kelvin probe, only. A summary of all measured GSP with both methods is given in Table 3.5, together with literature data, where available. A graphical summary is presented in Figure 3.14. Measured data is given with the PDMs calculated in-house, reference data with dipoles from literature, the literature values of the dipole moments can be found in Table 3.2. Specific features of the Kelvin probe measurements alone, including the existence of an inverse GSP for 1295 and CBP, have already been discussed in Section 3.1.2. When comparing data obtained by Kelvin probe and impedance spectroscopy to literature data, both values of Alq_3 lie within the error, although the error especially for KP data is considerably high. For OXD-7, the KP result lies between the two literature values, but is larger than the literature value for the same method. However, literature data exist for a different measurement method than KP as well. Noguchi *et al.* published 87 mV nm^{-1} for displacement current measurements (DCM) [12]. This technique also relies on the change in capacitive response upon carrier accumulation and might be better suited to compare to impedance spectroscopy. The published sheet charge density is still lower than what has been obtained in the scope of this work, but lies within the large error for impedance measurements on OXD-7. In contrast, the same reference lists a GSP of 34 mV nm^{-1} for Alq_3 obtained by DCM, which is lower

Name	GSP (mV nm^{-1})			
	lit. KP	lit. DCM	KP	IS
Alq_3	44.0 ± 7.8	34	32.7 ± 2.8	47.4 ± 1.4
OXD-7	68	87	77.9 ± 2.5	98.3 ± 16.0
$Ir(ppy)_2(acac)$	38	– –	54.9 ± 1.1	124 ± 34
NPB	5.3 ± 0.1	– –	1.12 ± 0.15	– –
CBP	0.7	−6.5	−1.95 ± 0.16	– –
1295	– –	– –	−51.7 ± 11.0	– –

Table 3.5.: Measured an literature data for the GSP and calculated data for the single molecule dipole moment. For sources of the respective values see text or Table 2.1. Data for displacement current measurements (DCM) comparable to IS from ref. [12].

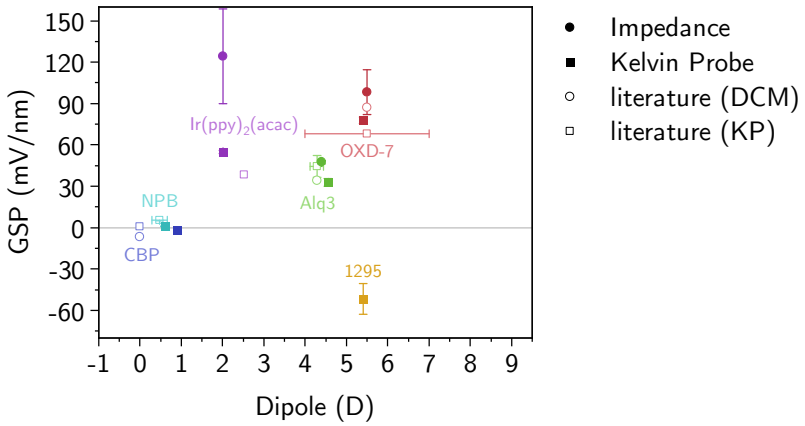

Figure 3.14.: Comparison of the measurements shown so far with literature data in the plotting scheme from ref. [6]. For sources of the literature data, see Section 3.1.2. Literature data is given in hollow symbols, data obtained by Kelvin probe series with filled squares and the data calculated from impedance spectroscopy in filled circles. In the graph, some error bars were omitted for increased readability.

than the data obtained by KP in the same publication [12]. For $Ir(ppy)_2(acac)$, both measurement methods presented exceed the literature data considerably, which is emphasized in Figure 3.14, where measurements and reference data of all materials but $Ir(ppy)_2(acac)$ lie in close vicinity to each other. Also, all values for the GSP obtained by IS are larger than the Kelvin probe counterparts.

Considering the various sources for measurement errors in both techniques and DCM as well, differences of 5 mV nm^{-1} to 10 mV nm^{-1} between different methods and laboratories are to be expected. A systematic over- or underestimation of the value by one or the other technique is also very well possible – the huge difference seen for $Ir(ppy)_2(acac)$, however, is not. It rather has to be considered that the processing parameters for both experiments are different, in fact, samples for Kelvin probe or impedance spectroscopy had to be manufactured in different vacuum chambers. To date, no single defining factor could be identified, however, a few additional

experiments allow to shed some light on the topic. At first, complete OLEDs were manufactured in both chambers, where the active layers processed in the Kelvin probe chamber had to be transferred to a different one to complete the cathode layers. This was replicated also for the second chamber, normally used for IS samples, that could in theory process the cathode without vacuum break. The extracted GSP of these samples resembles the same difference like the data presented here, albeit being measured with IS, only. From this point of view, the processing conditions in the KP-chamber are identified as the culprit, whereas the measurement technique does not play a role.

Additionally, it is known that light irradiation can destroy the GSP, as does ionic emission from the ion gauges needed for vacuum pressure monitoring [10, 253, 258]. These influences have been checked without avail. Blocking light shining into the chamber through the view ports did not change the GSP. Also, direct illumination with a blue LED could not change the GSP considerably, although the illuminated samples do show a slightly lower interface charge. Additionally, switching off any ion gauges did not change V_{tr} at all in impedance. At last, the temperature in the chamber used for IS has been monitored by applying a thermocouple to the device during evaporation. It has been found that the sample heats up by almost 10 °C during processing with the biggest heat input being the handling of the sample itself, chamber illumination and in the end the evaporation of the cathode metal layer. The evaporation of the organic layers did not provoke a big change in temperature. However, the thermocouple was applied to the backside of the sample and thus the thermal input to the layer itself could have been higher without being detected.

A temperature variation was then attempted in the Kelvin probe chamber, too, where the sample temperature can be precisely controlled via LN_2 cooling and electrical heating. The experiment was done with doped layers of 30 % OXD-7 in CBP, which, when processed at a temperature of −80 °C, exhibit a GSP of 111.8 mV nm^{-1} compared to 90.4 mV nm^{-1} when prepared at room temperature. The series alongside with data is available in the appendix in Section A.3. To fully elucidate the reason for the different GSP in both chambers more data and experiments are needed. Understanding the difference in preparation conditions between the two vacuum chambers would also help to further understand the mechanisms behind the orientation polarization.

3.4.2. GSP and degree of orientation polarization of dipolar doped hole transport layers

A short preview on the comparison between doped ETL and HTL GSP was already given in Section 3.2.5, where values of the interface charges of both, doped HTL and ETL, were comparable. This emphasizes the additive nature of the two layers' GSP that has also been predicted by Noguchi *et al.* in 2012 [12] and is the foundation for the theory behind the measurements. In simulation, however, a multiplicative error was found for the extracted GSP in comparison to the input interface charge density, see Section 3.2.4. So far, this has not been investigated further and remains an open issue. It could indicate, though, that the modeling of the GSP in simulation is not invariant to the adjacent charges between HTL and ETL. Also, the built-in voltage V_{bi}, used to extract the GSP, has been determined only once for an undoped HTL. It is known that the GSP can change the injection behavior of carriers into the

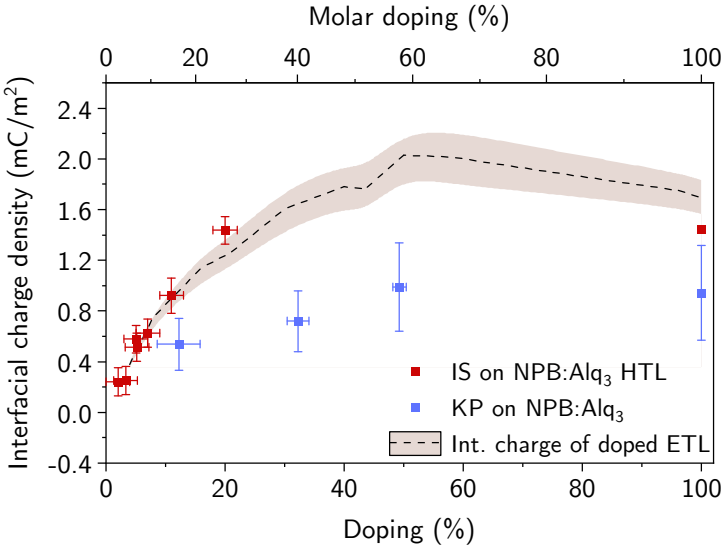

Figure 3.15.: Obtained interfacial charge density for doped NPB:Alq_3 HTL via IS (red), calculated equivalent values for the GSP obtained from KP (blue) and the data published by Jäger *et al.* in ref. [2] for doped ETL (dashed line). The top scale is given in the molar doping ratio calculated für an NPB:Alq_3 mixture as described in Section 2.2.1.

semiconductor [3, 11], which will also be discussed in detail in Chapter 6. Although no implicit influence of the GSP on the barrier has been included in the model, it is possible that the effective built-in field changes, which would lead to a falsely extracted giant surface potential.

For further discussion, experimentally obtained values of the GSP obtained using Kelvin probe are converted into sheet charge densities. To transfer the measured sheet charge density to a GSP in units of the electrical field and vice versa, the dielectric constant of the semiconductor has to be known. For Alq_3, the calculation of the interface charge density and the GSP can be done independently, as both necessary measurements are available with suitable accuracy. From the combination of both, the dielectric constant of neat Alq_3 can be calculated to $\varepsilon_{100\%} = 3.240 \pm 0.147$. The same is possible for each doping concentration, which in average also amounts to $\varepsilon = 3.2 \pm 1.0$. With exceptions, the individual dielectric constants rise with doping ratio, starting from (2.1 ± 1.1) for 3 % reaching (3.240 ± 0.147) % for neat Alq_3 in this case. Although a calculation of the dielectric constant for mixtures should be possible with an effective medium or similar approach [259], the dielectric for neat NPB was not determined within this work and thus no comparison is possible. Additionally, it has already been shown that the GSP in both measurements is different, the calculated dielectric constant will also resemble this error. Noguchi *et al.* published values of 3.3 and 3.2 for NPB and Alq_3, respectively [12], which is still in very good agreement of the general average. However, lower dielectric constants for low doping ratios would not be expected, but could be a result of the mismatch between the two preparation chambers for the samples for KP and IS. The interface charge density in Figure 3.15 was hence calculated using the average value of $\varepsilon_{Alq_3} = 3.2 \pm 1.0$.

Both datasets, interface charge density obtained from impedance spectroscopy on doped NPB:Alq_3 HTL and calculated data from the GSP measured by Kelvin probe on doped single layers are combined in Figure 3.15. The comparably high error for the data calculated from Kelvin probe mainly stems from the error in the dielectric constant of roughly 30 %. Similar to the situation for neat Alq_3 films, the charge densities for doped layers are also considerably lower in KP measurements and the absolute difference is larger for ratios approaching the 1:1 mixture. Also, the maximum usually observed for around 50 % of doping is less pronounced for KP data, although it might be more distinctively visible, if the dielectric constant for different doping ratios could have been determined accurately. Nevertheless, the principal trend is the same: The highest GSP or sheet charge density is observed for almost 1:1 mixtures, at least, if the volume percentage of doping is concerned, which is the case until now.

In order to further evaluate the orientation mechanism behind the maximum in the polarization the second material system CBP:OXD-7 was studied in details as well. To allow for a better comparison of the material systems concerning their normalized electrical alignment parameter Λ [2, 48], a transfer to molar doping ratio is needed to allow for comparison between NPB:Alq_3 and CBP:OXD-7 mixtures as described in Section 2.2.1. Parameters necessary for the conversion for Alq_3 are $M_{Alq_3} = 459.43\,\mathrm{g/mol}$ and $\rho_{Alq_3} = 1.31\,\mathrm{g/cm}$ [201], for NPB it is $M_{NPB} = 588.74\,\mathrm{g/mol}$ and $\rho_{NPB} = 1.19\,\mathrm{g/cm^3}$ [201]. For the CBP:OXD-7 mixture, the values to calculate the molar ratio are $M_{CBP} = 484.59\,\mathrm{g/mol}$ and $\rho_{CBP} = 1.18\,\mathrm{g/cm^3}$ [201], as well as $M_{OXD\text{-}7} = 478.58\,\mathrm{g/mol}$ and $\rho_{OXD\text{-}7} = 1.13\,\mathrm{g/cm^3}$ [87]. The top scale in Figure 3.15 is already given in molar ratio. In this scale, the maximum in interface charge density for the NPB:Alq_3 mixture shifts to almost 60 %. To calculate the alignment parameter as described in Section 1.1.7, both, density ρ and molar mass M of the dopant molecule are required, alongside its dipole moment p. Then,

$$\Lambda = \frac{\sigma_{x\%}}{\sigma_{max}} = \frac{\sigma_{x\%} \cdot p\rho N_A}{M} \,, \tag{3.12}$$

where $\sigma_{x\%}$ is the measured sheet charge density and σ_{max} the maximum possible value assuming perfect alignment. The dipole moments are $p_{Alq_3} = 4.6\,\mathrm{D}$ and $p_{OXD\text{-}7} = (5.40 \pm 1.35)\,\mathrm{D}$. In the latter case, three energetically very similar conformations exist, the weighted average based on a Boltzmann statistic yields the given average and standard deviation. Calculated alignment parameters for both mixtures are shown in Figure 3.17, Alq_3 on the left and OXD-7 on the right. Additionally, for Alq_3, the alignment parameter calculated from the interface charge density published by Jäger *et al.* [2] is included in the graph. The resulting alignment hence differs from what has been published in the article, as the parameters and the route to calculate the maximum alignment is different: Jaeger *et al.* have not used density and molar mass to calculate the molecular volume, it was instead estimated from crystallographic single crystal data. For Alq_3, the alignment of molecules in the doped HTL obtained from impedance spectroscopy coincides very well with that of the ETL, which is expected as both were calculated the same way and the sheet charge densities were comparable. Kelvin probe data is again lower and differs by a rough factor of two, whereas the general trend is similar.

In case of OXD-7, despite a larger GSP, the orientation measured with Kelvin probe seems to perfectly resemble the Alq_3 counterpart measured with IS, with only

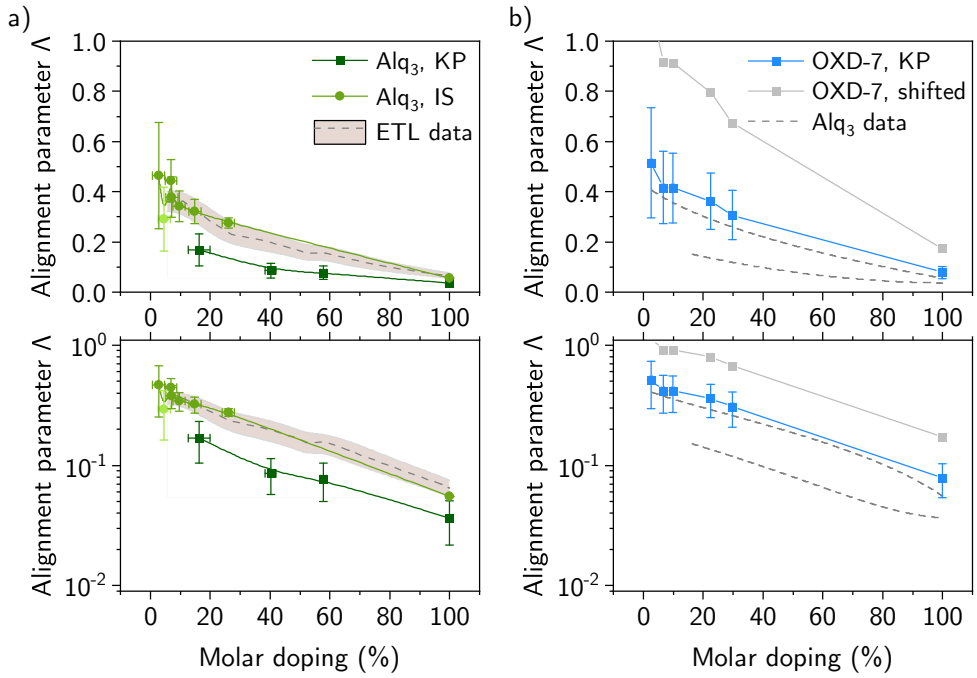

Figure 3.16.: Alignment factors in both linear and logarithmic scale. **a)** Alignment factor Λ for NPB:Alq_3 HTL obtained from impedance spectroscopy (light green, round), calculated of the GSP measured via Kelvin probe (dark green, squares) and the data published by Jäger *et al.* in ref. [2] for doped ETL. The latter has been calculated with the same parameters as the measurements conducted for this work, only the interface charge density is taken from the reference. **b)** Data for CBP:OXD-7 measured with Kelvin probe series (blue, round). Alq_3-data are included as a guide to the eye (dashed lines), as well as estimated OXD-7 dataset with the same difference as Alq_3 KP to IS (gray, squares).

a small offset. Note that, however, the calculated alignment of OXD-7 is based on a measured dielectric constant of 2.9 [12] to transfer the GSP to an interface charge density. Together with the uncertainty gained from averaging the dipole moment over all three conformations, the overall error in alignment factor is large for small doping ratios. To put the apparently equal trend in alignment between Alq_3 and OXD-7 in perspective, it has to be considered that OXD-7 data was only available in detail from samples produced in one chamber, the one, where Alq_3 shows considerably lower orientation. Assuming that the alignment of OXD-7 for different processing conditions, e.g. in the chamber used for samples tailored for impedance spectroscopy, would exhibit the same difference as observed for Alq_{3KP} and Alq_{3IS}, the OXD-7 alignment would have to be scaled by a factor of approximately 2.2. The calculated datapoints are included in Figure 3.17 with a dashed line. For low doping ratios, the values exceed 100 %. As this is impossible, the disadvantageous conditions leading to lower alignment in the chamber used for Kelvin probe measurements appear to be different for each molecule. Although the overall dynamic range is small, both materials seem to follow the same trend that can be described with an exponential

Material	p (D)	ρ (g/mol)	M (mol/m³)	ε	σ_{calc} (mC/m²)	σ_{max} (mC/m²)	Λ (%)
CBP	0.0	1.18	484.59	2.7	−0.05	−4.40	1.1
NPB	0.6	1.19	588.74	3.3	0.03	2.44	1.3
Alq_3	4.55	1.31	459.444	3.2	0.93	26.06	3.6
OXD-7	5.40	1.1	478.599	2.9	2.00	24.93	8.0
1295	5.4	1.324	934	3	−1.37	−15.38	8.9
$Ir(ppy)_2(acac)$	2.01	1.508	599.7	3	1.46	10.10	14.4

Table 3.6.: Alignment factors (far right column) calculated for all neat film Kelvin probe series measured during this work. All parameters except the measured GSP (see Table 3.5) are given. Errors are omitted here, as the range is far too large due to the uncertainties in dielectric constant, dipole moment and measured GSP.

law. From this point of view, exponential growth kinetics seem to overrule dipole-dipole interactions that scale with the inverse distance of dopant molecules and thus the concentration.

Although no further doping variation has been attempted, the alignment factor can also be calculated for those molecules measured in neat film. As those measurements have been conducted with Kelvin probe only, the dielectric constant is needed to calculate the alignment parameters. They have been taken from literature where available and for $Ir(ppy)_2(acac)$ and 1295 it was assumed to be $\varepsilon = 3$. The calculated alignment factors together with all necessary parameters are given in Table 3.6, the GSP is taken from Kelvin probe measurements with data available in Table 3.5. In this table, data is sorted with ascending alignment and the alignment parameter Λ is given in percent for convenience. The Iridium complex $Ir(ppy)_2(acac)$ is the by far highest oriented molecule, although the alignment calculated here from Kelvin probe is still far lower than the reference measured with impedance spectroscopy, which we have published earlier in ref. [48]. However, the samples measured for this publication were manufactured in the chamber normally used for IS experiments, resulting into an interface charge of approximately $3.3\,\mathrm{mC\,m^{-2}}$, with almost 30 % of alignment in neat film. The same fact has already been identified as the reason for lower alignment for Alq_3 also seen in this work. As briefly noted in Section 2.1.2, the batch of 1295 available for KP series was a mixture with above 95 % of the meridional isomer with a dipole moment of the given 5.4 D. The exact composition of the remaining 5 % is not known, however. Facial 1295 has a dipole moment of 8.6 D [91], other variants of the molecule with different ligands also differ in magnitude and direction of the PDM on the molecule, the calculated alignment factor therefore might contain a larger error.

When grouped by the hypothetical maximum in sheet charge density σ_{max}, three sets of molecules can be identified. One group is populated by the two iridium complexes 1295 and $Ir(ppy)_2(acac)$ with a maximum interface charge of $10\,\mathrm{mC\,m^{-2}}$ to $15\,\mathrm{mC\,m^{-2}}$, albeit of course 1295 is oriented in reverse. The second consists of Alq_3 and OXD-7, both with the almost doubled maximum sheet charge density, though their alignment differs significantly in this experiment. Usually non-polar materials CBP and NPB form the third group, with hypothetical charge densities

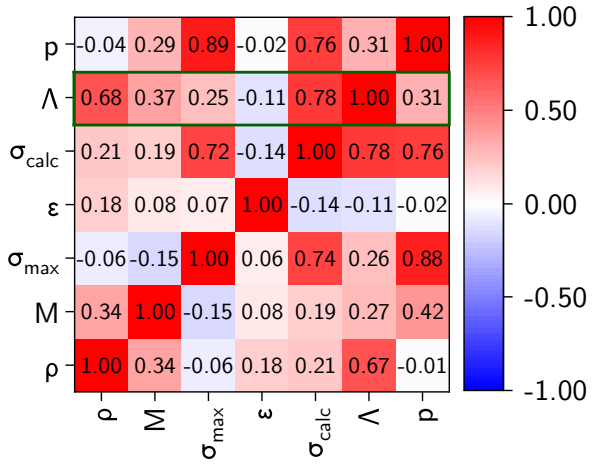

Figure 3.17.: Correlation matrix calculated for Table 3.6. Higher positive values mean direct linear, negative indirect linear correlation.

below $5\,\mathrm{mC\,m^{-2}}$, both having an almost identical alignment of roughly 1 %. The first two groups all show alignment factors of 4 % to 14 %, which is in range of what was reported so far [2, 48]. Also, the two Iridium complexes are highest oriented in this study, which is not surprising as both also show high orientation of their transition dipole moments [48,91]. In comparison, judging from the refractive indices published e.g. by Mayr *et al.* in 2015 [260], none of the other molecules investigated show considerable optical orientation, as this would lead to birefringence in the thin film [261]. This emphasizes a unique feature of the two electrical methods compared to optical investigation, as a preferred molecular orientation is detectable for all materials.

From this dataset, a Pearson correlation matrix was calculated, visible in Figure 3.17. Although the dataset does not include all measurements available and any measurement error was omitted for simplicity, the alignment coefficient seems to correlate with only two parameters significantly. Also, processing parameters such as vacuum pressure, purity and temperature were not included. Hereby, higher alignment seems to be reached with high density and, less surprisingly, high measured interface charge. Both correlations can be a hint to missing parameters as both parameters directly affect the calculation of Λ itself in a linear manor. Still, the dipole moment p does not seem to correlate with the alignment factor, which is in line with simulations by Friederich *et al.* [47] and Moon *et al.* [262]. In short, a high dipole moment and the resulting strong dipole-dipole interaction counteract a high parallel alignment of the PDMs.

4. The effect of interface charges on photoluminescence quenching

The following chapter deals with the observation of interface charges in a polar OLED by studying their effect on *photoluminescence* (PL) quenching. All data was already published elsewhere [263]. Samples were produced and PL quenching measurements conducted by Thomas Ferschke from the University of Würzburg. Impedance data and drift-diffusion simulations were measured and calculated by me. The experiment nicely demonstrates the validity of the model to simulate polar organic devices and allows a direct correlation of simulated and measured data besides the electrical quantities studied before. With this technique, charge carrier densities and the presence of a sheet charge at the NPB/Alq_3 interface could be probed at a working device by utilizing the fluorescent dye dibenzo-tetraphenyl-periflanthene (DBP) [264, 265] as absorber and sensing layer, which has also been successfully applied as donor in organic photovoltaic cells [50, 171, 266]. In the following, the initial experiment and findings by our colleagues in Würzburg will be shortly summarized. Afterwards, my impedance measurements on the same devices, as well as the drift-diffusion simulations will be discussed. Note that, besides the simulated data and electrical measurements, also measured PL quenching data is sometimes re-evaluated and fitted by myself, some of the values presented below can therefore differ slightly from the figures given in the publication.

4.1. Initial problem description

The sample structure consists of a standard NPB/Alq_3 OLED, where a thin layer with a thickness in the range of a few nanometers within the Alq_3 layer is doped with DBP in concentrations below 0.1 % in volume. A schematic layer stack is shown in Figure 4.1. The doping concentration is chosen as such that the signal to noise ratio in PL is large enough, but no change in bulk properties of the Alq_3 host is expected. After all, it is at least a factor of ten lower than what was used for dipolar doping in the previous sections. DBP features a broad absorption in the red to green wavelength range [171] and can hence be selectively excited with a 532 nm pump laser, where the Alq_3 and NPB extinction coefficients are already low [263]. Additionally, DBP PL emission is mostly orange with a tail to the far-red regime, whereas Alq_3 emits in the green with a peak at around 530 nm. This spectral separation allows to distinguish the guest luminescence from the host emission. An overlap of host emission and guest absorption, however, allows for a so-called *Förster resonant energy transfer* (FRET) and will have to be considered for high electric driving voltages [263]. In order to discuss and simulate the effect of the sheet charge on the PL quenching at low to moderate voltages, however, it might be neglected for now.

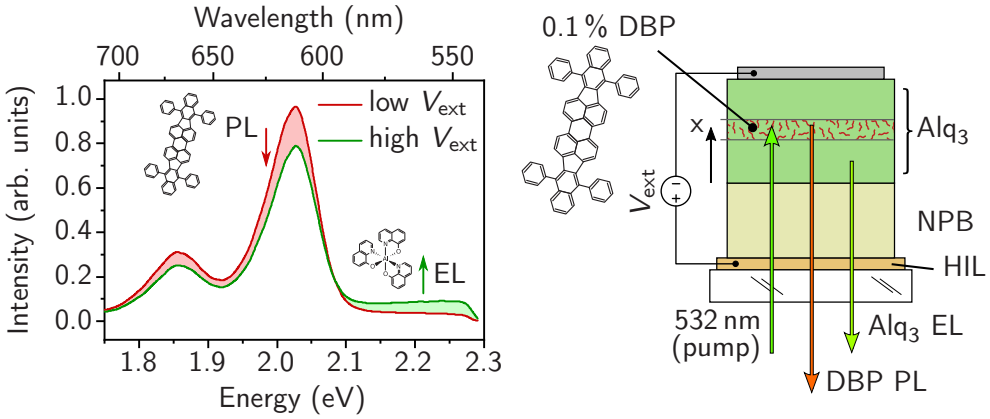

Figure 4.1.: Observation of photoluminescence quenching for NPB:Alq_3 devices with a thin layer doped with the fluorescent dye DBP. At low external bias (e.g. $V_{ext} = 0\,V$), the red PL intensity pumped with a 532 nm laser is high compared to the green Alq_3 electroluminescence. At high external bias, the PL vanishes, whereas EL is observed. The experiment at the University of Würzburg that led to these findings is sketched on the right, as well as the Lewis structure of dibenzo-tetraphenyl-periflanthene (DBP).

In the said devices, the DBP dye acts as a molecular sensor or sensing layer, which stems from the fact that the dynamics of photo-active materials are influenced by local variations of charge carrier density or electric field [267]. Accordingly, variations in the photoluminescence of the guest molecule can be a measure for changes in, e.g., local current or charge carrier density. Interesting in conjunction with the phenomenon of SOP or the existence of any GSP in polar organic layers, is the possibility to vary the position of the sensing layer within the Alq_3 host. Here, this position is indicated by the distance x relative to the NPB/Alq_3 interface, thus higher values move the layer towards the cathode. To allow for comparison between different positions and driving voltages V_{ext}, a quenching parameter Q is introduced to describe the change in photoluminescence as

$$Q\left(V_{ext}, x\right) = 1 - \frac{I_{PL}\left(V_{ext}, x\right)}{I_{PL}\left(0\,V, x\right)}\ , \tag{4.1}$$

where $I_{PL}\left(V_{ext}, x\right)$ is the PL intensity with applied external voltage at a sensing layer position x. Q is calculated with respect to the PL intensity with otherwise same parameters but at zero external bias, $I_{PL}\left(0\,V, x\right)$. With that definition, a positive Q corresponds to a decrease in photoluminescence and thus increasing quenching, whereas negative values indicate impaired quenching. PL intensities are calculated by integrating over the spectral range of DBP between 2.12 eV and 1.81 eV (585 nm and 685 nm) [263]. Unfortunately, a small overlap exists in Alq_3 and DBP emission, which is compensated for by subtracting a reference measurement performed without optically pumping and hence without optical excitation of the DBP guest [263].

Figure 4.2 plots the measurements made by Thomas Ferschke at the University of Würzburg, showing the quenching parameter for different positions of the sensing layer ($x = [0, 5, 45, 85]$ nm) for reverse and forward bias. In this device, the Alq_3 layer was 100 nm in total, with 40 nm of NPB underneath. Overall, devices with

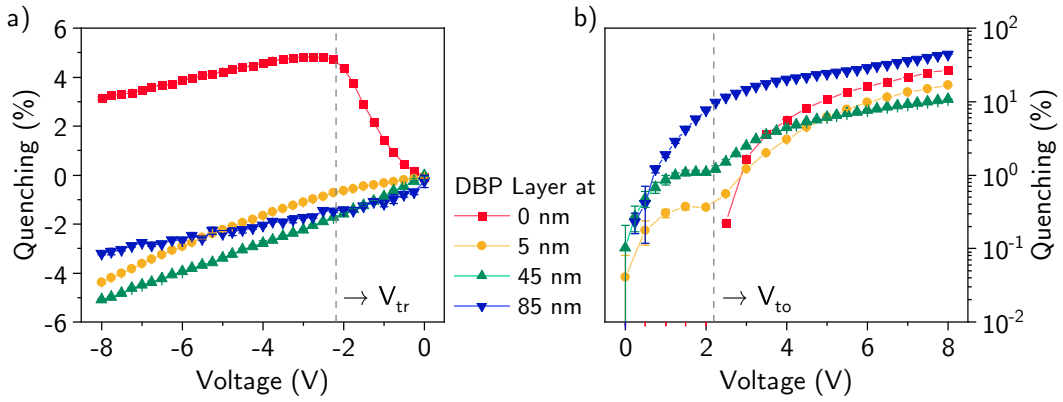

Figure 4.2.: Calculated PL quenching parameters for **a)** reverse and **b)** forward bias. Note the different scales in both graphs. While the reverse bias quenching stays within ±10 %, forward bias quenching spans two orders of magnitude. In forward bias, it is positive except for values at 0 nm below 2 V, which are thus not visible in the logarithmic scale. The possible positions of the two characteristic voltages for a polar OLED, V_{tr} and its turn-on voltage V_{to} are marked with a vertical line. Relative errors are calculated by averaging forward and backward sweep of the measurement. The device shown has a NPB layer thickness of 40 nm and a total thickness of Alq_3 of 100 nm.

three different Alq_3 thicknesses have been measured by our colleagues [263], where those with 80 nm and 120 nm are not shown here. Even without the gray eye guides in the figures, similarities in the voltage characteristics of the quenching parameter in Figure 4.2 and the electrical measurement shown later on in Figure 4.3 become clear. In forward bias shown in Figure 4.2b, the most pronounced feature for configurations with $x = [0, 5, 45]$ nm appears at the same position at roughly 2.0 V to 2.2 V, where Q rises steeply afterwards. However, also below that voltage, the signal is subject to some change, especially if the DBP layer is located away from the interfaces within the Alq_3 layer. In case of a sensing layer directly at the cathode interface (blue curve), only a change in slope is observed. Still the overall PL is already reduced by more than 10 % below the turn-on voltage V_{to}, which indicates a high electron density close to the cathode. With the sensing layer directly at the NPB/Alq_3 interface, small negative quenching parameters are gained for voltages below 2 V, they are thus not visible in the logarithmic scale. As the signal is extremely weak, it cannot be ruled out that the negative sign is caused by a measurement error. Thus, no conclusions on the physical meaning will be drawn.

In reverse bias, only the device with the sensing layer directly at the NPB/Alq_3 interface but still in Alq_3 (red line) exhibits a change in slope of the PL quenching parameter. All other samples are only subject to reduced quenching with increasingly negative external bias, while the slope is roughly the same for all measurements, including the case with $x = 0$ nm for voltages smaller than V_{tr}. It appears, though, that the process below −2.2 V is the same for all devices, whereas the increasing quenching above is linked to the vicinity of the sensing layer to the NPB/Alq_3 interface.

For further elaboration of the findings and different quenching mechanisms, imped-

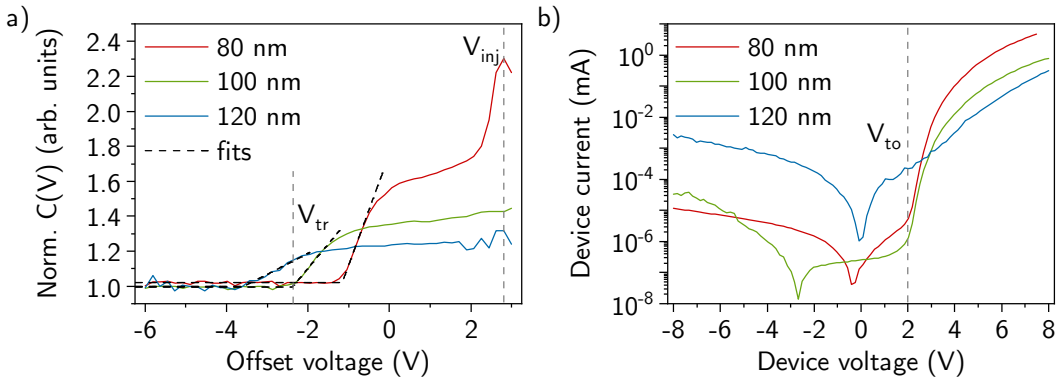

Figure 4.3.: a) Capacitance-voltage data for all three Alq_3 thicknesses investigated. Capacitances were normalized to the total capacitance for ease of comparison. Linear fits to extract V_{tr} are also shown. **b)** Current-voltage characteristics of the same devices and pixels. EL data is not shown in this case. In both graphs, characteristic quantities are marked with dashed lines.

ance spectroscopy and characteristics measured by myself in our laboratory shall be concerned. These devices do not include the sensing layer, but are otherwise identical in stack and architecture. Measurements of impedance (capacitance-voltage) and standard device characteristics are shown in Figure 4.3 for all three different Alq_3 thicknesses investigated. The big difference in thickness complicates direct comparison because of large differences in capacitance, the data was hence normalized on the total geometric capacitance. Characteristics shown here miss the EL data, as a measurement of the electroluminescence was not possible in our lab because of large differences in sample design. Two features of both, the impedance spectra and the characteristics are striking. At first, the accumulation transition voltage V_{tr} at around $-2.2\,V$ for the 100 nm device corresponds nicely to the reduction in PL quenching at the NPB/Alq_3 interface in reverse bias. Secondly, in forward bias, the large increase in quenching appears at roughly 2 V. In the characteristics, this corresponds to the turn-on voltage V_{to}. It is thus evident that the PL quenching of DBP is strongly linked to the charge carrier concentrations in the device.

At the beginning of the study, discussions lead to four quenching mechanisms that could be considered for the DBP doped NPB:Alq_3 device. A detailed evaluation is found in our publication in ref. [263], a brief summary can be given as follows:

1) The DBP radical anion can exhibit a **shift in absorption** when capturing quasi-free carriers from the Alq_3 host, which would reduce the PL intensity as the excitation wavelength stays the same.

2) A spin-exchange **singlet to triplet conversion** [268] would reduce the PL of the S_1 excited state, as the triplet T_1 is a only weakly phosphorescent state with long lifetime. The singlet state in turn is short lived with $\tau \approx 10^{-9}$ s [263].

3) So-called **field-assisted exciton dissociation** could be discussed as it has been previously reported for dye doped Alq_3 layers [269]. Due to the high exciton binding energy seen in organic semiconductors (see Section 1.1.2), the fields required for dissociation are in the range of $10^6\,V\,cm^{-1}$ to $10^7\,V\,cm^{-1}$ or

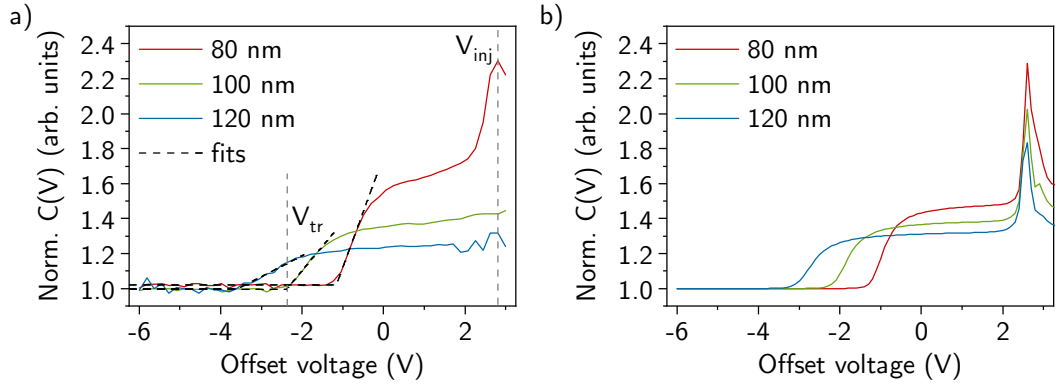

Figure 4.4.: a) Measured and **b)** simulated impedance spectra, both again normalized to the geometric capacitance. The difference in relative ETL capacitance can stem from errors in ETL thickness or discrepancies in ε and σ. The important fit parameters here, however, are the transition voltages and the injection peak.

$10^2\,\mathrm{mV\,nm^{-1}}$ to $10^3\,\mathrm{mV\,nm^{-1}}$. Thus, it will only play a role for higher external biases.

4) As a potential fourth process, a **Förster resonant energy transfer from exited DBP** to the Alq_3 anion might be possible. Although very weak, the negative Alq_3 ion does show absorption at around 2 eV [270].

To disentangle different contributions to quenching in forward and reverse bias, the devices were therefore re-created *in-silico* and drift-diffusion simulations were performed to calculate the carrier densities at various external parameters.

4.2. Drift-diffusion simulation of carrier densities

In simulation, the devices are calculated without any representation of the DBP dopants. This is, in fact, a valid assumption, as a doping density of 0.1 % is chosen deliberately to minimize effects on carrier transport in the device. An as small as possible impact on the overall device performance is also an important requirement for the molecular sensing approach [263].

Simulations were performed in steady state to mimic conditions during quenching measurements as well as in AC mode to calculate impedance spectra. The simulated capacitance voltage data for all three Alq_3 thicknesses is given in Figure 4.4 in direct comparison to the measured data. Main parameters for the simulation were the energy levels to represent V_{inj}, as well as the combination of change in relative thickness and V_{tr}. The discrepancy of C_{ETL} in relation to C_{geo} can be rooted in sub-optimal choice of the dielectric constant or errors in HTL thickness. However, transition voltages and V_{inj} match nicely, which should allow to inspect calculated charge carrier densities for the same simulated devices. Another attempt to further optimize the simulations was thus not made. Figure 4.5 shows calculated carrier density maps through the device at varied external bias for electrons and holes, as well as selected profiles in correlation with the measured photoluminescence quenching.

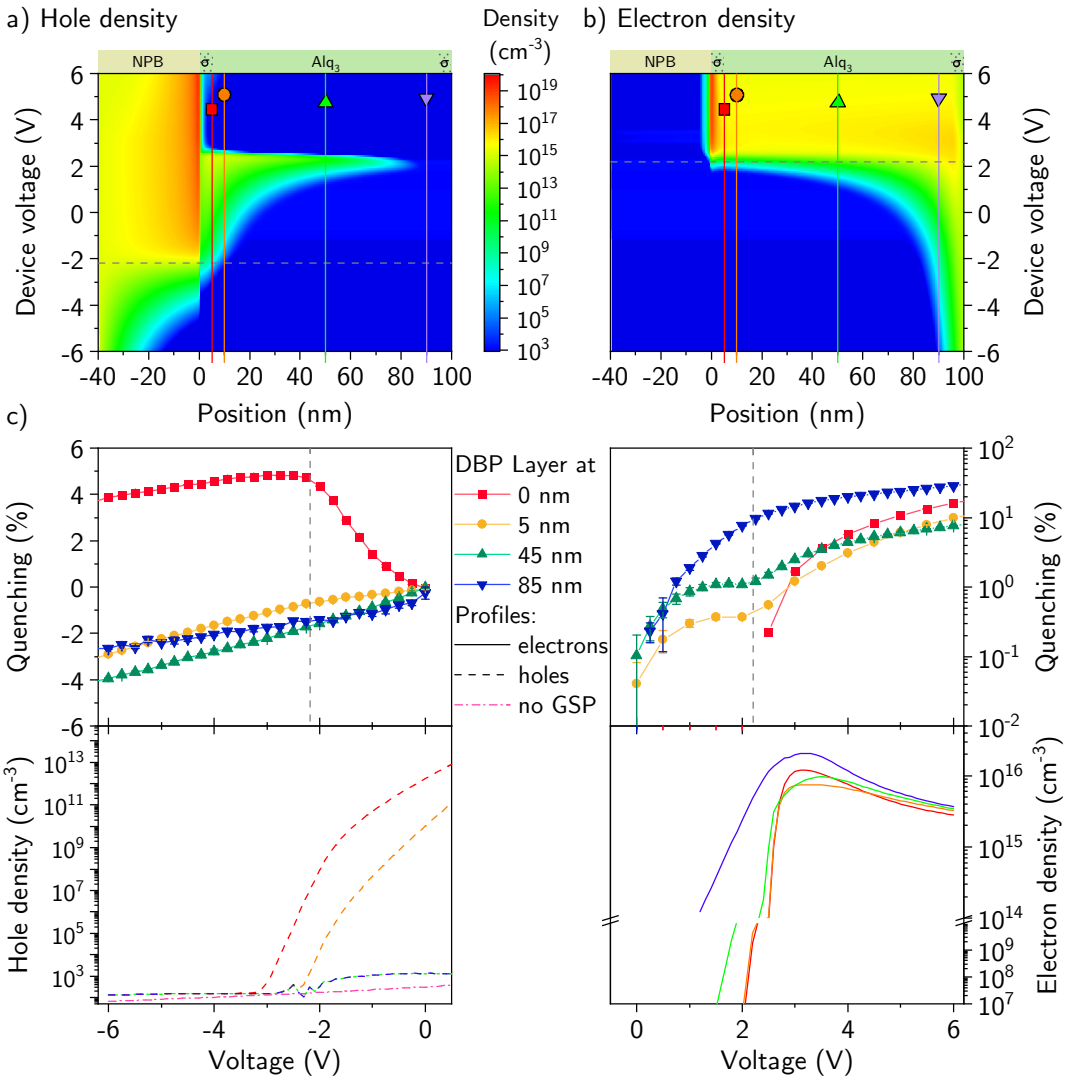

Figure 4.5.: **a)** False color maps of the density of holes and **b)** electrons given in cm^{-3}, each in dependence on position and external bias. Horizontal lines mark V_{tr} and V_{to}, vertical lines the position of evaluation for the single thickness profiles (colors indicated in symbols match to the graphs below). **c) left** plots the PL quenching measured on the diode with 100 nm Alq$_3$ in relation to extracted profiles of hole density in the middle of the sensing layer. Additionally, hole densities for a hypothetical non-polar Alq$_3$ are given in purple (same for all positions). Forward bias quenching is given in **c) right** with electron density profiles.

The line profiles were examined in the middle of the virtual sensing layer with a width of 10 nm, a position of $x = 0$ nm is thus extracted at 5 nm in the density map. The respective positions are marked in the density map with vertical lines.

At first, the case of positive bias will be discussed, shown in Figure 4.5 on the right. The major change observed in the PL quenching experiments, which occurs at roughly $V_{\mathrm{to}} = 2.2\,\mathrm{V}$, coincides with the onset of electron injection into the Alq_3 layer, quickly flooding the device with electrons to reasonable densities above $10^{15}\,\mathrm{cm}^{-3}$. For a moderate voltage range between 2 V to 5 V, the change in PL quenching then correlates with the change in electron density. This is also true for the relative amplitudes of electron density and PL quenching in this voltage range, suggesting the reduction in PL intensity to be directly related to the carrier density. In case of devices with $x = [0, 5, 45]$ nm, the electron density in simulation is extremely low with $10^{10}\,\mathrm{cm}^{-3}$, at least below the turn on voltage. To put that into perspective, the density of states in the device in simulation was set to $N_0 = 1.5 \times 10^{21}\,\mathrm{cm}^{-3}$; areas with densities of around $10^{10}\,\mathrm{cm}^{-3}$ and below can therefore be considered almost electron free. Still, devices with sensing layers at $x = 5$ nm and $x = 45$ nm show a clear signal in PL quenching even below V_{to}, indicating the presence of mobile charges in the device [263]. This demonstrates the sensitivity of the molecular sensing in this configuration, where the PL intensity can detect changes in carrier density eight orders of magnitude below normal device operation.

Close to the cathode located at 100 nm, the electron density is more than two orders of magnitude higher than in the bulk of the device, especially below the nominal turn on voltage, partly because of the good injection properties of polar organic layers [3, 11]. The PL of the DBP probe directly at the cathode therefore suffers from significant loss of more than 10 % at $V_{\mathrm{ext}} \leq V_{\mathrm{to}}$. Above a voltage of ≈5.5 V, the initially neglected direct energy transfer from the excited Alq_3 matrix molecules to the DBP dopant has increasing influence on the density of DBP exited states besides the absorption of the optical pump laser. This will lead to an overestimation of the electroluminescent contribution to the spectra and thus the intensity correction mentioned earlier is no longer valid. In the end, the quenching in presence of higher current densities is probably over estimated [263], a correlation with pure carrier densities is thus not possible in this case. Overall, it can be concluded that the luminescence quenching in forward bias at moderate voltages is caused by an interaction between the negatively charged species of Alq_3 and the DBP exciton.

On the left of Figure 4.5c, the reverse bias PL quenching is shown in relation to the hole density in the device. In this voltage regime, the electron densities are far below the detection range to allow for a similar explanation. All quenching processes related to injected charge carriers can therefore be ruled out. This is especially true for devices with $x = [5, 45, 85]$ nm, where in contrast to quenching an increase in PL intensity (negative Q) is observed. The effect can be attributed to detrapping from shallow trap states, which is caused by the applied field gradient, a discussion can be found in our publication [263]. Also, this finding is in theory expected to be present for all devices in reverse bias. In case of $x = 0$ nm, however, with the sensing layer in direct contact with the NPB/Alq_3 interface, PL quenching is still observed with a maximum of almost 5 %, before the expected increase in photoluminescent intensity is again visible at $V < -2.2\,\mathrm{V}$ with the same slope. This effect can be explained by the existence of an interface charge only present in polar organic layers like Alq_3.

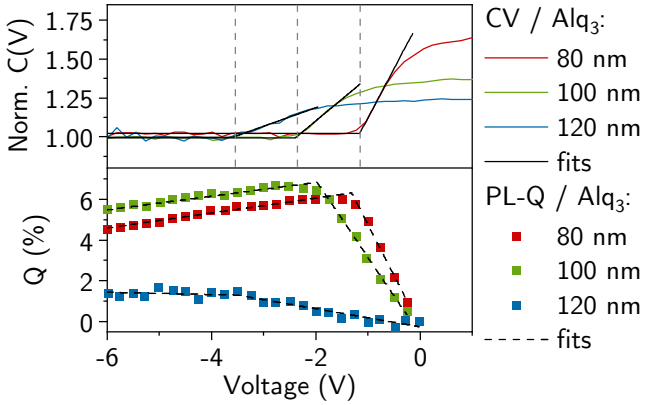

d_{Alq_3} (nm)	V_{CV} (V)	V_{PL} (V)
80	-1.15 ± 0.02	-1.31 ± 0.02
100	-2.39 ± 0.02	-1.97 ± 0.03
120	-3.58 ± 0.12	-3.51 ± 0.29

Figure 4.6.: Top: Measured impedance spectra for all three thicknesses together with PL quenching measurements on the same device configuration. Fits are done by a piecewise defined function, the transition voltages from impedance spectra are emphasized with vertical lines. **Bottom:** Fit parameters for V_{tr} from impedance and photoluminescence data

The negative sheet charges at the NPB/Alq_3 interface lead to Alq_3 radical anions that in turn will accept a FRET-like energy transfer [270] as proposed earlier as fourth quenching mechanism. Above the transition voltage V_{tr}, however, holes will accumulate at the NPB/Alq_3 interface and the hole density starts to rise also in Alq_3, leading to a partial compensation of the negative interface charges. Consequently, the accumulation of positive charges at the NPB/Alq_3 interface correlates with the diminishing of PL quenching above the transition voltage V_{tr}, when PL quenching starts to decrease and reaches almost zero at approximately 0 V. For comparison, the graph in Figure 4.5c, bottom left, includes the hole density calculated for a hypothetical device with non-polar Alq_3 as ETL. It is the same for all positions of the sensing layer and no rise in density is visible, emphasizing the link to the GSP.

To further test this hypothesis, impedance spectra of samples with 80 nm and 120 nm of Alq_3 thickness can also be compared to the respective PL quenching measurements. The measurements are shown in Figure 4.6, together with fit results to extract the transitions voltages. Note that the evaluation of the PL data here was done using a fit of a piecewise defined function, whereas a graphical approach was taken in the previous publication [263]. The absolute values therefore differ slightly. Although the data for transition voltages from PL and impedance is not equal for all measurements and no simple dependence of the deviation of measured data is visible, it is still a strong evidence that the compensation of the interface charges is responsible for the change in Q.

4.3. Summary of the PL quenching experiment

In summary, the photoluminescence quenching experiment can be widely explained with the help of simulated carrier density profiles using the framework created to simulate polar OLEDs. At least two regimes with different quenching mechanisms can be determined. Mechanisms dependent on electron density dominate in forward bias with moderate applied voltages, corresponding to the usual working point of an OLED. Hence, from the aforementioned processes, numbers 1, 2 and 4 can contribute to the loss in PL intensity of DBP for positive voltages. Features seen in reverse bias could be directly related to the existence of negative sheet charges present at the NPB/Alq_3 interface. This finding is remarkable, because it provides an additional direct proof for the existence of interface charges and their effect on the heterojunction.

Thus, the successful description of the observations made using the molecular sensing approach demonstrates that the model for polar OLEDs is able to describe even specific properties like carrier densities in the bulk and at the interface in good agreement with experimental data. So far, only electrical data in transient and steady state have successfully been described [3, 13].

Apart from this, the approach nicely demonstrates the proof-of-concept of a molecular sensing approach with high local sensitivity for OLEDs under operation. In conjunction with simulations, which lack any possible carrier trapping on the fluorescent dye, it is shown that the small amount of dopant molecules do not disturb device operation in any measurable way. The concept should therefore be adaptable to many different device types.

IV

Influence of dipolar doping on charge injection barriers and carrier dynamics

5. Transfer of the MIS-concept to polar OLEDs

Charge carrier mobility and injection properties are important figures of merit for organic semiconductors and manifold experimental techniques exist to measure both parameters. The charge carrier mobility can be determined from devices exhibiting space charge limited current [271] by fitting the corresponding equations given in Section 1.1.5. Furthermore, to name a few, the time-of-flight technique (TOF), which is briefly explained in Section 6.2, or the evaluation of organic field effect transistors [272] allows to determine charge carrier mobilities. In case of solar cells, photo-CELIV has been successfully applied to measure the mobilities of photo-induced carriers. A similar technique is possible with injection-CELIV on MIS diodes. However, none of these techniques allows to study the exact samples as employed for standard OLED characteristics, because they require device structures tailored to the specific experiment.

The same holds true for examining charge injection barriers. Here, mostly photoelectron spectroscopy as described in Section 2.7 or also the wet-chemical cyclic voltametry [273] are used to determine the energy levels of OSC. These can later provide an estimate to the contact barrier e.g. by comparing these values to the electrode workfunction. Again, those measurements cannot be conducted on the actual device.

In this chapter, two complementary methods are introduced that allow to measure charge injection barriers and charge carrier mobilities on actual OLEDs, given that the ETL exhibits a GSP larger than the HTL. For this purpose, temperature dependent MIS-CELIV and IS measurements are required. Both methods have been developed together with Simon Züfle from Fluxim AG in Winterthur, Switzerland, the Zürcher Hochschule für Angewandte Wissenschaften (ZHAW) located in the same city and our University. In this bilateral project funded by DFG and SNF called “CarDyn”, the experimental part comprising device fabrication, measurement and testing of the developed models was assigned to our University, where I was working on the project. These techniques and the insight gained during the work on the project played a crucial role in the investigation of the phenomena studied in the scope of this work, which will be discussed in the next chapter.

5.1. Polar MIS-CELIV

It has already been briefly mentioned in Section 1.2.3 that polar OLEDs and MIS-diodes share some important properties. This section will describe how the CELIV technique can be applied to polar OLEDs. In a MIS device, the insulating layer hinders charge transport through the whole device and will lead to accumulation of charge carriers at the semiconductor/insulator interface. This not only allows for

charge extraction experiments that are summarized in Section 2.5.3, it also provides excellent carrier selectivity compared to traditional CELIV, where electrons and holes are difficult to distinguish. Although OLEDs do allow the injection of both carrier species by design, the GSP in polar OLEDs promotes carrier injection into the HTL at much lower voltages. Thus, in a specific voltage range, carrier selectivity is still given. Regarding most known polar organic materials that also exhibit SOP, however, a negative sheet charge density at the HTL/ETL interface exists, favoring the measurement of hole properties. In this section, the validity of the MIS-CELIV approach on polar OLEDs will be discussed with the help of drift-diffusion simulations, followed by selected examples of extraction transients.

This section is based on the paper published together with Simon Züfle [13]. All simulations here were recalculated and evaluated by myself. Additional measurements shown here were previously not published.

5.1.1. Charge accumulation and distribution in polar organic diodes

In Section 2.5.3, two requirements for an ideal MIS-CELIV experiment have been elaborated based on the initial work by Juška *et al.* [218, 231] and others. To summarize, charge carriers have to be effectively driven to the semiconductor/insulator interface by the applied electric field, with thermal (backward) diffusion kept at a minimum. Additionally, the insulating capacitance was originally required to be larger than the semiconductor capacitance, which will additionally foster hole accumulation at the interface due to a larger field gradient and allows for approximations in the analytic solution. Both constraints have been discussed by various authors. A short summary of this discussion for devices not fulfilling the requirements is presented in Section 2.5.4. For polar OLEDs, the previous requirements will have to be relaxed.

A successful MIS-CELIV experiment on a standard MIS-diode requires the device to be pre-charged at a voltage above the built-in field to drive carriers to the semiconductor/insulator interface. On the left of Figure 5.1, a simulated CELIV experiment on a MIS device is shown with transient currents and hole densities, capacitance-voltage characteristic, energy bands and density profiles. An NPB layer with a thickness of 70 nm is interfaced to an insulating layer of 100 nm, the dielectric constant of this layer is set to $\varepsilon = 3.5$ to be equal to that of Alq_3 in simulation. Note, that this thickness will not directly lead to an insulating capacitance larger than the semiconducting capacitance, but will allow a better comparison with the simulated OLED with the same film thicknesses. The insulator energy gap is 5 eV and positioned with a LUMO at 2 eV resulting in an intrinsic hole barrier of 1.5 eV to the NPB HOMO level at 5.5 eV. The contact workfunctions of 5.1 eV for the anode at a position of -70 nm and 2.9 eV for the cathode at 100 nm lead to a built-in voltage of $V_{\mathrm{bi}} = 2.2$ V, which corresponds to the beginning of hole accumulation in the capacitance-voltage graph in Figure 5.1c. To pre-charge the device with holes for the extraction transient, a voltage of 4 V is used, as indicated by the dashed arrow in this figure. The energy levels of both, the organic and insulating layer at $V_{\mathrm{ext}} = 4$ V at a transient time of $t = 0$ µs is given in Figure 5.1d, alongside with the charge carrier densities of electrons and holes at the same initial condition. While the electron density is considerably low throughout the whole device, the density of holes peaks at the interface and quickly diminishes by an order of magnitude within

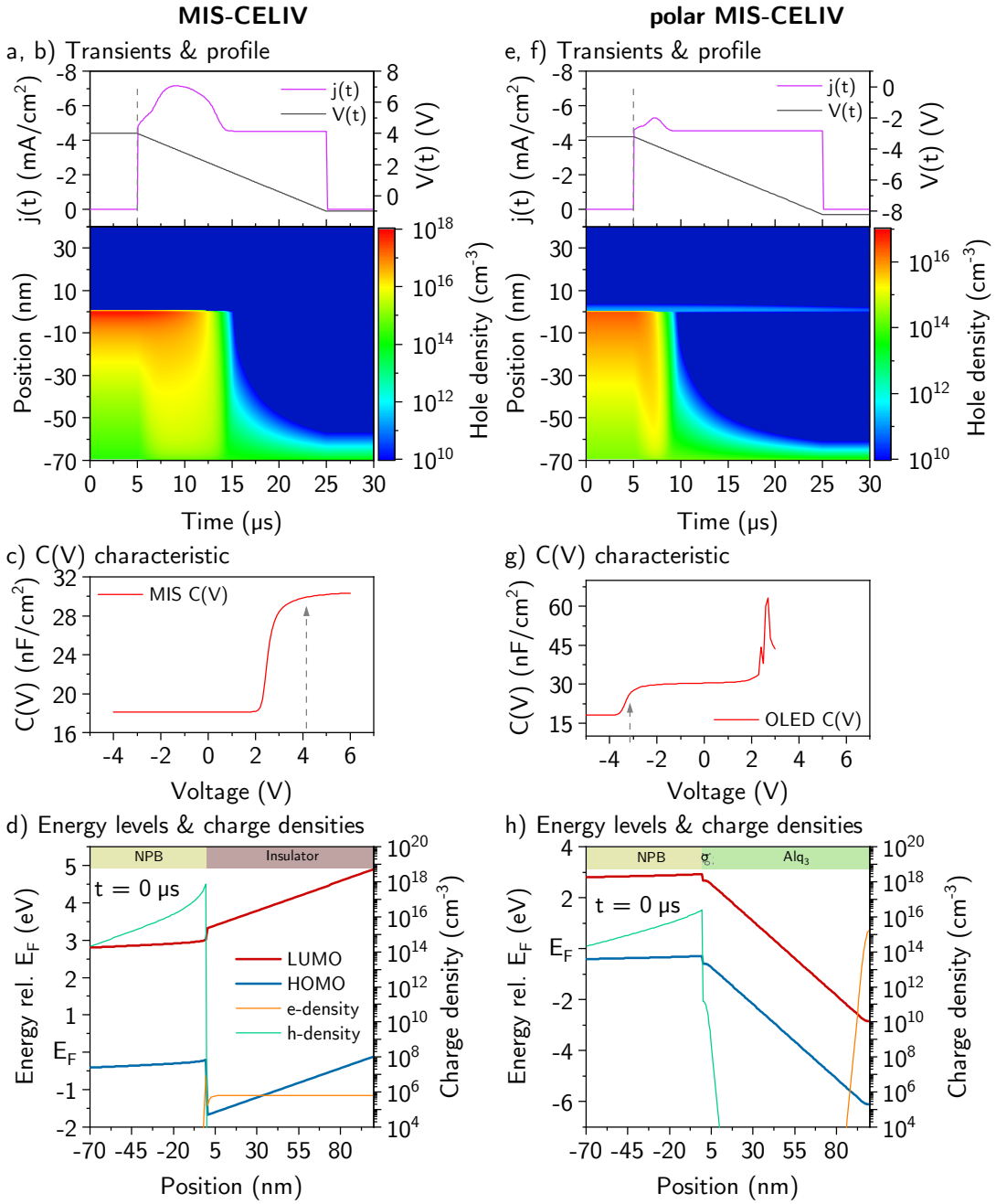

Figure 5.1.: Simulations of MIS-CELIV on a classic MIS diode (**left**) and on a polar OLED (**right**). From top to bottom the graphs are the CELIV transient with voltage, hole density depending on position and time, $C(V)$ characteristic and energy levels with a logarithmic representation of the hole and electron density at $t = 0\,\mu s$ before extracting the carriers.

10 nm. In further simulations, which are not shown here, the hole density at the interface could be increased by approximately one order of magnitude by using an insulating layer of only 30 nm thickness.

The extraction current transient, the applied external voltage and the hole density transient are given in Figure 5.1a and b, respectively. A 5 µs delay time at equilibrium conditions with $V_{\mathrm{ext}} = 4\,\mathrm{V}$ is followed by a linearly decreasing voltage slope of $S = 25\,\mathrm{kV\,s^{-1}}$. Shortly after the beginning of the ramp, the charge carrier cloud reaches the anode at $-70\,\mathrm{nm}$, with carrier densities near $-70\,\mathrm{nm}$ rising by more than two orders of magnitude. At around 10 µs after the start of the extraction, all carriers are extracted, indicated by an extreme decrease in carrier density in the whole semiconducting layer by more than eight orders of magnitude. In the CELIV transient itself, the beginning and end of the ramp is indicated by a step towards and back from the displacement current governed by the device capacitance. The drift current from extracted charge carriers adds to that current, which could be used to calculate e.g. the carrier mobility. When integrating over the drift current only, the total extracted charge resembles the equilibrium carrier density at the applied voltage prior to the start of the ramp [13].

These results can now be compared to the case of a polar OLED given on the right in Figure 5.1, with the same graphs. The polarity of the Alq_3 layer is again introduced by mimicking the interface charges through doping, which was set to resemble a sheet charge density of $1.8\,\mathrm{mC\,m^{-2}}$. Additionally, HOMO (5.8 eV) and LUMO (2.55 eV) have been adjusted to describe Alq_3 instead of an insulator, all other parameters remain unchanged. It has already been elaborated that the GSP in Alq_3 causes a shift in potential in the device, leading to a hole injection voltage far below the built-in field. This is seen in Figure 5.1g in the $C(V)$ plot, where the transition voltage is at $V_{\mathrm{tr}} \approx -3.5\,\mathrm{V}$ and the energy levels in sub-figure h), where a strong downward shift of the HOMO level in Alq_3 is observed at $t = 0\,\mu\mathrm{s}$ at an external bias of $-3.2\,\mathrm{V}$. However, the gradient in NPB is positive at this voltage, provoking a carrier drift of injected holes towards the interface, similar to a positively biased MIS diode. Similar to the classic MIS device, the OLED needs to be pre-charged at a voltage above the accumulation voltage V_{tr}. In this case, it was set to $V_{\mathrm{ext}}(t = 0) = -3.2\,\mathrm{V}$, just above the transition voltage, followed by a downward ramp of the same slope of $S = 25\,\mathrm{kV\,s^{-1}}$. The particular choice of this voltage will be elaborated in the next section, it does, however, affect the total hole density in the device. In Figure 5.1h, again the hole density throughout the device is given. Although the profile is broader in shape, it still peaks at the interface to the ETL.

The extraction transient in Figure 5.1e and the transient carrier profile in Figure 5.1f are comparable to the MIS case. A big difference, though, is the peak height of the drift current, which directly resembles the lower overall charge carrier density at the interface that can be extracted within about 3 µs compared to 10 µs in the MIS case. Additionally, a finite hole density is observed in Alq_3 in the vicinity of the interface, possibly trapped by the negative interface charge of the GSP. As this density is constant in time and voltage, it is not expected to influence the experiment.

After all, the polar nature of the ETL and its GSP that leads to a strong shift in energy levels allows for an accumulation of holes at the HTL/ETL interface that mimics the case in a classic MIS diode. The extracted charge density is solely deter-

mined by the hole density in the device, which can be confirmed by separating the individual contributions of electron and hole current (not shown here), where the electron drift current at the cathode is found to be almost nonexistent. Additionally, the current is not influenced by recombination losses, further tests on possible influences can be found in the publication [13].

5.1.2. Charge extraction in polar MIS-CELIV

An open issue that has to be discussed is the choice of the injection voltage applied before starting the CELIV experiment. To allow for carrier accumulation, it has to be above V_{tr}, but it should not exceed the injection voltage V_{inj} to preserve carrier selectivity and avoid the injection of electrons. For MIS-CELIV, two different analytic solutions with specific boundary conditions exist to relate a measurable quantity to the carrier transit time t_{tr}, which in turn can be used to calculate the mobility, both were discussed in Section 2.5.3. To summarize, a simple calculation of charge carrier mobility is possible, if the density of injected charge carriers is small and the observed current maximum thus roughly equals the transit time, $t_{\mathrm{tr}} = t_{\mathrm{max}}$. Alternatively, the transit time can be determined from the time t_1, where the current reaches two times its displacement current ($2j_0$) and if the transient reaches the total saturation current during measurement and is hence governed largely by space charge.

In the light of polar MIS-CELIV, it can be argued, which of the two regimes is possible to achieve. Three example measurements on different device architectures are shown in Figure 5.2. The device in Figure 5.2a is made with thicknesses of NPB and Alq_3 of 85 nm and 120 nm, respectively. In b), the HTL thickness is with 120 nm 4.8 times thicker than the ETL with 25 nm. The third device adds a dedicated electron blocking layer to a device similar to the one on b) and will be discussed later on. Capacitance-voltage characteristics for all three devices are shown in Figure 5.2d.

At first, the two standard OLED stacks will be discussed. In the device shown in Figure 5.2a, the saturation current is $j_{\mathrm{sat}} \approx 1.7 \cdot j_0$. Thus, a point in time t_1, where $j(t_1) = 2t_0$ cannot be determined. The mobility therefore will only be available through t_{max}. Also, Sandberg *et al.* have discussed a limit of $j_{\mathrm{sat}} \gtrapprox 3.3 \cdot j_0$ to minimize errors in mobility extraction using t_1, see Section 2.5.4. This condition could theoretically be met in the second device, where

$$\frac{j_{\mathrm{sat}}}{j_0} = \frac{\varepsilon_i d_{\mathrm{s}}}{\varepsilon_s d_{\mathrm{i}}} + 1 \approx 5.8 \ .$$

However, when looking closely to the transients seen in Figure 5.2b, in the region magnified in the inset, the current is already pulled below the initial value of j_0 by the onset of electron injection at the start of the ramp. Thus, the saturation current cannot be reached with this device without injecting the opposite charge carrier and an evaluation of the position of t_1 is probably invalid.

For both OLEDs, the technique relying on t_1, which is the most convenient in case of classic MIS devices [231, 233], is thus not suitable. Instead, the transient can be evaluated at a position just above V_{tr}, which fulfills the small-charge injection limit [13, 231] and should be possible with both device stacks.

Then, $t_{\mathrm{tr}} = t_{\mathrm{max}}$ and the mobility can be calculated using a theory for a small

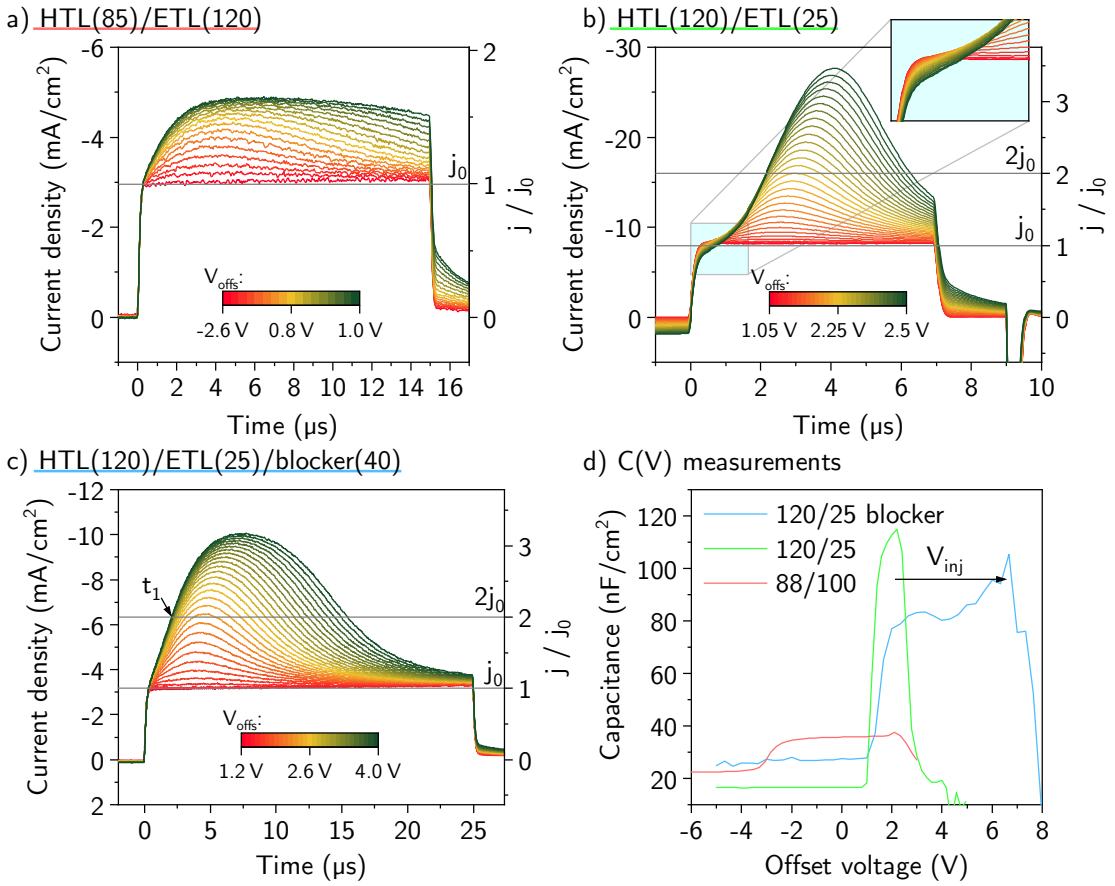

Figure 5.2.: Measurements of polar MIS-CELIV on three different devices **a) – c)**. The stack layout is given in the figure titles, colored underlines match to the $C(V)$ characteristics in sub-figure **d)**. In **b)**, the inset shows the highlighted region of the current transient, where injection of electrons is already expected. The offset voltage at the beginning of the transient is color coded and different for each of the three samples.

insulator capacitance, as discussed in Section 2.5.4. Rearranging Equation 2.64 yields

$$\mu = \frac{2{d_\mathrm{s}}^2}{St_\mathrm{tr}^2}\left(1+\frac{\varepsilon_\mathrm{s}d_\mathrm{i}}{\varepsilon_\mathrm{i}d_\mathrm{s}}\right) \tag{5.1}$$

for the small charge limit, where again

$$\frac{\varepsilon_\mathrm{s}d_\mathrm{i}}{\varepsilon_\mathrm{i}d_\mathrm{s}} = \frac{j_0}{j_\mathrm{sat}-j_0}\,.$$

Calculating the correction factor using this small charge limit is, however, not possible, if no saturation is seen and the layer thicknesses and dielectric constants are needed instead. For OSC, the latter is often not known and set to a constant value of $\varepsilon_{\mathrm{i,s}} \approx 3.5$, thus leaving the sample thickness ratio as defining parameter in the correction.

For the small charge injection method, the peak time can be determined by various methods, but the signal might have to be filtered or smoothed to improve the signal

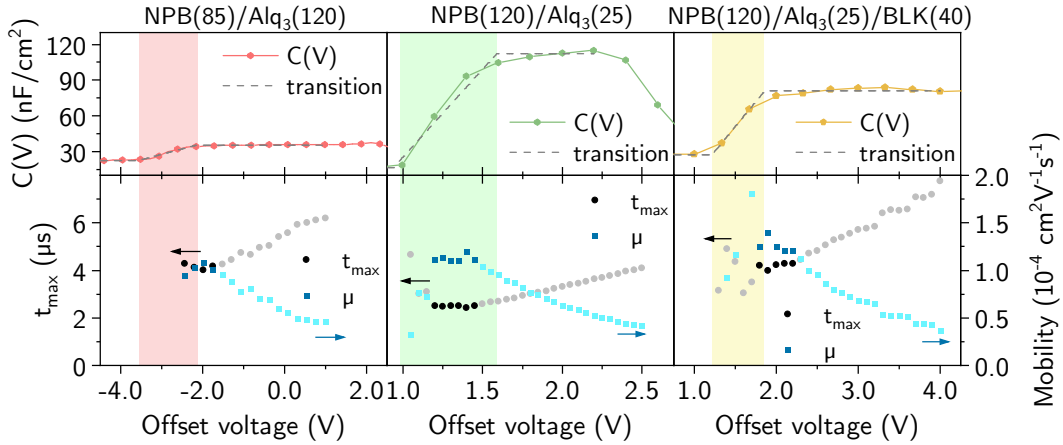

Figure 5.3.: Extracted peak maximum times t_{max}, calculated mobilities and the $C(V)$ characteristics for comparison for all three devices. The time scale for all graphs is on the left, the mobility scale on the right in $10^{-4}\,\mathrm{cm^2\,V^{-1}\,s^{-1}}$.

Sample	Mobility from t_{tr}	Mobility from t_1
85/120	$(1.02 \pm 0.06) \times 10^{-4}$	– –
120/25	$(1.12 \pm 0.03) \times 10^{-4}$	– –
120/25(40)	$(1.26 \pm 0.08) \times 10^{-4}$	$(8.62 \pm 0.42) \times 10^{-5}$

Table 5.1.: Results calculated from both methods for all three samples and statistical errors from all datapoints. The small charge injection method produces comparable results for all three sample geometries, the evaluation of t_1 is only possible for one sample.

to noise ratio. This was done by applying a suitable digital low-pass filter to the data directly in the Paios software suite, or by applying e.g. a moving average filter in post processing. In both cases, a cut-off frequency or equivalent window size in the order of 1 MHz was found to be suitable for the setup available during this work and for CELIV ramps of an order of magnitude of $10^5\,\mathrm{V\,s^{-1}}$. The peak maximum can then either be determined by hand, or e.g. by examining the first derivative of the signal; both methods were found to produce comparable results. For both standard OLEDs shown in Figure 5.2, the mobility is calculated using the transient maximum approach and the results are shown in Table 5.1. Raw data is available in Figure 5.3 with peak times and calculated mobilities for all transients, where an evaluation was possible. In none of the MIS-CELIV formulas to calculate the mobility, any dependence on the offset voltage at the beginning of the ramp is found. The linear rising of $t_{tr} = t_{max}$ accompanied by a linear decrease of the calculated mobility is thus a clear hint for a deviation from the small charge injection regime. Hence, to calculate the average given in Table 5.1, only the values where no voltage dependence is observed are considered, which are plotted in darker colors in Figure 5.3. This voltage independent regime is also in close vicinity to or completely enveloped by the transition region for charge accumulation obtained from the $C(V)$ data, indicated by the shaded areas. As flat band conditions for the NPB layer are known to occur around V_{tr}, this is expected.

To test the extraction of the mobility using the t_1 approach, an attempt was made to inhibit electron injection and move V_{inj} to higher voltages by adding an electron blocking layer of 40 nm Spiro2-CBP (2,7-bis(carbazol-9-yl)-9,9-spirobifluorene) on top of the ETL. The material exhibits a considerably low LUMO level of 1.7 eV [274] leading to a high electron injection barrier. In Figure 5.2d, the shift of the injection voltage by approximately 5 V is visible in the $C(V)$ characteristic. The CELIV transients in Figure 5.2c show a saturation at $j_{\mathrm{sat}} \approx -10\,\mathrm{mA\,cm^{-2}}$, suggesting effective blocking. However, the OLED is now a three-layer device, with only the middle layer being polar. The transition voltage of both devices with the same Alq_3 thickness is almost similar, with $V_{\mathrm{tr}} = 0.98\,\mathrm{V}$ without and $V_{\mathrm{tr}} = 1.22\,\mathrm{V}$ including the additional blocking layer. As Spiro2-CBP is non-polar, the change in field gradient is rooted in the Alq_3 GSP only and the difference is probably caused by an error in thickness – it was not possible to check the Alq_3 thickness of the three-layer device after deposition. For calculating the CELIV mobilities, the Alq_3/Spiro2-CBP combination is considered the insulator with a combined thickness of 65 nm. This allows to calculate the ratio of j_0 and j_{sat} to $j_{\mathrm{sat}}/j_0 \approx 2.86$ using the thickness-based formula. However, with the measurement quantities of $j_0 \approx -3.12\,\mathrm{mA\,cm^{-2}}$ and $j_{\mathrm{sat}} \approx -10\,\mathrm{mA\,cm^{-2}}$, the ratio is $j_{\mathrm{sat}}/j_0 \approx 3.26$. Considering the thickness of the semiconductor of 120 nm being accurate, the insulating thickness would then calculate to 37 nm instead of 65 nm, which is very low compared to the usual variation expected in the vacuum chamber in question. Obviously, the physics behind the saturation of the current during extraction with a combined polar and non-polar layer is not well described by the simple linear combination assumed above. Nevertheless, the blocking approach can be used to change the injection voltage into a regime, where polar OLEDs reach a saturation current in CELIV transients. With current ratios near the minimum required for a successful calculation using the t_1 approach, the results are included in Table 5.1. It is worth noting, however, that this value is only obtained by applying the diffusion corrected model published by Sandberg *et al.* [233], as discussed in Section 2.5.4. The resulting value of $(8.62 \pm 0.42) \times 10^{-5}\,\mathrm{cm^2\,V^{-1}\,s^{-1}}$ is lower, but close to the result gained with the small charge injection method. Instead, if the standard approach for classic MIS-CELIV is applied, where the transit time is related to t_1 with $4t_1 = \pi t_{\mathrm{tr}}$, the mobility is over-estimated to $(5.04 \pm 0.08) \times 10^{-4}\,\mathrm{cm^2\,V^{-1}\,s^{-1}}$, as expected [233].

As a side note, also other materials have been investigated in the scope of this work using the presented polar MIS-CELIV approach. One example is the amorphous OPVC donor material DBP, which replaced the NPB HTL. Spectra of the electroluminescence of those devices (not shown here) suggest that the DBP layer solely acts as charge transport layer and charge recombination is taking place in Alq_3, just as in standard NPB/Alq_3 OLEDs. Measurements conducted on a device with 70 nm of DBP and 60 nm of Alq_3 are shown in Figure 5.4. Again, no saturation is observed or at all expected from the device structure and the small-charge approach is used accordingly. The resulting hole mobility of $(2.57 \pm 0.05) \times 10^{-6}\,\mathrm{cm^2\,V^{-1}\,s^{-1}}$ is two orders of magnitude lower than the previously reported value in the order of $10^{-4}\,\mathrm{cm^2\,V^{-1}\,s^{-1}}$ [275]. While it is possible that the material exhibits different mobilities depending on purity, measurement type or also electric field, the most likely cause in this case is something different. With DBP, no clear accumulation was observed in the $C(V)$ characteristic shown in Figure 5.4b, despite of the 60 nm thick

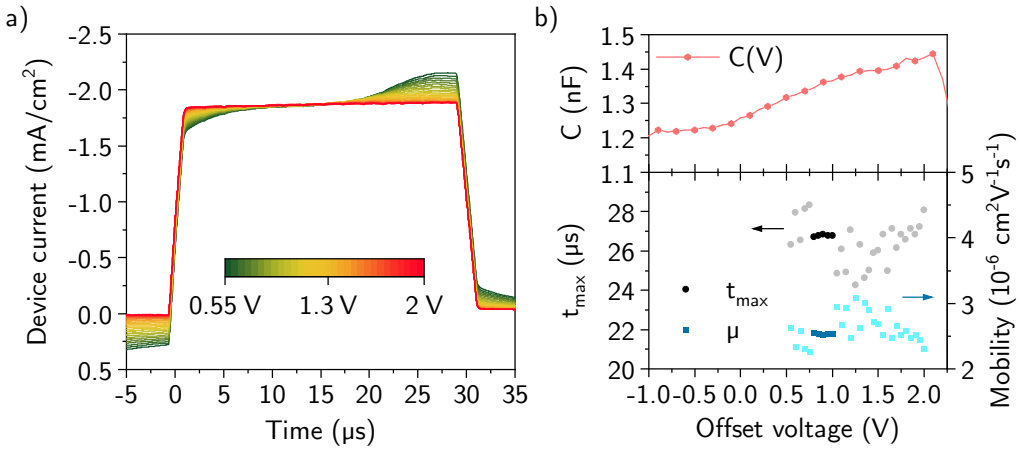

Figure 5.4.: Measurements on the OPV donor material DBP. **a)** CELIV transients. Offset voltages above 1 V start to show electron injection. **b)** $C(V)$ characteristic and extracted peak times with calculated mobilities.

Alq_3 layer that should lead to a clear transition a few volts below V_{bi}. Consequently, high bias voltages at the beginning of the ramp were needed, where the peak of the transient is shifted towards higher values in time. Additionally, electron injection in the device is already possible, indicated by a shift of the transient towards zero, which might allow carrier recombination.

From this, a definitive requirement can be affirmed that was already visible from Section 5.1.1. For a successful polar MIS-CELIV experiment, high accumulation of the charge carrier species to be investigated is necessary. If the material features high parasitic recombination, low charge transport or also low shunt resistance, the evaluation of the transients is increasingly challenging.

5.1.3. Summary on polar MIS-CELIV

It has been shown that the MIS concept can be successfully applied to polar OLEDs in combination with the CELIV technique. The GSP of a polar layer with SOP provokes a charge carrier accumulation at the non-polar/polar layer interface, leading to a carrier distribution similar to the case of a MIS device with high forward bias. As most available polar materials, which exhibit a PDM, orient as such that a negative sheet charge density arises at the interface, the technique is most suited to probe hole transport properties in a subjacent layer. Besides, different device configurations or layers with reversed GSP can be discussed that would allow to study e.g. electron transport in the ETL. However, only hole transport in the HTL was successfully measured so far, for a more detailed discussion on alternative device configurations please refer to our publication in reference [13].

In the previous section the hole mobility for NPB was calculated to a global average over all three devices of $(1.13 \pm 0.12) \times 10^{-4}\,\mathrm{cm^2\,V^{-1}\,s^{-1}}$ using the recommended technique of small charge injection. This is in very good agreement to typical values published in literature, which are usually also given with an order of magnitude of $10^{-4}\,\mathrm{cm^2\,V^{-1}\,s^{-1}}$ [13]. Examples are $2 \times 10^{-4}\,\mathrm{cm^2\,V^{-1}\,s^{-1}}$ to $3 \times 10^{-4}\,\mathrm{cm^2\,V^{-1}\,s^{-1}}$ obtained by admittance spectroscopy [276, 277] or, measured

by time-of-flight, $3 \times 10^{-4}\,\mathrm{cm^2\,V^{-1}\,s^{-1}}$ to $5 \times 10^{-4}\,\mathrm{cm^2\,V^{-1}\,s^{-1}}$ [277–279]. Lower values down to $2 \times 10^{-5}\,\mathrm{cm^2\,V^{-1}\,s^{-1}}$ are reportedly gained using purely electrical measurements like examining space charge limited currents [71]. Later on in this work, time-of-flight measurements will be presented on undoped NPB that result to mobilities of roughly $5 \times 10^{-4}\,\mathrm{cm^2\,V^{-1}\,s^{-1}}$.

However, also limiting factors could be identified. With the OPVC donor DBP, no successful CELIV experiment could be performed. Although charges can be injected into the device and DBP can replace NPB as HTL in an Alq_3 based OLED, no clear or only little charge accumulation is found. The CELIV transient is thus only visible for high offset voltages at the start of the ramp, which allow electron injection and falsify the extracted transit time. For a successful polar MIS-CELIV measurement, impedance spectra therefore must show clear accumulation, while electron injection has to be avoided.

5.2. Correlating impedance spectroscopy and injection barriers

With a versatile tool to extract the charge carrier mobility of holes in real OLEDs at hand, it is now possible to investigate carrier injection into the HTL on full working OLEDs as well. In this section, a combination of the aforementioned polar MIS-CELIV technique and impedance spectroscopy, both performed at varied sample temperatures, is used to calculate the hole injection barrier into the HTL. At first, a short theoretical introduction is given to sketch the idea of the experiment, followed by the results of drift-diffusion simulations to check the validity of the method.

This section is based on the paper published together with Simon Züfle [14], the simulation results have already been presented there. All example measurements, however, are previously unpublished.

5.2.1. Combining mobility and impedance activation energies

The transition between the accumulated and non-accumulated regimes in polar OLEDs has been thoroughly investigated in terms of its voltage dependence. Additionally, the accumulation occurs at a temperature dependent relaxation frequency f_{rel}. $C(f,T)$ measurements have in the past been successfully used to study the thermal activation of the hole current in OSCs [280–282]. Usually, an Arrhenius-type activation is found, which is also the case for f_{rel}, where

$$f_{\mathrm{rel}} \propto \exp\left(\frac{E_{\mathrm{act}}}{\mathrm{k_B}T}\right) \ . \tag{5.2}$$

The frequency dependence of the capacitance in a device with two serial capacitors is described in Section 2.6.2 in Equation 2.81 with

$$f_{\mathrm{rel}} = \frac{1}{2 \cdot \pi} \cdot \frac{R_1 + R_2}{R_1 R_2 \cdot (C_1 + C_2)} \ .$$

In accumulation, the HTL resistance is $R_{\mathrm{HTL}} \ll R_{\mathrm{ETL}}$, leading to the expression

$$f_{\mathrm{rel}} \propto \frac{1}{R_{\mathrm{HTL}} \cdot (C_{\mathrm{HTL}} + C_{\mathrm{ETL}})} \ . \tag{5.3}$$

A temperature dependence of the individual capacitances is unlikely. Instead, the dependence on the HTL resistance, or in turn on the conductance, can be identified as the reason for the Arrhenius activation of the relaxation frequency.

The conductance G_{HTL} of the NPB layer in an NPB/Alq_3 polar OLED can be written as

$$G_{\mathrm{HTL}} = \frac{1}{R_{\mathrm{HTL}}} = \mathrm{e} \cdot \rho_{\mathrm{HTL}} \cdot \mu_{\mathrm{h,HTL}} \ . \tag{5.4}$$

Here, ρ_{HTL} is the density of holes in the HTL and $\mu_{\mathrm{h,HTL}}$ the hole mobility. Note, that only the hole conductance is of interest in the accumulated regime and below an external bias of V_{inj} as no electrons are present in the HTL. Both, the hole density and the mobility, are temperature activated. The density of holes in the HTL can be described with

$$\rho\left(E_{\mathrm{inj}}, T\right) = \rho_0 \cdot \exp\left(\frac{-E_{\mathrm{inj}}}{\mathrm{k_B}T}\right) \ . \tag{5.5}$$

This assumes the anode/HTL contact to be ohmic, i.e. with Fermi level alignment in place. The same assumption is also usually made in simulation, see Section 1.3. However, in simulation, the hole density is not constant in the whole layer as given in Equation 5.5, but calculated self-consistently using drift- and diffusion equations [14]. Additionally, the mobility can be temperature dependent. Depending on the underlying mobility model, the temperature dependence will be described differently. A very simple temperature activation found in some organic semiconductors [283,284] is given by

$$\mu\left(E_{\mu}, T\right) = \mu_0 \cdot \exp\left(\frac{-E_{\mu}}{\mathrm{k_B}T}\right) \ , \tag{5.6}$$

similar to the barrier or hole density activation. Combining Equations 5.5 and 5.6 yields the temperature dependent HTL conductance with

$$G_{\mathrm{HTL}}\left(E_{\mu}, E_{\mathrm{inj}}, T\right) = \mathrm{e}\rho_0\mu_0 \cdot \exp\left(-\frac{E_{\mathrm{inj}} + E_{\mu}}{\mathrm{k_B}T}\right) \ . \tag{5.7}$$

Thus, the total activation energy of the relaxation frequency in Equation 5.2 is

$$E_{\mathrm{act}} = E_{\mathrm{inj}} + E_{\mu} \ . \tag{5.8}$$

It is evident that in order to disentangle the influence of injection barriers and mobility activation on the relaxation frequency, at least one of the two has to be determined independently. Therefore, temperature dependent polar MIS-CELIV transients can serve to get the mobility activation. Because the CELIV method can be applied to actual OLEDs, measurements can be conducted on the same samples and in direct succession to impedance spectroscopy, thus minimizing systematic errors otherwise existent between different samples.

Simulated CELIV transients and impedance spectra have been evaluated with varied input hole barrier $E_{\mathrm{inj,in}}$, hole mobility activation $E_{\mu,\mathrm{in}}$ and temperature. Values for $E_{\mathrm{inj,in}}$ were changed from close to 0.0 eV to 0.6 eV in 50 meV steps, $E_{\mu,\mathrm{in}}$ was swept from 0.1 eV to 0.5 eV in 0.1 eV steps. CELIV transients obtained from simulation were evaluated using the small-charge injection method, where $t_{\mathrm{tr}} = t_{\mathrm{max}}$. The evaluation of impedance spectra is shown in Section 5.2.2. For each set of $E_{\mathrm{inj,in}}$ and $E_{\mu,\mathrm{in}}$, a temperature sweep is then fitted with the Arrhenius-type activation of

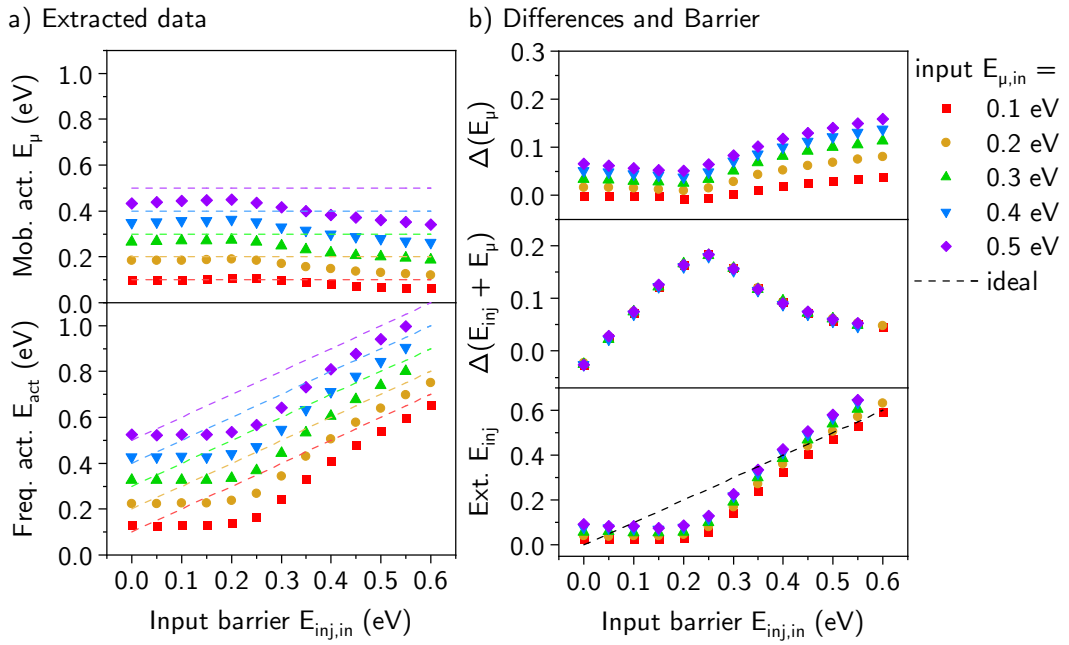

Figure 5.5.: Comparison of input parameters and determined quantities on simulated OLEDs. **a)** Extracted mobility activation energies (E_μ, top) and frequency activation ($E_\mu + E_{\text{inj}}$, bottom). Ideal values are given in dashed lines, input barriers E_{inj} are given on the X-axis, input mobility activation E_μ is coded in colors given in the legend. **b)** Difference between ideal (input) value and extracted quantities. Top to bottom is the difference between extracted and actual E_μ, $E_{\text{act}} = E_\mu + E_{\text{inj}}$ and E_{inj}.

Equations 5.2 and 5.6 to extract the relaxation frequency and the mobility activation from simulations. The resulting data is plotted in Figure 5.5a, where the injection barrier programmed in the simulation is given on the abscissa and the input mobility activation is color coded and described in the legend.

At first, the results from the CELIV transients will be discussed. In the simulated experiment, it is assumed that the mobility in the HTL is not influenced by the electric field, but only by thermal activation. Also, in general no charge extraction barrier is present, the temperature activation is thus only dependent on the mobility activation E_μ [14]. The calculated values are given in the top portion of Figure 5.5a, together with ideal values plotted with dashed lines. The deviation of the calculated value and the input into the simulation is larger for high mobility activation energies and barriers, $\Delta(E_\mu)$ is also plotted in Figure 5.5b. Below injection barriers of $E_{\text{inj,in}} = 250\,\text{meV}$, the difference in mobility activation from the ideal, programmed value is nearly constant and below 100 meV. In total, the lowest errors are obtained with either low mobility activation or low injection barriers. As most organic materials observe mobility activation energies between 0.1 eV and 0.3 eV [14, 285], the CELIV technique should be able to determine E_μ with suitable accuracy for low to moderate injection barriers.

A similar plot can be made for the extracted frequency activation energy, which is seen in the bottom part of Figure 5.5a. The extracted value from $f_{\text{rel}}(T)$ is almost

constant and resembles the temperature dependence of the mobility until an input barrier of about $E_{\mathrm{inj,in}} = 250\,\mathrm{meV}$. Thus, for low injection barriers, the mobility activation might also be determined from $C - f - T$ graphs [14]. The deviation from the presumed input data of $E_{\mu,\mathrm{in}} + E_{\mathrm{inj,in}}$ is given in Figure 5.5b, middle graph. Again, the error is largest with 200 meV at about $E_{\mathrm{inj,in}} = 250\,\mathrm{meV}$, but decreasing for higher input barriers down to 50 meV. Because the impedance measurement is simulated at thermodynamic equilibrium, the choice of mobility activation does not influence the error in E_{act} [14]. In the bottom of Figure 5.5b, the extracted barrier with $E_{\mathrm{inj}} = E_{\mathrm{act}} - E_{\mu}$ is also given. Following the errors for E_{μ} and E_{inj} discussed before, the extracted barrier is getting more accurate for higher barriers and low mobility activation energies, or very low barriers. It is worth noting that the error in both, mobility and the frequency activation energy is mostly positive. Any extracted value for E_{μ} and E_{act} will therefore always give the lower limits, only. This is not generally true for the calculated injection barrier, which can be overestimated for high mobility activation, but is likely to be underestimated for low injection barriers.

The main reason for this deviation for low barriers is the charge carrier density at the anode. For low barriers, simulations show that a considerable amount of holes is not accumulated at the HTL/ETL interface, but resides in the HTL close to the anode [14]. Thus, the simple assumption of a homogenous distribution of holes in Equation 5.5 does not hold.

5.2.2. Parameter extraction from temperature variation in $C(f)$

Both, CELIV and $C(f)$ measurements have to be evaluated with varied temperature. The determination of the CELIV mobility has been discussed in Section 5.1.2, which is still valid also for temperature dependent transients. For $C(f)$ spectra, the exact choice of the offset voltage has been found to play a minor role in ideal devices [14]. However, it has to be well above the transition voltage V_{tr} and below V_{inj}. Also, the decision on the DC offset can be important, if the device exhibits high leakage currents or other temperature dependent features in its conductance.

To extract f_{rel} from the $C(f)$ measurements, different methods can be discussed. Basically, the position of the inflection point is well defined in a device with two semiconducting layers only and the analytic solution [242] is given in Equation 2.81 as

$$f_{\mathrm{rel}} = \frac{1}{2 \cdot \pi} \cdot \frac{R_1 + R_2}{R_1 R_2 \cdot (C_1 + C_2)} \ .$$

However, depending on the signal quality, other methods exist, some of which are shown in Figure 5.6 and are summarized as follows

a) Figure 5.6a) shows the fit of the *capacitance* calculated for a two-RC circuit to the measured data. The fit yields the capacitance and the parallel resistance of both RC oscillators and the transition frequency is then calculated with Equation 2.81. The model can be extended e.g. with a series resistance affecting the high frequency range (not shown in the graph), which can improve the convergence for samples with higher relaxation frequencies. For a well-behaving device without leakage currents or low parallel resistance, this method is most accurate. Otherwise, the simple fits are often not possible.

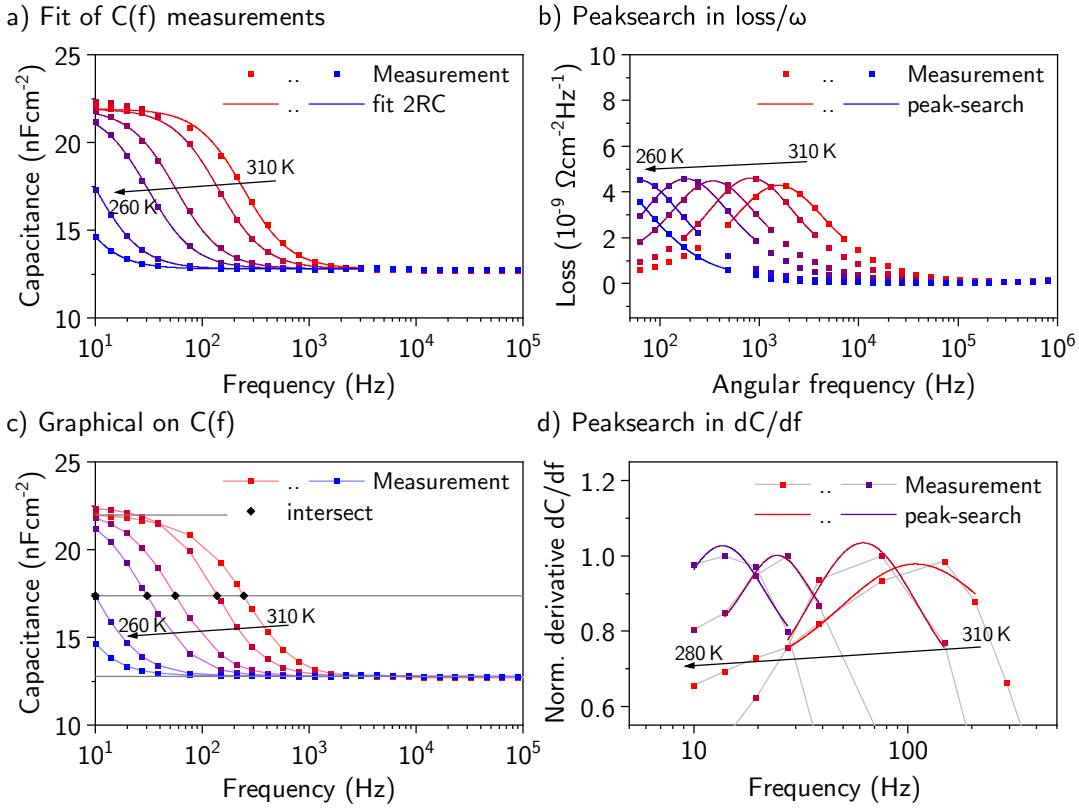

Figure 5.6.: Four different methods to determine the relaxation frequencies on an exemplary measurement with NPB/Alq_3 directly on ITO. The different methods are: **a)** A direct fit of a 2RC-model to the measured data, **b)** peak-search without model on the dielectric loss, **c)** a graphical method to determine the inflection point and **d)** a peak-search on the first derivative of the measured capacitance.

b) Figure 5.6b) shows an example for evaluating the *dielectric loss* or the conductance divided by the angular frequency ω with a simple peak-search. Alternatively, the RC-model can also be fitted to the loss term. Depending on the fitting algorithm, this method provides better convergence compared to the step-like function in a).

c) Figure 5.6c) depicts an example of determining the inflection point with a graphical method. Maximum and minimum capacitance, reflecting C_{ETL} and C_{tot}, respectively, are determined and the frequency, where the capacitance equals the mid-point of both is chosen to be f_{rel}.

d) a fourth method, taking the *derivative* of the $C(f)$ measurement and performing a peak-fit on the slope, is shown in Figure 5.6d).

The extracted relaxation frequencies for different methods are shown in Figure 5.7 including an additional fifth method, where a 2RC-model is fitted on the loss term, which was not shown in Figure 5.6. It is worth a note that the actual transition, either the position of the inflection point in $C(f)$ or the maximum in the loss term,

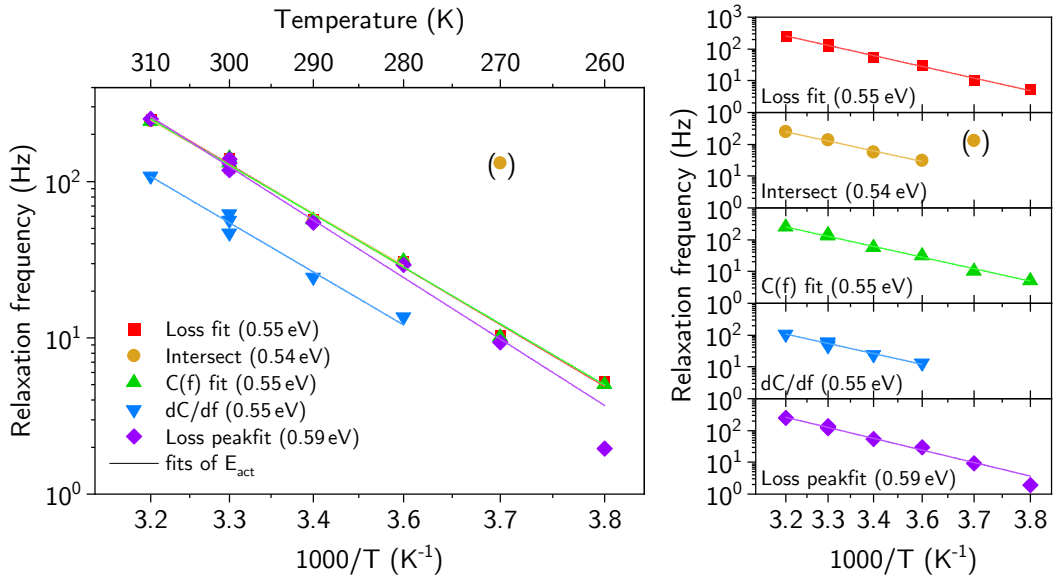

Figure 5.7.: Comparison of different methods to determine the relaxation frequency, the values given in brackets are the extracted activation energies. The slopes are all similar except for the peak-fit on the loss term. To increase lucidity, the same graphs and fits as repeated individually on the right.

have not been measured for temperatures below 270 K. The extraction is hence based on a prediction by the underlain 2RC model and this kind of evaluation is thus only possible for a device that is well described by this model.

Both methods fitting an RC equivalent circuit, either to the dielectric loss ("Loss fit") with $E_{\mathrm{act}} = (0.55 \pm 0.02)\,\mathrm{eV}$ or the $C(f)$ measurement directly ("C(f) fit") with $E_{\mathrm{act}} = (0.55 \pm 0.03)\,\mathrm{eV}$), lead to perfectly exponential behavior with almost no difference visible (red and green). They also allow to extract the transition voltage for spectra at low temperatures, where only a small portion of the transition was actually measured. The intersect method seems to be very accurate on this device as well. Only the point of lowest frequency, where the relaxation frequency is close to the minimum frequency measured, is way off the general trend and was therefore excluded from the fit. The calculated activation energy for the intersect method is similar to the two model fits with $E_{\mathrm{act}} = (0.54 \pm 0.04)\,\mathrm{eV}$. A peak-search on the dielectric loss (purple) shows a deviation from the exponential ideal for low temperatures, which causes a different slope ($E_{\mathrm{act}} = (0.59 \pm 0.03)\,\mathrm{eV}$). This is somewhat expected, as the simple logarithmic Gaussian that seems to describe the peak well for higher temperatures, is not able to accurately predict the position of the maximum for missing data points. Interestingly, the peak-search on the derivative $\mathrm{d}C/\mathrm{d}f$ yields overall lower frequencies by half an order of magnitude, although the slope fits well with $E_{\mathrm{act}} = (0.55 \pm 0.05)\,\mathrm{eV}$. Again, spectra where the transition is not fully covered in the chosen frequency range cannot be evaluated.

In general, it was tried to use the method of fitting a 2RC equivalent circuit on the measurements first. This method only fails, if the stray capacitance caused by the lateral conductance of a possible HIL gets large for low frequencies, or the series resistance changes significantly with decreasing temperature. However, it might allow

to evaluate also those measurements, where the complete transition is not visible in the chosen frequency range. In this case, the "Loss fit" method can still see a possible transition below the HIL signal. The fitting of a model on the dielectric loss is less error prone in that case, as the peak in loss during the transition is still a distinct feature, where the change in capacitance might not be visible.

5.3. Summary on the extraction of injection barriers in polar OLEDs

By using a combination of polar MIS-CELIV and impedance spectroscopy, it is possible to decouple the influence of the mobility activation energy E_μ and the injection barrier E_{inj} on both measurements. With temperature dependent CELIV transients, the mobility activation energy E_μ for most organic materials is accessible, with errors in the range of 50 meV or below, if both E_μ and the injection barrier are not larger than 0.3 eV. The frequency activation energy E_{act} extracted from $C(f,T)$ measurements, however, is more affected by the injection barrier. Extracted values for E_{act} and E_μ differ from the input value by up to 0.2 eV as seen in Figure 5.5, mainly caused by the inhomogeneous charge carrier profile in the HTL leading to a non-constant conductivity throughout the layer. This error becomes less pronounced for higher injection barriers, where the disentanglement of E_μ and E_{inj} is very well possible. As a side effect from the investigation, one benefit of the CELIV technique in investigating carrier mobilities has come to attention. Where methods relying on the overall sample current, like evaluating space charge limited currents on monopolar devices, will always measure a combination of barriers and mobility activation, CELIV was proven not to be dependent on the injection barrier. Then, by rearranging Equation 5.8 to

$$E_{\text{inj}} = E_{\text{act}} + E_\mu \ ,$$

the injection barrier E_{inj} can be calculated. The approach presented here can thus be applied to materials to extract the injection barrier and the temperature dependence of the mobility.

As pointed out in Section 5.1, CELIV transients are best evaluated using the small-charge injection approach. Care has to be taken, when choosing the offset voltage, however, as the minimum required offset for a visible peak in the transient will be higher for lower temperatures due to decreasing mobility and lower carrier injection. Note, that the evaluation of the simple Arrhenius model compared to impedance spectroscopy and CELIV transients was done using a drift-diffusion approach. The possibility to simulate impedance spectra of polar OLEDs with the model utilized here, however, has already been shown in this work as well as in literature [3]. Also, CELIV transients are successfully reproduced in drift-diffusion [13, 230, 286] In a combined experiment, the technique will be tested and compared to the injection barrier and mobilities gained from ultraviolet photoelectron spectroscopy or time-of-flight in Section 6.1.2.

6. Properties of dipolar doped layers

This chapter deals with the manifold consequences of dipolar doping on the OLED device performance, mainly concerning carrier injection and transport. Big parts of this chapter have already been published previously [49], some passages are taken literally from this publication.

In this chapter, the focus is set on the effect of SOP on device performance in polar OLEDs, especially on carrier injection into the active layers. One of the most important effects of the dipolar nature of the respective layer is that it induces a change in electric field distribution provoked by the buildup of interface charges. The electric field would otherwise be determined mostly by the contact potentials and the applied voltage [1]. Previously, the effect of dipole-induced interface charges on electron injection from the cathode into the electron transport layer (ETL) of such a polar OLED has been investigated by Noguchi et al. They compared devices with Alq_3 and $Al(7\text{-Prq})_3$ (tris(7-propyl-8-hydroxyquinolinato aluminum) as ETL [11], where electron injection was improved or hindered, respectively. The main difference between those two materials is the sign of their overall orientation polarization and hence the sign of the interface charge at the ETL-cathode interface [11]. $Al(7\text{-Prq})_3$ is one of the very few known materials that, like 1295, exhibit an inverse GSP. This difference was later on successfully described using drift-diffusion simulation by Altazin *et al.* [3], a possible microscopic explanation for the effect was given by Kinjo *et al.* [287].

To study the influence of a surface potential on hole injection at the anode side, OLEDs incorporating a polar HTL with preferably tunable magnitude of the GSP are needed. While many common electron transporting materials are indeed polar with a non-zero permanent dipole moment and also show a giant surface potential in vacuum-evaporated organic films due to SOP [6, 12], most available hole conducting materials are either non-polar or show isotropic orientation.

Therefore, the concept of dipolar doping, that was introduced in Chapter 3, is now studied with a focus on carrier dynamics and injection. For this purpose, the injection barrier is investigated by impedance spectroscopy, whereas the impact on hole mobility is studied using polar MIS-CELIV. Further investigations include complementary measurements with ultraviolet photo-electron spectroscopy (UPS), conducted during my stay at Chiba University, Japan, during the JSPS Summer Program 2017, as well as time-of-flight measurements of my samples contributed by Motiur Raman Kahn, then at the University of Potsdam, Germany.

6.1. Investigating carrier injection into dipolar doped HTL

In the following sections, all different device configurations initially introduced in Section 1.2, including solar cells for time-of-flight experiments, will subsequently be dis-

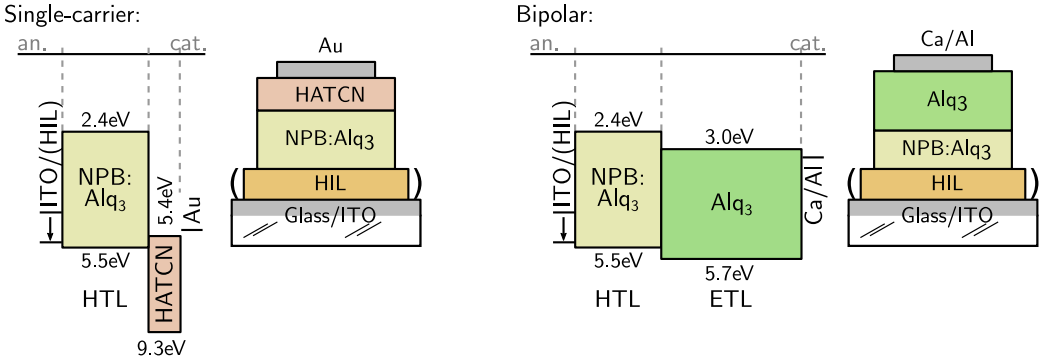

Figure 6.1.: Sketch of the energy levels for both device types under investigation. The top and bottom electrodes (cathode and anode, respectively) are marked. The substrate workfunction was changed between ≈4.6 eV and 5.7 eV. Energy levels are taken from refs. [117] and [1] or measured with UPS and IPES. Schematic stack layouts for both types of samples are drawn on the right of each energy diagram.

cussed. The layer stack for monopolar devices is ITO/(HIL)/NPB:Alq_3/HATCN/-Au, where the use of HILs at both electrodes leads to mostly hole current dominated characteristics. For impedance and CELIV measurements the stack design is ITO/-(HIL)/NPB:Alq_3/Alq_3/Ca/Al, as has been used before when discussing the GSP of doped layers. A sketched energy level diagram with layer structure is given in Figure 6.1 for these two sample types, the stack for TOF samples is given in Section 6.2. For both, monopolar and bipolar devices, the bottom contact or anode can either be bare ITO, or ITO covered with the commercially available PEDOT:PSS formulation Clevios HIL1.3. Furthermore, for some devices, additional workfunctions are available with Clevios CH8000 and AI4083, also PEDOT:PSS formulations. It was shown in Section 3.1.1 that these substrates all exhibit different workfunctions, which should consequently lead to different hole injection barriers in the devices.

6.1.1. Barrier dependent I-V characteristics on monopolar devices

In single carrier devices, when electron injection is effectively blocked from both contacts, the current through the device is dependent on the bulk transport properties as well as the injection of holes only. If one contact is held constant, while injection properties are altered at the other one by changing the anode material and workfunction, the difference in current can be a measure for the hole injection barrier from the latter.

Nominal workfunctions as determined in Section 3.1.1 are 4.5 eV, 5.0 eV, 5.1 eV and 5.7 eV for the different bottom contacts ITO, AI4083, CH8000 and HIL1.3, respectively. For the top contact, a sequence of HATCN and Gold is evaporated on the device, which is reported to show very low barriers [159] and might hence serve as a reference for hole injection compared to the bottom contact. On top of all different HILs at the bottom contact, varying doping ratios for Alq_3 in NPB are processed and measured, with an interface charge density ranging from 0 mC m^{-2} for neat NPB to roughly 0.9 mC m^{-2} with 11 % of Alq_3 doped into NPB. Note, that the sheet charge densities cannot be measured directly at the monopolar devices,

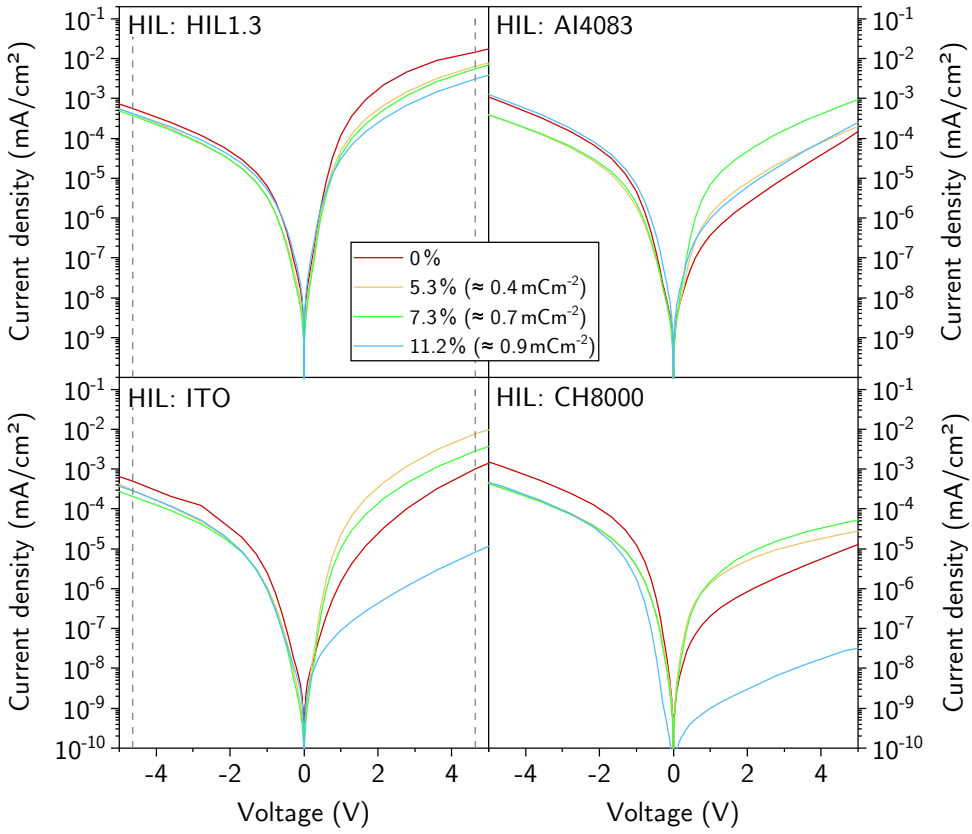

Figure 6.2.: Measurements on NPB/Alq_3 mixtures in hole-only devices. The contacts are as such that the current on the left side or with negative voltage resembles injection through the HATCN/Gold interface, whereas the positive voltage range / right side shows injection over the bottom contact/NPB:Alq_3 interface. The bottom contact materials used for each device are noted in the graph. Vertical lines denote the voltage used to extract the injection quality discussed below.

the given values are instead taken from reference measurements discussed earlier in Section 3.4.

The current-voltage characteristics for all four bottom contact materials are shown in Figure 6.2, where in this graph, only the forward sweep is given. However, only those measurements are included for investigation, where forward and backward sweep are equal within errors. The normal, undoped NPB hole-only device with no GSP is given in red, which will be discussed first. Here, the hole current is almost one order of magnitude higher with HIL1.3 on the bottom contact compared to bare ITO, which can be related to the high substrate workfunction of HIL1.3 and the corresponding low hole injection barrier. Also, for both HIL1.3 and bare ITO, currents injected through the bottom contact are higher than those, when HATCN/Au is the injection contact, which is not the case for CH8000 and AI4083. When comparing the neat NPB HTL with different doping ratios, a similar trend is visible for all bottom contacts, but HIL1.3. For HIL1.3, rising doping ratios lead to a steady decrease of the current by almost one order of magnitude. In case of low workfunction

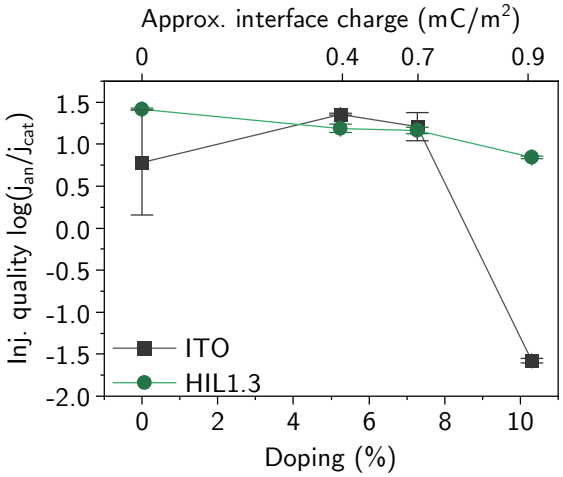

Figure 6.3.: Logarithm of the forward to reverse current ratio evaluated at 4.65 V. Higher values therefore represent an improved contact at the anode, as does a rising trend indicate improved injection.

or high-barrier hole injection through ITO on the bottom/NPB:Alq_3 side, however, moderate doping of roughly 5 % leads to the highest currents in the device. Likewise, also bottom electrodes with AI4083 and CH8000, whose workfunctions appear to be similar and in the range of 5.0 eV to 5.1 eV, show a maximum current for doping ratios greater than 0 % but below the maximum of 11 %. Still, the investigation is limited to the extreme cases of HIL1.3 and bare ITO, which should result in the smallest and highest barrier, respectively. AI4083 and CH8000 do show the same trend, but the current through the bottom contact is still exceptionally low, which is unexpected especially for AI4083 – CH8000, however, is known to have very low conductance. Additionally, the top contact side is subject to more change compared to ITO and HIL1.3. It is therefore assumed that additional limits exist for those two PEDOT:PSS formulations that for now will not be discussed further.

For better comparison and to further investigate those findings, a figure of merit describing the "injection quality" of the bottom contact is introduced. In the described devices, the contact through HATCN/Au is reproducibly good with only little influence on the current and this side is therefore taken as a reference. The injection quality Q_{inj} is then calculated by logarithm of the ratio of the current injected through the HATCN/Au top contact and that through the ITO/(HIL) bottom contact taken at a high injection voltage above the usual driving voltage of an NPB:Alq_3 OLED of $V_{\mathrm{ext}} = \pm 4.65\,\mathrm{V}$. Note, that the exact choice of this voltage will not influence the result as measured curves do not intersect. Thus,

$$Q_{\mathrm{inj}} = \log\left(\frac{j_{\mathrm{bottom}}}{j_{\mathrm{top}}}\right)\Bigg|_{V=\pm 4.65\,\mathrm{V}} . \tag{6.1}$$

The position of this evaluation is marked in Figure 6.2 with gray vertical lines and the result is shown in Figure 6.3. Positive values of Q_{inj} indicate a higher current and hence better hole injection though the bottom contact, while negative values state the opposite. Likewise, a positive slope of the plot in Figure 6.3 indicates improving and a negative slope impaired injection through the ITO/(HIL)-side interface. As

a side effect, by division, effects of changes in bulk charge transport alone due to changed mobility are minimized as they appear on both sides equally. In turn, of course, mobility dependent effects at the contacts like space charge or diffusion-limited injection [75] will still be visible. Please note, that the description of carrier injection through this HATCN layer is non-trivial [288] and the influence of the polar nature of the active layer on carrier injection through HATCN is also unknown and not subject of this work.

At first, the case of pure ITO as bottom, hole injecting contact is considered. For low doping of up to 5 % to 7 %, the measurement shows higher current or better injection for rising Alq_3 concentration, leading to a positive trend in the injection-quality plot. With further increasing doping ratio the graph does not show any saturation, instead the injected current decreases again, as indicated by a negative trend in the injection quality graph. The second case, with HIL1.3 at the bottom contact, shows a negative trend over all different doping ratios. Interestingly, the current injected through HIL1.3 is clearly higher by approximately one order of magnitude compared to the HATCN/Au contact, directly evident due to positive values in the plot. The HIL1.3 samples also outperform the ITO stack at 0 % and 10 % doping, but not at the optimal doping ratio around 5 %.

When the presumed barrier into NPB is already low, which is the case for HIL1.3 with $\Phi_{\mathrm{HIL1.3}} \approx 5.7\,\mathrm{eV}$ [117], the effective barrier is subject to Fermi-level pinning: Greiner *et al.* have shown that the resulting injection barrier saturates at a finite, non-zero value, even if the substrate workfunction is near or larger than the ionization potential (IP) of the organic material [72]. It is therefore unlikely that any improvement of injection due to GSP is possible, considering the ionization potential of NPB at 5.3 eV. Instead, the measurement in Figure 6.3 shows a small negative trend, indicating impaired injection through the HIL/HTL interface. By contrast, with an ITO workfunction of roughly 4.6 eV, a nominal injection barrier of up to 1 eV can be expected in the first case, which gives room for improvement. Up to roughly 5 % the current is indeed positively influenced. This is in good agreement with previous observations of the effect of the GSP on electron injection from the cathode to the ETL in polar OLEDs [3, 11]. The decreasing current through the ITO/NPB:Alq_3 interface for higher doping ratios, however, is surprising, not only because it differs by more than two orders of magnitude from the undoped case. From the calculation of the aforementioned figure of merit one can conclude that a change in bulk carrier transport of the NPB:Alq_3 mixture alone cannot be the root cause for the observed optimum, as its influence would affect both the forward and reverse side of the current-voltage characteristic equally. Hence, interface-bound effects such as changes in barrier e.g. by altered energy levels of NPB and/or mobility limited carrier injection have to be accounted for.

6.1.2. Mobility determination by MIS-CELIV

A changed doping ratio of Alq_3 in NPB might change the mobility in the device by increasing the length of individual percolation paths [277] or by changing the disorder in the material. NPB is reported to show signs for correlated disorder in charge transport [129], added dipolar disorder might thus influence the charge transport. In Section 5.1, the application of the MIS-CELIV technique on polar OLEDs has been successfully described, which will now be used to extract the charge carrier mobility

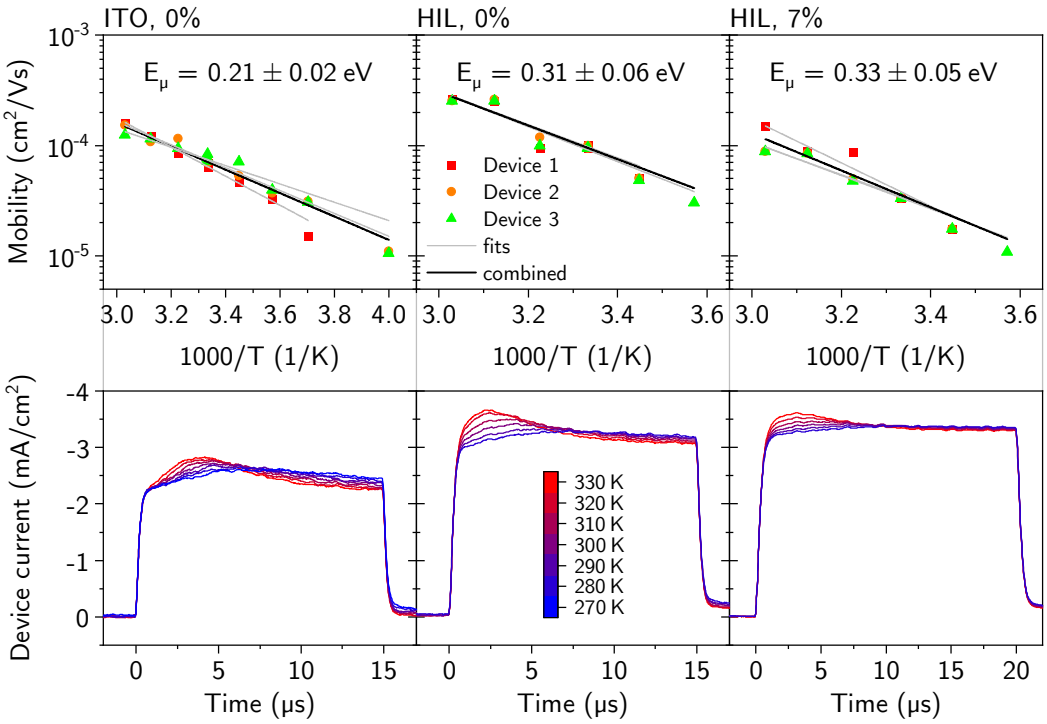

Figure 6.4.: Three example temperature series on ITO (0 %) and HIL1.3 (0 % and 7 %). Both the extracted mobilities and example CELIV transients are shown, although not all temperatures are included in the CELIV series to enhance lucidity of the individual graphs. Fits to obtain E_μ are given individually to emphasize the difference between individual devices (gray line) and the average (black line).

and activation energy for doped NPB:Alq_3/Alq_3 OLEDs.

CELIV transients are evaluated using the small-charge injection technique and the mobility is calculated using the analytic formulas discussed in Section 5.1. The measurements are conducted in a LN_2 cryostat from 330 K down to 230 K. However, in most cases, measurements below 270 K are dominated by lateral conductance of the hole injection layer, if present. Peak-search and calculating the mobility is done with the Paios software suite with a 1 MHz low pass filter applied to remove residual noise. Two datasets can be extracted from the measurements, the doping-dependent mobility at room temperature to be compared e.g. with time-of-flight measurements discussed later on in Section 6.2 and the change in mobility activation energy.

In Figure 6.4, three examples of CELIV transients and the extracted mobilities are shown. For each combination of doping ratio and anode layer, ITO or HIL1.3 in this case, multiple devices are available. For some parameter sets, the individual devices differ more than for others – in the graph, individual fits of the activation energy are thus shown in light gray, whereas the average fit is given in black to emphasize the difference. This effect is especially large for ITO based samples, where the signal-to-noise ratio is weak because samples directly on ITO are manufactured with four times smaller sample area to avoid short circuits. All transients were recorded with a ramp rate of 200 V ms^{-1} and the ramp time is adapted for low mobility devices.

Doping (%)	on ITO E_μ (meV)	on ITO σ (meV)	on HIL1.3 E_μ (meV)	on HIL1.3 σ (meV)
0	211 ± 16	111 ± 4	310 ± 60	134 ± 13
3.3	197 ± 25	107 ± 7	338 ± 68	140 ± 14
5.3	253 ± 47	121 ± 11	338 ± 35	140 ± 7
7	279 ± 106	127 ± 24	328 ± 47	138 ± 10
11.3	– –	– –	254 ± 31	122 ± 7

Table 6.1.: Extracted mobility activation energies E_μ and disorder parameters σ for all doping ratios and with anode materials being ITO or HIL1.3. For 11.3 % of doping, no successful CELIV transient was possible with bare ITO, so no data is available here.

At first, the change in activation energy with respect to the doping ratio is discussed. The results for all doping ratios and the two anode materials ITO and HIL1.3 are given in Table 6.1 and noted in Figure 6.4. A graphical representation of all values obtained from CELIV transients is given in Figure 6.7 in Section 6.1.3 together with data from impedance spectroscopy.

Directly visible from the data is that the extracted activation energy is different for samples with HIL1.3 and ITO. This is in line with the findings discussed in Section 5.2, where a higher systematic error is expected and the extracted mobility activation energy is by trend under-estimated for higher barriers, which is the case for ITO. Thus, absolute values extracted here should be treated with care, a comparison of the trends and relative changes is, however, still valid. Although the lateral conductance of samples directly on ITO is very low and measured $j(V)$ characteristics or impedance spectroscopy usually produces good results, CELIV suffers from overall low sample current due to the small sample area. A possible remedy would have been to increase the CELIV ramp speed, however, the setup in question involved several meters of coaxial cable, partly immersed into the cryostat, which makes higher frequencies or faster transients difficult to handle.

Nevertheless, the resulting activation energies are in the range of what is expected and has been seen in the past for different devices, see e.g. our publication in reference [14]. For NPB, the correlated disorder model for the mobility has been suggested in the past [129]. A direct fit of the model equation for the mobility given in Equation 1.13 on the measured data is challenging because of missing parameters. However, a simple transfer to the width of the DOS in the simpler Gaussian disorder model can be attempted with the relation

$$\frac{E_\mu}{\mathrm{k_B}T} = \left(\frac{2\sigma}{3\mathrm{k_B}T}\right)^2 , \tag{6.2}$$

the resulting values for σ are given in Table 6.1 alongside to E_μ. With increased doping, a clear rise of σ or E_μ could have been expected. Instead, it is rising for devices with ITO at the anode and lowering in the case of HIL1.3. From this point of view, the width of the DOS of NPB does not seem to be widened significantly by dipolar doping of Alq_3.

Still, the absolute mobility changes by almost one order of magnitude, as seen

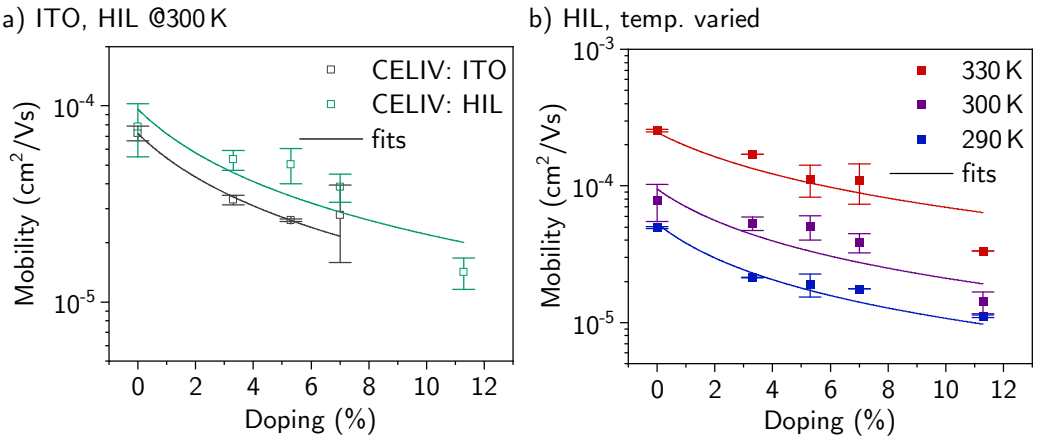

Figure 6.5.: **a)** Extracted absolute mobilities for both HIL1.3 and ITO at the anode. No measurement was possible on ITO with 11.3 % of doping. The values are taken from the temperature series measured on all samples, it is thus measured exactly at 300 K and not at room temperature. Straight lines show the fits using a trap-affected mobility. **b)** Fits on temperature dependent series on HIL1.3 only.

in Figure 6.5. In contrast to the activation energies, where $E_{\mu,\mathrm{ITO}}$ is always lower than for the HIL1.3-based samples, only a small systematic difference in absolute mobilities at 300 K is observed, where in addition $\mu_{\mathrm{HIL1.3}} > \mu_{\mathrm{ITO}}$. Given the HOMO level of Alq_3 being approximately 0.3 eV higher than the NPB HOMO, classic charge trapping is unexpected for holes in Alq_3-doped NPB. However, as both transport levels are subjected to disorder and a Gaussian shape, the difference between both levels can be in fact smaller. Assisted by the ordered dipoles in possible Alq_3 agglomerates, carriers might be held at Alq_3 dopants, even if the activation energy for leaving the captured state is very small. Additionally, charge transport through doped NPB is hindered by extended percolation paths, if Alq_3 is not considered a transport site for holes in the system [277].

Still, in case of trap limited mobility, a relation to the trap-free mobility is given in Equation 1.14 with

$$\mu = \mu_{\mathrm{tl}} \left[1 + c \exp\left(\frac{E_{\mathrm{t}}}{k_{\mathrm{B}} T} \right) \right]^{-1} , \tag{6.3}$$

where the concentration of traps c affects the trap-free mobility μ_{tl} and requires the additional activation energy E_{t} for de-trapping. The fits of Equation 6.3 to the data of the CELIV mobility at 300 K are presented in Figure 6.5a, which indeed describe the decay of the mobility reasonably well with $E_{\mathrm{t}} = (91 \pm 5)$ meV. The model holds true also for temperature dependent data, as seen in Figure 6.5b for HIL1.3 based measurements. However, a simple exponential decay would also fit the change in mobility resembling a straight line in a semi-logarithmic plot. Furthermore, only one order of magnitude of dynamic range is available to fit the exponential on the measured mobility, which leaves a large amount of uncertainty also when fitting is done with weighted input data. Even if trapping is not a factor in the device, the additional energy needed for charge carriers to travel through the bulk with a larger

number of hopping sites due to the increased path length might be modeled similar to an activation energy. A deeper investigation of the change in mobility with doping due to changed percolation paths, however, would require microscopic simulations such as kinetic Monte Carlo modeling that has not been done in the scope of this work.

6.1.3. Impedance on bi-layer MIS structures

To investigate injection barriers between anode and NPB, temperature dependent impedance spectra are recorded on bilayer devices with doping ratios between 0 % and 11 % of Alq_3 in NPB. Again, the anode material was varied, in this case bare ITO and HIL1.3 is compared. Example measurements of two devices and fits against the 2RC model to determine relaxation frequencies are shown in Figure 6.6a. The fits converge with very low error over the whole frequency range for ITO and the 2RC model thus describes those devices very well. In case of HIL1.3, a divergence from the model is visible for low frequencies below 1 kHz. This is due to the lateral conductance of PEDOT:PSS or HIL1.3 leading to an effective increase of the active area of the device for low frequencies [241]. The error in the extracted relaxation frequency is still low, as the relevant portion of the spectra is in good agreement with the model. The extracted absolute relaxation frequencies for all devices are shown in an Arrhenius plot alongside with fits used to determine the activation energies in Figure 6.6b.

From the raw relaxation frequencies, without extracting activation energies or barriers, the difference in nominal barrier is already visible. On bare ITO (dashed lines in Figure 6.6b), the larger energetic offset leads to considerably higher resistivity and hence orders of magnitude lower relaxation frequencies compared to samples with HIL1.3 (solid lines) as hole injection layer. Also, for ITO, highest relaxation frequencies are observed for moderate doping ratios, whereas samples with HIL1.3 on the anode follow a steady decay in relaxation frequency with doping ratio. Additionally, it is already visible by bare eye that the fits to the data for the ITO based samples vary stronger in slope, with the 5 % mixture showing the smallest slope alongside with the highest relaxation frequency among this series. Likewise, the high temperature relaxation frequency of ITO based samples exhibit a spread of 2.5 orders of magnitude, whereas samples with HIL1.3 on the anode all reside within one order of magnitude. This is consistent with the findings from current-voltage characteristics, where the highest current in case of ITO was observed for 5 % of doping alongside with larger differences for higher doping, too, while HIL1.3 only changes by one order or magnitude to lower currents.

From the slopes of the temperature dependent measurements, the activation energies for charge carrier injection can be obtained. Figure 6.7 shows the extracted activation energies calculated by fitting the exponentially activated injection as described in Section 5.2 on temperature dependent $C(f)$ measurements. Additionally, the mobility activation obtained from temperature dependent CELIV mobilities in Section 6.1.2 is included. Subtracting mobility activation from the measured overall frequency activation calculates to the injection barrier given by $E_{\mathrm{inj}} = E_{\mathrm{act}} - E_{\mu}$, which is depicted in the bottom part of the graph. In case of a high-workfunction substrate like HIL1.3 with $\Phi_{\mathrm{HIL1.3}} \approx 5.7\,\mathrm{eV}$, the presumed effective barrier for hole injection into NPB is already low and additionally affected by Fermi-level pinning [72],

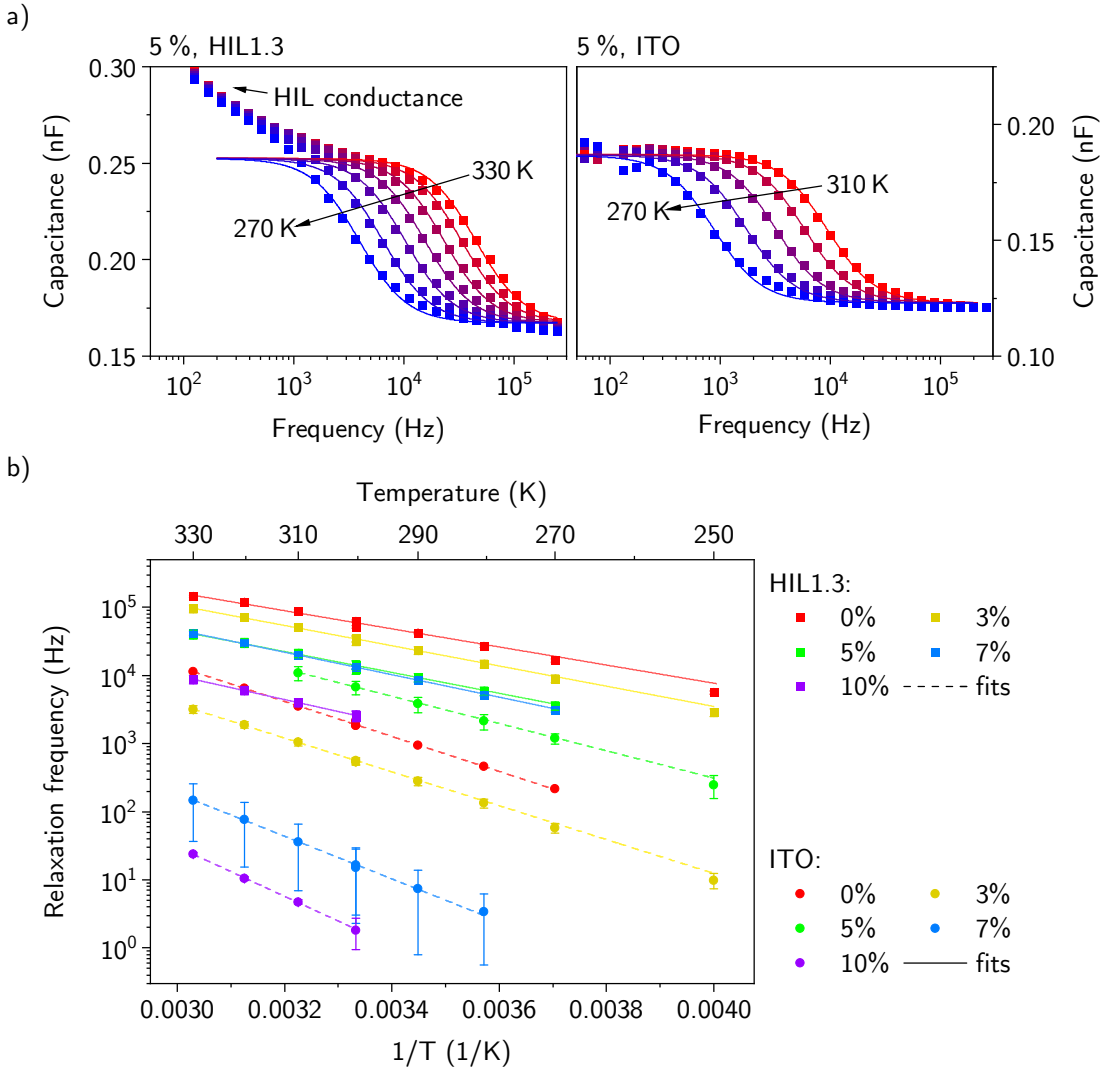

Figure 6.6.: **a)** Examples for C-f measurements on ITO and HIL1.3 with 5 % of doping. The ITO based sample degraded above 310 K and the measurements at 320 K and 330 K are hence not shown. Straight lines connecting the datapoints are fits based on a simple 2RC model. **b)** Results of the temperature dependence of the relaxation frequency determined by the fits for different doping ratios. Shown are results with ITO (dashed line fits) and HIL1.3 (straight line fits) based devices. Points and squares denote the measurements at various temperatures averaged over different pixels, lines are the fits. Temperature is varied between 330 K and 250 K, depending on the stability of the respective samples and contacting.

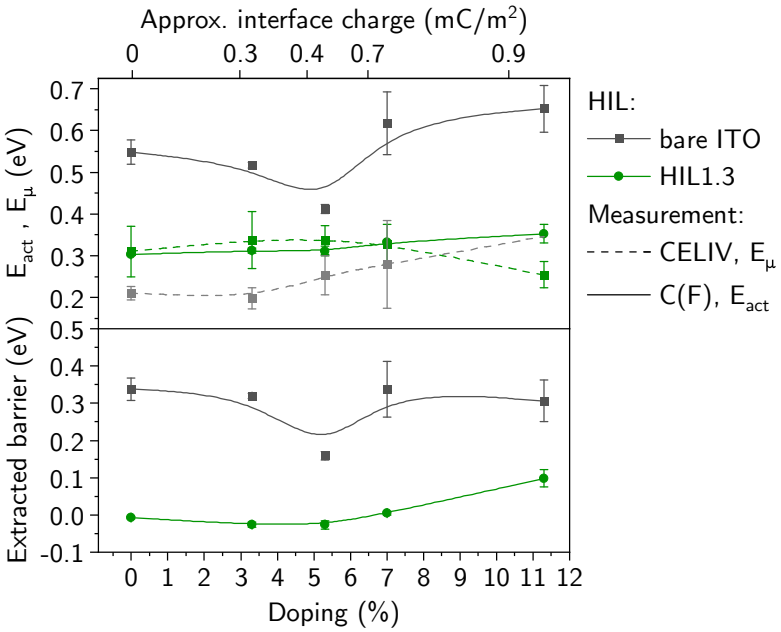

Figure 6.7.: Extracted parameters from impedance spectroscopy and MIS-CELIV for different doping and barriers. Samples with the same anode material are connected with a spline as a guide to the eye. The top portion shows the measurement quantities, solid lines belong to the frequency activation, dashed lines to the mobility activation. The bottom portion shows the calculated injection barrier.

as seen in current-voltage characteristics, too. However, as seen in Section 5.2, the method used to determine the barriers can underestimate the extracted value for injection barriers below 300 meV, which can also be seen here with values around zero. Still, the overall picture shows a very small barrier that is not further lowered by the increasing interfacial charge density introduced with doping.

For bare ITO with $\Phi_{\mathrm{ITO}} \approx 4.6\,\mathrm{eV}$, however, a lowering of the barrier with increasing interfacial charge density is possible and indeed observed for moderate doping of up to 5 %. Given that the subtraction of the mobility activation already accounted for the mobility effect at the interface in the case of impedance spectroscopy, the rise in barrier for higher dilutions must be attributed to different processes at the ITO/NPB:Alq_3 interface or in the bulk of the doped NPB. Furthermore, although CELIV is well established to extract carrier mobilities, different pitfalls for determining the exact value are known [13, 233], see also Chapter 5. To get another view on the change in charge carrier mobility due to dipolar doping, time-of-flight measurements are conducted on four different samples with doping ratios ranging again from 0 % to 10 %.

6.2. Time-of-flight measurements of dipolar doped NPB

Time-of-flight (TOF) is a well-established method to determine the carrier mobility of (photo-)excited carriers in semiconductors. It was probably first used by Spear *et al.* to measure carrier mobilities in Selenium [289]. At that time, however, an

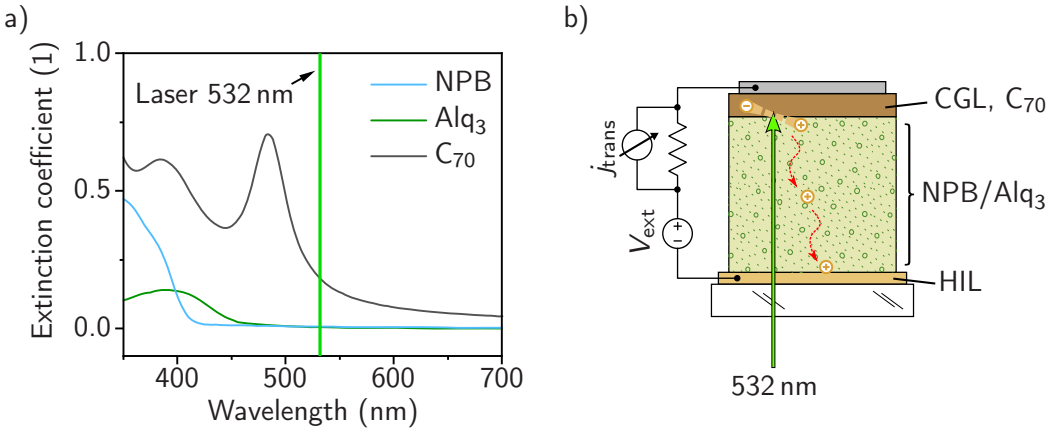

Figure 6.8.: a) Extinction coefficients (k) of NPB, Alq_3 and C_{70} in relation to the excitation wavelength at 532 nm. Data available from refs. [124, 168] **b)** Schematic sketch of the TOF experiment on solar cells with charge generation layer (CGL). The external field drives the charge carriers to the respective electrode, the majority of the time is needed for the hole-drift through NPB.

electron gun was used to excite charge carriers. The experiment was since adopted to optical excitation and for organic samples [290] and has evolved to one of the most prominent techniques to determine charge carrier mobilities [222]. All TOF measurements were conducted by Motiur Rahman Kahn, then employed at the Soft Matter Physics Group at the University of Potsdam, Germany, on samples that I specifically manufactured for TOF experiments. Evaluation and comparison of the measurement results is done by myself.

A detailed discussion of the TOF experiment would leave the scope of this work, thus a brief introduction is given in the following. For explanation, the basic principle is sketched in Figure 6.8 alongside with the absorption spectra of the materials in question. TOF measures the transit time of photogenerated carriers by evaluating the measured current transient in dependence of time. The applied electric field can additionally be varied to study field dependent mobilities. For this purpose, the material (mixture) in question has to be incorporated in a solar cell stack allowing effective light absorption and carrier generation. In traditional TOF experiments, light absorption can theoretically take place in the whole sample area. The layer thickness and optical density at the excitation wavelength, however, should ensure that the light is absorbed in a region much thinner than the sample thickness [290]. In the case of doped NPB:Alq_3, this approach would pose two major problems. At first, NPB as well as Alq_3 absorb mostly in the deep-blue to near-UV wavelength range and thus only a small window is available for excitation wavelength until the substrate with ITO on standard borosilicate glass starts to become opaque. Additionally, absorption of NPB and Alq_3 is weak and both overlap considerably, a strong laser intensity or thick films would be required for a suitable signal. However, hole transport in electrical devices is most likely taking place in NPB only, as Alq_3 has a very low hole mobility [63] and direct hole injection is difficult [291]. The overlapping absorption of NPB and Alq_3 would not allow to restrict carrier generation to NPB only and a different charge generation layer is therefore needed [222].

To accomplish this, solar cells are built with the (doped) NPB layer as donor and C_{70} as acceptor. The acceptor layer is acting as a charge generation layer [222], injecting holes into NPB. Its thickness needs to be small enough not to overlay the electron extraction current with any measured hole transient. Though no reference data is available for NPB in solar cells, its sister-molecule α-NPD that was briefly introduced in Section 2.1.1, has successfully been used in this cell design in the past [167]. Furthermore, C_{70} features high absorption in the visible wavelength range, where almost no overlap is existent with NPB or Alq_3 absorption.

The cells used for this work feature a 200 nm thick transport or donor layer of doped NPB on unstructured ITO topped with a thin (≈20 nm) charge generation or acceptor layer of C_{70}. An exciton blocking layer of 5 nm bathocuproine (BCP) topped with Aluminum comprise the cathode. Measurements are carried out by exciting the samples with a wavelength-tunable, diode pumped, Q-switched Nd:YAG laser (NT242, EKSPLA) with 8 ns pulse duration time at an excitation wavelength of 532 nm and 500 Hz repetition frequency. A 50 Ω resistor is used to measure the current, which is recorded with an Agilent Infiniium DSO9054H oscilloscope.

Four transients of the cells measured are shown in Figure 6.9a for pure NPB and doped with 2 %, 5 % and 10 % of Alq_3, all in double-logarithmic plot. Ideally, a TOF transient would feature a plateau after the initial current spike induced by the laser pulse, followed by a decrease starting at the transit time t_{tr}, which relates to the carrier mobility with [222]

$$\mu = \frac{d^2}{V_{\mathrm{ext}} t_{\mathrm{tr}}} \ . \tag{6.4}$$

The transit time is usually obtained by fitting a triangular shape or two straight lines and calculating the intersect. At the end of the transient, prior to the decrease in photocurrent, a peak or cusp is sometimes observed. This was the case for pure NPB measured at higher excitation energies (not shown here) and can be a hint to an inhomogeneous electric field in the layer, which arises from a space charge effect at high carrier density [292]. In case of dispersive transport, no plateau is observed. Instead, the photocurrent decays steadily after excitation in linear space, though sometimes a kink or change in slope can be observed in a double-logarithmic plot that is also dependent on t_{tr} [222, 290, 292].

Although no qualitative investigation of the dispersive nature of the transport was made, the increasing downward slope of the asymptote at the plateau region (before t_{tr}) is already visible by bare eye for all doped devices. Similar observations for doped NPB have been reported in literate by Fleissner *et al.* [293], although in this case, the dopant did introduce hole traps into NPB. In case of Alq_3 the HOMO is lower than in NPB and Alq_3 doping will thus not introduce hole traps. Instead, scattering and extended pathways for holes through NPB are expected to cause the dispersive nature of transport. A comparative study by Tong *et al.* addressed the influence of dopants introducing traps or scattering sites [277] with one doping concentration only, nevertheless it supports the finding of this work. Thus, although no hole traps are expected to be found, the increasingly "blocked" pathways for carriers through NPB provoke dispersive transport.

The extracted mobilities for different doping ratios are given in Figure 6.9b. Before referring to the absolute values, the field dependence of the results is discussed. According to the Poole-Frenkel law of field dependent mobility (see Section 1.1.3,

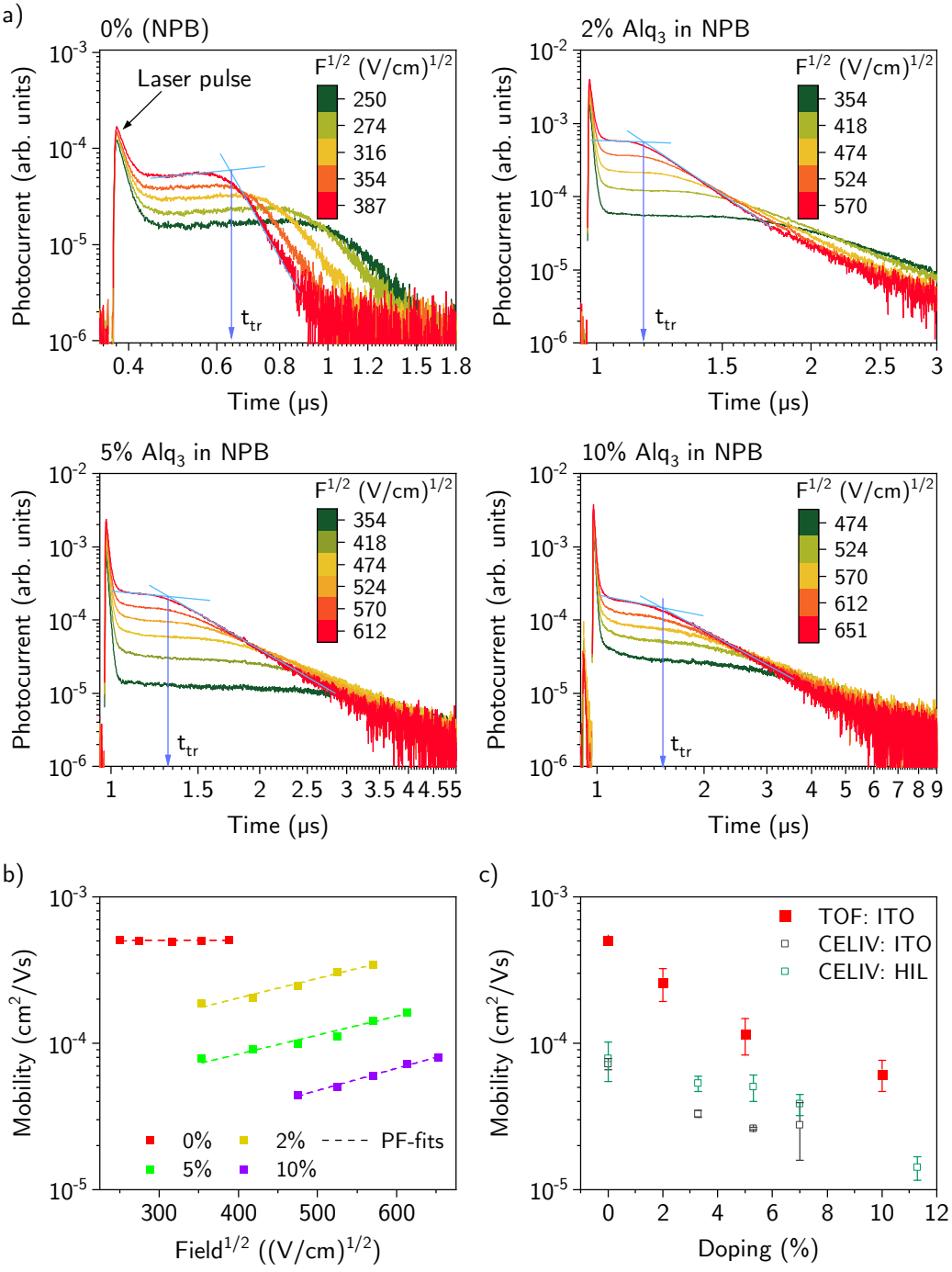

Figure 6.9.: **a)** Time-of-flight transients with different applied fields for neat and doped NPB. Pure NPB transients feature only a small upward slope in the plateau region before t_{tr}. In contrast, the doped NPB film shows a strong downward slope indicating dispersive transport. **b)** Measured mobilities in dependence of applied field with fits of the Poole-Frenkel mobility shown. **c)** Absolute mobilities extracted from CELIV and TOF measurements. Averaging took place over different samples of the same ratio for CELIV and different fields ranging from 300 $(V/cm)^{1/2}$ to 400 $(V/cm)^{1/2}$ for TOF.

Equation 1.11) $\mu \propto \exp\left(\beta\sqrt{E}\right)$. The characterization of the field dependence is thus done by fitting a simplified version of the Poole-Frenkel law with

$$\mu = \mu_0 \exp\left(\beta\sqrt{E}\right) \ ,$$

where β is a constant describing the slope of the semi-log plot. It is thus common practice to plot the mobility semi-logarithmic in dependence of the square root of the applied field. If the field dependence of the mobility follows the Poole-Frenkel law, it will yield a straight line, which is the case for all doping ratios.

The measurement of undoped NPB does not show a pronounced slope with increasing field, indicating almost no field dependence of charge transport in this NPB layer. This can point to a thin film of high purity, though no clear picture exists in literature. Multiple authors found a field dependence of pure NPB [277, 294], whereas others state NPB mobility to be mostly field-independent [1, 293]. The β-parameter for field dependence in undoped NPB is $5.83 \times 10^{-5}\,(\mathrm{cm/V})^{1/2}$ and therefore two orders of magnitude lower compared to the doped films, which all exhibit $\beta \approx 3.2 \times 10^{-3}\,(\mathrm{cm/V})^{1/2}$ without considerable difference. For Alq_3 doped NPB, the field dependence is thus independent of the doping ratio, only the zero-field mobility is subject to change. A more detailed analysis of the doping effect on field dependence or disorder would require temperature dependent measurements, which were not available with the measurement setup used here. Fits to more sophisticated mobility models like Gaussian or correlated disorder are thus not attempted.

The absolute values of the obtained mobilities match nicely to previously reported literature data. For undoped NPB, Fleissner *et al.* published values that average to $5.5 \times 10^{-4}\,\mathrm{cm^2\,V^{-1}\,s^{-1}}$ [293] in the same range of fields investigated in this work. Tong *et al.* published $3.9 \times 10^{-4}\,\mathrm{cm^2\,V^{-1}\,s^{-1}}$ [277] and Chen *et al.* $5.3 \times 10^{-4}\,\mathrm{cm^2\,V^{-1}\,s^{-1}}$ [294], again averaged over fields between $200\,(\mathrm{V/cm})^{1/2}$ to $400\,(\mathrm{V/cm})^{1/2}$. No literature data is available for higher doping ratios. Tong *et al.*, however, published TOF measurements doped with 1.5 % of Alq_3 [277]. The absolute values and field dependence in their work match the measurements made here with 2 % of doping almost quantitatively.

It can therefore be assumed that the calculated mobilities are correct also for higher doping ratios, which allows to compare the results with CELIV. Figure 6.9c shows the absolute mobilities extracted from CELIV and TOF dependent on the doping ratio. It is apparent that TOF, compared to CELIV, yields mobilities higher by approximately one order of magnitude. The field present in the device during CELIV transients is usually calculated at the point in time, where the mobility is calculated [13] and amounts to $400\,(\mathrm{V/cm})^{1/2}$ to $600\,(\mathrm{V/cm})^{1/2}$, which is the same range as in case of TOF and thus cannot be the reason. However, the mobility can depend on the carrier density besides the electric field, which was determined neither from TOF nor CELIV transients. Especially for very high charge carrier densities possible in TOF, holes can occupy lower energetic states and will not fully relax to the usual transport level, if the layer thickness is not large enough, which will lead to higher mobilities [51]. This difference has also been found previously [13], where it was found that the CELIV mobilities calculated with the standard formulas can yield lower values in comparison to e.g. fitting using drift-diffusion. This was, however, not done here.

In general, the effect of doping concentration on the mobility is systematic from both CELIV and TOF and follows an exponential decay (straight line in semi-log plot). Similar to the case with CELIV in Section 6.1.2 and despite trapping of charges is unlikely in the NPB:Alq_3 system, a fit according to the trapped charge mobility estimation presented in Equation 1.14 results to an activation energy of (108 ± 7) meV for TOF only and (95 ± 4) meV in average for CELIV and TOF.

6.3. Investigation of the injection barrier using UPS

In this section, the ultraviolet photoelectron spectroscopy measurements conducted at Chiba University, Japan, will be discussed. The principal setup design and theory of parameter extraction is described in Section 2.7. These samples feature an incomplete layer stack of ITO/NPB:Alq_3 to measure the contact barrier between ITO and the HTL with a maximum thickness of 10 nm, measured in steps of 1 nm, 2 nm, 3 nm and 10 nm. In evaporation, doping concentrations of 2 %, 5 % and 10 % were realized alongside with pure NPB. No measurement of pure Alq_3 was attempted and thus existing data had do be used instead. Measurements are conducted using low-energy UPS [248] with excitation energies between 4.4 eV and 21.22 eV to accurately map the HOMO region of the samples and determine the barriers. Excitation energies are tuned by a monochromator (Bunkoukeiki M25GTM-DZ) from 4 eV to 5 eV using a Xe lamp. The range up to 8 eV was available with a D_2 lamp, where the standard excitation wavelength of 7.7 eV corresponds to the emission peak of the D_2 lamp in the UV. For wide range scans of the levels $HOMO^{1+n}$, a He discharge lamp was available, with a principal transition at 21.22 eV. Photoelectron analysis is done with a model RESOLVE120 hemispherical analyzer from PSP Vacuum Technology.

6.3.1. Pure NPB spectra and ITO workfunction

At first, different UPS measurements on pure NPB are evaluated according to the barrier. Additionally, the ITO workfunctions can be determined from UPS spectra and put into comparison with existing data. This allows to compare the results gained within this work with literature data for NPB on ITO and serves as a benchmark for data extraction. All spectra obtained for pure NPB films at 10 nm thickness are visible in Figure 6.10a.

From the spectra, the HOMO onset and secondary electron cutoff (SECO) is extracted in linear scale with a sectionally defined line fit. As described in Section 2.7, the injection barrier is gained from the distance of the HOMO onset to the Fermi level, which in the graph has already been set to 0 eV of binding energy. The position of the Fermi edge with respect to the detector's energy scale is determined from the spectra recorded to measure the substrate workfunction for each new substrate by fitting a Fermi-Dirac statistic. Respective data and fits are depicted in Section A.2 of the appendix. To determine the ionization potential (IP) of the NPB layers, the difference between HOMO onset and SECO is calculated. The dataset contains five measurements of which the first two are measured on the same sample created as part of the series to vary the doping concentration. These measurements differ only in the width of the detector energy window, the higher intensity spectrum is recorded with a greater window. Both extracted values should yield the same result and indeed

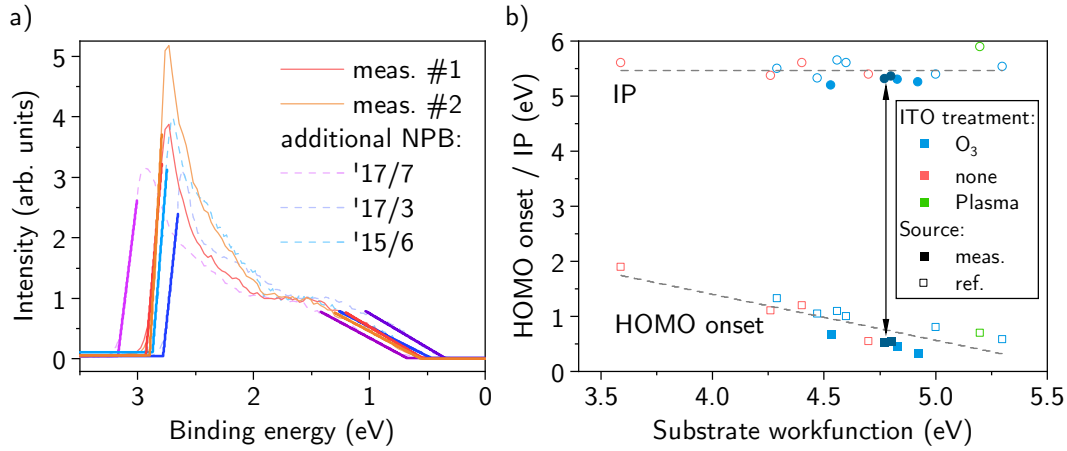

Figure 6.10.: **a)** UPS spectra in linear scale for different neat NPB layers. Measurements number one and two are made on the same NPB layer grown in the series of doping ratio variation, but with a different detector window in energy. Other spectra have been recorded with the same instrument at different times. **b)** Ionization potential (IP, top) and barrier (HOMO onset, bottom) versus substrate workfunction. In this regime, the barrier still scales linearly with the workfunction. The IP is constant. Literature data for various substrate treatments is given with hollow datapoints, measurements from this work are filled. The datapoints marked with the arrow are those taken from the series of doping ratios. For sources of literature data see the text.

differ only slightly in IP or HOMO onset by approximately 30 meV each. The three additional measurements were conducted at the same setup but at different times prior to my own measurement, the date is given in the legend. These measurements are otherwise unpublished and were supplied to me for comparison to allow for a greater spread of substrate workfunctions.

Extracted IP and barriers are given in Figure 6.10b alongside with literature data. It is directly evident that the data obtained within the scope of this work (given with filled datapoints) fits well into the general trend defined by literature (hollow points). Different references have been evaluated for this plot [159,295–302], where the HOMO onset or barrier and the substrate workfunction was usually taken directly from the publication. To obtain data for the ionization potential, some of the data had to be re-evaluated based on published measurements. Not all publications provided data on a possible vacuum-level shift or interface dipole. Where this information was available, however, it was considered for calculating the HOMO onset.

The ITO workfunction calculated from the SECO position amounts to 4.8 eV roughly for the samples investigated in the doping series. This is approximately 0.2 eV higher compared to the ITO substrates used for electrical measurements and can be attributed to different manufacturers and sample processing for the substrates, as plasma treatment was not available in the UPS workflow. The additional samples evaluated also showed a workfunction of about that value, only one sample amounted to only 4.5 eV. In theory, all samples had been treated and cleaned the

same way, the difference is therefore unexpected.

The ionization potential of NPB is found to be (5.33 ± 0.11) eV in average from our data, which matches with the average from literature data of (5.53 ± 0.16) eV, the total average over both data sources is at (5.46 ± 0.18) eV. In case of the barrier, our measurements also fit well to the general slope obtained from all datapoints, see Figure 6.10b. The characteristic dependence of the barrier on substrate workfunction has been observed before by different authors [72, 303] and indicates vacuum level alignment (with a slope of ≈ 1). Greiner *et al.* and others have demonstrated also for different materials [72, 303–305] that no vacuum level alignment is possible any more, if the substrate workfunction is equal to or higher than the IP of the organic. Instead, Fermi level alignment or pinning is expected with a, then workfunction independent, minimum barrier observed. In the case of the samples measured within this work with UPS this is however not the case, as the substrate workfunction is low enough and no plateau in the slope is visible nor expected until a workfunction of approximately 5.4 eV. With this comparison, the validity of parameter extraction using UPS measurements can be assumed. It can be noted that this is also true for the one sample with very low workfunction, which leads to the conclusion that the low value is indeed a device property and not a measurement error.

6.3.2. Deducing the band diagram from UPS

Low-energy ultraviolet photoelectron spectroscopy (LE-UPS) is measured for samples with 0 %, 2 %, 5 % and 10 % of doping processed on ITO. The excitation energies range from 4.4 eV to 21.22 eV to accurately map energies in the region of the highest occupied molecular orbitals (HOMO) of the mixtures for different film thicknesses in 1 nm steps. To extract the barriers from UPS, however, a high dynamic range measurement is usually not needed and thus only data obtained at 7.7 eV photon energy is evaluated in this section. For complete LE-UPS spectra, refer to Section 6.3.4.

Figure 6.11a shows the UPS measurements for all measured thicknesses on ITO obtained with 7.7 eV excitation energy. The injection barriers are determined from the difference between the HOMO onset as indicated by the gray fits and the Fermi energy at 0 eV, the same holds for the workfunction by fitting the SECO at the high binding energy side. In Figure 6.11b, the extracted barriers taken from these measurements for all thicknesses and doping ratios are plotted in a simple band diagram, as well as in Figure 6.11c against doping ratio. They seem to follow the trend seen in the activation energies extracted from electrical measurements, with a minimum for low to moderate doping concentrations. However, this minimum moves to higher ratios with increasing film thickness, while its relative depth is further lowered. The grey arrow in Figure 6.11c indicates this change as a guide to the eye. Additionally, the dashed horizontal line resembles the value for neat NPB at 1 nm. A minimum is observed for 2 % in case of a 1 nm film, shifting to approximately 5 % at 10 nm. In case of low thicknesses, the minimum is about 200 meV deep, whereas the difference amounts to only 50 meV when the samples gets thicker. The exact reason for this barrier lowering is yet to be determined. Because the HOMO level of Alq_3 is deeper by approximately 300 meV, however, a simple superposition of the two materials' signals can be excluded, as no lowering would be expected at all. Instead, a superposition would thus rather lead to an increasing barrier with increasing doping concentration. When compared to the initial value without any Alq_3 doping, the

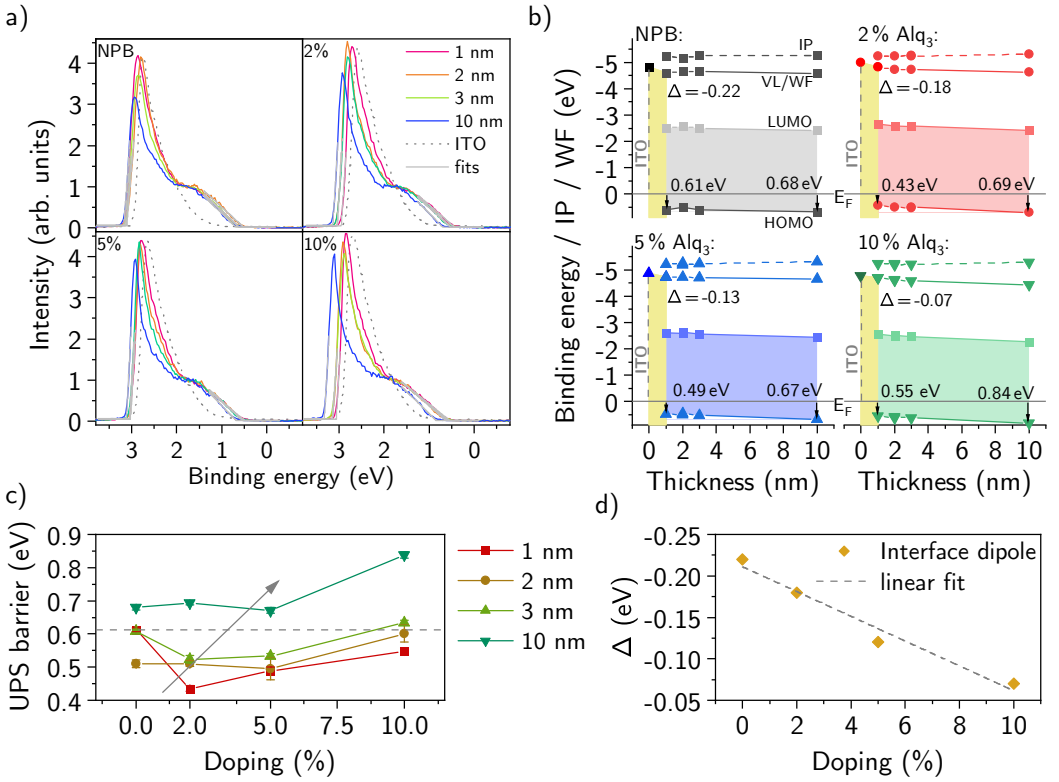

Figure 6.11.: **a)** All UPS spectra measured at 7.7 eV normalized to the HOMO shoulder. Fits are shown on the left for the SECO (workfunction calculation) and on the right for the HOMO onset (barrier). **b)** Band diagram extracted from UPS. VL, IP and the HOMO-onset are gained from UPS spectra, the LUMO is calculated by offsetting the optical gap as a reference. The energy scale is chosen to be the binding energy relative to the Fermi-level at 0 eV. **c)** Barriers per doping ratio for all thickness steps, the gray line indicates the value at 1 nm and no doping for comparison. **d)** The interface dipole with respect to the doping ratio.

barriers appear to be lower for higher doping ratios, with exceptions being the 10 nm and 2 nm sample, although for the latter the first datapoint appears out of line. In most cases, the barrier is also higher for higher doping ratios in samples of the same thickness. However, to put the UPS data into perspective, the complete band structure should be analyzed.

Besides the HOMO onset, also the ionization potential and the workfunction of the layers can be extracted from UPS, all included in Figure 6.11b. For all films, an IP of approximately 5.3 eV is gained for all four doping ratios, which is shown as dashed line in Figure 6.11b. Note, that this value is the same also for neat NPB only, thus no change in IP is observed for increasing doping concentration. This is already a hint that the spectra measured here mainly show NPB features and no contribution of Alq_3 is directly visible, because the Alq_3 IP amounts to approximately 5.7 eV [306]. Also, the barrier is thus expected to be un-pinned in all cases [72], considering an ITO workfunction of 4.8 eV.

From the change in vacuum level observed through a workfunction shift when going from ITO at 0 nm to 1 nm of organic film, the formation of an interface dipole at the metal-organic interface upon evaporation of the organic layer is visible. This is common to metal-organic interfaces and reported for NPB [307] as well als Alq_3 [10] and will be discussed in the next paragraph. A second apparent feature is the slight, but steadily shifting HOMO onset observed without further pronounced features for increasing film thickness. Both, HOMO onset and vacuum level or effective workfunction (solid lines), are shifting towards higher binding energies with increasing thickness, while the ionization potential (dashed line) is almost constant (**??**b). This band bending can be a result of the dipolar surrounding of NPB when doped with Alq_3. A similar dependence has been directly observed and related to the giant surface potential for neat Alq_3 layers [10] and has also been seen in kinetic Monte Carlo simulations for neat polar layers by Friederich et al [47]. With this assumption, the change in vacuum level for the doped layers should be related to the ordered Alq_3 dipoles, also leading to the GSP measured e.g. with Kelvin probe. See the next section for a discussion of the GSP observed by UPS.

While the interface dipole leads to a strong shift in vacuum level for neat NPB, for Alq_3 doped in NPB the magnitude of Δ is lowered with increased doping, as seen in Figure 6.11d. In fact the change in interface dipole is almost linear with doping concentration with a downward slope of $(14.9 \pm 1.2)\,\mathrm{meV}/\%$. Unfortunately, no higher doping concentrations were measured to see, if Δ can be reversed to positive values, which, at this slope, would already happen at 14 % of Alq_3. The modification of the interface dipole using dipolar layers is a known concept to tune the substrate workfunction, though usually undoped layers of e.g. self-assembled monolayers of dipolar molecules are used [308, 309]. The potential difference induced by the dipole layer [309] can be estimated to

$$\Delta V = -\frac{p^*}{\varepsilon\varepsilon_0 A} = -\frac{\sigma^*}{\varepsilon\varepsilon_0} d \tag{6.5}$$

where p^*/A in this case is the dipole moment per unit area connected to a fictive sheet charge density σ^* similar to Equation 1.37 discussed in Section 1.1.7. In the case observed here, the initial interface dipole is lowered, the additional polar species therefore induce a relative interface dipole change $d\Delta$ that in theory should follow the same rules as the GSP, see Equation 3.1. Unfortunately, however, an interface dipole at a metal-organic interface is not solely governed by the PDM of the molecule and the relative change of Δ is thus not directly linked to the GSP. Still, the relative change in interface dipole can be calculated to approximately $-0.150\,\mathrm{eV}$ for 10 % of doping. With a triclinic unit cell of almost rectangular shape and a volume of $2.224\,\mathrm{nm}^3$ containing four molecules [310], the height of one monolayer Alq_3 can be estimated to be around 0.8 nm. A GSP in film would thus need to reach $180\,\mathrm{mV\,nm^{-1}}$ at 10 % of doping to allow for the change in interface dipole without additional effects. Besides the effect of dipoles directly on the interface, the interface charge density introduced with the giant surface potential can have an effect on the interface dipole, refer to Section 6.4.3 for a discussion.

As a result, at least two processes determine the extracted UPS barrier: the lowered interface dipole with Alq_3 at the ITO/organic interface and the shift to higher binding energy of the overall HOMO level with increased density of Alq_3 dipoles in NPB.

Although the change in Δ and the HOMO energy cannot be investigated completely independent from each other, it is possible that both effects influence the barrier into the opposite direction, eventually forming a barrier minimum. As the interface dipole lowering is an effect bound to the first few monolayers of NPB:Alq_3 on ITO, this effect subsequently looses influence on the observed barrier for thicker layers.

To conclude, low film thickness measurements of up to 10 nm on the anode comprising only a few monolayers, all exhibit a HOMO onset closer to the Fermi level compared to neat NPB. The lowered barrier will enhance carrier injection into the device, but cannot explain the minimum observed in electrical measurement alone (see Section 6.1.3 or Section 6.1.1).

6.3.3. Visibility of the GSP in UPS spectra

Although the giant surface potential as a macroscopic quantity is typically measured only for thicker layers for example via Kelvin probe [6, 10], the same shift in energy levels could be present also on a molecular level. Friederich *et al.* have shown by simulation that the change in workfunction is continuous through the film and applies to all energy levels equally. Thus, also the HOMO and LUMO levels are subject to band bending due to the GSP. With Kelvin probe, the substrate workfunction is measured for increasing thickness of the organic layer and the slope then determines the GSP as seen in Section 3.1. The same calculation should be possible with the slope of the vacuum level change obtained by UPS as a change in effective workfunction.

Usually, Kelvin probe series are measured on samples of a few 10 nm to 100 nm. Depending on the substrate and the amount of molecule orientation in the first monolayers, the overall layer thickness of only 10 nm with four points of measurement is ambitious to use to calculate the GSP. Also, in many cases, a clear change in workfunction is seen after only a few nanometer have been deposited, see Section 3.1.2. Still, the giant surface potential ranges between $(5 \pm 3)\,\mathrm{mV\,nm^{-1}}$ for neat NPB to $(25 \pm 4)\,\mathrm{mV\,nm^{-1}}$ for 10 % of doping. With Kelvin probe, the GSP of NPB was determined to be $(1.12 \pm 0.15)\,\mathrm{mV\,nm^{-1}}$ within this work, whereas Noguchi *et al.* reported $5\,\mathrm{mV\,nm^{-1}}$ [12]. When extrapolating the KP-data in Section 3.2.5 towards 0 % doping, a similar value of $(5.1 \pm 2.2)\,\mathrm{mV\,nm^{-1}}$ is gained.

For a 10 % mixture, the UPS workfunction slope amounts to $(18 \pm 2)\,\mathrm{mV\,nm^{-1}}$. This is similar to the value gained with Kelvin probe at 12 % of doping, which amounts to $(18.58 \pm 1.25)\,\mathrm{mV\,nm^{-1}}$, which is, however, smaller than approximately $30\,\mathrm{mV\,nm^{-1}}$ for 10 % of doping obtained via impedance spectroscopy.

Still, it is reasonable to assume that the increased band-shift for higher doping ratios and the thickness dependence of the extracted barrier is a result of the SOP and thus the giant surface potential.

6.3.4. Investigation of the energy landscape of NPB:Alq_3

For each sample from the set of four different doping ratios, low-energy UPS (LE-UPS) spectra were recorded at a thickness of 1 nm and 10 nm. Intermediate steps with 2 nm and 3 nm were measured only with 7.7 eV photon energy to reduce damage induced to the sample and to limit the required time to approximately one day per sample. At the end of each series of thicknesses, one high energy UPS spectrum with 21.2 eV of excitation energy was recorded, which will be discussed at the end of this section.

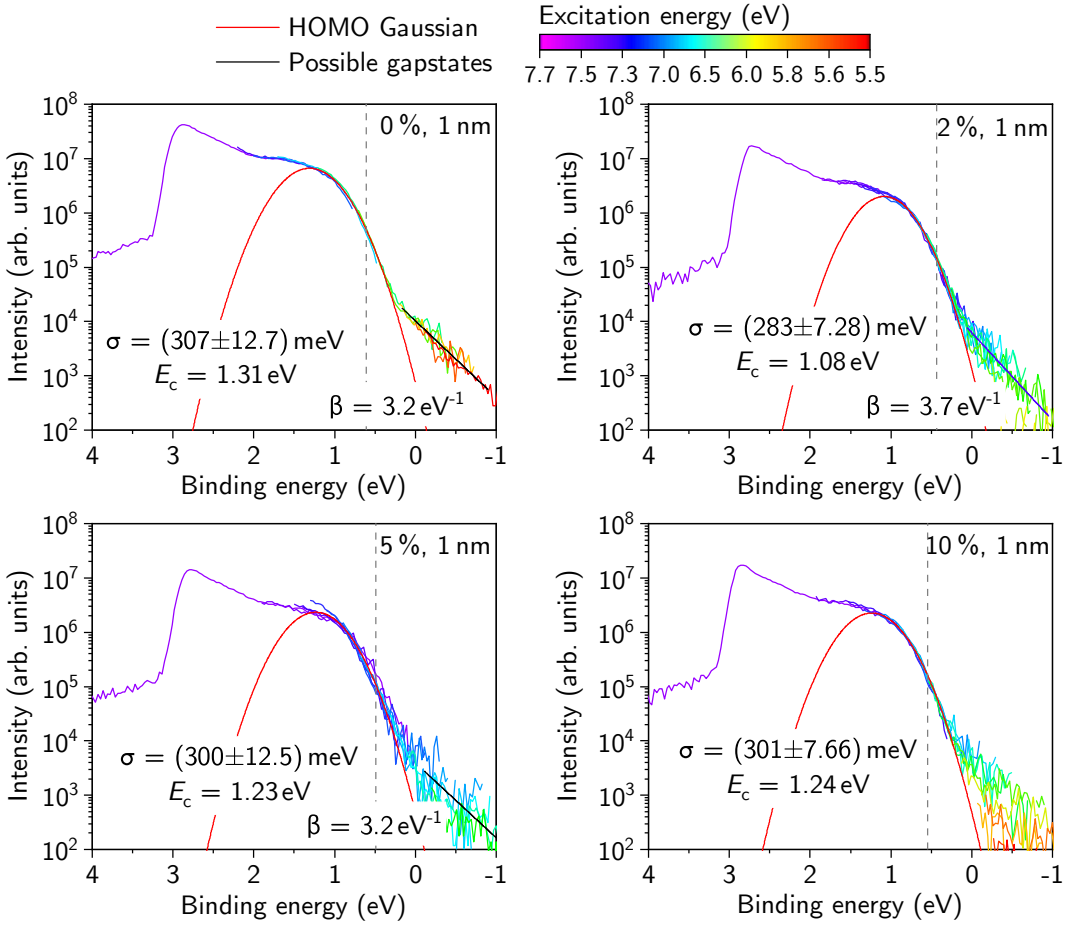

Figure 6.12.: Stacked LE-UPS spectra for excitation energies between 5.5 eV to 7.7 eV. Stacking was done manually. Although a exponential tail seems to be existent for all doping ratios, only neat NPB exhibits a low noise exponential tail. Fitted HOMO Gaussians are drawn in red with center energy E_c, an exponential fit to the bandgap region is given in black except for 10 %, where no convergence was reasonably achievable.

Spectra of low energy UPS for 1 nm thick samples of all four doping ratios are given in Figure 6.12, the coloring reflects the excitation energy used to measure the individual portions. To create these combined graphs, different methods have evolved over time. Ideally, the intensity of the incident light in the UPS chamber is known precisely. If this is the case, the spectra could be combined using the so-called *constant final state* approach, where individual measurements are scaled based on the light intensity and evaluated at a constant kinetic energy larger than the SECO cutoff. This approach is known in the field of inorganic semiconductors [311, 312] and was transferred to OSCs by Ishii *et al.*, although yet unpublished (Presentation given by Prof. Hisao Ishii at a seminar held at the University of Augsburg, November 12, 2019). The spectra here, however, had to be converted with the second approach published earlier by Sato *et al.* [248], which is also applied to spectra in different works from our group [116, 167] because they lack exact information on the incident

light intensity. Therefore, they were stacked by overlapping areas of equal binding energy through scaling of each recorded spectrum.

The main objective behind the LE-UPS measurement, in contrast to much faster single-energy spectra needed to extract the HOMO onset, was to study the existence of possible mid-bandgap states. These states can act as traps and recombination centers [248] and play a major role in charge injection and the energetic position of the HOMO level [313]. Secondly, the shape and width of the HOMO area can be a measure for energetic disorder as well as the exact material of the film. Thus, it should be possible to distinguish, if the measured spectra originate from NPB or a mixture of NPB and Alq_3, which would complicate the calculation of an injection barrier into NPB. This question has also been addressed with high-energy spectra, which will be discussed later.

HOMO region and gap states

In Figure 6.12, the first HOMO peak is fitted with a Gaussian function given in red, with the fitting parameters noted in the graph. Additionally, the position of the HOMO-onset as evaluated in linear scale is given with a dashed vertical line, as well as an exponential fit to the tail besides the HOMO Gaussian. The center of the Gaussian largely follows the trend of the extracted linear energy barrier with the highest distance from the Fermi level observed for neat NPB and an increasing distance afterwards. For the width of the Gaussian, which resembled the width of the density of states (DOS) at the HOMO, no clear trend is observed. Instead, except the 2 %, it is equal within error. As already observed in the mobility measurements in Table 6.1 this indicates that the addition of the polar species of Alq_3 in NPB does not increase the disorder in the DOS, but instead only provokes a shift in energy.

The width of the DOS itself is in average (298 ± 10) meV, which is high but similar to what is reported for other organic semiconductors. Sato *et al.* published a FWHM of the DOS-Gaussian for the donor polymer PTB7 of 0.59 eV, resulting to $\sigma_{\mathrm{PTB7}} \approx 250$ meV [248]. In a recent publication, we found $\sigma_{\mathrm{DBP}} = 251$ meV for the amorphous donor DBP [116], Horowitz *et al.* listed a mean value of 280 meV for pentacene [314]. In case of NPB, two adjacent molecular orbitals HOMO-1 and HOMO-2 are reported, both observe a width of $\sigma \approx 0.2$ eV [315]. In fact, a similar shape is seen in high energy UPS spectra shown further on in this section. For simulations of the HOMO region with individual molecular orbitals visible please refer to Section A.4 in the appendix. Surprisingly, the two peaks are only very faintly visible in the LE-UPS spectra and best seen in the 2 % mixture, where a second step exists roughly 0.5 eV apart to higher binding energies. It is thus indeed possible that the single Gaussian fit presented here does not accurately describe the system. A convolution of two Gaussians would lead to a broadening of the extracted DOS width.

A value of $\sigma \approx 0.2$ eV for NPB, however, is still larger than the result gained from CELIV transients when investigating the mobility activation energy, which resulted to a global average of (127 ± 12) meV. One possibility for that difference has only recently been discussed by Muñoz *et al.* on PEDOT:PSS films. The observed intensity in the UPS measurement does not only depend on the DOS of the HOMO region alone, but also on the DOS of the vacuum level at the semiconductor/vacuum interface [316]. Depending on the film surface, this might lead to a broadening of the DOS.

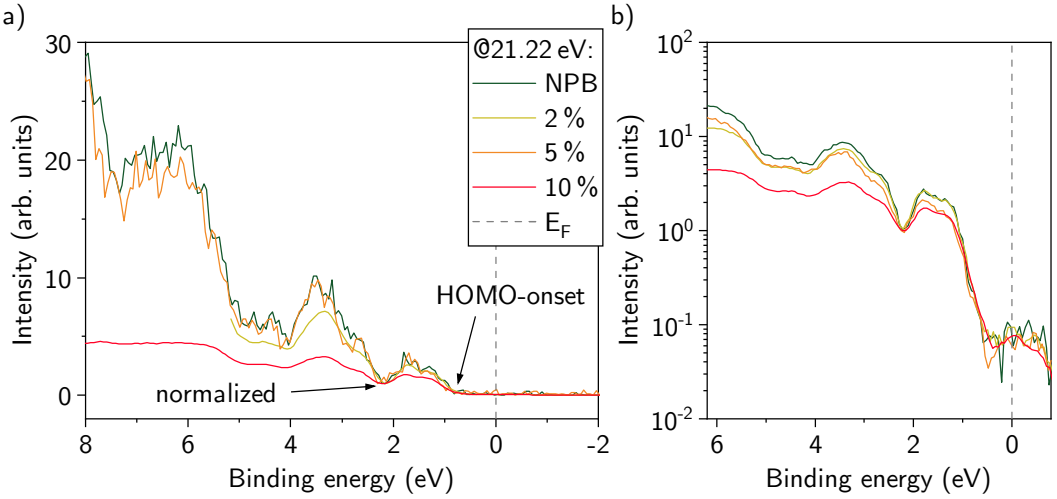

Figure 6.13.: a) He1 spectra recorded at hν = 21.22 eV of all four samples with low intensity and high energy resolution. **b)** Logarithmic plot of high intensity resolution spectra. The spectra are shifted and normalized to the point indicated with an arrow.

Concerning the gap states, no clear picture could be obtained. The exponential decay usually termed *Urbach tail* is fitted with a single exponential decay with either an Urbach slope β [248] or the Urbach energy E_U [317] as fitting parameter, where

$$N(E) = N_0 \exp\left(-\beta[E_0 - E]\right) = N_0 \exp\left(\frac{E - E_0}{E_U}\right) . \tag{6.6}$$

E_0 is the energy at the beginning of the Urbach tail and N_0 the initial density of states or intensity. Both versions of the function are mutually equal with $\beta = 1/E_U$. The Urbach energy allows to draw conclusions on the energetic depth of the tail state.

For 0 % of doping, the tail above the HOMO onset appears to be clearly visible with only low noise. However, noise levels rise for higher doping concentrations, up to the extent that no good fit was possible for 10 % of doping. This might indicate an increased influence of the Alq_3 species on the UPS signal. Unfortunately, though, LE-UPS spectra of pure Alq_3 could not be obtained up to now, a comparison is thus not directly possible. The obtained Urbach slopes are given in the graph, the Urbach energies calculate to 309 meV for neat NPB, 269 meV for a 2 % mixture and 315 meV in case of 5 %. These values appear considerably large, although no literature data for NPB is available. The Urbach energy for Alq_3 is reported to be 134 meV [318], other small molecular systems range from 50 meV for the highly ordered donor Diindenoperylene to 30 meV for DBP [116], however determined by optical measurements instead of UPS. Sato *et al.* published $\beta = 8.3$ /eV for the polymer PTB7, which amounts to roughly 120 meV [248]. Thus, assuming deep level tail states of 0.3 eV in NPB is probably erroneous. A single systematic source of error could, however, not be identified.

High-energy spectra on NPB:Alq_3 mixtures

A further hint to the assumption that the extracted barrier is indeed the position of the NPB HOMO onset can be seen in high-energy UPS spectra covering a larger range of binding energies. In Figure 6.13 these measurements are shown for all four samples at 10 nm thickness. On the left side, in Figure 6.13a, the spectra were recorded over a broad range of binding energies with short integration time, whereas in Figure 6.13b a higher accuracy in measurements was applied to a smaller range of binding energies. The spectra are aligned and normalized to the first minimum seen from the Fermi level for easier comparison. Both in linear and logarithmic scale, no change in shape of the HOMO peak is observed and the form of the spectra stays the same. Excluding the 10 % measurement, the spectra all are of similar shape and only small changes in relative peak heights are visible in the logarithmic scale. At 10 %, the intensity is much lower compared to the other three, although they were all aligned to the same minimum, which is similar in depth compared to the first HOMO peak. It is therefore assumed that the huge difference in intensity is rooted in an erroneous measurement, though no definitive answer can be given.

Although NPB and Alq_3 are reported to be not distinguishable in standard UPS measurements [306], a closer look to the first HOMO peak in low and high energy UPS, however, suggests that the observed shift in HOMO onset discussed in Section 6.3.2 and visible in Figure 6.11 is rooted on a change in NPB HOMO level. To the best of my knowledge, measured UPS HOMO onsets hence correlate to the NPB injection barrier.

6.4. Possible descriptions of the GSP effect on carrier injection

In this section, possible models to describe the observed effect of dipolar doping on carrier injection are discussed. At first, carrier injection into disordered films as proposed by Scott and Malliaras [75] is evaluated in the light of the barriers measured with UPS and the change in mobility observed for doped layers. Parts of this section have already been published in ref. [49] and are reproduced literally. Then, current-voltage characteristics of hole only devices as well as impedance spectra and CELIV transients for bi-layers are calculated using drift-diffusion simulations on polar OLEDs. In these simulations, different effects of the GSP can be considered separately.

6.4.1. Scott and Malliaras model

The basic physics governing charge carrier injection into OSCs have been elaborated in Section 1.1.4. In the Schottky model, which is based on thermionic emission, the effect of image charge barrier lowering is a central property. As a result, the relevant barrier for carrier injection is not directly at the interface, but rather a few nanometers away. The maximum in potential corresponding to the effective barrier $E_{\mathrm{b,eff}}$ is dependent on the applied electric field, including the GSP by the dipolar dopants as well as the barrier at the interface in the absence of the field $E_{\mathrm{b},0}$, i.e. the difference between Fermi level of the anode and organic HOMO energy. At first, in the Schottky model, the external electric field causes an effective barrier lowering

ΔE_b derived in Equation 1.21, with

$$\Delta E_\mathrm{b} = \mathrm{e}\sqrt{\frac{\mathrm{e}F_\mathrm{ext}}{4\pi\varepsilon\varepsilon_0}} \ ,$$

where F_ext is the external field. The injected current is then proportional to

$$j \propto T^2 \exp\left(-\frac{E_{\mathrm{b},0} - \Delta E_\mathrm{b}}{\mathrm{k_B}T}\right) \ , \tag{6.7}$$

with the device temperature T and the injection barrier represented by the difference of organic HOMO level and contact workfunction, $E_{\mathrm{b},0} = \Phi_\mathrm{a} - E_\mathrm{HOMO}$. For amorphous organic materials surface recombination and hopping across the effective potential barrier a few nanometers away from the interface are also heavily dependent on the carrier mobility. To describe injection of carriers from a metallic contact into an amorphous organic material, Scott and Malliaras have introduced an extension of the classic Schottky model, taking the diffusive motion of carriers within the finite width of the potential barrier into account [75]. The injection current for such a device as shown in Equation 1.25 is

$$j = 4\Psi(f)^2 N_0 \mathrm{e}\mu F \exp\left(-\frac{E_{\mathrm{b},0}}{\mathrm{k_B}T}\right) \exp\left(\sqrt{f}\right) \ , \tag{6.8}$$

where $f = F\mathrm{e}^2/\left(4\pi\varepsilon\varepsilon_0(\mathrm{k_B}T)^2\right)$ is the reduced electric field, N_0 is the carrier density at the interface, μ the carrier mobility and Ψ is a polynomial factor depending on f alone with no order higher than 1. It is worth noting that the individual quantities' errors have significantly different impact on the overall injected current. For example, while the mobility has linear influence on the current, the barrier multiplies exponentially to the result. A small error or change in barrier can hence have a huge impact on the calculated current.

To estimate the injection current for the devices presented in this chapter by using the Scott and Malliaras model, carrier mobility and the injection barrier have to be known for different doping concentrations. The mobility has been determined by CELIV and TOF as seen in Section 6.2. Both exhibit a very similar doping dependence, thus only the results of the latter method will be used here. From UPS, the injection barrier can be gained from the HOMO onset, however, the distance to the electrode has to be taken into account, see Section 1.1.4. That is, the HOMO onset should not be evaluated directly at the ITO/NPB:$\mathrm{Alq_3}$ interface, but at a distance x a few nanometers away. The maximum in potential and hence the energetic minimum for carrier injection is field dependent and given by Equation 1.20 with

$$x = \sqrt{\frac{\mathrm{e}}{16\pi\varepsilon\varepsilon_0 F}} \ . \tag{6.9}$$

For $\varepsilon = 3$ it calculates to roughly 3 nm for reasonable fields. Note that, in UPS, the electrostatic influence of the ordered dipoles forming the GSP on the NPB molecules is already present, the external field, however, is zero.

Figure 6.14 shows the results of the calculated current from Equation 6.8 for different doping ratios for the barriers gained from UPS measurements directly at the interface with 1 nm of evaporated film, 3 nm away and at 10 nm in the film. For

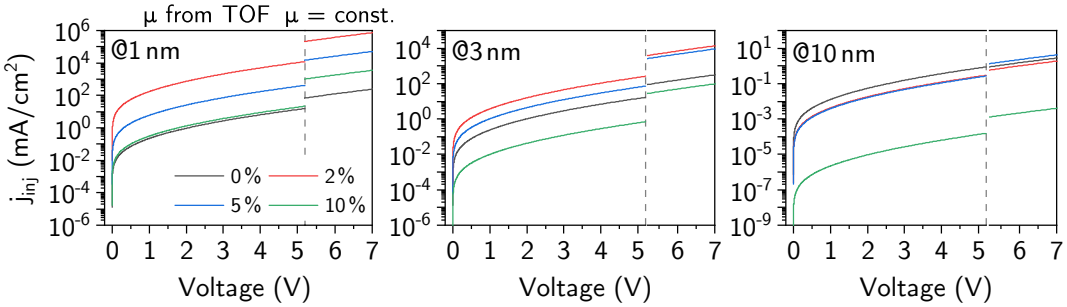

Figure 6.14.: Calculated injection current based on the model by Scott and Malliaras [75]. Sources for parameters are the UPS barriers at various thicknesses and TOF mobility on the left side of the graph. The right portion shows the extension of the curves calculated with a constant mobility of $5 \times 10^{-4}\,\mathrm{cm^2\,V^{-1}\,s^{-1}}$ for all ratios, which is the TOF result for neat NPB. Note the individual scales of each set of graphs. In the 10 nm case, the currents for 2 % and 5 % are almost equal.

1 nm and 3 nm, the injection current for 2 % doping is highest, whereas in both cases the 10 % mixture is lower by more than 2 orders of magnitude. As expected from the results of Equation 6.9, the injection current calculated with the barriers at 3 nm distance resembles the experimental data best, with the optimum being at moderate doping ratios and higher ratios falling behind even the undoped case.

For comparison, on the right side of the dashed line in Figure 6.14 also currents calculated with the mobility held constant at the value for pure NPB as measured with TOF ($5 \times 10^{-4}\,\mathrm{cm^2\,V^{-1}\,s^{-1}}$) are included. The currents then resemble the change in barrier alone and, although the moderately doped devices are still dominating in most cases, the difference is not as pronounced. Note, that the maximum in current for 3 nm of thickness is at 2 % and not at 5 %, as it is the case for current-voltage characteristics discussed in Section 6.1.1. A mixture below 5 % was not measured in single-carrier devices, in case of impedance spectroscopy a 3 % mixture is available but does not differ much from undoped NPB, see Section 6.1.3. This difference is most likely stemming from small inaccuracies in calculating the exact doping ratio as well as differing processing conditions for UPS and electric measurements in different labs. As stated above, a small error on extracted barriers could shift the optimum calculated here by a few percent in doping ratio.

Concerning charge injection, it is therefore reasonable to assume that neither the change in barrier, nor the change in mobility alone can explain the observed optimum in current discussed in Section 6.1.1. Instead, a superposition of both processes is needed to describe the behavior. However, two facts about the calculations presented here are worth a note. Firstly, the currents resemble only the injection current alone. Further processes governing overall device current, like space charge and bulk conductivity are not included. Secondly, the thermionic emission model that is underlain both the basic Schottky formula and the Scott and Malliaras addition is accused of not to be accurate for low barriers [14], though a discussion of the relative differences should still be feasible.

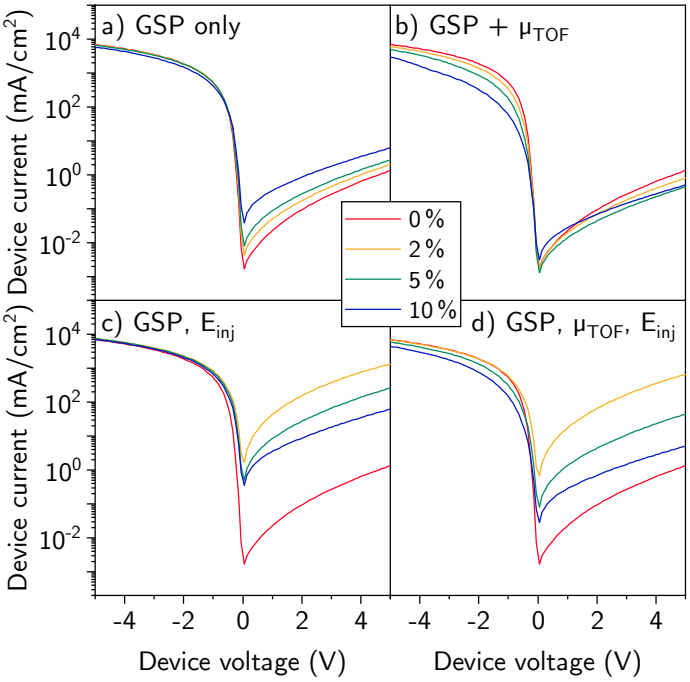

Figure 6.15.: Simulated current-voltage characteristics for different parameter sets gained from experiments. **a)** With only the GSP included, **b)** with GSP and mobility, **c)** with GSP and changed barriers and **d)** with GSP, barriers and mobility affected by doping.

6.4.2. Drift-diffusion simulations

In Section 3.2.4 and following, simulations of capacitance-voltage characteristics have been introduced. Despite some minor differences, the model could describe the trends observed in measurements very well, at least concerning impedance spectra and capacitance-voltage characteristics. The same model will now be used to simulate impedance spectra and CELIV transients, but also current-voltage characteristics on monopolar devices with only the polar HTL present. Additionally, the model describing the mobility can be extended to include correlated disorder.

At first, current-voltage characteristics are calculated for simple hole-only devices. The simulated device structure simplifies the monopolar devices to bottom contact, polar organic layer of 70 nm thickness and top contact; the HATCN hole injection layer is omitted. Both contacts are set to resemble carrier densities defined by the barriers with a Boltzmann statistic, refer to Section 1.3 for further information. Input parameters in the simulation are the mobility as measured by TOF, the injection barriers measured with UPS and the magnitude of the GSP gained from Kelvin probe measurements for the same doping ratios. Other parameters for the NPB layer are unchanged compared to the bilayer-devices simulated in the previous sections. In simulation, individual parameters can be excluded e.g. by using a constant mobility instead of a gradually decreasing mobility observed with increased doping. Thus, individual influences of the different parameters can be elucidated.

The graph in Figure 6.15a includes four different current-voltage characteristics with varied GSP, while the mobility and barrier at the anode are kept the same at

	measured			tailored	
Doping (%)	μ (TOF) ($cm^2\,V^{-1}\,s^{-1}$)	σ (KP) ($mC\,m^{-2}$)	E_{inj} (UPS) (eV)	μ ($cm^2\,V^{-1}\,s^{-1}$)	σ ($mC\,m^{-2}$)
0	5.0×10^4	0.0	0.61	5.0×10^4	0.0
2	2.0×10^4	0.3	0.43	3.5×10^4	0.33
5	0.8×10^4	0.54	0.49	2.0×10^4	1.0
10	0.4×10^4	1.22	0.55	0.4×10^4	1.33

Table 6.2.: Important input parameters for the simulations shown in Figure 6.15 and Figure 6.16. The left portion is based on measured parameters from the previous chapter, the right portion was fitted manually to resemble the measured characteristics.

$5 \times 10^{-4}\,cm^2\,V^{-1}\,s^{-1}$ and 0.6 eV, respectively. A field dependence of the mobility is included in the simulation, but is set independent of the doping ratio. This mimics a device with ITO at the bottom contact and compared with the measurements in Figure 6.2, an optimum in current at moderate doing concentrations near 5 % is expected. The workfunction of the top contact resembling the HATCN/Au combination is chosen to resemble a hole-barrier of 0.2 eV. At first it is evident that the GSP does indeed have a pronounced effect on the current injected through the bottom contact (positive voltages), while the top contact side remains largely unaffected (negative voltages). To achieve this effect that is also seen in measurements, the barrier at the top contact has to be comparably small. Otherwise hole injection from Gold to the HOMO of NPB would be suppressed through the GSP, which has been seen for electron injection into Al(7-Prq)$_3$ [3, 11]. Note, that carrier injection through the HATCN layer is non-trivial and best described using a hopping model not included in these simple simulations [288]. Still, by varying the barrier at the NPB:Alq_3/HATCN/Au interface in simulation, it can be concluded that the value is indeed at least below 0.4 eV. However, no decrease in current occurs for higher doping or GSP as it is the case in experiment.

Figure 6.15b includes the change in mobility similar to what is observed with CELIV or TOF into the simulation, see Table 6.2 for a list of input parameters. Now, the positive influence of the sheet charge density on the current is diminished, although the difference is not as pronounced as in the measurement. Additionally, the changed mobility also affects the current through the top contact in the negative voltage range and the simulation without any GSP or mobility change at 0 % still shows the highest current for rising voltages.

The two graphs at the bottom of Figure 6.15 include the barriers measured with UPS, where Figure 6.15c omits the change in mobility and Figure 6.15d was calculated with GSP, mobility and barriers set to the measured values. In simulation, the HOMO level of the NPB layer was changed to resemble the modified barrier observed in UPS with values of 0.61 eV for pure NPB and 0.43 eV, 0.49 eV and 0.55 eV for doped layers from 2 % to 10 %, respectively. Note, that this resembles the situation directly at the interface in contrast to the previous section, where the barrier was evaluated a few nanometers away from the interface. However, in drift-diffusion changes in local potentials and carrier densities are part of the simulation and would otherwise be included twice. To keep the hole barrier at the top contact constant,

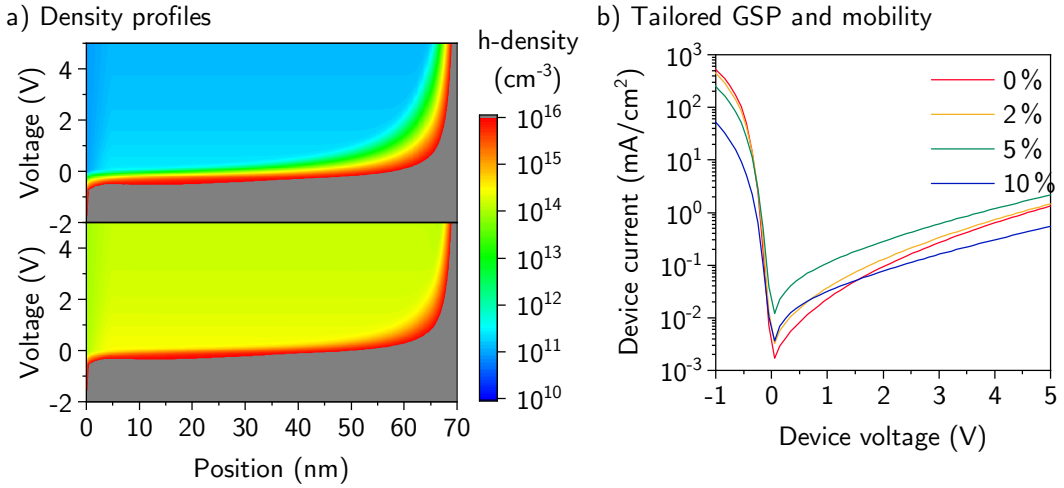

Figure 6.16.: a) Carrier density profiles for holes corresponding to the graphs in Figure 6.15a (top) and c) (bottom) at 2 % of doping. The change in barrier by 0.2 eV provokes a change in hole density by four orders of magnitude. **b)** Current-voltage characteristics of devices with parameters set to resemble the trend seen in measurements.

the workfunction has to be changed accordingly. As a result, the 2 % device exhibits the by far highest current, which is a direct result of the lowest barrier, followed by 5 %, 10 % and 0 %, as seen in Figure 6.15c. This trend is preserved, if the change in mobility is included in Figure 6.15d. In conclusion, the change in barrier in simulation has the largest effect on the device current in comparison to the GSP and the mobility. An explanation can be given by investigating the charge carrier densities of holes in the diode. Simulated carrier density profiles for the devices in Figure 6.15a and Figure 6.15c, i.e. without the change in mobility, at 2 % of doping are shown in Figure 6.16a. While the carrier density is equally high in both cases at the top contact with $x = 70\,\text{nm}$ and for negative voltage due to the small barrier, the bulk density in the positive voltage regime is largely influenced by the bottom contact barrier. The change of roughly 200 meV in barrier provokes a change in charge carrier density by four orders of magnitude. For comparison, the GSP alone changes the bulk carrier density by a factor of two (not shown).

So far, all parameters in the simulations are based on measured quantities that are gained by various experimental methods. Depending on the accuracy of the theoretical models behind the calculations, the exact effect of a specific change of one parameter can be different in simulation and the real device. Thus, a cross check is performed to adapt the simulation parameters to resemble the observed trend in measurement, most importantly, the maximum at 5 % of doping density. The simulated current-voltage characteristics are shown in Figure 6.16b, the values for the GSP and the mobility required for the simulation are given in the right portion of Table 6.2. The maximum at 5 % doping ratio is achieved by drastically increasing the sheet charge density by a factor of two compared to the measured value. Additionally, the change of the mobility has to be reduced, which would otherwise cancel the effect of the high GSP. As a result, in simulation, it is possible

to achieve a maximum at 5 % with a change in GSP and mobility, only. However, the differences between measured and required parameters is in part large. Also, unlike in experiment, the lowered bulk mobility is visible in the negative voltage regime, although this could again be rooted in the insufficiently accurate description of the HATCN/Gold interface.

Possible effects of correlated disorder

Until now, all simulations were calculated using first-generation models for the mobility, which lack the influence of Gaussian or correlated disorder. In theory, increasing dipolar surrounding could lead to increased disorder in the film. Friederich *et al.* also stated that a strong GSP and high mobility is thus contradictory in organic films [47]. When discussing the charge carrier mobility measured with CELIV in Section 6.1.2 and TOF in Section 6.2, the impact of doping NPB with Alq_3 on the electronic disorder was briefly addressed. Remarkably, no strong evidence for a rise in disorder was found. Instead, it seemed to stay mostly constant. Therefore, the mobility model is now changed to the so-called *extended correlated disorder model* (ECDM) to allow for a systematic screening of the disorder parameter σ. From simulated current-voltage characteristics, the injection quality is extracted using the same method that was applied to the experimental data discussed in Section 6.1.1 to assess a possible influence on the characteristic that was previously undetected. ECDM extends the correlated disorder model briefly introduced in Section 1.1.3 by a dependence on the charge carrier density in the device [319]. It is worth a note, that the description of the boundary conditions and coupling equations given in Section 1.3 are complicated by the introduction of carrier density dependent mobilities. A direct correlation between injection barriers, built-in field and the corresponding input parameters like electrode workfunction is thus not directly possible between models including and excluding disorder.

The simulated characteristics for two different workfunctions with the mobility described by the ECDM are presented in Figure 6.17a. σ_{dis} describes the disorder parameter and is set to 100 meV as published by van Mensfoort *et al.* [129] as a default value, if not otherwise noted. σ_{int} denotes the sheet charge density, which is swept from $0.0\,\mathrm{mC\,m^{-2}}$ to $2.0\,\mathrm{mC\,m^{-2}}$. Additionally, different workfunctions for the bottom contact are included in the simulations. As visible in Figure 6.17a, lower pane, no positive effect of the GSP is seen for a contact with high workfunction. Note, that this is not a distinctive feature of the ECDM model, but is also seen with models excluding disorder. Furthermore, likewise to the simple first generation mobility model used above, the current injected through the bottom contact or HIL side will never exceed the ohmic boundary set by the low barrier at the top contact. The injection quality in Figure 6.17b, given for different GSP and workfunctions, is thus always less or equal zero for all simulations. This fact could be addressed in further simulations by improving the model for the HATCN contact and investigating the effect of the GSP to non-ohmic contacts. However, it should not interfere with the discussion on the effect of the disorder parameter. As expected, because σ_{dis} is constant at first, also the experimentally observed worsening of injection for higher doping ratios and the maximum for moderate doping concentrations or interfacial charge densities are not reproduced in the simulation shown in Figure 6.17a.

For further investigation, the disorder parameter σ_{dis} is thus varied to see, if a possibly undetected rise of sigma would cause such a feature. A minimum in ex-

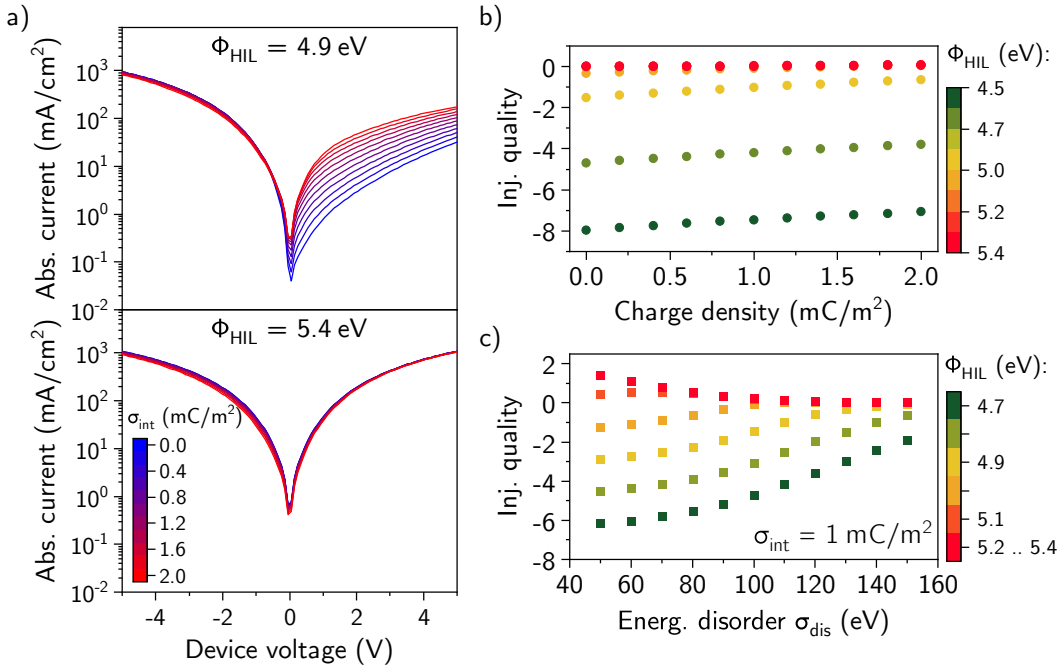

Figure 6.17.: a) Simulated current-voltage characteristics for low top and varied bottom contact barriers and different interfacial charge densities. b) Extracted injection quality for the plots of a), again with varied HIL-side barrier. In simulation, the current will not exceed the ohmic boundary set by the top contact, therefore no negative values are seen. c) Injection quality plots with varied ECDM disorder parameter, the sheet charge density is fixed at 1.0 mC/m^2.

tracted barrier or maximum in injection quality requires a change of the shape of the current-voltage characteristic and σ_{dis} is known to be a crucial parameter capable of affecting the shape [129]. Figure 6.17c shows simulated injection quality for a fixed sheet charge density of 1.0 mC m^{-2} and σ_{dis} swept from 50 meV to 150 meV, with the default value of 100 meV of the former calculation in the middle. Such a large variation of the disorder parameter would probably have been detected in the CELIV experiment. Moreover, σ_{dis} would have to be lowered for higher doping ratios to lead to a lower injection quality. As a lowered disorder with increasing doping concentration is unlikely to occur, this will also not lead to a maximum in current for moderate doping concentrations. From these simulations it becomes clear that a change of the film disorder plays a minor role for the observed effects. Only very low barriers, higher disorder can lead to impaired currents (red datapoints in Figure 6.17c).

Impedance spectra and CELIV transients

In simulated current-voltage characteristics, the positive effect of the GSP on hole injection is reproduced. Similar to the case with the injection model proposed by Scott and Malliaras discussed in Section 6.4.1, a decrease in mobility due to doping of NPB with Alq_3 could explain the existence of the optimum. With a model device stack with two polar layers and temperature dependent mobility, a combination of

$C(f)$ and CELIV simulations can be used to investigate the change on effective injection barrier similar to the experiment.

Input parameters are the mobility activation energy set to $E_\mu = 0.3\,\mathrm{eV}$ and the energy difference between bottom contact and HTL HOMO level, $E_\mathrm{inj} = [0.3, 0.4, 0.5]\,\mathrm{eV}$. Furthermore, the HTL thickness is set to 70 nm, whereas the simulated Alq_3 layer is 100 nm thick. The temperature and field dependent mobility model implemented in the Setfos software suite can be described with the equation

$$\mu = \mu_0 \exp\left[-\frac{E_\mu}{\mathrm{k_B}T} + B\left(\frac{1}{\mathrm{k_B}T} - \frac{1}{\mathrm{k_B}T_0}\right)\sqrt{F}\right] , \tag{6.10}$$

where μ_0 is the zero field, high temperature mobility, T_0 the characteristic temperature and B the field parameter [126]. Both B and T_0 are empirical parameters that would have to be determined with temperature and field dependent mobility measurements. Unfortunately, the CELIV experiment is conducted on only one ramp rate and therefore electric field, whereas TOF is available only at room temperature. The parameters were therefore adapted to exhibit the observed room temperature mobility with the measured activation energy of $E_\mu = 0.3\,\mathrm{eV}$ and to reproduce the impedance spectra with respect to the transition frequency of the temperature-independent simulations. Thus, the required parameters are set to $\mu_0 = 12\,\mathrm{cm^2\,V^{-1}\,s^{-1}}$, $B = 5.6 \times 10^{-5}\,(\mathrm{cm/V})^{1/2}$ and $T_0 = 600\,\mathrm{K}$. These parameters are similar to what has been reported for the polymer PVK by Gill *et al.* [284]. Note, that the field dependence could have been disabled by setting $B = 0$, which would require changing μ_0 to again reproduce the impedance spectra calculated without a temperature dependence of the mobility. Either way, as an exact reproduction of the measurement is not attempted, the parameters should describe the semiconductor reasonably well.

In Figure 6.18a, example CELIV transients simulated with a ramp rate of 0.5 MV/s, all starting at the same offset voltage, are shown for various temperatures. The device has the injection barrier set to 0.5 eV and the sheet charge density is $0.5\,\mathrm{mC\,m^{-2}}$. Evaluation of the peak time is done by investigating the first derivative. The results from temperature dependent simulations are shown in the left graph of Figure 6.18c, where the color coding corresponds to E_inj. All calculated activation energies are lower by approximately 0.2 eV compared to the input parameter of 0.3 eV (dashed line) with an average value of $(93 \pm 10)\,\mathrm{meV}$. Also, no distinctive relationship of E_μ and the programmed sheet charge density is found that would be systematic to all injection barriers. Instead, the mobility activation energy appears to be unchanged. The underestimation of the extracted mobility activation energy is expected from previous investigations presented in Section 5.2, although the magnitude of the change is a little larger in the simulations presented here compared to those in Section 5.2. Note, that, unlike the measurements, the lowest temperature transient observes the highest injected carrier density in the example shown in Figure 6.18a. This is due to the fact that low relaxation frequencies result in a slight change in transition voltage, which in turn causes a higher accumulation at the chosen offset voltage. However, the small charge injection requirement to extract the transit time from the peak time should still be valid, though a small systematic error cannot be ruled out. To counter that error, more detailed simulations with each transient offset voltage chosen according to the temperature, in order to achieve roughly the same amount

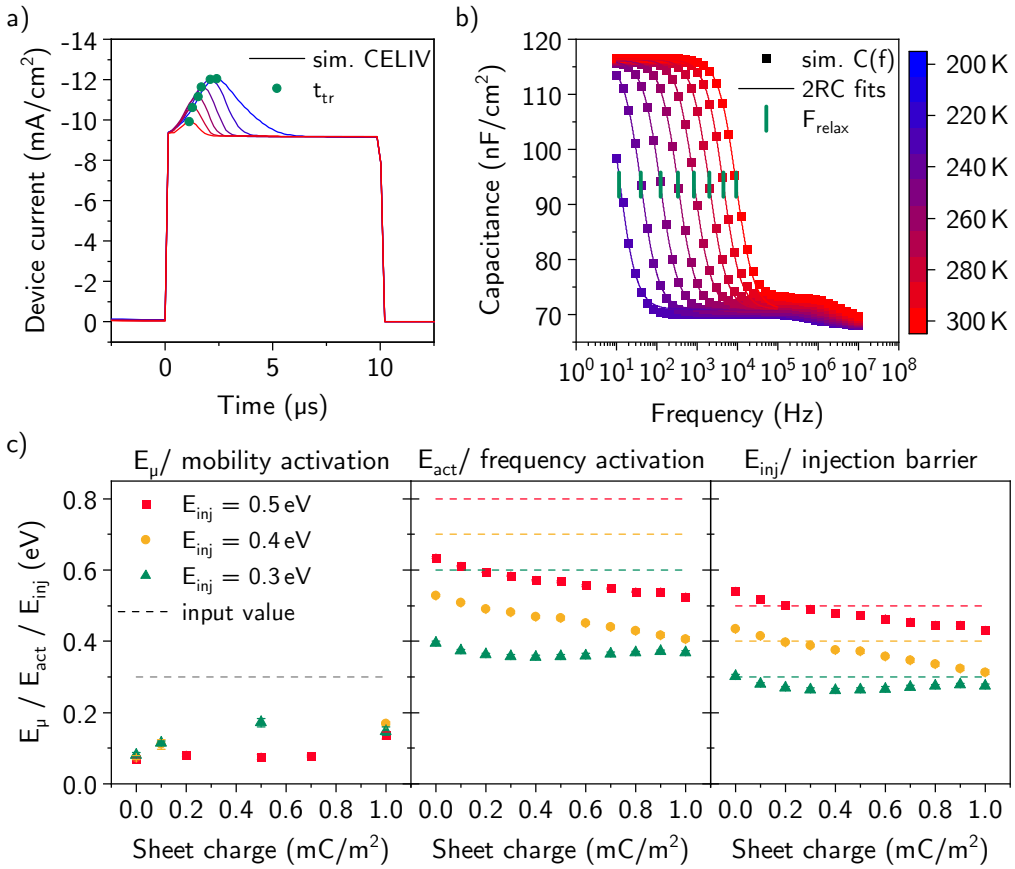

Figure 6.18.: **a)** Exemplary simulated CELIV transients and **b)** impedance spectra at varied temperature for a device with 0.5 eV injection barrier and 0.5 mC m^{-2} sheet charge density. **c)** Extracted mobility activation, frequency activation energies and injection barriers. Ideal values are given with dashed lines, error bars are included in the graph, although hardly visible.

of injected charge carriers could be conducted, as it was done in measurement. This, however, would require a considerable amount of additional simulation time.

Capacitance-frequency calculations for the same device are shown in Figure 6.18b. Evaluation of the simulated spectra is done by fitting a 2RC-model to the data, the fits are shown with straight lines and the positions of the relaxation frequency with vertical stripes. The extracted frequency activation energy is shown in the middle portion of Figure 6.18c for all three injection barriers; ideal values with $E_{\mathrm{act}} = E_{\mu,\mathrm{in}} + E_{\mathrm{inj,in}}$ are given with horizontal, dashed lines. Again, the extracted frequency activation energy is underestimated considerably, although the difference at 0.0 mC m^{-2} is similar for all input barriers. For higher GSP, only simulated devices with barriers greater than 0.3 eV show a reduction in activation energy, the low barrier device with $E_{\mathrm{inj}} = 0.3\,\mathrm{eV}$ is largely unaffected.

From both, E_μ and E_{act}, the injection barrier is calculated with $E_{\mathrm{inj}} = E_{\mathrm{act}} - E_\mu$ and plotted in Figure 6.18c, right graph. The mobility activation in that calculation is set to the average of $E_\mu = 93\,\mathrm{meV}$, as no definitive trend in dependence of the

sheet charge density can be seen in the extracted data. The zero-GSP values for E_{inj} correspond well with the ideal values and the error is below 50 meV, which is again in good agreement with the general observation in Section 5.2. In case of a low input barrier, an average of (273 ± 11) meV is extracted with no significant dependence on the GSP, compared to the ideal value of 0.3 eV. For higher barriers, however, a linear dependence of the extracted barrier on the interface charge density is observed, with a slope of roughly $0.1\,\mathrm{eV}/(\mathrm{mC/m^2})$. This agrees with the experiment, where no positive effect of the GSP on the extracted barrier could be found for HIL1.3, while the ITO sample showed a reduction in E_{inj} up to 5 % of doping or approximately $0.4\,\mathrm{mC\,m^{-2}}$. The slope in measurement, however, is with about $0.35\,\mathrm{eV}/(\mathrm{mC/m^2})$ much larger.

In total, the change in activation energy induced by the GSP is reproduced in simulation also with transient and impedance calculations. Additionally, a low initial injection barrier will not allow any positive effect, which is in line with the measurement. However, because no model exists in the simulation for a percolation theory of charge transport, the effect of the Alq_3 dopants on the NPB mobility can only be estimated or included directly through simulation. Furthermore, the exact effect of the GSP on the injection barrier is probably only partly reproduced in simulation. While a change in carrier density and local electric field will provoke a change in the potential of the simulated organic semiconductors, a change in interface dipole or HOMO level due to the existence of polar species at the interface cannot be modeled intrinsically and also needs to be included externally into the simulation parameters.

6.4.3. Electrostatic effect of Alq_3 on the injection

The barrier between organic semiconductors and various substrates is usually subject to Fermi level pinning, leading to an effective minimum barrier in the range of a few 100 meV, even if the nominal energy difference between workfunction and organic HOMO level is smaller. A comprehensive report on the energy alignment has been published by Greiner *et al.* in 2012 [72], though the effect itself has been studied before [303–305]. In 2013, Ley *et al.* published an analytic, theoretical description of the barrier reduction and pinning based on the image charge effect and the arising interface dipole [73]. In his approach, the potential drop $\Delta\Phi$ across an oxide layer at the interface is defined by the negative image charge per unit area Q in the metal layer, that arises by the positive charges in the HOMO level of the organic semiconductor. A sketch of the effect is given in Figure 6.19a with Fermi level pinning in effect. Note, that in the same publication, the effect is proven to be also valid for interfaces without an intermediate oxide layer like on PEDOT:PSS. However, as the calculation is more complicated, the simplified equation with a finite oxide thickness is used instead. It is

$$\Delta\Phi = \mathrm{e}\frac{Q}{C_{\mathrm{ox}}}\ , \tag{6.11}$$

where C_{ox} is the capacity of the oxide layer. The positive charge density in the organic layer, which equals Q, is given by a Fermi-Dirac statistic with

$$Q = \mathrm{e}n\left[1 + \exp\left(\frac{I_{\mathrm{C}} - \Phi_{\mathrm{subst}} + \mathrm{k_B}T\ln g + \Delta\Phi}{\mathrm{k_B}T}\right)\right]^{-1}\ , \tag{6.12}$$

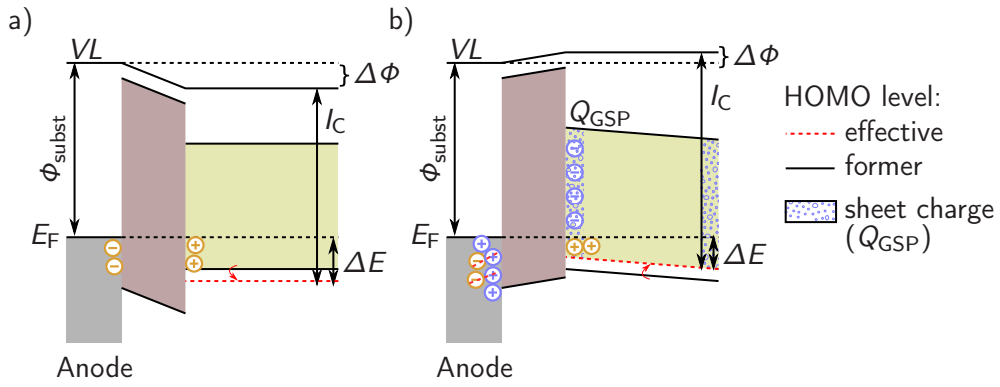

Figure 6.19.: a) Sketch of the energy levels with an insulating layer in the pinning regime. Negative image charges in the anode arise from positive charges in the HOMO level of the organic, causing a potential drop $\Delta\Phi$ in the oxide. This interface dipole will then limit the effective barrier to a finite minimum. **b)** With a GSP, an additional negative sheet charge density (G_{GSP}) exists at the organic interface, causing positive image charges in the metal counteracting the effect. It is only possible in case of large differences between substrate workfunction Φ_{an} and organic ionization potential I_C, i.e. without Fermi-level pinning in effect.

where n is the density of molecules at the interface, I_C is the ionization potential of the organic layer and Φ_{subst} the substrate workfunction. g is termed the degeneracy factor and describes the weak temperature dependence of the energy difference $I_C - \Phi_{subst}$ [73]. The injection barrier can be calculated with

$$\Delta E = I_C - \Phi_{eff} = I_C - \Phi_{subst} + \Delta\Phi \ , \tag{6.13}$$

because the effective substrate workfunction is reduced by the potential drop caused by the image charges, with $\Phi_{eff} = \Phi_{subst} - \Delta\Phi$. Note, that in this calculation, the sign-convention is different from the usual definition of the interface dipole. Ley *et al.* defined an interface dipole that is leading to an increased barrier to be positive, thus the subtraction from the substrate workfunction. To allow comparison with the original paper, it is left unchanged here.

For devices exhibiting a GSP, this framework can be extended to include the usually negative interface charge density at the substrate/organic interface. The image charge density caused by the positive charges in the HOMO level is then reduced by the image charge of the negative sheet charges. Thus, Equation 6.11 is changed to

$$\Delta\Phi = \mathrm{e}\frac{Q - Q_{GSP}}{C_{ox}} \ , \tag{6.14}$$

where Q_{GSP} is the density of positive interface charges in the metal layer caused by the interface charges of the GSP. With Equations 6.12 and 6.14, a relation for the potential drop can be found with

$$\Delta\Phi = \mathrm{e}^2\frac{n}{C_{ox}}\left[1 + \exp\left(\frac{I_C - \Phi_{subst} + \mathrm{k_B}T\ln g + \Delta\Phi}{\mathrm{k_B}T}\right)\right]^{-1} - \mathrm{e}\frac{Q_{GSP}}{C_{ox}} \ , \tag{6.15}$$

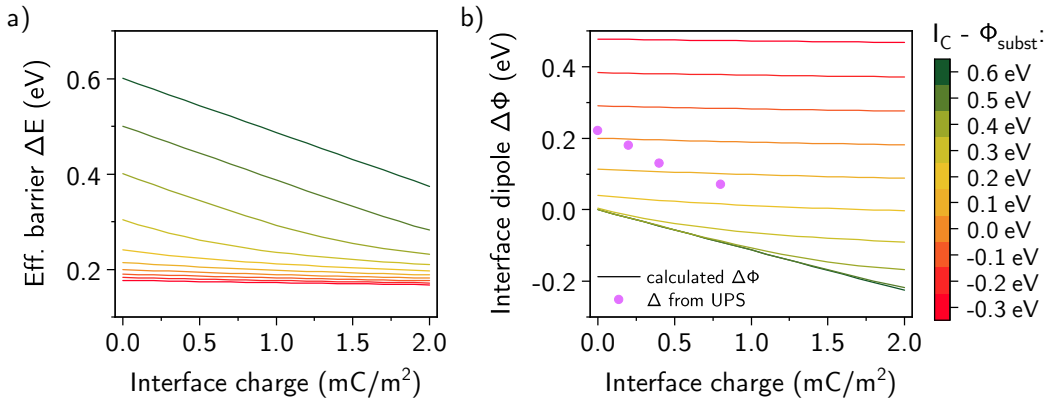

Figure 6.20.: a) Effective injection barrier calculated from Equation 6.13 by solving Equation 6.15. **b)** The interface dipole arising from image charges. With lowered input barrier ($I_C - \Phi_{subst}$, color coded), an interface dipole arises that limits the minimum barrier. Only high barriers with low induced interface dipoles can be affected by the GSP. Note the described difference in sign-convention: The interface dipole measured with UPS is given positive here to conform with the definition of Ley *et al.*.

which in the unmodified form without the GSP has been solved analytically with specific boundaries [73]. In this work, the solution is gained numerically by finding the zero-point of Equation 6.15 with a least-square fit. The simulated effective barriers ΔE calculated with Equation 6.13 are given in Figure 6.20a and the accompanying interface dipole $\Delta\Phi$ in Figure 6.20b. In the calculation, the ionization potential is set to $I_C = 5.3\,\mathrm{eV}$, the surface coverage or number density of NPB at the interface is assumed to be $n = 2.5 \times 10^{15}\,\mathrm{cm}^{-2}$ as used by Ley *et al.* [73] and the oxide capacitance $C_{ox} = 0.89\,\mu\mathrm{F\,cm}^{-2}$. In short, for a high input barrier, a rising GSP leads to a decreasing effective barrier by inducing a negative interface dipole. Still, the minimum barrier is limited by the rise of the image-charge dipole $\Delta\Phi$, if the nominal difference of the ionization potential and the anode workfunction $I_C - \Phi_{subst}$ is decreasing or inverses, indicated with negative initial barriers (color-coded in Figure 6.20). The effect of Fermi-level pinning initially described by Ley *et al.* [73] or Greiner *et al.* [72] is thus not affected by the GSP, which is also observed in experiment. However, if the difference is high enough, the effect of the GSP on the interface dipole is almost linear.

With UPS, a barrier of $\Delta E \approx 0.5\,\mathrm{eV}$ was obtained in this work alongside with an almost linear decrease of the interface dipole with an initial value of $\Delta \approx 0.2\,\mathrm{eV}$. If $\Delta = \Delta\Phi$ is assumed, the difference between ionization potential and substrate workfunction would amount to $I_C - \Phi_{subst} \approx 0.3\,\mathrm{eV}$, which is still high enough for the GSP to cause a considerable difference. The data obtained from UPS for the interface dipole Δ is also given in Figure 6.20b with single points. Although the measured data is shifted towards higher energies by the initial value of 0.22 eV, the relative change is also linear with the sheet charge density. A direct comparison of a slope-fit, however, is not feasible as the exact values for the interfacial charge density in UPS are not known and were therefore taken from a comparison of doped layers with the same doping ratio measured with impedance spectroscopy. Furthermore,

the slope of the simulated interface dipole depends on the chosen parameters of the oxide layer, which is not existent in the devices investigated in this work.

Note, that the calculation presented here does only refer to the induced interface dipole by injected holes and the negative sheet charge density due to the GSP. Any other surface bound effect leading to a dipole formation is not included. In fact, observations published by de Boer *et al.* show an increased interface dipole and barrier with self-assembled monolayers that point the negative end of the dipole towards the surface [308], just as Alq_3. A decrease in the interface dipole was in turn achieved with the fluorinated version of the molecule hexadecanethiol, with the dipole pointing in the opposite direction. The decrease in interface dipole seen here is thus unlikely to be the effect by ordered Alq_3 dipoles at the surface, which could actually lead to an increase in Δ and thus ΔE, but is rather caused by the negative net sheet charge density of the GSP in the film.

Additionally, in the simple picture provided above, the change in charge density in the HOMO of NPB:Alq_3 due to the negative sheet charge that is observed in simulation, is not included. These charges could act as a third term in Equation 6.14 partially lowering the effect of the negative interface charges, though no model exists for their density. Also, the doping of NPB with Alq_3 will introduce species of different ionization potential in the vicinity of the interface. For NPB, the ionization potential was determined to be $I_{\mathrm{C,NPB}} = (5.33 \pm 0.11)\,\mathrm{eV}$, for Alq_3 a larger value of $I_{\mathrm{C,Alq_3}} \approx 5.7\,\mathrm{eV}$ is reported [306]. Assuming the coverage of the surface with NPB in Equation 6.12 is reduced to $n_{\mathrm{d,NPB}} = (1-c)\cdot n$ with a doping concentration c and the total amount of molecules at the interface n, the remaining sites would be occupied with Alq_3, thus $n_{\mathrm{d,Alq_3}} = c \cdot n$. Equation 6.14 is then changed to

$$\Delta\Phi = \mathrm{e}\frac{\left(Q_{\mathrm{NPB}} + Q_{\mathrm{Alq_3}}\right) - Q_{\mathrm{GSP}}}{C_{\mathrm{ox}}} \ ,$$

where Q_{NPB} and $Q_{\mathrm{Alq_3}}$ correspond to Equation 6.12 calculated with the ionization potential and coverage of NPB and Alq_3, respectively. The effect on the interface dipole, however, is small and amounts to an order of magnitude of 10 meV for 10 % to 20 % of doping concentration.

In conclusion it could be shown that the effect of the negative interface charges of the GSP might be described on the basis of image charges induced in the metal contact. However, as the above calculation is based on an oxide contact, further research is needed to see if the assumptions are correct for all types of contacts. Furthermore, the change in carrier density in the semiconductor seen in simulation as well as possible influences of the dipolar species themselves are not included.

6.5. Summary and discussion

In the previous sections, different aspects of the influence of Alq_3 dopants in NPB have been presented. At the beginning in Section 6.1.1, measurements on monopolar devices show an increased current through the bottom contact of ITO with rising doping ratio until roughly 5 % of Alq_3 in NPB. Higher doping ratios, however, show the opposite effect, as well as devices with low nominal hole injection barriers, where no positive effect of the doping is found. This is supported by extracting the injection

barriers by impedance spectroscopy combined with CELIV transients that also lead to an optimum at 5 % of doping for a high barrier device only, see Section 6.1.3.

Sections 6.1.2 and 6.2 deal with the change in charge carrier mobility, where a decrease by one order of magnitude is found for the hole mobility in doped NPB:Alq_3 layers at 10 % of doping in both CELIV and TOF measurements. Additionally, temperature dependent CELIV transients reveal a large but mostly constant mobility activation energy and energetic disorder. This leads to the conclusion that neither the Alq_3 dopants alone, nor their dipoles have a strong effect on the energetic disorder of NPB. Instead extended percolation paths for holes in NPB seem to be the cause for the decreased mobility due to spatial disorder, if Alq_3 is not considered a transport site. Additionally, weak charge trapping or capturing at NPB:Alq_3 boundaries might occur.

To get a more detailed view on the energetics at the ITO/organic interface, UPS measurements at NPB:Alq_3 deposited on ITO are discussed in Section 6.3. From low-energy UPS spectra, no change in shape or width of the first HOMO Gaussian can be found as seen in Section 6.3.4. This supports the findings in Section 6.1.2, where the disorder parameter extracted from temperature dependent mobility measurements also shows no systematic dependence on the doping density. Furthermore, it allows to assume that any further data obtained from the UPS spectra refers to the NPB levels and is not superimposed by an Alq_3 signal. From the spectra, the ionization potential of the material, its workfunction and HOMO level are calculated for different doping ratios and film thicknesses. The injection barrier is defined by the difference between substrate Fermi level and the linear onset of the HOMO level of NPB. A subsequent decrease of the interface dipole at the ITO/NPB:Alq_3 interface is found with rising doping ratio. Additionally, the injection barrier is lowered considerably from neat NPB to 2 % of doping, but is rising again for higher ratios. Last, but not least, the giant surface potential in the doped layers causes a shift in the potential of the film, leading to a linear decrease in workfunction and HOMO level with rising film thickness that agrees with the GSP slope observed in Kelvin probe measurements, see Sections 6.3.3 and 3.1.3.

In drift-diffusion simulations, the current-voltage characteristics reproduced measured data, but only if the changed barrier is included directly as an input parameter to the calculation. Modeling of the charge transport in doped NPB is also only possible by combining NPB and Alq_3 to one mixed virtual material with respective combined properties. The positive effect of the giant surface potential on carrier injection is also described well in simulation, however, no worsening of the current through the device is seen without manually reducing the mobility for doped layers to values seen in measurement. By consulting the theoretical description of the injected current in disordered systems in Section 6.4.1, it is possible to reproduce the trend observed in measurement by including the change in barrier and mobility. Furthermore, the effect of the GSP on Fermi level pinning in Section 6.4.3 and a resulting change in interface dipole are described.

The overall scenario in those devices can therefore be summed up to multiple competing factors (see also Figure 6.21b):

a) Barrier lowering due to a lowered interface dipole. The initial value of the dipole with pure NPB on ITO is $\Delta = 0.22\,\mathrm{eV}$ as observed in this work and it is reduced down to only 70 meV at 10 % of doping. One possible explanation for

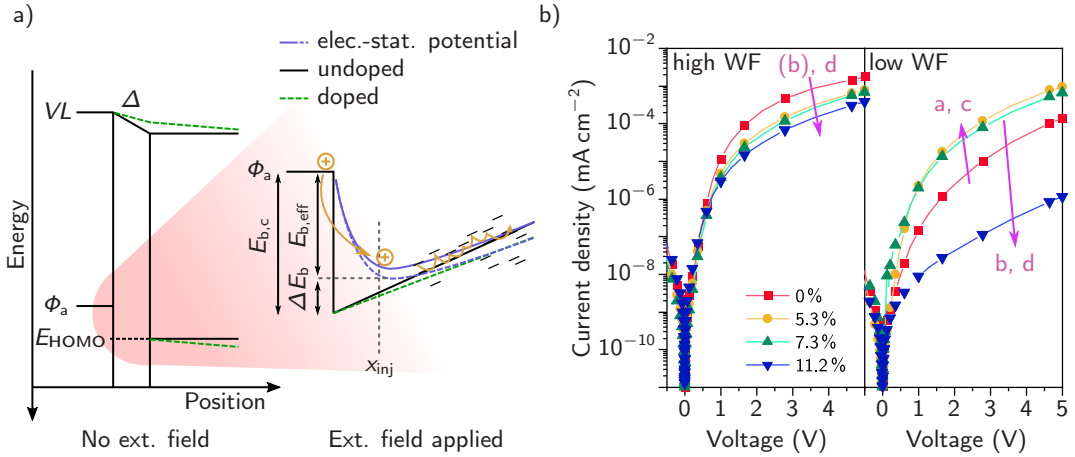

Figure 6.21.: a) Sketch of energy levels in doped and undoped cases. Dipolar doping leads to a change in the interface dipole. However, the polar species also cause shift and bending of the HOMO in NPB counteracting the field, leading to different injection conditions for both cases. Note, that the energy is increasing downwards. The magnification shows the levels and electrostatic potentials according to a Richardson–Schottky type injection with applied external field. **b)** Single-carrier $j(V)$ characteristics with low and high workfunction substrates. Relevant processes are marked with a – d, corresponding to the list in this section.

the lowering is given in Section 6.4.3 and relates to the existence of negative sheet charges in NPB:Alq_3.

b) A shift of the HOMO level of NPB towards higher binding energies, thus leading to an increasing barrier with higher doping ratio. This is most likely caused by the electrostatic potential generated by the ordered dipoles of Alq_3. With rising film thickness, the same effect also leads to the observed giant surface potential, which is additionally visible in bent energy levels in UPS.

c) Increasing injection due to changing local charge carrier densities, which are also reproduced in drift-diffusion simulations for holes in this work and elsewhere for electrons [3].

d) Decreasing mobility due to spatial disorder or trapping, leading to dispersive transport in doped NPB. Because of the mobility dependence of charge carrier injection in disordered systems, a reduced mobility will inevitably also reduce the injection current.

Processes a) and b) affect the barrier between NPB HOMO and the substrate Fermi level. Depending on the workfunction of the bottom contact, or the zero-GSP barrier, two different regimes can be distinguished. For devices, where the workfunction is near the ionization potential of the organic (e.g. with HIL1.3), the effective injection barrier for a simple two-layer interface will not reach below a few 100 meV due to Fermi-level pinning [72]. In this case, a rising doping density and hence interface charge in NPB is not expected to lower the barrier for hole

injection, which is indeed not observed. For low-workfunction substrates like ITO, however, process a) lowers the interface dipole at the ITO/NPB:Alq_3 interface. Upon rising doping concentration, however, the injection barrier into NPB increases as the HOMO onset again shifts to higher binding energies with process b), leading to the observed minimum in the UPS barrier. In theory, the change of HOMO levels is expected to occur independent of the substrate workfunction. As no UPS measurements are available for NPB:Alq_3 on HIL1.3, however, the high-workfunction case is not available with measurements within this work. In Figure 6.21b, these processes hence can be assigned to rising or falling currents through the bottom or HIL-side contact.

Because the negative interface charges are residing on the anode/organic interface, the potential change in the film caused by the GSP at first is expected to have a negative influence on carrier injection. Regarding mobility dependent charge injection, Figure 6.21a sketches the situation at the interface, both with and without a GSP or doped and undoped, respectively. As described by the Schottky model, later extended by Scott and Malliaras (see Section 6.4.1), the potential for a charge carrier to be injected into a semiconductor is highest a few nanometers away from the interface. For amorphous organic materials, hopping across the effective potential barrier and thus surface recombination are also heavily dependent on the carrier mobility. With the potential change due to the GSP and worsening transport because of lowered mobility, charge injecting is hence impaired for higher doping ratios independent of the injection barrier. The magnification in Figure 6.21a sketches this dependence in more detail. The GSP causes a band-bending, leading to a larger injection distance and the hopping mobility additionally affects carrier injection. In Figure 6.21b, the process d) is therefore assigned to lowered currents.

It is thus reasonable to assume that neither the change in barrier, nor the change in mobility alone will explain the observed optimum in current seen in Section 6.1.1 and Figure 6.21b, but a superposition of both processes is needed to describe the observed behavior. Most importantly, dipolar doping allows to add a tunable GSP to originally unpolar layers in the device stack. Besides an impact on the carrier mobility, it directly influences the charge injection of holes into the device, if applied to the HTL. Additionally to conductivity doping, dipolar doping can hence be a versatile tool with which to tune device performance. Furthermore, the doping concentrations of below 10 % that cause a huge impact here, are well in the range of what is used in case of dye doping in current OLED stacks, where many of the emitter molecules can be polar [6].

V

Summary and outlook

Summary

The focus of this work lies on the investigation of possible effects of dipolar doping on the performance of organic semiconducting devices. In this regard, dipolar doping describes the dilution of a non-polar host material, such as NPB or CBP, by a polar guest molecule like Alq_3 or OXD-7. If, upon film growth by vacuum deposition, the permanent dipole moment of these polar molecules orients with a certain amount of order perpendicular to the film surface, the permanent dipole moment of polar species leads to the buildup of a giant surface potential. Using this doping approach, the overall GSP of the organic mixed layer can be tuned to a specific magnitude.

Until now, the effect of dipolar doping has only been investigated with respect to the electron transport layer (ETL) of a polar OLED [2]. Furthermore, Noguchi *et al.* have shown by comparing two molecules of opposite GSP, that the direction or polarity of the surface potential can effectively enhance or hinder carrier injection [11]. However, the effect was only shown for electrons and no systematic study regarding the influence of the magnitude of GSP was performed. A later publication reproduced the findings by Noguchi *et al.* in drift-diffusion simulations, but again only for two different materials [3].

Dipolar doping of organic semiconductors

In this work, the concept of dipolar doping is utilized to systematically investigate the GSP effect on carrier transport and injection of holes in organic semiconductors. Additionally, a model for drift-diffusion simulations on polar OLEDs is extended and tested. The first experimental part therefore focuses on the exact measurement and evaluation of the GSP with two available methods, Kelvin probe (Section 3.1) and impedance spectroscopy (Section 3.2). The influence of the doping concentration on the magnitude of the GSP is measured on two exemplary doped systems, NPB:Alq_3 and CBP:OXD-7. Moreover, undoped polar and non-polar neat-films are measured and compared using Kelvin probe in Section 3.1.2, including a particularly interesting Iridium complex with reversed GSP. With impedance spectroscopy full OLED stacks with dipolar doped hole transport layer (HTL) are investigated. In Sections 3.2.1 and 3.2.3 the transition voltage V_{tr} in $C(V)$ measurements as characteristic quantity for the sheet charge density is discussed for non-polar and polar HTLs, respectively. This framework is applied to standard OLEDs with non-polar HTL and different polar ETL first, where especially the validity of the simulation model is tested. The results of this investigation are presented in Section 3.2.2, where the simulations are found to reproduce the experimental results well. Also, some requirements on the chosen measurement conditions and available sample parameters like thickness or area are elaborated with respect to different routes to calculate the magnitude of the GSP from impedance data. For OLEDs with two polar layers, i.e. doped HTL, simulations presented in Section 3.2.4 also coincide with experimental results and provide an estimate of possible errors. In Section 3.2.5, measurements of OLEDs with polar HTL are compared to those with diluted ETL published earlier by Jäger

et al. [2]. As expected, both device types show a comparable GSP for the same doping ratio of either the HTL or ETL.

To calculate the GSP form impedance spectra, the transition voltage and the value of the built-in field is required. However, especially the transition voltage is found to depend on the workfunction of the anode material at the interface to the HTL. Previous methods to determine the built-in field from impedance spectroscopy proved to be independent of the choice of anode workfunction, which is a priory not expected. In Section 3.3, possible influences of that discrepancy are evaluated using drift-diffusion simulations. It was found that the alternative method to determine V_{bi} from a fit on V_{tr}, determined from multiple samples with different ETL layer thickness, is more reliable.

In Section 3.4, both Kelvin probe and impedance spectroscopy measurements available for various material combinations are compared and discussed. At first, a strong dependence on the preparation conditions was found, leading to a much lower GSP in one evaporation chamber. Despite multiple efforts, a single determining factor for the deviation could not be identified. However, preliminary results show a strong temperature dependence of the GSP that was not previously seen or investigated and might lead to different results in both chambers.

For dipolar doped NPB, as well as neat films comprising only polar species, the alignment factor is calculated and presented in Section 3.4.2. This dimensionless value is a figure of merit for the amount of oriented molecules in the film and is calculated from the measured sheet charge density and a hypothetical maximum value of perfectly oriented dipoles [7, 48]. For both NPB:Alq_3 and CBP:OXD-7, a maximum in interface charge is found for an approximate 1:1 mixture. The alignment factor, however, steadily decreases with rising doping, both is in agreement with previous results [2]. In fact, an exponential dependence of the alignment factor on doping concentration with almost equal slopes in a semi-logarithmic plot is found, indicating similar growth kinetics as decisive factor for the GSP in both materials.

In Chapter 3, the sheet charge density and underlying orientation polarization is investigated only electrically. With a photoluminescence-quenching experiment presented in Chapter 4, an optical method adds to the list. The chapter is based on a joint project with the University of Würzburg and is also published in reference [263]. Basically, the red luminescence of the fluorescent dye DBP is quenched, if doped in Alq_3 with strong dependence on the externally applied voltage and the spatial position of the DBP molecules in the Alq_3 film. A combination of drift-diffusion simulation of the charge carrier densities present in the device at specific driving voltages with measured and simulated impedance spectra reveals two distinct quenching mechanisms. In forward bias, negatively charged Alq_3 molecules at the cathode side lead to a reduction of the DBP PL signal. For negative voltages, the negative sheet charge density of the GSP at the NPB/Alq_3 interface leads to a similar observation. With this experiment, not only the presence of a negative interface charge is again demonstrated, but also the validity of the simulation model is proven.

Influence of dipolar doping on barriers and carrier dynamics

With many individual aspects of the GSP in doped organic layers known and accessible, Part IV focuses on the effect of a dipolar doped HTL in fully working OLEDs on carrier dynamics and injection. Therefor, two new measurement techniques are introduced in Chapter 5. In this chapter, which is based on a joint project with

Fluxim AG and the ZHAW Winterthur in Switzerland, the concept of MIS-diodes is transferred to polar OLEDs. Both sections in this chapter were already published elsewhere in references [13] and [14].

Section 5.1 begins with the application of MIS-CELIV on OLEDs with polar ETL. In simulations, the hole density in a NPB/Alq_3 OLED is compared with a "real" MIS device utilizing a wide band-gap insulator instead of Alq_3. It is found that both devices exhibit a comparably high charge accumulation at the internal interface, whereas the bulk density is low. This qualifies the polar OLED for a CELIV charge extraction experiment, if electron injection into the device is effectively suppressed. The offset or injection voltage for the CELIV transient is therefore chosen just above the transition voltage obtained from $C(V)$ characteristics and well below the injection voltage V_{inj}. With this initial condition, the device fulfills the so-called small charge injection requirement for a simple evaluation of the charge carrier mobility from the transient peak time. A second approach, which is recommended for classic MIS diodes [231], requires the device to reach a space charge regime during measurement. It is thus not feasible for OLEDs, mainly because the required offset voltage would be to high to block electron injection. Still, it is shown that by adding a third, electron blocking layer, this second method is also possible with polar OLEDs, without the need for a classic insulating layer.

The second section in this chapter, Section 5.2, aims to provide a framework to extract hole injection barriers and mobility activation energies from the same device. Traditionally, these quantities are measured on different device stacks, e.g. by photoelectron spectroscopy and time-of-flight experiments. In this work, a combination of polar MIS-CELIV and impedance spectroscopy on OLEDs is shown to provide a good estimate of both, the barrier and the mobility activation energy. For this purpose, simulated, temperature dependent CELIV transients and $C(f)$ spectra are evaluated the same way as done with measurements. From the temperature dependence of the mobility extracted from CELIV, the mobility activation energy is gained from an Arrhenius analysis. Likewise, the relaxation frequency of the charge carrier accumulation in the polar OLED is modeled also with a temperature activated exponential law. As a hypothesis, a linear combination of both, mobility activation and injection barrier is expected to be responsible for the temperature dependence of the relaxation frequency, where the mobility is only dependent on its activation. From simulations, this could be verified. Also, depending on the nominal barrier at the anode and the mobility activation energy, the error is found to be very low. Of course, the investigations in this chapter are based on simulations and the validity of the parameter extraction using the simple analytic model is proven for the simulated devices, only. However, in the following chapter, it is applied to real devices and compared to complementary UPS and TOF measurements, suggesting it to be legitimate also for measured data.

In Chapter 6, the lessons learned in the previous chapters are finally put into use to study the effect of dipolar doping on real devices. Two major stack designs are used: monopolar devices with only the doped NPB:Alq_3 layer and full OLED stacks, where the ETL is comprised of neat Alq_3. Additionally, the TOF measurement requires the doped HTL to be incorporated into a different stack with a charge generation layer and UPS measurements limit the samples to ITO/NPB:Alq_3. With the different device stacks, the two main quantities possibly affected by dipolar doping, hole

mobility and the injection barrier, are investigated.

At first, measurements on monopolar devices are presented in Section 6.1.1. There, an increased current through the bottom contact of ITO is observed with rising doping ratio until roughly 5 % of Alq_3 in NPB. Higher doping ratios show the opposite effect, as well as devices with low nominal hole injection barriers, where no positive effect of the doping is found. Measurements on dipolar doped OLEDs with the techniques introduced in Chapter 5 support this finding by extracting the injection barriers by impedance spectroscopy combined with CELIV transients. Again, the effect of barrier lowering with an optimum at 5 % of doping is observed for devices with high difference of substrate workfunction and organic ionization potential. At the same time, however, a decrease in hole mobility is seen in both, CELIV (Section 6.1.2) and time-of-flight (Section 6.2). Remarkably, this comes without a significant change in mobility activation energy found in temperature dependent CELIV experiments, which suggests no significant increase in energetic disorder in NPB, despite the doping with Alq_3.

A more detailed investigation of the energetics at the ITO/organic interface is gained by UPS measurements on NPB:Alq_3 deposited on ITO in Section 6.3. Again, an optimum is observed with a minimum barrier measured for 2 % of doping, alongside with a gradual decrease of the magnitude of the interface dipole (see Section 6.3.2). Following the minimum in barrier, higher doping ratios, however, provoke a shift of the NPB HOMO level to higher binding energies suggesting a negative effect of the Alq_3 species on the NPB barrier. Additionally, low-energy UPS spectra in Section 6.3.4 also reveal no change in shape or width of the first HOMO Gaussian, which also suggests that no relevant increase in disorder is present in NPB:Alq_3. Although no UPS spectra with dipolar doped NPB on high-workfunction substrates like HIL1.3 are available, the observations made with an ITO-substrate are in good consistency with the combined findings from CELIV and IS introduced in Chapter 5.

With data on mobility and barrier dependence on the doping ratio, simulations can be performed to reproduce and explain the experimental data in both mono- and bipolar devices. At first, a simple calculation of the injection current using the disorder enhanced thermionic injection model by Scott and Malliaras allows to elucidate the role of the mobility change in charge carrier injection. As explained in Section 6.4.1, especially the highly doped samples with 5 % or more suffer from low mobility, which shifts the optimum away from the minimum in barrier of 2 %. In Section 6.4.2 drift-diffusion simulations serve to disentangle the role of the barrier and the carrier density affected by the GSP itself. The simulated current-voltage characteristics reproduce the measured data, but only if the changed barrier is included directly as an input parameter to the calculation. Additionally, a possible influence of increased disorder is discussed. Last but not least, a possible description of the GSP effect on Fermi level pinning and the resulting interface dipole due to image charges is given in Section 6.4.3, which is provided for further discussion.

Overall, the observed increase in current and device performance for low doping ratios can be ascribed to a decrease in interface dipole caused by the sheet charge density of the GSP. The dipolar species, however, shift the NPB HOMO level away from the Fermi level. This increases the barrier, which, assisted by the decrease in mobility, counteracts the positive effect of the GSP on charge injection. Still, one order of magnitude higher injection current is reached in monopolar devices with 5 % of doping, promoting dipolar doping as a versatile tool to tune device performance.

Outlook

In this work, the basic foundations are laid to understand positive and negative effects of a GSP introduced by dipolar doping. This can enable different devices, besides OLEDs, to benefit from a giant surface potential, especially where non-polar molecules are usually found, as in OPV. However, further research is needed to elucidate the exact mechanisms of orientation and the interplay with processing conditions and doping concentration. In the following, possible continuative work is briefly summarized:

- In Section 3.4, the **impact of processing conditions** on the magnitude of the SOP is already visible. Previously, a dependence on the glass transition temperature has been reported for the orientation of the transition dipole and thus the molecule [199], as well as the disappearance of the GSP, if polar molecules are processed from solution [88]. In this work, a dependence of the GSP on **substrate temperature** is observed, which should be investigated further. For this purpose, liquid nitrogen cooling and resistive heating is already installed at the sample holder for the Kelvin probe experiment. A re-design of the sample geometry could allow to study the change in GSP also with impedance spectroscopy, if suitable contacts can be applied. More details on the growth conditions and the difference in both evaporation chambers briefly discussed in Section 3.4.1 can also lead to a deeper understanding of the alignment mechanisms.

- The **exponential growth** of the **alignment factor** with decreased doping is striking. Arguably, a pure dipole-dipole interaction governing the alignment should lead to a growth proportional to the inverse square of the distance and thus doping ratio. Besides the mixtures of NPB:Alq_3 and CBP:OXD-7, also CBP doped with $Ir(ppy)_2(acac)$ has been studied in our lab, although not as part of this work. A similar trend is visible for the alignment factor of this material combination in Figure V.1a, though with a different growth constant or slope in the semi-logarithmic plot. Further investigations should include a systematic study of the impact of various material parameters on the increase in alignment, as well as a higher dynamic range concerning doping concentration and alignment factor in order to distinguish different growth kinetics.

- Promising progress made with dipolar doping of OLEDs suggests the effect to be studied on **polar solar cells** as well. At the moment, most materials tailored for the use in OPV are non-polar. Despite many top performing cells are processed from solution with no GSP expected upon dipolar doping, also vacuum evaporated small molecule solar cells are still under investigation. In Figure V.1b, the current-voltage characteristics of three hypothetical organic planar heterojunction cells are shown. A GSP is added to both donor and

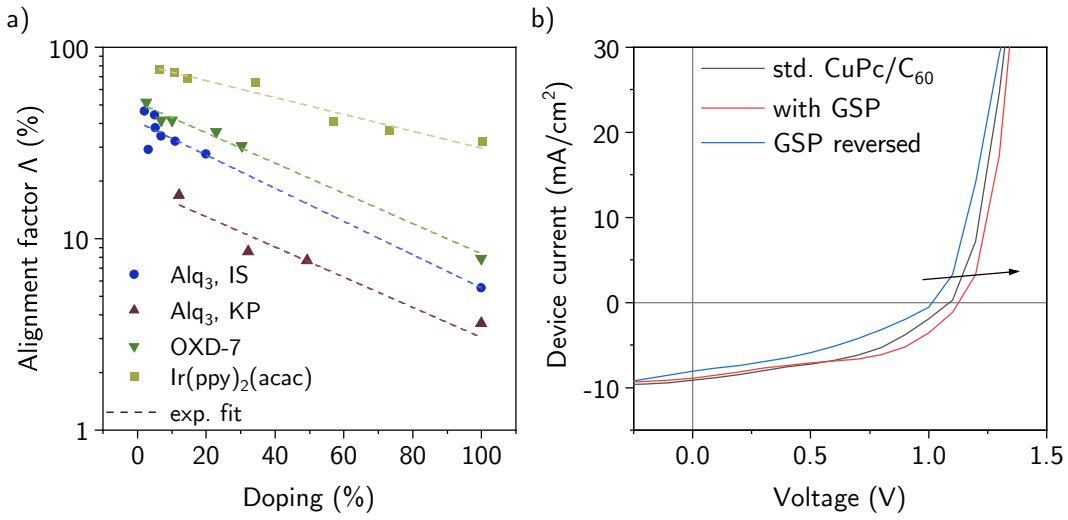

Figure V.1.: a) In the present work, mixtures of NPB:Alq_3 and CBP:OXD-7 are discussed. A previously published set of CBP doped with $Ir(ppy)_2(acac)$ shows a similar trend but with different slope; more devices with different host and guest molecules could shed light on the governing parameters. **b)** Drift-diffusion simulations of a solar cell with the donor copper-phthalocyanine (CuPc) and C_{60} as acceptor show an increased open circuit voltage and fill factor, if a GSP is present and constant throughout the while device. An inverted GSP would decrease device performance.

acceptor with the same direction and sheet charge density or doping concentration, which leads to an **increased open circuit voltage** in simulation. Reversing the GSP will introduce S-shapes and reduce the fill factor, which is in line with increased barriers reported elsewhere [117]. However, the solar cells simulated here lack the influence of the mobility as well as possible effects on charge separation or exciton dissociation.

- Up to now, NPB performed best in polar MIS-CELIV experiments, whereas the solar cell donor DBP proved difficult to measure. Molecules with very high or low mobility should be investigated in **CELIV transients** to further narrow down possible limits of the technique. Ideally, samples with real insulators or alternatively with wide-bandgap organic semiconductors will complement the measurements. Additionally, a **reversed GSP** in the Iridium complex 1295 might allow to study **electron transport** via polar MIS-CELIV.

- While conducting temperature dependent impedance spectra, $j(V)$ or $C(V)$ characteristics and CELIV transients, the need for a **fast and reliable temperature control** during measurement became evident. During this work, a small, thermoelectrically controlled cryostat, which is integrated into the glovebox in N_2 atmosphere has been developed. The system also includes a thermographic camera capable of recording changes in the sample temperature during measurement with a 786-pixel thermal image. A short description of the device is given in Appendix B. Careful design of suitable non-reflecting over-layers could allow to **study self-heating** of devices during measurement.

A. Appendix

A.1. List of suppliers for organic materials

Material	Supplier	Code	Notes
Alq_3	Sensient Imaging	ST 1095S	used as received
Alq_3 (PL)	Aldrich	697737	2x gradient sub.
OXD-7	Lumtec	LT-N855	used as received
NPB	Lumtec	LT-E101	used as received
NPB (PL)	Aldrich	556696	2x gradient sub.
CBP	Lumtec	LT-E409	used as received
C_{70}	Lumtec	LT-S967	used as received
DBP (PL)	Lumtec	LT-N4003C	used as received
BCP	Aldrich	699152	used as received
	Lumtec	LT-E304	
BPhen	Aldrich	133159	used as received
ITO	Thin Film Devices,	N/A	different batches,
& substrate	Inc., Anaheim, CA.		factory patterned
Spiro-2CBP	Lumtec	LT-N420	used as received
$Ir(ppy)_2(acac)$	Lumtec	LT-E505	used as received
PEDOT:PSS	Heraeus	various	used as received

A.2. Determination of ITO workfunction and Fermi edge

Referring to Section 6.3.1, the graphs in Figure A.1 show UPS data of the ITO substrates measured before depositing the organic layers. The data was recorded at 7.7 eV excitation energy to determine the position of the Fermi edge within in the Kinetic-energy scale. By fitting a Fermi-Dirac statistic, the position of the Fermi edge can be determined precisely, where

$$W(E) = \frac{1}{\exp\left(\frac{E-E_\mathrm{F}}{\mathrm{k_B}T}\right)} \ . \tag{A.1}$$

However, because of the width of the detection window and resulting broadening of the spectra, the substrate temperature does not match the temperature gained by fitting. Three different calculated Fermi statistics are given: the first (colored, straight lines) are fits with the temperature being a free parameter, these fits are later used to get the position of the Fermi edge. Colored, dashed lines give results of a fit with fixed temperature of 300 K, while gray lines show the calculated statistic with $T = 300\,\mathrm{K}$ and the fixed energy gained from the free fit. Further elaboration of the UPS experiment is found in Section 2.7.

With the energy scale calibrated to $E_F \stackrel{!}{=} 0\,\text{eV}$, the binding energy plot can now be used to determine the secondary electron cutoff of ITO, leading to the workfunction of the substrate – see Figure A.1, bottom part.

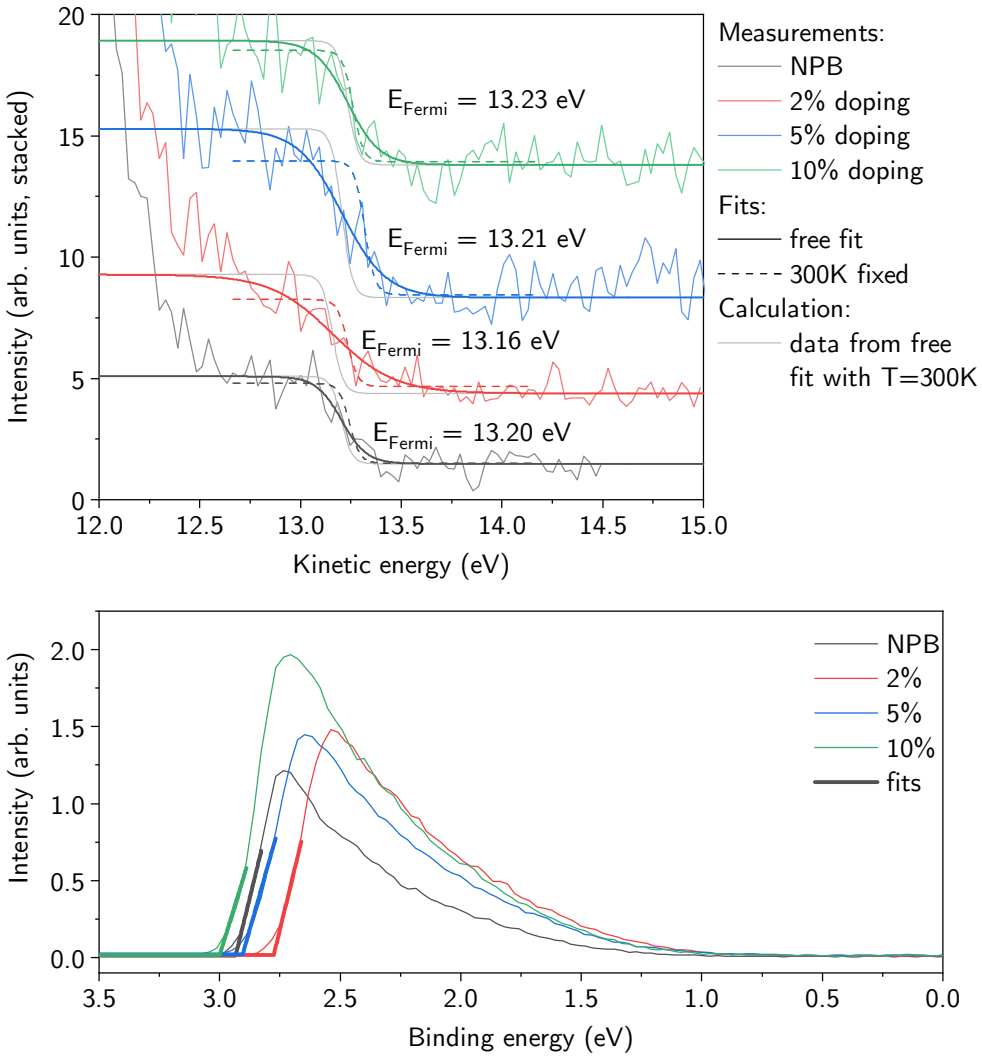

Figure A.1.: top: UPS data of the Fermi-edge for four ITO substrates. The doping ratios of the films that were later deposited on these substrates is given in the legend. **bottom:** After calibration at the Fermi edge, the SECO of the ITO substrates can be used to determine the substrate workfunction. All spectra are measured at 7.7 eV excitation energy.

A.3. Cooled KP measurement on CBP:OXD-7

To check the orientation of CBP:OXD-7 at below room temperature (RT), the sample was cooled to −80 °C during evaporation and measurement. The initial contact potential difference does not differ between RT and cooled KP on ITO, which means that the workfunction of ITO is not changed much when cooled. A change in doping concentration or growth kinetics cannot be excluded completely and unfortunately no further evaluation regarding that topic was possible. However, the sample was continuously monitored during warm-up for about 24 hours. No change was observed in the CPD after warm-up, which is still at about 97 % of the initial value after deposition (light green star in Figure A.2). The film is thus stable from the Kelvin probe point of view and no metastable low-temperature phase is observed.

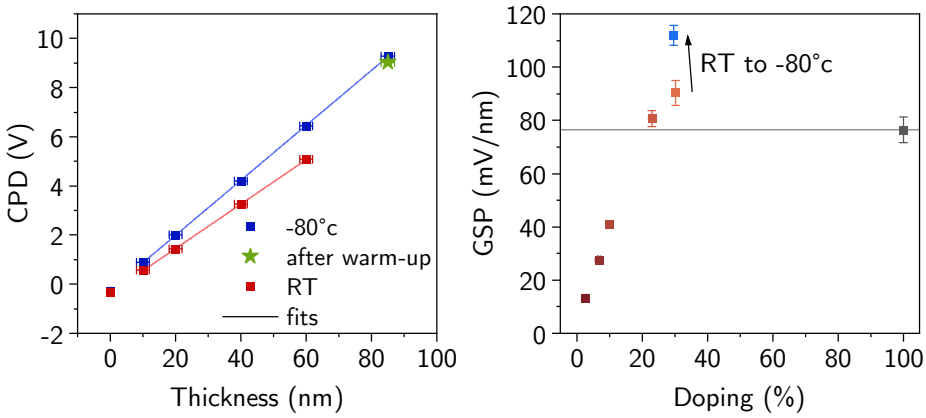

Figure A.2.: **left:** Kelvin probe series with 30 % of nominal doping, cooled and at room temperature. **right:** The measurement combined with the RT series of different doping ratios.

A.4. Comparison of measured and simulated UPS spectra for NPB

A comparison of simulated NPB UPS spectra with measured spectra was attempted. Simulations were made by calculating the position of the single-molecule molecular orbitals in vacuum with the Gaussian09 software using the B3LYP functional and the diffusive 6-31G basis set. The resulting, discrete positions of the molecular orbitals were then overlain using a simple Gaussian with a FWHM of 0.6 eV. No direct connection between the thin-film binding energies and the single-molecule molecular orbital energies exist. The energetic positioning of both measured and simulated spectra is thus done by offsetting the simulated spectra by hand. However, it was not possible to compare any mixtures to the measured spectra, as the simulation could not include the influence of the two species to each other. In the case of neat NPB, however, simulations and measured spectra match considerably well; most importantly, the two HOMO levels close to the HOMO-onset, HOMO-1 and -2, are in good agreement.

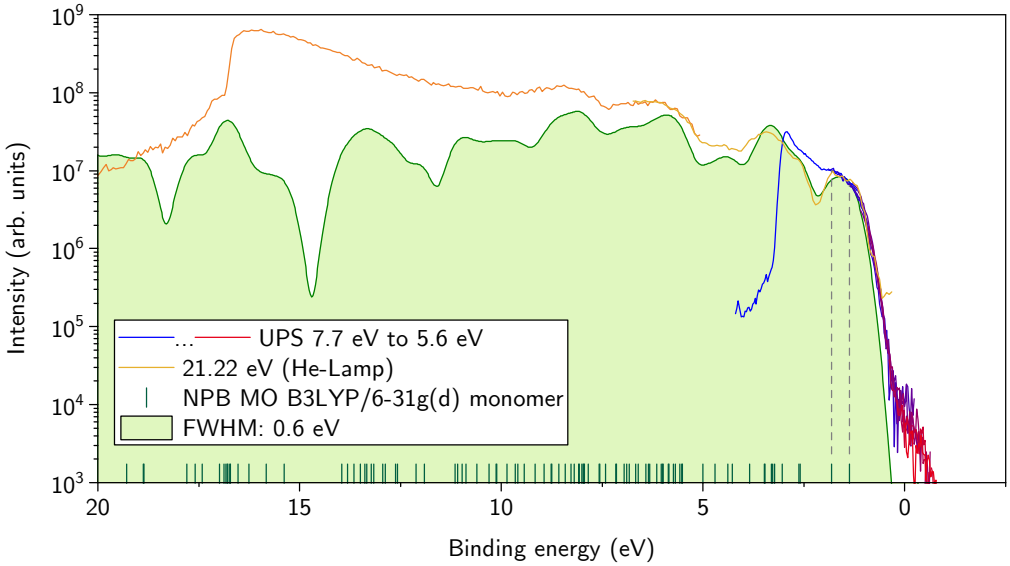

Figure A.3.: Measured and simulated DOS. Although the absolute height is not reproduced perfectly, the relative positions of the molecular orbitals are largly retained in thin film. The first two HOMO levels with lowest binding energy are matched to the measured spectra by gray vertical lines.

B. Design of a glovebox Peltier cryostat

Reliable and fast temperature control is a requirement for extracting activation energies and barriers via CELIV and impedance spectroscopy as described in Section 5.2. Previously, this was accomplished with a LN_2 bath cryostat. Unfortunately, the time taken for the sample to reach a stable temperature can be as long as 30 min per setpoint. Additionally, being a separate setup, it requires the sample to be transferred from the inert glovebox atmosphere to the cryostat using a evacuated transfer rod, which bares the risk of exposure to ambient conditions. To speed up measurement and keep the sample in the glovebox, a thermoelectrically cooled, fast cryostat was built and fitted to the glove box. Requirements for the design of the system are a temperature range of −30 °C to 40 °C, a small footprint and no risk of water contamination of the box from coolant. Additionally, a temperature measurement of the sample surface was preferred over e.g. measuring the sample seating temperature, only. The goals were accomplished by the system shown in Figure B.1. Main, features of the setup are:

- Steel housing compatible to ISO-K with 63 mm nominal width. A screw-on, sealed feed-through is attached to a hole drilled in the glovebox bottom plate. The copper heat-exchanger block is attached, electrically insulated, to a steel tube that is affixed to the feed-through. Water piping is welded to the heat-exchanger from the bottom, inner side of the steel tubing, which is open to the atmosphere. Any leaking water from the building coolant supply will thus never built up pressure against the sealing to the glove box, preventing water contamination of the N_2 atmosphere.

- Temperature regulated using two cascaded Peltier elements with a maximum combined electrical power of 120 W reaching a temperature difference of roughly 50 °C in operation. Regulation is provided by a dedicated Peltier temperature controller model TC2812 from CoolTronic. Two platinum wire temperature sensors attached to the sample seating and copper heat-exchanger allow accurate temperature control and monitoring. The sample stage is electrically and thermally isolated against the cryo table and glovebox as good as possible. A plastic shielding covered with a copper foil provides thermal and electrical shielding. The system is calibrated to a thermocouple glued to a glass slide using thermal compound.

- Round, 20 cm diameter magnetic table to attach the probe station. Probes are positioned to contact the six contact-pads of the standard sample layout; all four pixels can be addressed individually.

- 768 pixel far infrared camera (Melexis MLX90640) capable of capturing at up to 64 fps. Currently, two frames per second are transferred to the software

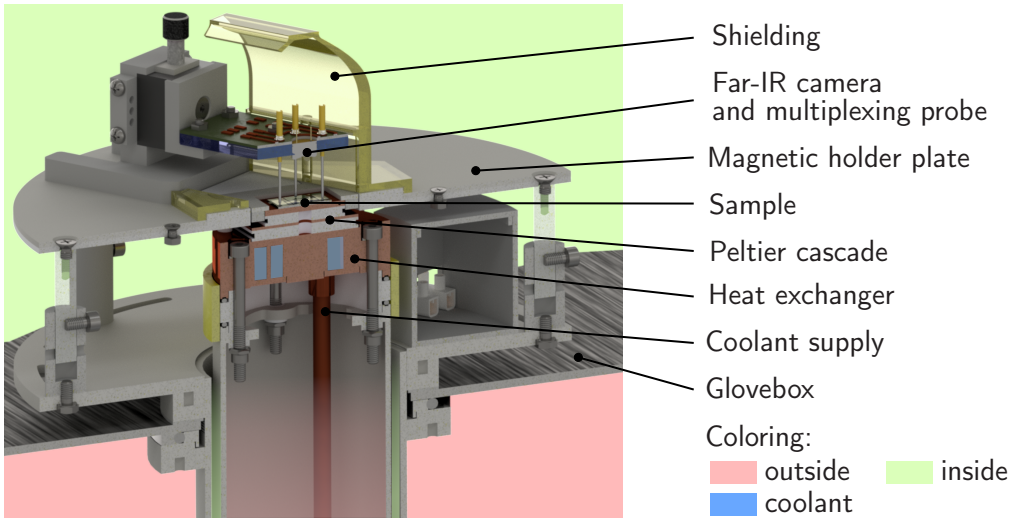

Figure B.1.: 3D rendering of a split section of the cryo assembly, without cabling. Green coloring in the background depicts the part within the glovebox, red is outside. Coolant paths through the copper heat-exchanger are sealed in the outside part preventing leakage into the box. Further parts are marked in the graph.

to provide monitoring and control temperature feedback. Camera control is provided by a network server running on a Raspberry Pi microcomputer.

- The software is designed as an add-on to the Paios software suite, but can also be run stand alone. Thermal images of the sample are recorded and stored, as no such feature is available with Paios.

Optimizing temperature control and imaging

To capture all pixels equally, the camera is mounted directly above the sample, between the spring-loaded contact pins. With a field of view of 110° wide and 75° deep, this includes the sample itself, probes and parts of the sample copper seat at operational distance. Like in visible imaging, the camera captures emitted and reflected light, which has to be accounted for. Additionally, far infrared emission at a specific object temperature is affected by the materials' emissivity. It is defined as a dimension-less quantity from 0 to 1 stating the amount of emitted light with respect to the ideal black-body radiation at the specific temperature and therefore is, strictly speaking, wavelength dependent [320]. For highly smooth metals like a freshly evaporated aluminum cathode or polished copper, the emissivity is given below 0.05 [320]. In contrast, glass or plastics emit close to the black-body spectrum. The temperature calculated from the far infrared light detected at the aluminum cathode will thus mainly resemble the reflected temperature of the sensor itself, being mounted exactly opposite to the mirror plane. With an emissivity near unity, the substrate (glass) and also the organic semiconducting materials are thus less prone to show reflected images. Additionally, the sensor is designed to correct the reflected portion of the light, if the object emissivity and reflected temperature is known, which in turn can be assumed to be the ambient temperature of the camera

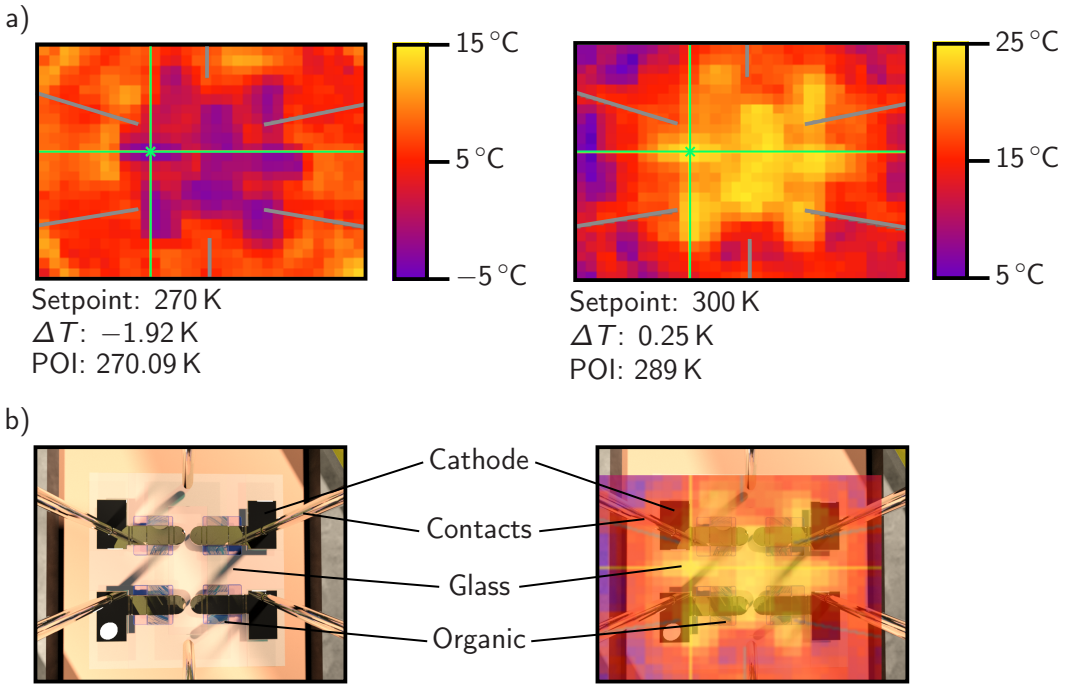

Figure B.2.: a) Example images of a sample at 270 K after cooling (left) and at 300 K after heating. The temperature read out at the POI (green) resembles the expected and calibrated result, whereas the metal layer and ITO appears at a higher temperature after cooling or a lower one after heating. **b)** Rendered image in the direction of the far infrared camera (left) and combined with the thermal data from the 300 K image.

when mounted directly above the mirror plane.

Two example images are shown in Figure B.2a alongside with a rendered view of the sample from the direction of the thermal camera. In the left image, the cryostat was set to a target temperature of 270 K, the image is taken a few seconds after the setpoint was reached. A calibration factor of $\Delta T = -1.92\,\mathrm{K}$ is applied to the cryostat setpoint that was determined prior to the measurement using a thermocouple glued to a glass plate with a thermal compound. The *point of interest* (POI) is set to sample a point in the image, where the camera films glass or organic. As intended, it equals the expected (calibrated) value. Reflective parts of the sample, however, show a by roughly 10 K higher temperature as the surrounding of the sample. Especially the sensor and contact assembly, are still warm. The opposite effect is observed when heating the sample from cooled state. Although the sample itself quickly reaches a temperature near to the setpoint, all reflecting and surrounding parts are still cold, effectively inverting the recorded picture.

As an intermediate summary, the system allows to control the sample temperature fast and reproducibly. Because of the reflections in thermal imaging, the exact pixel temperature is not accessible at the moment, but can possibly be measured by applying an insulating layer on top of the sample with a thermal emissivity near unity. Further modifications will include a light-mixing rod or Y-fiber to allow also optical excitation and detection of electroluminescence.

Bibliography

[1] W. Brütting, S. Berleb & A. G. Mückl. *Device physics of organic light-emitting diodes based on molecular materials*. Organic Electronics **2**(1):1 (2001).

[2] L. Jäger, T. D. Schmidt & W. Brütting. *Manipulation and control of the interfacial polarization in organic light-emitting diodes by dipolar doping*. AIP Advances **6**(9):095220 (2016).

[3] S. Altazin, S. Züfle, E. Knapp, C. Kirsch, T. Schmidt, L. Jäger, Y. Noguchi, W. Brütting & B. Ruhstaller. *Simulation of OLEDs with a polar electron transport layer*. Organic Electronics **39**:244 (2016).

[4] B. Lüssem, M. Riede & K. Leo. *Doping of organic semiconductors*. physica status solidi (a) **210**(1):9 (2013).

[5] C. W. Tang, S. A. VanSlyke & C. H. Chen. *Electroluminescence of doped organic thin films*. Journal of Applied Physics **65**(9):3610 (1989).

[6] K. Osada, K. Goushi, H. Kaji, C. Adachi, H. Ishii & Y. Noguchi. *Observation of spontaneous orientation polarization in evaporated films of organic light-emitting diode materials*. Organic Electronics **58**(January):313 (2018).

[7] Y. Noguchi, W. Brütting & H. Ishii. *Spontaneous orientation polarization in organic light-emitting diodes*. Japanese Journal of Applied Physics **58**(SF):SF0801 (2019).

[8] U. Hörmann. *V_{oc} from a morphology point of view: On the open circuit voltage of polycrystallineorganic heterojunction solar cells*. Dissertation, University of Augsburg (2014).

[9] J. Frischeisen, D. Yokoyama, C. Adachi & W. Brütting. *Determination of molecular dipole orientation in doped fluorescent organic thin films by photoluminescence measurements*. Applied Physics Letters **96**(7):073302 (2010).

[10] E. Ito, Y. Washizu, N. Hayashi, H. Ishii, N. Matsuie, K. Tsuboi, Y. Ouchi, Y. Harima, K. Yamashita & K. Seki. *Spontaneous buildup of giant surface potential by vacuum deposition of Alq_3 and its removal by visible light irradiation*. Journal of Applied Physics **92**(12):7306 (2002).

[11] Y. Noguchi, H. Lim, T. Isoshima, E. Ito, M. Hara, W. Won Chin, J. Wook Han, H. Kinjo, Y. Ozawa, Y. Nakayama & H. Ishii. *Influence of the direction of spontaneous orientation polarization on the charge injection properties of organic light-emitting diodes*. Applied Physics Letters **102**(20) (2013).

[12] Y. Noguchi, Y. Miyazaki, Y. Tanaka, N. Sato, Y. Nakayama, T. D. Schmidt, W. Brütting & H. Ishii. *Charge accumulation at organic semiconductor interfaces due to a permanent dipole moment and its orientational order in bilayer devices*. Journal of Applied Physics **111**(11) (2012).

[13] S. Züfle, S. Altazin, A. Hofmann, L. Jäger, M. T. Neukom, T. D. Schmidt, W. Brütting & B. Ruhstaller. *The use of charge extraction by linearly increasing voltage in polar organic light-emitting diodes*. Journal of Applied Physics **121**(17) (2017).

[14] S. Züfle, S. Altazin, A. Hofmann, L. Jäger, M. T. Neukom, W. Brütting & B. Ruhstaller. *Determination of charge transport activation energy and injection barrier in organic semiconductor devices*. Journal of Applied Physics **122**(11) (2017).

[15] B. Zhou, Z. Li & C. Chen. *Global Potential of Rare Earth Resources and Rare Earth Demand from Clean Technologies*. Minerals **7**(11):203 (2017).

[16] K. M. Goodenough, F. Wall & D. Merriman. *The Rare Earth Elements: Demand, Global Resources, and Challenges for Resourcing Future Generations*. Natural Resources Research **27**(2):201 (2018).

[17] H.-M. Henning & A. Palzer. *Was kostet die Energiewende*. Report, Fraunhofer-Institut für Solare Energiesysteme ISE, Freiburg (2015).

[18] R. Wiser, G. Barbose, J. Heeter, T. Mai, L. Bird, M. Bolinger, A. Carpenter, G. Heath, D. Keyser, J. Macknick, A. Mills & D. Millstein. *A retrospective analysis of benefits and impacts of U.S. renewable portfolio standards*. Report, Lawrence Berkeley National Laboratory and National Renewable Energy Laboratory (2016).

[19] J. Wille, Klimareporter°. *Peak Oil in Sicht* (2019). (accesed 2019/11/07). `https://www.klimareporter.de/gesellschaft/peak-oil-in-sicht`

[20] A. Y. Ku, A. A. Setlur & J. Loudis. *Impact of Light Emitting Diode Adoption on Rare Earth Element Use in Lighting: Implications for Yttrium, Europium, and Terbium Demand*. Electrochemical Society Interface **24**(4):45 (2015).

[21] F. Hütz-Adams. *Von der Mine bis zum Konsumenten*, Volume 1. SÜDWIND e.V., Siegburg (2012).

[22] World Economic Forum. *A New Circular Vision for Electronics*. (accessed 2020/01/14). `http://www3.weforum.org/docs/WEF_A_New_Circular_Vision_for_Electronics.pdf`

[23] G. Cook, E. Jardim & N. Bach. *Guide to greener electronics*. Report October, Greenpeace Reports (2017).

[24] H. Heidenreich. *Steckbrief Gold*. Report, Kampagne "Bergwerk Peru - Reichtum geht, Armut bleibt" (2017).

[25] Amnesty International. *This is what we die for: Human rights abuses in the democratic republic of the congo power the global trade in cobalt* (2016). https://www.amnestyusa.org/files/this_what_we_die_for_-_report.pdf

[26] Y. Palacios-Torres, J. D. de la Rosa & J. Olivero-Verbel. *Trace elements in sediments and fish from Atrato River: an ecosystem with legal rights impacted by gold mining at the Colombian Pacific*. Environmental Pollution **256**:113290 (2020).

[27] Fairphone. *Fairphone Suppliers, Smelters and Refiners* (2018). (accessed 2020/01/13). https://www.fairphone.com/wp-content/uploads/2019/05/016_005_List_Suppliers_and_Smelters_05_19_DEF.pdf

[28] Fairphone. *Mapping the journey of your phone* (2017). (accessed 2020-01-13). https://www.fairphone.com/en/impact/source-map-transparency/

[29] NREL. *Solar Cell Efficiency Chart* (2019). https://www.nrel.gov/pv/cell-efficiency.html

[30] M. A. Green, Y. Hishikawa, E. D. Dunlop, D. H. Levi, J. Hohl-Ebinger, M. Yoshita & A. W. Ho-Baillie. *Solar cell efficiency tables (Version 53)*. Progress in Photovoltaics: Research and Applications **27**(1):3 (2019).

[31] H. Wirth. *Aktuelle Fakten zur Photovoltaik in Deutschland. Fraunhofer ISE*. Report, Fraunhofer-Institut für Solare Energiesysteme ISE, Freiburg (2020).

[32] J. D. Bergesen, L. Tähkämö, T. Gibon & S. Suh. *Potential Long-Term Global Environmental Implications of Efficient Light-Source Technologies*. Journal of Industrial Ecology **20**(2):263 (2016).

[33] J. Y. Tsao, H. D. Saunders, J. R. Creighton, M. E. Coltrin & J. A. Simmons. *Solid-state lighting: an energy-economics perspective*. Journal of Physics D: Applied Physics **43**(35):354001 (2010).

[34] S. Reineke, F. Lindner, G. Schwartz, N. Seidler, K. Walzer, B. Lüssem & K. Leo. *White organic light-emitting diodes with fluorescent tube efficiency*. Nature **459**(7244):234 (2009).

[35] S.-F. Wu, S.-H. Li, Y.-K. Wang, C.-C. Huang, Q. Sun, J.-J. Liang, L.-S. Liao & M.-K. Fung. *White Organic LED with a Luminous Efficacy Exceeding* $100\,\mathrm{lm\,W^{-1}}$ *without Light Out-Coupling Enhancement Techniques*. Advanced Functional Materials **27**(31):1701314 (2017).

[36] C. Adachi, M. A. Baldo, M. E. Thompson & S. R. Forrest. *Nearly* 100 % *internal phosphorescence efficiency in an organic light-emitting device*. Journal of Applied Physics **90**(10):5048 (2001).

[37] G. Zhan, Z. Liu, Z. Bian & C. Huang. *Recent advances in organic light-emitting diodes based on pure organic room temperature phosphorescence materials*. Frontiers in Chemistry **7**(MAY):1 (2019).

[38] D. Das, P. Gopikrishna, D. Barman, R. B. Yathirajula & P. K. Iyer. *White light emitting diode based on purely organic fluorescent to modern thermally activated delayed fluorescence (TADF) and perovskite materials*. Nano Convergence **6**(1):1 (2019).

[39] OLED info. *OLED lighting introduction and market status* (2019). (accessed 2020/01/12).
`https://www.oled-info.com/oled-lighting`

[40] L. Meng, Y. Zhang, X. Wan, C. Li, X. Zhang, Y. Wang, X. Ke, Z. Xiao, L. Ding, R. Xia, H. L. Yip, Y. Cao & Y. Chen. *Organic and solution-processed tandem solar cells with 17.3% efficiency*. Science **361**(6407):1094 (2018).

[41] i-MEET & ZAE, HI ERN, Forschungszentrum Jülich. *New Efficiency World Record for Organic Solar Modules* (2019). (accessed 2020/01/12).
`https://www.fz-juelich.de/SharedDocs/Pressemitteilungen/UK/EN/2019/2019-11-11-opv-record.html`

[42] P. P. Khlyabich, B. Burkhart, A. E. Rudenko & B. C. Thompson. *Optimization and simplification of polymer–fullerene solar cells through polymer and active layer design*. Polymer **54**(20):5267 (2013).

[43] *Heliatek's organische Solarfolien – Eine wirklich grüne Technologie zur Stromerzeugung* (2019). (accessed 2020/01/15).
`https://www.heliatek.com/de/blog/heliateks-organische-solarfolien-eine-wirklich-gruene-technologie-zur-stromerzeugung/`

[44] N. Espinosa, M. Hösel, D. Angmo & F. C. Krebs. *Solar cells with one-day energy payback for the factories of the future*. Energy Environ. Sci. **5**(1):5117 (2012).

[45] Opvious. *OPV Technology* (2020). (accessed 2020/01/12).
`http://www.opvius.com/en/lab.html`

[46] T. D. Schmidt, D. S. Setz, M. Flämmich, J. Frischeisen, D. Michaelis, B. C. Krummacher, N. Danz & W. Brütting. *Evidence for non-isotropic emitter orientation in a red phosphorescent organic light-emitting diode and its implications for determining the emitter's radiative quantum efficiency*. Applied Physics Letters **99**(16):163302 (2011).

[47] P. Friederich, V. Rodin, F. Von Wrochem & W. Wenzel. *Built-In Potentials Induced by Molecular Order in Amorphous Organic Thin Films*. ACS Applied Materials and Interfaces **10**(2):1881 (2018).

[48] T. Morgenstern, M. Schmid, A. Hofmann, M. Bierling, L. Jäger & W. Brütting. *Correlating Optical and Electrical Dipole Moments To Pinpoint Phosphorescent Dye Alignment in Organic Light-Emitting Diodes*. ACS Applied Materials & Interfaces **10**(37):31541 (2018).

[49] A. J. L. Hofmann, S. Züfle, K. Shimizu, M. Schmid, V. Wessels, L. Jäger, S. Altazin, K. Ikegami, M. R. Khan, D. Neher, H. Ishii, B. Ruhstaller & W. Brütting. *Dipolar Doping of Organic Semiconductors to Enhance Carrier Injection*. Phys. Rev. Applied **12**:064052 (2019).

[50] A. J. L. Hofmann. *Transient electrical measurements on organic solar cells.* Diploma thesis, University of Augsburg (2014).

[51] A. Köhler & H. Bässler. *Electronic Processes in Organic Semiconductors*. Wiley-VCH Verlag GmbH & Co. KGaA, Weinheim, Germany (2015).

[52] M. Pope & C. E. Swenberg. *Electronic Processes in Organic Crystals and Polymers.* Oxford university press (1999).

[53] W. Brütting (Editor). *Physics of Organic Semiconductors*. Wiley (2005).

[54] M. Schwoerer & H. C. Wolf. *Organic Molecular Solids*. Wiley (2006).

[55] B. A. Gregg, S.-G. Chen & R. A. Cormier. *Coulomb Forces and Doping in Organic Semiconductors*. Chemistry of Materials **16**(23):4586 (2004).

[56] E. G. Barbagiovanni, D. J. Lockwood, R. N. Costa Filho, L. V. Goncharova & P. J. Simpson. *Quantum confinement in Si and Ge nanostructures: effect of crystallinity*. In P. Cheben, J. Schmid, C. Boudoux, L. R. Chen, A. Delâge, S. Janz, R. Kashyap, D. J. Lockwood, H.-P. Loock & Z. Mi (Editors), *Photonics North 2013*, Volume 8915, S. 891515 (2013).

[57] T. G. Pedersen. *Excitons on the surface of a sphere*. Physical Review B **81**(23):233406 (2010).

[58] B. A. Gregg & M. C. Hanna. *Comparing organic to inorganic photovoltaic cells: Theory, experiment, and simulation*. Journal of Applied Physics **93**(6):3605 (2003).

[59] B. A. Gregg. *Excitonic Solar Cells*. The Journal of Physical Chemistry B **107**(20):4688 (2003).

[60] N. Karl. *Charge carrier transport in organic semiconductors*. Synthetic Metals **133-134**(0):649 (2003).

[61] B. Ruhstaller, S. A. Carter, S. Barth, H. Riel, W. Riess & J. C. Scott. *Transient and steady-state behavior of space charges in multilayer organic light-emitting diodes*. Journal of Applied Physics **89**(8):4575 (2001).

[62] N. Karl, K.-H. Kraft, J. Marktanner, M. Münch, F. Schatz, R. Stehle & H.-M. Uhde. *Fast electronic transport in organic molecular solids?* Journal of Vacuum Science & Technology A **17**(4):2318 (1999).

[63] H. H. Fong & S. K. So. *Hole transporting properties of tris(8-hydroxyquinoline) aluminum (Alq3).* Journal of Applied Physics **100**(9):094502 (2006).

[64] H. Bässler. *Charge Transport in Disordered Organic Photoconductors a Monte Carlo Simulation Study*. physica status solidi (b) **175**(1):15 (1993).

[65] D. Hertel & H. Bässler. *Photoconduction in amorphous organic solids.* Chemphyschem : a European journal of chemical physics and physical chemistry **9**(5):666 (2008).

[66] Y. Gartstein & E. Conwell. *High-field hopping mobility in molecular systems with spatially correlated energetic disorder*. Chemical Physics Letters **245**(4-5):351 (1995).

[67] H. Ishii, K. Sugiyama, E. Ito & K. Seki. *Energy Level Alignment and Interfacial Electronic Structures at Organic/Metal and Organic/Organic Interfaces*. Advanced Materials **11**(8):605 (1999).

[68] C. S. Lee, J. X. Tang, Y. C. Zhou & S. T. Lee. *Interface dipole at metal-organic interfaces: Contribution of metal induced interface states*. Applied Physics Letters **94**(11):113304 (2009).

[69] I. H. Campbell, S. Rubin, T. A. Zawodzinski, J. D. Kress, R. L. Martin, D. L. Smith, N. N. Barashkov & J. P. Ferraris. *Controlling Schottky energy barriers in organic electronic devices using self-assembled monolayers*. Physical Review B **54**(20):R14321 (1996).

[70] N. B. Kotadiya, H. Lu, A. Mondal, Y. Ie, D. Andrienko, P. W. Blom & G. J. A. Wetzelaer. *Publisher Correction: Universal strategy for Ohmic hole injection into organic semiconductors with high ionization energies*. Nature Materials **17**(April):1 (2018).

[71] T. Matsushima, Y. Kinoshita & H. Murata. *Formation of Ohmic hole injection by inserting an ultrathin layer of molybdenum trioxide between indium tin oxide and organic hole-transporting layers*. Applied Physics Letters **91**(25):253504 (2007).

[72] M. T. Greiner, M. G. Helander, W. M. Tang, Z. B. Wang, J. Qiu & Z. H. Lu. *Universal energy-level alignment of molecules on metal oxides*. Nature Materials **11**(1):76 (2012).

[73] L. Ley, Y. Smets, C. I. Pakes & J. Ristein. *Calculating the Universal Energy-Level Alignment of Organic Molecules on Metal Oxides*. Advanced Functional Materials **23**(7):794 (2013).

[74] V. I. Arkhipov, U. Wolf & H. Bässler. *Current injection from a metal to a disordered hopping system. II. Comparison between analytic theory and simulation*. Physical Review B **59**(11):7514 (1999).

[75] J. C. Scott & G. G. Malliaras. *Charge injection and recombination at the metal–organic interface*. Chemical Physics Letters **299**(2):115 (1999).

[76] B. A. Gregg, S. E. Gledhill & B. Scott. *Can true space-charge-limited currents be observed in π-conjugated polymers?* Journal of Applied Physics **99**(11):17 (2006).

[77] P. Stallinga. *Electrical Characterization of Organic Electronic Materials and Devices*. John Wiley & Sons, Ltd, Chichester, UK (2009).

[78] C. Adachi. *Third-generation organic electroluminescence materials*. Japanese Journal of Applied Physics **53**(6):060101 (2014).

[79] A. R. Smith, P. L. Burn & B. J. Powell. *Spin-orbit coupling in phosphorescent iridium(III) complexes*. ChemPhysChem **12**(13):2429 (2011).

[80] D. Y. Kondakov, T. D. Pawlik, T. K. Hatwar & J. P. Spindler. *Triplet annihilation exceeding spin statistical limit in highly efficient fluorescent organic light-emitting diodes*. Journal of Applied Physics **106**(12):124510 (2009).

[81] N. C. Giebink, B. W. D'Andrade, M. S. Weaver, P. B. Mackenzie, J. J. Brown, M. E. Thompson & S. R. Forrest. *Intrinsic luminance loss in phosphorescent small-molecule organic light emitting devices due to bimolecular annihilation reactions*. Journal of Applied Physics **103**(4):044509 (2008).

[82] J. Frischeisen, D. Yokoyama, A. Endo, C. Adachi & W. Brütting. *Increased light outcoupling efficiency in dye-doped small molecule organic light-emitting diodes with horizontally oriented emitters*. Organic Electronics **12**(5):809 (2011).

[83] T. D. Schmidt, T. Lampe, D. Sylvinson M. R., P. I. Djurovich, M. E. Thompson & W. Brütting. *Emitter Orientation as a Key Parameter in Organic Light-Emitting Diodes*. Physical Review Applied **8**(3):037001 (2017).

[84] *Schrödinger Release 2019-3* (2019). Maestro, Schrödinger, LLC, New York, NY.
`https://www.schrodinger.com/`

[85] *Schrödinger Release 2019-3* (2019). Jaguar, Schrödinger, LLC, New York, NY.
`https://www.schrodinger.com/`

[86] A. D. Bochevarov, E. Harder, T. F. Hughes, J. R. Greenwood, D. A. Braden, D. M. Philipp, D. Rinaldo, M. D. Halls, J. Zhang & R. A. Friesner. *Jaguar: A high-performance quantum chemistry software program with strengths in life and materials sciences*. International Journal of Quantum Chemistry **113**(18):2110 (2013).

[87] S. Emelyanova, V. Chashchikhin & A. Bagaturyants. *Atomistic multiscale simulation of the structure and properties of an amorphous OXD-7 layer*. Chemical Physics Letters **590**:101 (2013).

[88] T. Lampe, T. D. Schmidt, M. J. Jurow, P. I. Djurovich, M. E. Thompson & W. Brütting. *Dependence of Phosphorescent Emitter Orientation on Deposition Technique in Doped Organic Films*. Chemistry of Materials **28**(3):712 (2016).

[89] M. J. Jurow, C. Mayr, T. D. Schmidt, T. Lampe, P. I. Djurovich, W. Brütting & M. E. Thompson. *Understanding and predicting the orientation of heteroleptic phosphors in organic light-emitting materials*. Nature Materials **15**(1):85 (2016).

[90] S. Berleb, W. Brütting & G. Paasch. *Interfacial charges and electric field distribution in organic hetero-layer light-emitting devices*. Organic Electronics **1**(1):41 (2000).

[91] T. Morgenstern. *Preferential alignment of anisotropic transition dipole moments in organic and perovskite thin films*. Dissertation, University of Augsburg (2019).

[92] A. Bernanose. *Electroluminescence of organic compounds*. British Journal of Applied Physics **6**(S4):S54 (1955).

[93] M. Pope, H. P. Kallmann & P. Magnante. *Electroluminescence in Organic Crystals*. The Journal of Chemical Physics **38**(8):2042 (1963).

[94] C. W. Tang & S. A. VanSlyke. *Organic electroluminescent diodes*. Applied Physics Letters **51**(12):913 (1987).

[95] R. Springer, B. Y. Kang, R. Lampande, D. H. Ahn, S. Lenk, S. Reineke & J. H. Kwon. *Cool white light-emitting three stack OLED structures for AMOLED display applications*. Optics Express **24**(24):28131 (2016).

[96] C. Adachi, T. Tsutsui & S. Saito. *Confinement of charge carriers and molecular excitons within 5-nm-thick emitter layer in organic electroluminescent devices with a double heterostructure*. Applied Physics Letters **57**(6):531 (1990).

[97] T. Tsutsui, E. Aminaka, C. P. Lin & D. U. Kim. *Extended molecular design concept of molecular materials for electroluminescence: sublimed–dye films, molecularly doped polymers and polymers with chromophores*. Philosophical Transactions of the Royal Society of London. Series A: Mathematical, Physical and Engineering Sciences **355**(1725):801 (1997).

[98] W. Brütting, J. Frischeisen, T. D. Schmidt, B. J. Scholz & C. Mayr. *Device efficiency of organic light-emitting diodes: Progress by improved light outcoupling*. physica status solidi (a) **210**(1):44 (2013).

[99] H. Uoyama, K. Goushi, K. Shizu, H. Nomura & C. Adachi. *Highly efficient organic light-emitting diodes from delayed fluorescence*. Nature **492**(7428):234 (2012).

[100] W. Shockley. *The Theory of p-n Junctions in Semiconductors and p-n Junction Transistors*. Bell System Technical Journal **28**(3):435 (1949).

[101] G.-J. A. H. Wetzelaer & P. W. M. Blom. *Diffusion-driven currents in organic-semiconductor diodes*. NPG Asia Materials **6**(7):e110 (2014).

[102] P. Würfel. *Physik der Solarzellen*. Springer (2000).

[103] S. Sze & K. K. Ng. *Physics of Semiconductor Devices*. John Wiley & Sons, Inc., Hoboken, NJ, USA (2006).

[104] U. Hörmann, J. Kraus, M. Gruber, C. Schuhmair, T. Linderl, S. Grob, S. Kapfinger, K. Klein, M. Stutzman, H. J. Krenner & W. Brütting. *Quantification of energy losses in organic solar cells from temperature-dependent device characteristics*. Physical Review B **88**(23):235307 (2013).

[105] Y. Canivez. *Quick and easy measurement of the band gap in semiconductors*. European Journal of Physics **4**(1):42 (1983).

[106] P. E. Burrows, Z. Shen, V. Bulovic, D. M. McCarty, S. R. Forrest, J. A. Cronin & M. E. Thompson. *Relationship between electroluminescence and current transport in organic heterojunction light-emitting devices*. Journal of Applied Physics **79**(10):7991 (1996).

[107] J. Wu, A. Fischer & S. Reineke. *Investigating Free Charge-Carrier Recombination in Organic LEDs Using Open-Circuit Conditions*. Advanced Optical Materials **7**(7):1801426 (2019).

[108] C. W. Tang. *Two-layer organic photovoltaic cell*. Applied Physics Letters **48**(2):183 (1986).

[109] H. Spanggaard & F. C. Krebs. *A brief history of the development of organic and polymeric photovoltaics*. Solar Energy Materials and Solar Cells **83**(2-3):125 (2004).

[110] A. Opitz, J. Wagner, W. Brütting, I. Salzmann, N. Koch, J. Manara, J. Pflaum, A. Hinderhofer & F. Schreiber. *Charge Separation at Molecular Donor–Acceptor Interfaces: Correlation Between Morphology and Solar Cell Performance*. IEEE Journal of Selected Topics in Quantum Electronics **16**(6):1707 (2010).

[111] J. G. Xue, B. P. Rand, S. Uchida & S. R. Forrest. *A hybrid planar-mixed molecular heterojunction photovoltaic cell*. Advanced Materials **17**(1):66 (2005).

[112] S. R. Forrest. *The Limits to Organic Photovoltaic Cell Efficiency*. MRS Bulletin **30**:28 (2005).

[113] J. Nelson. *Organic photovoltaic films*. Current Opinion in Solid State and Materials Science **6**(1):87 (2002).

[114] J.-L. Bredas. *Molecular understanding of organic solar cells: The challenges*. In *AIP Conference Proceedings*, Volume 1519, S. 55–58 (2013).

[115] T. Linderl, T. Zechel, M. Brendel, D. Moseguí González, P. Müller-Buschbaum, J. Pflaum & W. Brütting. *Energy Losses in Small-Molecule Organic Photovoltaics*. Advanced Energy Materials **7**(16):1700237 (2017).

[116] T. Linderl, T. Zechel, A. J. L. Hofmann, T. Sato, K. Shimizu, H. Ishii & W. Brütting. *Crystalline vs. amorphous donor-acceptor blends: Influence of layer morphology on the charge-transfer density of states*. Physical Review Applied (2020). Accepted.

[117] J. Wagner, M. Gruber, A. Wilke, Y. Tanaka, K. Topczak, A. Steindamm, U. Hörmann, A. Opitz, Y. Nakayama, H. Ishii, J. Pflaum, N. Koch & W. Brütting. *Identification of different origins for s-shaped current voltage characteristics in planar heterojunction organic solar cells*. Journal of Applied Physics **111**(5):054509 (2012).

[118] W. Tress, K. Leo & M. Riede. *Influence of Hole-Transport Layers and Donor Materials on Open-Circuit Voltage and Shape of I–V Curves of Organic Solar Cells*. Advanced Functional Materials **21**(11):2140 (2011).

[119] K. Vandewal, K. Tvingstedt, A. Gadasi, O. Inganäs & J. V. Manca. *On the origin of the open-circuit voltage of polymer–fullerene solar cells*. Nature Materials **8**(11):904 (2009).

[120] K. Vandewal, K. Tvingstedt, A. Gadisa, O. Inganäs & J. V. Manca. *Relating the open-circuit voltage to interface molecular properties of donor:acceptor bulk heterojunction solar cells*. Physical Review B **81**(12):125204 (2010).

[121] A. Wilke, J. Endres, U. Hörmann, J. Niederhausen, R. Schlesinger, J. Frisch, P. Amsalem, J. Wagner, M. Gruber, A. Opitz, A. Vollmer, W. Brütting, A. Kahn & N. Koch. *Correlation between interface energetics and open circuit voltage in organic photovoltaic cells*. Applied Physics Letters **101**(23):233301 (2012).

[122] T. Linderl, U. Hörmann, S. Beratz, M. Gruber, S. Grob, A. Hofmann & W. Brütting. *Temperature dependent competition between different recombination channels in organic heterojunction solar cells*. Journal of Optics **18**(2):24007 (2016).

[123] C.-H. Lin & C. W. Liu. *Metal-Insulator-Semiconductor Photodetectors*. Sensors **10**(10):8797 (2010).

[124] *Semiconducting thin film optics simulator (SETFOS) by Fluxim AG, Switzerland*.
`http://www.fluxim.com`

[125] *Platform for all-in-one characterization (PAIOS) by Fluxim AG, Switzerland*.
`http://www.fluxim.com`

[126] Fluxim AG. *Setfos User Manual Version 5.0* (2019).

[127] E. Knapp, R. Häusermann, H. U. Schwarzenbach & B. Ruhstaller. *Numerical simulation of charge transport in disordered organic semiconductor devices*. Journal of Applied Physics **108**(5):054504 (2010).

[128] A. Ligthart, X. de Vries, L. Zhang, M. C. Pols, P. A. Bobbert, H. van Eersel & R. Coehoorn. *Effect of Triplet Confinement on Triplet–Triplet Annihilation in Organic Phosphorescent Host–Guest Systems*. Advanced Functional Materials **28**(52):1 (2018).

[129] S. L. M. van Mensfoort, V. Shabro, R. J. de Vries, R. A. J. Janssen & R. Coehoorn. *Hole transport in the organic small molecule material α-NPD: evidence for the presence of correlated disorder*. Journal of Applied Physics **107**(11):113710 (2010).

[130] R. Meerheim, S. Scholz, S. Olthof, G. Schwartz, S. Reineke, K. Walzer & K. Leo. *Influence of charge balance and exciton distribution on efficiency and lifetime of phosphorescent organic light-emitting devices*. Journal of Applied Physics **104**(1):014510 (2008).

[131] H. M. Mattoussi, H. Murata, C. D. Merritt & Z. H. Kafafi. *Photoluminescence quantum yield of molecular organic thin films*. In Z. H. Kafafi (Editor), *Organic Light-Emitting Materials and Devices II*, Volume 3476, S. 49–60 (1998).

[132] T. Zhang, Y. Liang, J. Cheng & J. Li. *A CBP derivative as bipolar host for performance enhancement in phosphorescent organic light-emitting diodes*. J. Mater. Chem. C **1**(4):757 (2013).

[133] M. E. Kondakova, T. D. Pawlik, R. H. Young, D. J. Giesen, D. Y. Kondakov, C. T. Brown, J. C. Deaton, J. R. Lenhard & K. P. Klubek. *High-efficiency, low-voltage phosphorescent organic light-emitting diode devices with mixed host*. Journal of Applied Physics **104**(9):094501 (2008).

[134] I. Iwakura, H. Ebina, K. Komori-Orisaku & Y. Koide. *A theoretical and experimental study on meridional–facial isomerization of tris(quinolin-8-olate)aluminum (Alq_3)*. Dalton Trans. **43**(34):12824 (2014).

[135] G. G. Malliaras, Y. Shen, D. H. Dunlap, H. Murata & Z. H. Kafafi. *Nondispersive electron transport in Alq_3*. Applied Physics Letters **79**(16):2582 (2001).

[136] S. Barth, P. Müller, H. Riel, P. F. Seidler, W. Rieß, H. Vestweber & H. Bässler. *Electron mobility in tris(8-hydroxy-quinoline)aluminum thin films determined via transient electroluminescence from single- and multilayer organic light-emitting diodes*. Journal of Applied Physics **89**(7):3711 (2001).

[137] K. Okumoto, H. Kanno, Y. Hamaa, H. Takahashi & K. Shibata. *Green fluorescent organic light-emitting device with external quantum efficiency of nearly 10 %*. Applied Physics Letters **89**(6) (2006).

[138] Y. Hamada, C. Adachi, T. Tsutsui & S. Saito. *Organic electroluminescent devices with bright blue emission*. Optoelectronics - Devices and Technologies **7**(1):83 (1992).

[139] M. K. Mathai, V.-E. Choong, S. A. Choulis, B. Krummacher & F. So. *Highly efficient solution processed blue organic electrophosphorescence with 14 lm/W luminous efficacy*. Applied Physics Letters **88**(24):243512 (2006).

[140] K. H. Yeoh, C. Y. B. Ng, C. L. Chua, N. AzrinaTalik & K. L. Woon. *High power efficiency solution-processed double-layer blue phosphorescent organic light-emitting diode by controlling charge transport at the emissive layer and heterojunction*. physica status solidi (RRL) - Rapid Research Letters **7**(6):421 (2013).

[141] K. S. Yook & J. Y. Lee. *Small Molecule Host Materials for Solution Processed Phosphorescent Organic Light-Emitting Diodes*. Advanced Materials **26**(25):4218 (2014).

[142] Q. Zhang, X. Zhang & B. Wei. *Highly efficient ultraviolet organic light-emitting diodes and interface study using impedance spectroscopy*. Optik **126**(18):1595 (2015).

[143] D. Yokoyama, A. Sakaguchi, M. Suzuki & C. Adachi. *Enhancement of electron transport by horizontal molecular orientation of oxadiazole planar molecules in organic amorphous films*. Applied Physics Letters **95**(24):243303 (2009).

[144] T. Yasuda, Y. Yamaguchi, D.-C. Zou & T. Tsutsui. *Carrier Mobilities in Organic Electron Transport Materials Determined from Space Charge Limited Current*. Japanese Journal of Applied Physics **41**(Part 1, No. 9):5626 (2002).

[145] S. Y. Kim, W. I. Jeong, C. Mayr, Y. S. Park, K. H. Kim, J. H. Lee, C. K. Moon, W. Brütting & J. J. Kim. *Organic light-emitting diodes with 30 % external quantum efficiency based on a horizontally oriented emitter*. Advanced Functional Materials **23**(31):3896 (2013).

[146] Y.-S. Park, S. Lee, K.-H. Kim, S.-Y. Kim, J.-H. Lee & J.-J. Kim. *Exciplex-Forming Co-host for Organic Light-Emitting Diodes with Ultimate Efficiency*. Advanced Functional Materials **23**(39):4914 (2013).

[147] H. Sasabe, J.-i. Takamatsu, T. Motoyama, S. Watanabe, G. Wagenblast, N. Langer, O. Molt, E. Fuchs, C. Lennartz & J. Kido. *High-Efficiency Blue and White Organic Light-Emitting Devices Incorporating a Blue Iridium Carbene Complex*. Advanced Materials **22**(44):5003 (2010).

[148] Y.-J. Cho, S.-Y. Kim, J.-H. Kim, J. Lee, D. W. Cho, S. Yi, H.-J. Son, W.-S. Han & S. O. Kang. *Probing photophysical properties of isomeric N-heterocyclic carbene Ir(III) complexes and their applications to deep-blue phosphorescent organic light-emitting diodes*. Journal of Materials Chemistry C **5**(7):1651 (2017).

[149] X. Crispin, S. Marciniak, W. Osikowicz, G. Zotti, a. W. D. van der Gon, F. Louwet, M. Fahlman, L. Groenendaal, F. De Schryver & W. R. Salaneck. *Conductivity, morphology, interfacial chemistry, and stability of poly(3,4-ethylene dioxythiophene)-poly(styrene sulfonate): A photoelectron spectroscopy study*. Journal of Polymer Science Part B: Polymer Physics **41**(21):2561 (2003).

[150] J. Ouyang, C. Chu, F. Chen, Q. Xu & Y. Yang. *Polymer Optoelectronic Devices with High-Conductivity Poly(3,4-Ethylenedioxythiophene) Anodes*. Journal of Macromolecular Science, Part A **41**(12):1497 (2004).

[151] Z. Yu, Y. Xia, D. Du & J. Ouyang. *PEDOT:PSS Films with Metallic Conductivity through a Treatment with Common Organic Solutions of Organic Salts and Their Application as a Transparent Electrode of Polymer Solar Cells*. ACS Applied Materials & Interfaces **8**(18):11629 (2016).

[152] S. Naithani, R. Mandamparambil, H. Fledderus, D. Schaubroeck & G. V. Steenberge. *Fabrication of a laser patterned flexible organic light-emitting diode on an optimized multilayered barrier*. Applied Optics **53**(12):2638 (2014).

[153] S. D. Chavhan, R. Hansson, L. K. Ericsson, P. Beyer, A. Hofmann, W. Brütting, A. Opitz & E. Moons. *Low temperature processed NiO x hole transport layers for efficient polymer solar cells*. Organic Electronics **44**:59 (2017).

[154] D. Kurrle & J. Pflaum. *Exciton diffusion length in the organic semiconductor diindenoperylene*. Applied Physics Letters **92**(13):133306 (2008).

[155] S. Sapp, S. Luebben, Y. B. Losovyj, P. Jeppson, D. L. Schulz & A. N. Caruso. *Work function and implications of doped poly(3,4-ethylenedioxythiophene)-co-poly(ethylene glycol)*. Applied Physics Letters **88**(15):152107 (2006).

[156] Heraeus. *Product Datasheet Clevios P VP AI4083*. (Datasheet).

[157] N. Koch, A. Elschner, J. P. Rabe & R. L. Johnson. *Work Function Independent Hole-Injection Barriers Between Pentacene and Conducting Polymers*. Advanced Materials **17**(3):330 (2005).

[158] J. H. Youn, Y. I. Lee, M. S. Ryu, A. Elschner, W. Lövenich, A. Scheel, H. T. Moon & J. Jang. *Effect of Solution Processed Hole Injection Layers on Device Performance of Phosphorescent Green OLEDs*. Journal of The Electrochemical Society **158**(11):J321 (2011).

[159] S. M. Park, Y. H. Kim, Y. Yi, H.-Y. Oh & J. Won Kim. *Insertion of an organic interlayer for hole current enhancement in inverted organic light emitting devices*. Applied Physics Letters **97**(6):063308 (2010).

[160] L.-S. Cui, Y. Liu, X.-D. Yuan, Q. Li, Z.-Q. Jiang & L.-S. Liao. *Bipolar host materials for high efficiency phosphorescent organic light emitting diodes: tuning the HOMO/LUMO levels without reducing the triplet energy in a linear system*. Journal of Materials Chemistry C **1**(48):8177 (2013).

[161] Y.-K. Kim, J. Won Kim & Y. Park. *Energy level alignment at a charge generation interface between 4,4'-bis(N-phenyl-1-naphthylamino)biphenyl and 1,4,5,8,9,11-hexaazatriphenylene-hexacarbonitrile*. Applied Physics Letters **94**(6):063305 (2009).

[162] J.-H. Jou, J.-W. Weng, S. D. Chavhan, R. A. K. Yadav & T.-W. Liang. *Investigation of charge-transporting layers for high-efficiency organic light-emitting diode*. Journal of Physics D: Applied Physics **51**(45):454002 (2018).

[163] H. Glowatzki, B. Bröker, R.-P. Blum, O. T. Hofmann, A. Vollmer, R. Rieger, K. Müllen, E. Zojer, J. P. Rabe & N. Koch. *"Soft" Metallic Contact to Isolated C_{60} Molecules*. Nano Letters **8**(11):3825 (2008).

[164] H. W. Kroto, J. R. Heath, S. C. O'Brien, R. F. Curl & R. E. Smalley. *C_{60}: Buckminsterfullerene*. Nature **318**(6042):162 (1985).

[165] N. S. Sariciftci, L. Smilowitz, a. J. Heeger & F. Wudl. *Photoinduced electron transfer from a conducting polymer to buckminsterfullerene.* Science (New York, N.Y.) **258**(5087):1474 (1992).

[166] A. Wadsworth, M. Moser, A. Marks, M. S. Little, N. Gasparini, C. J. Brabec, D. Baran & I. McCulloch. *Critical review of the molecular design progress in non-fullerene electron acceptors towards commercially viable organic solar cells*. Chemical Society Reviews **48**(6):1596 (2019).

[167] T. A. Linderl. *Charge Transfer States and Energy Losses in Organic Solar Cells*. Dissertation, University of Augsburg (2017).

[168] G. Chen, D. Yokoyama, H. Sasabe, Z. Hong, Y. Yang & J. Kido. *Optical and electrical properties of a squaraine dye in photovoltaic cells*. Applied Physics Letters **101**(8):083904 (2012).

[169] J. Wagner, M. Gruber, A. Hinderhofer, A. Wilke, B. Bröker, J. Frisch, P. Amsalem, A. Vollmer, A. Opitz, N. Koch, F. Schreiber & W. Brütting. *High Fill Factor and Open Circuit Voltage in Organic Photovoltaic Cells with Diindenoperylene as Donor Material*. Advanced Functional Materials **20**(24):4295 (2010).

[170] B. R. Patil, M. Ahmadpour, G. Sherafatipour, T. Qamar, A. F. Fernández, K. Zojer, H. G. Rubahn & M. Madsen. *Area dependent behavior of bathocuproine (BCP) as cathode interfacial layers in organic photovoltaic cells*. Scientific Reports **8**(1):1 (2018).

[171] D. Fujishima, H. Kanno, T. Kinoshita, E. Maruyama, M. Tanaka, M. Shirakawa & K. Shibata. *Organic thin-film solar cell employing a novel electron-donor material*. Solar Energy Materials and Solar Cells **93**(6-7):1029 (2009).

[172] R. C. Haddon, R. E. Palmer, H. W. Kroto & P. A. Sermon. *The Fullerenes: Powerful Carbon-Based Electron Acceptors*. Philosophical Transactions: Physical Sciences and Engineering **343**(1667):53 (1993).

[173] S. Pfuetzner, J. Meiss, A. Petrich, M. Riede & K. Leo. *Improved bulk heterojunction organic solar cells employing C_{70} fullerenes*. Applied Physics Letters **94**(22):223307 (2009).

[174] W.-C. Su, S.-W. Liu, C.-W. Cheng, C.-C. Chou, J.-C. Huang & C.-C. Lee. *Efficient planar-mixed heterojunction photovoltaic device based on subphthalocyanine:C_{70} structure*. In Z. H. Kafafi, C. J. Brabec & P. A. Lane (Editors), *SPIE Organic Photonics + Electronics*, S. 84771E. International Society for Optics and Photonics (2012).

[175] P. Peumans, V. Bulović & S. R. Forrest. *Efficient photon harvesting at high optical intensities in ultrathin organic double-heterostructure photovoltaic diodes*. Applied Physics Letters **76**(19):2650 (2000).

[176] B. P. Rand, J. Li, J. Xue, R. J. Holmes, M. E. Thompson & S. R. Forrest. *Organic Double-Heterostructure Photovoltaic Cells Employing Thick Tris(acetylacetonato)ruthenium(III) Exciton-Blocking Layers*. Advanced Materials **17**(22):2714 (2005).

[177] H.-W. Lin, C.-W. Lu, L.-Y. Lin, Y.-H. Chen, W.-C. Lin, K.-T. Wong & F. Lin. *Pyridine-based electron transporting materials for highly efficient organic solar cells*. Journal of Materials Chemistry A **1**(5):1770 (2013).

[178] P. Peumans, A. Yakimov & S. R. Forrest. *Small molecular weight organic thin-film photodetectors and solar cells*. J. Appl. Phys. **93**(7):3693 (2003).

[179] C.-C. Chang, C.-F. Lin, J.-M. Chiou, T.-H. Ho, Y. Tai, J.-H. Lee, Y.-F. Chen, J.-K. Wang, L.-C. Chen & K.-H. Chen. *Effects of cathode buffer layers on the efficiency of bulk-heterojunction solar cells*. Applied Physics Letters **96**(26):263506 (2010).

[180] T. D. Schmidt, L. Jäger, Y. Noguchi, H. Ishii & W. Brütting. *Analyzing degradation effects of organic light-emitting diodes via transient optical and electrical measurements*. Journal of Applied Physics **117**(21):215502 (2015).

[181] G. Xie, Y. Meng, F. Wu, C. Tao, D. Zhang, M. Liu, Q. Xue, W. Chen & Y. Zhao. *Very low turn-on voltage and high brightness tris-(8-hydroxyquinoline) aluminum-based organic light-emitting diodes with a MoOx p-doping layer*. Applied Physics Letters **92**(9):093305 (2008).

[182] N.-n. Wang, J.-s. Yu, H. Lin & Y.-d. Jiang. *Organic Photovoltaic Cells with Improved Performance Using Bathophenanthroline as a Buffer Layer*. Chinese Journal of Chemical Physics **23**(1):84 (2010).

[183] S. Naka, H. Okada, H. Onnagawa & T. Tsutsui. *High electron mobility in bathophenanthroline*. Applied Physics Letters **76**(2):197 (2000).

[184] M. Y. Chan, S. L. Lai, K. M. Lau, C. S. Lee & S. T. Lee. *Application of metal-doped organic layer both as exciton blocker and optical spacer for organic photovoltaic devices*. Applied Physics Letters **89**(16):163515 (2006).

[185] E. Fortunato, D. Ginley, H. Hosono & D. C. Paine. *Transparent Conducting Oxides for Photovoltaics*. MRS Bulletin **32**(3):242 (2007).

[186] A. Klein, C. Körber, A. Wachau, F. Säuberlich, Y. Gassenbauer, S. P. Harvey, D. E. Proffit & T. O. Mason. *Transparent conducting oxides for photovoltaics: Manipulation of fermi level,work function and energy band alignment*. Materials **3**(11):4892 (2010).

[187] Thin Film Devices. *Product specifications for ITO substrates.* (Datasheet).

[188] M. Benoy, E. Mohammed, M. Suresh Babu, P. Binu & B. Pradeep. *Thickness dependence of the properties of indium tin oxide (ITO) FILMS prepared by activated reactive evaporation*. Brazilian Journal of Physics **39**:629 (2009).

[189] R. Schlaf, H. Murata & Z. Kafafi. *Work function measurements on indium tin oxide films*. Journal of Electron Spectroscopy and Related Phenomena **120**(1-3):149 (2001).

[190] D. Lu, Y. Wu, J. Guo, G. Lu, Y. Wang & J. Shen. *Surface treatment of indium tin oxide by oxygen-plasma for organic light-emitting diodes*. Materials Science and Engineering: B **97**(2):141 (2003).

[191] B.-s. Kim, D.-e. Kim, Y.-k. Jang, N.-s. Lee, O.-k. Kwon & Y.-s. Kwon. *UV-Ozone Surface Treatment of Indium-Tin-Oxide in Organic Light Emitting Diodes*. Journal of the Korean Physical Society **50**(6):1858 (2007).

[192] G. Kumar, Y.-D. Li, S. Biring, Y.-N. Lin, S.-W. Liu & C.-H. Chang. *Highly efficient ITO-free organic light-emitting diodes employing a roughened ultra-thin silver electrode*. Organic Electronics **42**:52 (2017).

[193] D. Angmo & F. C. Krebs. *Flexible ITO-free polymer solar cells*. Journal of Applied Polymer Science **129**(1):1 (2013).

[194] L. Tan, H. Zhou, T. Ji, L. Huang & Y. Chen. *High conductive PEDOT via post-treatment by halobenzoic for high-efficiency ITO-free and transporting layer-free organic solar cells*. Organic Electronics **33**:316 (2016).

[195] X. Wan, G. Long, L. Huang & Y. Chen. *Graphene – a promising material for organic photovoltaic cells*. Advanced Materials **23**(45):5342 (2011).

[196] A. C. Dürr, F. Schreiber, M. Müch, N. Karl, B. Krause, V. Kruppa & H. Dosch. *High structural order in thin films of the organic semiconductor diindenoperylene*. Applied Physics Letters **81**(12):2276 (2002).

[197] A. C. Dürr, N. Koch, M. Kelsch, A. Rühm, J. Ghijsen, R. Johnson, J.-J. Pireaux, J. Schwartz, F. Schreiber, H. Dosch & A. Kahn. *Interplay between morphology, structure, and electronic properties at diindenoperylene-gold interfaces*. Physical Review B **68**(11):115428 (2003).

[198] U. Hörmann, C. Lorch, A. Hinderhofer, A. Gerlach, M. Gruber, J. Kraus, B. Sykora, S. Grob, T. Linderl, A. Wilke, A. Opitz, R. Hansson, A. S. Anselmo, Y. Ozawa, Y. Nakayama, H. Ishii, N. Koch, E. Moons, F. Schreiber & W. Brütting. *Voc from a morphology point of view: The influence of molecular orientation on the open circuit voltage of organic planar heterojunction solar cells*. Journal of Physical Chemistry C **118**(46):26462 (2014).

[199] C. Mayr & W. Brütting. *Control of Molecular Dye Orientation in Organic Luminescent Films by the Glass Transition Temperature of the Host Material*. Chemistry of Materials **27**(8):2759 (2015).

[200] C. Buzea & K. Robbie. *State of the art in thin film thickness and deposition rate monitoring sensors*. Reports on Progress in Physics **68**(2):385 (2005).

[201] H.-F. Xiang, Z.-X. Xu, V. A. L. Roy, C.-M. Che & P. T. Lai. *Method for measurement of the density of thin films of small organic molecules*. Review of Scientific Instruments **78**(3):034104 (2007).

[202] D. Meyerhofer. *Characteristics of resist films produced by spinning*. Journal of Applied Physics **49**(7):3993 (1978).

[203] W. W. Flack, D. S. Soong, A. T. Bell & D. W. Hess. *A mathematical model for spin coating of polymer resists*. Journal of Applied Physics **56**(4):1199 (1984).

[204] D. W. Schubert & T. Dunkel. *Spin coating from a molecular point of view: its concentration regimes, influence of molar mass and distribution*. Materials Research Innovations **7**(5):314 (2003).

[205] S. Wolf & R. F. Smith. *Student Reference Manual for Electronic Instrumentation Laboratories*. Pearson, 2nd Eddition (2003).

[206] R. G. Lyons. *Understanding Digital Signal Processing*. Pearson Education, 3 Eddition (2011).

[207] J. R. Taylor. *An Introduction to Error Analysis: The Study of Uncertainties in Physical Measurements*. University Science Books (1997).

[208] R. Walden. *Analog-to-digital converter survey and analysis*. IEEE Journal on Selected Areas in Communications **17**(4):539 (1999).

[209] L. Kelvin. *Contact electricity of metals*. The London, Edinburgh, and Dublin Philosophical Magazine and Journal of Science **46**(278):82 (1898).

[210] J. Wagner. *Electronic properties of interfaces in organic devices studied by Kelvin probe and impedance spectroscopy*. Diploma thesis, Institut für Physik, Universität Augsburg (2008).

[211] W. A. Zisman. *A new Method of measuring Contact Potential differences in Metals*. Review of Scientific Instruments **3**(7):367 (1932).

[212] H. Ishii, N. Hayashi, E. Ito, Y. Washizu, K. Sugi, Y. Kimura, M. Niwano, Y. Ouchi & K. Seki. *Kelvin probe study of band bending at organic semiconductor/metal interfaces: examination of Fermi level alignment*. physica status solidi (a) **201**(6):1075 (2004).

[213] H. Huang, H. Wang, J. Zhang & D. Yan. *Surface potential images of polycrystalline organic semiconductors obtained by Kelvin probe force microscopy*. Applied Physics A **95**(1):125 (2009).

[214] I. D. Baikie, E. Venderbosch, J. A. Meyer & P. J. Z. Estrup. *Analysis of stray capacitance in the Kelvin method*. Review of Scientific Instruments **62**(3):725 (1991).

[215] N. A. Surplice & R. J. D'Arcy. *A critique of the Kelvin method of measuring work functions*. Journal of Physics E: Scientific Instruments **3**(7):201 (1970).

[216] McAllister Technical Services. *Kelvin Probe User's Manual* (2004).

[217] V. L. Eden & R. C. McAllister. *On the Elimination of Spacing Dependent Errors in the Kelvin Probe* (2013). (accessed 2019/08/29). `https://old.mcallister.com/library/straycap.html`

[218] G. Juška, K. Arlauskas & M. Viliūnas. *Extraction Current Transients: New Method of Study of Charge Transport in Microcrystalline Silicon*. Physical Review Letters **84**(21):4946 (2000).

[219] G. Juška, K. Arlauskas, M. Viliūnas, K. Genevičius, R. Österbacka & H. Stubb. *Charge transport in π-conjugated polymers from extraction current transients*. Physical Review B **62**(24):R16235 (2000).

[220] G. Juška, N. Nekrašas, K. Genevičius, J. Stuchlik & J. Kočka. *Relaxation of photoexited charge carrier concentration and mobility in μc-Si:H*. Thin Solid Films **451-452**:290 (2004).

[221] A. J. Mozer, N. S. Sariciftci, L. Lutsen, D. Vanderzande, R. Österbacka, M. Westerling & G. Juška. *Charge transport and recombination in bulk heterojunction solar cells studied by the photoinduced charge extraction in linearly increasing voltage technique*. Applied Physics Letters **86**(11):112104 (2005).

[222] S. Tiwari & N. Greenham. *Charge mobility measurement techniques in organic semiconductors*. Optical and Quantum Electronics **41**(2):69 (2009).

[223] A. Baumann, J. Lorrmann, D. Rauh, C. Deibel & V. Dyakonov. *A New Approach for Probing the Mobility and Lifetime of Photogenerated Charge Carriers in Organic Solar Cells Under Real Operating Conditions*. Advanced Materials **24**(32):4381 (2012).

[224] A. Pivrikas, N. S. Sariciftci, G. Juška & R. Österbacka. *A review of charge transport and recombination in polymer/fullerene organic solar cells*. Progress in Photovoltaics: Research and Applications **15**(8):677 (2007).

[225] A. Armin, M. Velusamy, P. L. Burn, P. Meredith & A. Pivrikas. *Injected charge extraction by linearly increasing voltage for bimolecular recombination studies in organic solar cells*. Applied Physics Letters **101**(8):083306 (2012).

[226] A. Armin, G. Juska, M. Ullah, M. Velusamy, P. L. Burn, P. Meredith & A. Pivrikas. *Balanced carrier mobilities: Not a necessary condition for high-efficiency thin organic solar cells as determined by MIS-CELIV*. Advanced Energy Materials **4**(4) (2014).

[227] J. Lorrmann, B. H. Badada, O. Inganäs, V. Dyakonov & C. Deibel. *Charge carrier extraction by linearly increasing voltage: Analytic framework and ambipolar transients*. Journal of Applied Physics **108**(11):113705 (2010).

[228] S. Bange, M. Schubert & D. Neher. *Charge mobility determination by current extraction under linear increasing voltages: Case of nonequilibrium charges and field-dependent mobilities*. Physical Review B **81**(3):035209 (2010).

[229] C. Deibel. *Charge carrier dissociation and recombination in polymer solar cells*. physica status solidi (a) **206**(12):2731 (2009).

[230] M. T. Neukom, N. A. Reinke & B. Ruhstaller. *Charge extraction with linearly increasing voltage: A numerical model for parameter extraction*. Solar Energy **85**(6):1250 (2011).

[231] G. Juška, N. Nekrašas & K. Genevičius. *Investigation of charge carriers transport from extraction current transients of injected charge carriers*. Journal of Non-Crystalline Solids **358**(4):748 (2012).

[232] B. Homa, M. Andersson & O. Inganäs. *Photogenerated charge carrier transport and recombination in polyfluorene/fullerene bilayer and blend photovoltaic devices*. Organic Electronics **10**(3):501 (2009).

[233] O. J. Sandberg, M. Nyman, S. Dahlström, S. Sandén, B. Törngren, J.-H. Smått & R. Österbacka. *On the validity of MIS-CELIV for mobility determination in organic thin-film devices*. Applied Physics Letters **110**(15):153504 (2017).

[234] J. Važgėla, K. Genevičius & G. Juška. *i-CELIV technique for investigation of charge carriers transport properties*. Chemical Physics **478**:126 (2016).

[235] E. Barsoukov & J. R. Macdonald (Editors). *Impedance Spectroscopy*. John Wiley & Sons, Inc., Hoboken, NJ, USA (2018).

[236] H. C. F. Martens, H. B. Brom & P. W. M. Blom. *Frequency-dependent electrical response of holes in poly(p-phenylene vinylene)*. Physical Review B **60**(12):R8489 (1999).

[237] D. C. Tripathi, A. K. Tripathi & Y. N. Mohapatra. *Mobility determination using frequency dependence of imaginary part of impedance (Im Z) for organic and polymeric thin films*. Applied Physics Letters **98**(3):033304 (2011).

[238] J. Fischer, D. Ray, H. Kleemann, P. Pahner, M. Schwarze, C. Koerner, K. Vandewal & K. Leo. *Density of states determination in organic donor-acceptor blend layers enabled by molecular doping*. Journal of Applied Physics **117**(24):245501 (2015).

[239] L. Burtone, D. Ray, K. Leo & M. Riede. *Impedance model of trap states for characterization of organic semiconductor devices*. Journal of Applied Physics **111**(6):064503 (2012).

[240] P. Pahner, H. Kleemann, L. Burtone, M. L. Tietze, J. Fischer, K. Leo & B. Lüssem. *Pentacene Schottky diodes studied by impedance spectroscopy: Doping properties and trap response*. Physical Review B **88**(19):195205 (2013).

[241] S. Nowy, W. Ren, J. Wagner, J. A. Weber & W. Brütting. *Impedance spectroscopy of organic hetero-layer OLEDs as a probe for charge carrier injection and device degradation*. In F. So & C. Adachi (Editors), *Organic Light Emitting Materials and Devices XIII*, Volume 7415, S. 79 – 90. International Society for Optics and Photonics, SPIE (2009).

[242] S. Nowy, W. Ren, A. Elschner, W. Lövenich & W. Brütting. *Impedance spectroscopy as a probe for the degradation of organic light-emitting diodes*. Journal of Applied Physics **107**(5):054501 (2010).

[243] S. K. Gupta, L. S. Pali & A. Garg. *Impedance spectroscopy on degradation analysis of polymer/fullerene solar cells*. Solar Energy **178**:133 (2019).

[244] S. L. M. van Mensfoort & R. Coehoorn. *Determination of Injection Barriers in Organic Semiconductor Devices from Capacitance Measurements*. Physical Review Letters **100**(8):086802 (2008).

[245] E. von Hauff. *Impedance Spectroscopy for Emerging Photovoltaics*. The Journal of Physical Chemistry C **123**(18):11329 (2019).

[246] M. Schönleber, D. Klotz & E. Ivers-Tiffée. *A Method for Improving the Robustness of linear Kramers-Kronig Validity Tests*. Electrochimica Acta **131**:20 (2014).

[247] H. Ishii, K. Kudo, T. Nakayama & N. Ueno (Editors). *Electronic Processes in Organic Electronics*, Volume 209 of *Springer Series in Materials Science*. Springer Japan, Tokyo (2015).

[248] T. Sato, H. Kinjo, J. Yamazaki & H. Ishii. *10^{15} $cm^{-3}eV^{-1}$ level detection of density of states of a p-type polymer by hν-dependent high-sensitivity ultraviolet photoemission spectroscopy*. Applied Physics Express **10**(1):011602 (2017).

[249] T. Manaka, K. Yoshizaki & M. Iwamoto. *Investigation of the surface potential formed in Alq_3 films on metal surface by Kelvin probe and nonlinear optical measurement*. Current Applied Physics **6**(5):877 (2006).

[250] D. Yamashita, A. Ishizaki & T. Yamamoto. *In Situ Measurements of Work Function of Indium Tin Oxide after UV/Ozone Treatment*. MATERIALS TRANSACTIONS **56**(9):1445 (2015).

[251] D. York, N. M. Evensen, M. L. Martínez & J. De Basabe Delgado. *Unified equations for the slope, intercept, and standard errors of the best straight line*. American Journal of Physics **72**(3):367 (2004).

[252] *OriginPro, Version 2019b* (2019). OriginLab Corporation, Northampton, MA, USA.
`https://www.originlab.com/`

[253] K. Sugi, H. Ishii, Y. Kimura, M. Niwano, E. Ito, Y. Washizu, N. Hayashi, Y. Ouchi & K. Seki. *Characterization of light-erasable giant surface potential built up in evaporated Alq_3 thin films*. Thin Solid Films **464-465**:412 (2004).

[254] N. Kajimoto, T. Manaka & M. Iwamoto. *Decay process of a large surface potential of Alq_3 films by heating*. Journal of Applied Physics **100**(5):053707 (2006).

[255] T. Isoshima, Y. Okabayashi, E. Ito, M. Hara, W. W. Chin & J. W. Han. *Negative giant surface potential of vacuum-evaporated tris(7-propyl-8-hydroxyquinolinolato) aluminum(III) [$Al(7\text{-}Prq)_3$] film*. Organic Electronics **14**(8):1988 (2013).

[256] S. Torabi, F. Jahani, I. Van Severen, C. Kanimozhi, S. Patil, R. W. A. Havenith, R. C. Chiechi, L. Lutsen, D. J. M. Vanderzande, T. J. Cleij, J. C. Hummelen & L. J. A. Koster. *Strategy for Enhancing the Dielectric Constant of Organic Semiconductors Without Sacrificing Charge Carrier Mobility and Solubility*. Advanced Functional Materials **25**(1):150 (2015).

[257] H. B. Michaelson. *The work function of the elements and its periodicity*. Journal of Applied Physics **48**(11):4729 (1977).

[258] Y. Noguchi, N. Sato, Y. Miyazaki & H. Ishii. *Light- and ion-gauge-induced space charges in tris-(8-hydroxyquinolate) aluminum-based organic light-emitting diodes*. Applied Physics Letters **96**(14):143305 (2010).

[259] V. Myroshnychenko & C. Brosseau. *Finite-element method for calculation of the effective permittivity of random inhomogeneous media*. Physical Review E **71**(1):016701 (2005).

[260] C. E. Mayr. *Influence of molecular orientation in organic light-emitting diodes*. Dissertation, University of Augsburg (2015).

[261] C.-K. Moon, S.-Y. Kim, J.-H. Lee & J.-J. Kim. *Luminescence from oriented emitting dipoles in a birefringent medium*. Opt. Express **23**(7):A279 (2015).

[262] C.-K. Moon, K.-H. Kim & J.-J. Kim. *Unraveling the orientation of phosphors doped in organic semiconducting layers*. Nature Communications **8**(1):791 (2017).

[263] T. Ferschke, A. Hofmann, W. Brütting & J. Pflaum. *Application of Fluorescent Molecules as Non-Invasive Sensors for Opto-Electronic Characterization on Nanometer Length Scales*. ACS Applied Electronic Materials (2019).

[264] K. Okumoto, H. Kanno, Y. Hamada, H. Takahashi & K. Shibata. *High efficiency red organic light-emitting devices using tetraphenyldibenzoperiflanthene-doped rubrene as an emitting layer*. Applied Physics Letters **89**(1):013502 (2006).

[265] T. Higuchi, H. Nakanotani & C. Adachi. *High-Efficiency White Organic Light-Emitting Diodes Based on a Blue Thermally Activated Delayed Fluorescent Emitter Combined with Green and Red Fluorescent Emitters*. Advanced Materials **27**(12):2019 (2015).

[266] Y.-q. Zheng, W. J. Potscavage, T. Komino, M. Hirade, J. Adachi & C. Adachi. *Highly efficient bulk heterojunction photovoltaic cells based on C 70 and tetraphenyldibenzoperiflanthene*. Applied Physics Letters **102**(14):143304 (2013).

[267] M. Nothaft, S. Höhla, A. Nicolet, F. Jelezko, N. Frühauf, J. Pflaum & J. Wrachtrup. *Optical Sensing of Current Dynamics in Organic Light-Emitting Devices at the Nanometer Scale*. ChemPhysChem **12**(14):2590 (2011).

[268] Y. Luo, H. Aziz, G. Xu & Z. D. Popovic. *Electron-Induced Quenching of Excitons in Luminescent Materials*. Chemistry of Materials **19**(9):2288 (2007).

[269] Y. Luo, H. Aziz, Z. D. Popovic & G. Xu. *Electric-field-induced fluorescence quenching in dye-doped tris(8-hydroxyquinoline) aluminum layers*. Applied Physics Letters **89**(10):103505 (2006).

[270] V. V. N. Ravi Kishore, N. Periasamy, B. Bhattacharjee, R. Das, P. L. Paulose & K. L. Narasimhan. *On the stability and optical spectra of Alq_3 negative ion in solution and thin films*. Chemical Physics Letters **367**(5-6):657 (2003).

[271] P. W. M. Blom, M. J. M. de Jong & M. G. van Munster. *Electric-field and temperature dependence of the hole mobility in poly(p-phenylene vinylene)*. Physical Review B **55**(2):R656 (1997).

[272] G. Horowitz. *Organic Field-Effect Transistors*. Advanced Materials **10**(5):365 (1998).

[273] N. Elgrishi, K. J. Rountree, B. D. McCarthy, E. S. Rountree, T. T. Eisenhart & J. L. Dempsey. *A Practical Beginner's Guide to Cyclic Voltammetry*. Journal of Chemical Education **95**(2):197 (2018).

[274] H. Lee, J. Kwak, C.-M. Kang, Y.-Y. Lyu, K. Char & C. Lee. *Trap-level-engineered common red layer for fabricating red, green, and blue subpixels of full-color organic light-emitting diode displays*. Optics Express **23**(9):11424 (2015).

[275] M. Hirade & C. Adachi. *Small molecular organic photovoltaic cells with exciton blocking layer at anode interface for improved device performance*. Applied Physics Letters **99**(15):153302 (2011).

[276] N. D. Nguyen, M. Schmeits & H. P. Loebl. *Determination of charge-carrier transport in organic devices by admittance spectroscopy: Application to hole mobility in α-NPD*. Physical Review B **75**(7):075307 (2007).

[277] K. L. Tong, S. W. Tsang, K. K. Tsung, S. C. Tse & S. K. So. *Hole transport in molecularly doped naphthyl diamine*. Journal of Applied Physics **102**(9):093705 (2007).

[278] S. Naka, H. Okada, H. Onnagawa, Y. Yamaguchi & T. Tsutsui. *Carrier transport properties of organic materials for EL device operation*. Synthetic Metals **111-112**:331 (2000).

[279] E. W. Forsythe, M. A. Abkowitz, Y. Gao & C. W. Tang. *Influence of copper phthalocynanine on the charge injection and growth modes for organic light emitting diodes*. Journal of Vacuum Science & Technology A: Vacuum, Surfaces, and Films **18**(4):1869 (2000).

[280] J. Scherbel, P. H. Nguyen, G. Paasch, W. Brütting & M. Schwoerer. *Temperature dependent broadband impedance spectroscopy on poly-(p-phenylene-vinylene) light-emitting diodes*. Journal of Applied Physics **83**(10):5045 (1998).

[281] O. Armbruster, C. Lungenschmied & S. Bauer. *Investigation of trap states and mobility in organic semiconductor devices by dielectric spectroscopy: Oxygen-doped P3HT:PCBM solar cells*. Physical Review B **86**(23):235201 (2012).

[282] S. Berleb. *Raumladungsbegrenzte Ströme und Hoppingtransport in organischen Leuchtdioden aus Tris(8-hydroxyquinolin)-Aluminium (Alq_3)*. Dissertation, Universität Bayreuth (2001).

[283] L. Bozano, S. A. Carter, J. C. Scott, G. G. Malliaras & P. J. Brock. *Temperature- and field-dependent electron and hole mobilities in polymer light-emitting diodes*. Applied Physics Letters **74**(8):1132 (1999).

[284] W. D. Gill. *Drift mobilities in amorphous charge-transfer complexes of trinitrofluorenone and poly-n-vinylcarbazole*. Journal of Applied Physics **43**(12):5033 (1972).

[285] N. I. Craciun, J. Wildeman & P. W. M. Blom. *Universal Arrhenius Temperature Activated Charge Transport in Diodes from Disordered Organic Semiconductors*. Physical Review Letters **100**(5):056601 (2008).

[286] M. Neukom, S. Züfle & B. Ruhstaller. *Reliable extraction of organic solar cell parameters by combining steady-state and transient techniques*. Organic Electronics **13**(12):2910 (2012).

[287] H. Kinjo, H. Lim, T. Sato, Y. Noguchi, Y. Nakayama & H. Ishii. *Significant relaxation of residual negative carrier in polar Alq_3 film directly detected by high-sensitivity photoemission*. Applied Physics Express **9**(2):021601 (2016).

[288] S. Altazin, C. Kirsch, E. Knapp, A. Stous & B. Ruhstaller. *Refined drift-diffusion model for the simulation of charge transport across layer interfaces in organic semiconductor devices*. Journal of Applied Physics **124**(13):135501 (2018).

[289] W. E. Spear. *Transit Time Measurements of Charge Carriers in Amorphous Selenium Films*. Proceedings of the Physical Society. Section B **70**(7):669 (1957).

[290] H. Scher & E. W. Montroll. *Anomalous transit-time dispersion in amorphous solids*. Physical Review B **12**(6):2455 (1975).

[291] A. S. Wan, A. J. Mäkinen, P. A. Lane & G. P. Kushto. *Photoemission study of direct hole injection into Alq_3 by PEDOT:PSS polymer anode*. Chemical Physics Letters **446**(4-6):317 (2007).

[292] E. Pavlica & G. Bratina. *Time-of-flight mobility of charge carriers in position-dependent electric field between coplanar electrodes*. Applied Physics Letters **101**(9):093304 (2012).

[293] A. Fleissner, H. Schmid, C. Melzer & H. von Seggern. *Trap-controlled hole transport in small molecule organic semiconductors*. Applied Physics Letters **91**(24):242103 (2007).

[294] B. Chen, C.-S. Lee, S.-T. Lee, P. Webb, Y.-C. Chan, W. Gambling, H. Tian & W. Zhu. *Improved Time-of-Flight Technique for Measuring Carrier Mobility in Thin Films of Organic Electroluminescent Materials*. Japanese Journal of Applied Physics **39**(3A):1190 (2000).

[295] X. M. Ding, L. M. Hung, L. F. Cheng, Z. B. Deng, X. Y. Hou, C. S. Lee & S. T. Lee. *Modification of the hole injection barrier in organic light-emitting devices studied by ultraviolet photoelectron spectroscopy*. Applied Physics Letters **76**(19):2704 (2000).

[296] P. Jeon, H. Lee, J. Lee, K. Jeong, J. Lee & Y. Yi. *Interface state and dipole assisted hole injection improvement with 1,4,5,8,-naphthalene-tetracarboxylic-dianhydride in organic light-emitting devices*. Applied Physics Letters **99**(7):073305 (2011).

[297] F. Wang, X. Qiao, T. Xiong & D. Ma. *The role of molybdenum oxide as anode interfacial modification in the improvement of efficiency and stability in organic light-emitting diodes*. Organic Electronics: physics, materials, applications **9**(6):985 (2008).

[298] J. Kim, Y. Yi, J. W. Kim, S. H. Noh & H. Kang. *Interfacial energetics of NaCl-organic composite layer at an OLED anode*. Journal of Physics D: Applied Physics **45**(45):455304 (2012).

[299] K. Jung, S. Park, Y. Lee, Y. Youn, H.-I. Shin, H.-K. Kim, H. Lee & Y. Yi. *Energy level alignments at the interface of N,N'-bis-(1-naphthyl)-N,N'-diphenyl-1,1'-biphenyl-4,4'-diamine (NPB)/Ag-doped In_2O_3 and NPB/Sn-doped In_2O_3*. Applied Surface Science **387**:625 (2016).

[300] D. Q. Gao, M. Y. Chan, S. W. Tong, F. L. Wong, S. L. Lai, C. S. Lee & S. T. Lee. *Application of an evaporable fluoro-molecule as an anode buffer layer in organic electroluminescent devices*. Chemical Physics Letters **399**(4-6):337 (2004).

[301] H.-Y. Oh, I. Yoo, Y. M. Lee, J. W. Kim, Y. Yi & S. Lee. *The Real Role of 4,4'-Bis[N-[4-{N,N-bis(3-methylphenyl)amino}phenyl]-N-phenylamino] biphenyl (DNTPD) Hole Injection Layer in OLED: Hole Retardation and Carrier Balancing*. Bulletin of the Korean Chemical Society **35**(3):929 (2014).

[302] S. M. Tadayyon, H. M. Grandin, K. Griffiths, P. R. Norton, H. Aziz & Z. D. Popovic. *CuPc buffer layer role in OLED performance: A study of the interfacial band energies*. Organic Electronics: physics, materials, applications **5**(4):157 (2004).

[303] S. Braun, W. R. Salaneck & M. Fahlman. *Energy-Level Alignment at Organic/Metal and Organic/Organic Interfaces*. Advanced Materials **21**(14-15):1450 (2009).

[304] S. Braun, W. Osikowicz, Y. Wang & W. R. Salaneck. *Energy level alignment regimes at hybrid organic–organic and inorganic–organic interfaces*. Organic Electronics **8**(1):14 (2007).

[305] C. Tengstedt, W. Osikowicz, W. R. Salaneck, I. D. Parker, C.-H. Hsu & M. Fahlman. *Fermi-level pinning at conjugated polymer interfaces*. Applied Physics Letters **88**(5):053502 (2006).

[306] E. W. Forsythe, V.-E. Choong, T. Q. Le & Y. Gao. *Interface analysis of naphthyl-substituted benzidine derivative and tris-8-(hydroxyquinoline) aluminum using ultraviolet and x-ray photoemission spectroscopy*. Journal of Vacuum Science & Technology A: Vacuum, Surfaces, and Films **17**(6):3429 (1999).

[307] Q. T. Le, F. Nüesch, L. J. Rothberg, E. W. Forsythe & Y. Gao. *Photoemission study of the interface between phenyl diamine and treated indium–tin–oxide*. Applied Physics Letters **75**(10):1357 (1999).

[308] B. de Boer, A. Hadipour, M. M. Mandoc, T. van Woudenbergh & P. W. M. Blom. *Tuning of Metal Work Functions with Self-Assembled Monolayers*. Advanced Materials **17**(5):621 (2005).

[309] G. Heimel, L. Romaner, E. Zojer & J.-L. Bredas. *The Interface Energetics of Self-Assembled Monolayers on Metals*. Accounts of Chemical Research **41**(6):721 (2008).

[310] M. Braun, J. Gmeiner, M. Tzolov, M. Coelle, F. D. Meyer, W. Milius, H. Hillebrecht, O. Wendland, J. U. von Schütz & W. Brütting. *A new crystalline phase of the electroluminescent material tris(8-hydroxyquinoline) aluminum exhibiting blueshifted fluorescence*. The Journal of Chemical Physics **114**(21):9625 (2001).

[311] M. Sebastiani, L. Di Gaspare, G. Capellini, C. Bittencourt & F. Evangelisti. *Low-Energy Yield Spectroscopy as a Novel Technique for Determining Band Offsets: Application to the c-Si (100)/a-Si:H Heterostructure*. Physical Review Letters **75**(18):3352 (1995).

[312] L. Korte & M. Schmidt. *Investigation of gap states in phosphorous-doped ultra-thin a-Si:H by near-UV photoelectron spectroscopy*. Journal of Non-Crystalline Solids **354**(19-25):2138 (2008).

[313] J.-P. Yang, F. Bussolotti, S. Kera & N. Ueno. *Origin and role of gap states in organic semiconductor studied by UPS: as the nature of organic molecular crystals*. Journal of Physics D: Applied Physics **50**(42):423002 (2017).

[314] G. Horowitz. *Validity of the concept of band edge in organic semiconductors*. Journal of Applied Physics **118**(11):115502 (2015).

[315] J. Gassmann, S. V. Yampolskii, Y. A. Genenko, T. C. Reusch & A. Klein. *Functional Interfaces for Transparent Organic Electronic Devices: Consistent Description of Charge Injection by Combining In Situ XPS and Current Voltage Measurements with Self-Consistent Modeling*. The Journal of Physical Chemistry C **120**(19):10466 (2016).

[316] W. A. Muñoz, X. Crispin, M. Fahlman & I. V. Zozoulenko. *Understanding the Impact of Film Disorder and Local Surface Potential in Ultraviolet Photoelectron Spectroscopy of PEDOT*. Macromolecular Rapid Communications **39**(4):1700533 (2018).

[317] N. A. Ran, J. A. Love, C. J. Takacs, A. Sadhanala, J. K. Beavers, S. D. Collins, Y. Huang, M. Wang, R. H. Friend, G. C. Bazan & T.-Q. Nguyen. *Harvesting the Full Potential of Photons with Organic Solar Cells*. Advanced Materials **28**(7):1482 (2016).

[318] M. Ramar, V. Yadav, R. Srivastava & C. K. Suman. *Effect of titanyl phthalocyanine doping on opto-electrical properties of Alq_3 thin films*. Journal of Materials Science: Materials in Electronics **26**(9):7165 (2015).

[319] M. Bouhassoune, S. van Mensfoort, P. Bobbert & R. Coehoorn. *Carrier-density and field-dependent charge-carrier mobility in organic semiconductors with correlated Gaussian disorder*. Organic Electronics **10**(3):437 (2009).

[320] M. Q. Brewster. *Thermal Radiative Transfer and Properties*. A Wiley-Interscience publication. Wiley (1992).

List of Publications

2020

- T. Linderl, T. Zechel, A. J. L. Hofmann, T. Sato, K. Shimizu, H. Ishii & W. Brütting. *Crystalline vs. amorphous donor-acceptor blends: Influence of layer morphology on the charge-transfer density of states*. Physical Review Applied *Accepted* (2020).

- T. Ferschke, A. Hofmann, W. Brütting & J. Pflaum. *Application of Fluorescent Molecules as Noninvasive Sensors for Optoelectronic Characterization on Nanometer Length Scales*. ACS Applied Electronic Materials **2**(1):186 (2020).

2019

- A. J. L. Hofmann, S. Züfle, K. Shimizu, M. Schmid, V. Wessels, L. Jäger, S. Altazin, K. Ikegami, M. R. Khan, D. Neher, H. Ishii, B. Ruhstaller & W. Brütting. *Dipolar Doping of Organic Semiconductors to Enhance Carrier Injection*. Phys. Rev. Applied **12**:064052 (2019).

2018

- T. Morgenstern, M. Schmid, A. Hofmann, M. Bierling, L. Jäger & W. Brütting. *Correlating Optical and Electrical Dipole Moments To Pinpoint Phosphorescent Dye Alignment in Organic Light-Emitting Diodes*. ACS Applied Materials & Interfaces **10**(37):31541 (2018).

2017

- S. Züfle, S. Altazin, A. Hofmann, L. Jäger, M. T. Neukom, W. Brütting & B. Ruhstaller. *Determination of charge transport activation energy and injection barrier in organic semiconductor devices*. Journal of Applied Physics **122**(11) (2017).

- S. Züfle, S. Altazin, A. Hofmann, L. Jäger, M. T. Neukom, T. D. Schmidt, W. Brütting & B. Ruhstaller. *The use of charge extraction by linearly increasing voltage in polar organic light-emitting diodes*. Journal of Applied Physics **121**(17) (2017).

- S. D. Chavhan, R. Hansson, L. K. E. Ericsson, P. Beyer, A. Hofmann, W. Brütting, A. Opitz & E. Moons. *Low temperature processed NiO_x hole transport layers for efficient polymer solar cells*. Organic Electronics **44**:59 (2017).

2016

- T. Linderl, U. Hörmann, S. Beratz, M. Gruber, S. Grob, A. Hofmann & W. Brütting. *Temperature dependent competition between different recombination channels in organic heterojunction solar cells*. Journal of Optics **18**(2):24007 (2016).

Acknowledgments - Danksagung

An dieser Stelle möchte ich mich bei einigen Personen bedanken, die mich in den letzten Jahren unterstützt und somit zum Gelingen dieser Arbeit beigetragen haben:

- Zunächst bedanke ich mich bei **Prof. Dr. Wolfgang Brütting** für die Aufnahme in seiner Arbeitsgruppe und die Möglichkeit, meine Promotion dort durchzuführen. Insbesondere das mir entgegengebrachte Vertrauen und die stets freundliche und ausgezeichnete Betreuung verdienen meinen Dank, sowie die Freiheit, meine Schwerpunkte in der Forschung selbst zu wählen. Ebenso bedanke ich mich für die Motivation und finanzielle Unterstützung zur Teilnahme an Tagungen im Ausland sowie dem Sommeraufenthalt an der Universität in Chiba, Japan.

- Außerdem bedanke ich mich bei **Prof. Dr. Manfred Albrecht** für die Aufnahme am Lehrstuhl für Experimentalphysik IV.

- I am very grateful to the **Japan Society for the Promotion of Science** (JSPS) to grant me a research fellowship within their JSPS Summer Program 2017. This allowed me to stay at the "Ishii laboratory for organic electronics" at the Chiba University, Japan. My stay there enabled me to conduct the UPS measurements that play a major role in understanding the phenomena observed in this work and awakened my enthusiasm for the Japanese country and culture.

- My sincere thanks are given to **Prof. Dr. Hisao Ishii** and all members of his laboratory for the great support and warm welcome in Japan and his group. Especially **Kohei Shimizu** and **Kaitero Ikegami** deserve words of thank for their unlimited patience and support during the measurements in Chiba. Without their commitment to support me in my research, the UPS measurements would not have been possible. I also want to thank **Ms Kuniko Ito** for her great support and organization during my stay. Also, the visits of **Dr. Tomoya Sato**, **Dr. Yuya Tanaka** and **Kohei Shimizu** in our lab have been very enriching for me.
どうもありがとうございます!

- Zusätzlich bedanke ich mich bei **Prof. Dr. Hubert Krenner** für die Bereitschaft das zweite Gutachten für diese Arbeit zu erstellen.

- Diese Arbeit wäre außerdem nicht möglich gewesen ohne die finanzielle Förderung der **Deutschen Forschungsgemeinschaft** im Rahmen des bilateralen Projektes „CarDyn" (Br 1728/15-1) in Zusammenarbeit mit dem Schweizerischen Nationalfonds.

- Ebenso bedanke ich mich bei meinen schweizer Projektpartnern, **Prof. Dr. Beat Ruhstaller**, **Dr. Simon Züfle** und **Dr. Martin Neukom** von der Fluxim AG bzw. der ZHAW für die hervorragende und freundschaftliche Zusammenarbeit. Die Projekttreffen fanden immer in sehr angenehmer und kreativer Atmosphäre statt. Auch die Möglichkeit, die Entwicklung der Messsysteme mitzuerleben und Ideen zu diversen Testversionen beizusteuern hat mir die Möglichkeit gegeben, viel Erfahrung zu sammeln.

- Auch meinen Studenten **Florian Graßl**, **Vivien Wessels** und **Harry Karpenko** möchte ich für ihre gute und zuverlässige Arbeit danken, die ich weniger als reine Betreuung, sondern vielmehr als Mitarbeit im Team empfand. Sie haben mich bei zahlreichen Messungen tatkräftig unterstützt und somit einen großen Teil zu dieser Arbeit beigetragen. Ebenso unterstützt haben mich **Markus Bierling** während seiner Zeit als HiWi und **Jonas Nekrasovas** während seines Laborpraktikums.

- Ich danke meinen Bürokollegen **Dr. Tobias Schmidt**, **Dr. Björn Gallheber**, **Lars Jäger**, **Manuel Engelmayer**, **Markus Schmid** und **Eduard Meister** für all die interessanten Diskussionen, die gläsernen Anekdoten aus aller Welt und die schöne Zeit in 456.

- Den hilfsbereiten Mitarbeitern der **feinmechanischen** und der **Elektronik-Werkstatt** danke ich für die unkomplizierte und kompetente Hilfe bei der Anfertigung meiner Laborausrüstung. Sie haben große und kleine Projekte, ohne die vieles nicht möglich wäre, immer professionell umgesetzt und mir auch viel über die Herstellung elektronischer und mechanischer Gerätschaften beigebracht.

- Ein herzliches Dankeschön geht auch an meine ehemaligen Kollegen in der Arbeitsgruppe „Organische Halbleiter“, **Dr. Mark Gruber** und **Dr. Ulrich Hörmann**, die mich während meiner Bachelor- und Masterarbeiten betreuten. Ihre Arbeit hat mich letztlich dazu motiviert, selbst die Promotion zu beginnen.

- Ebenfalls unterstützt hat mich **PD Dr. Andreas Opitz**, Humboldt Universität zu Berlin, der mir in Bezug auf die UPS Messungen mit seinem Rat zur Seite stand.

- Ich danke meinen Kollegen in der Organik-Arbeitsgruppe **Dr. Shaimaa M. Abdalbaqi**, **Manuel Engelmayer**, **Markus Schmid**, **Dr. Mark Gruber**, **Thomas Zechel**, **Florian Graßl**, **Dr. Thomas Morgenstern**, **Hongwon Kim**, **Bilal Abbas Naqvi**, **Tassilo Naujoks** und **Prakhar Sahay** für die freundliche Atmosphäre, die gute Zusammenarbeit und die vielen guten Diskussionen. Aber auch für die vielen gemeinsamen Unternehmungen und den vielen Spaß den wir zusammen hatten. Dieser Dank gilt selbstverständlich auch meinen ehemaligen Kollegen **Bert Scholz**, **Sebastian Wehrmeister**, **Stefan Grob**, **Lars Jäger**, **Christian Mayr**, **Dr. Tobias Schmidt**, **Dr. Ulrich Hörmann**, **Dr. Mark Gruber** und **Dr. Theresa Linderl**.

- Besonders bedanken möchte ich mich auch bei **Dr. Theresa Linderl** und **Markus Schmid** für das Korrekturlesen dieser Arbeit.

- Zu danken habe ich auch allen weiteren **Mitgliedern des Lehrstuhls Experimentalphysik IV** für die arbeitsgruppenübergreifende Hilfsbereitschaft und die freundliche Arbeitsatmosphäre. Ebenso danke ich **Prof. Dr. Helmut Karl** und **Dr. Matthias Schreck** für die vielen interessanten Diskussionen. Zusätzlich möchte ich mich insbesondere bei **Wolfgang Reiber**, **Birgit Knoblich**, **Olga Lik**, **Simon Stork** sowie **Bettina Schestak** und **Claudia Löflath** für die große Hilfe bei allen technischen oder verwaltungstechnischen Fragen bedanken. Ohne diese Unterstützung wäre die Arbeit am Lehrstuhl erheblich komplizierter!

- Zuletzt danke ich meiner **Familie** für die viele Freude und die große Unterstützung und den bedingungslosen Rückhalt zu jeder Zeit. Meiner Freundin **Theresa** danke ich im Speziellen für die unendliche Geduld, gerade in letzter Zeit, die viele Freude und die schöne gemeinsame Zeit!